



Tsunami-Seabed Interactions

Larsen, Bjarke Eltard

Publication date:
2018

Document Version
Publisher's PDF, also known as Version of record

[Link back to DTU Orbit](#)

Citation (APA):
Larsen, B. E. (2018). *Tsunami-Seabed Interactions*. Technical University of Denmark. DCAMM Special Report

General rights

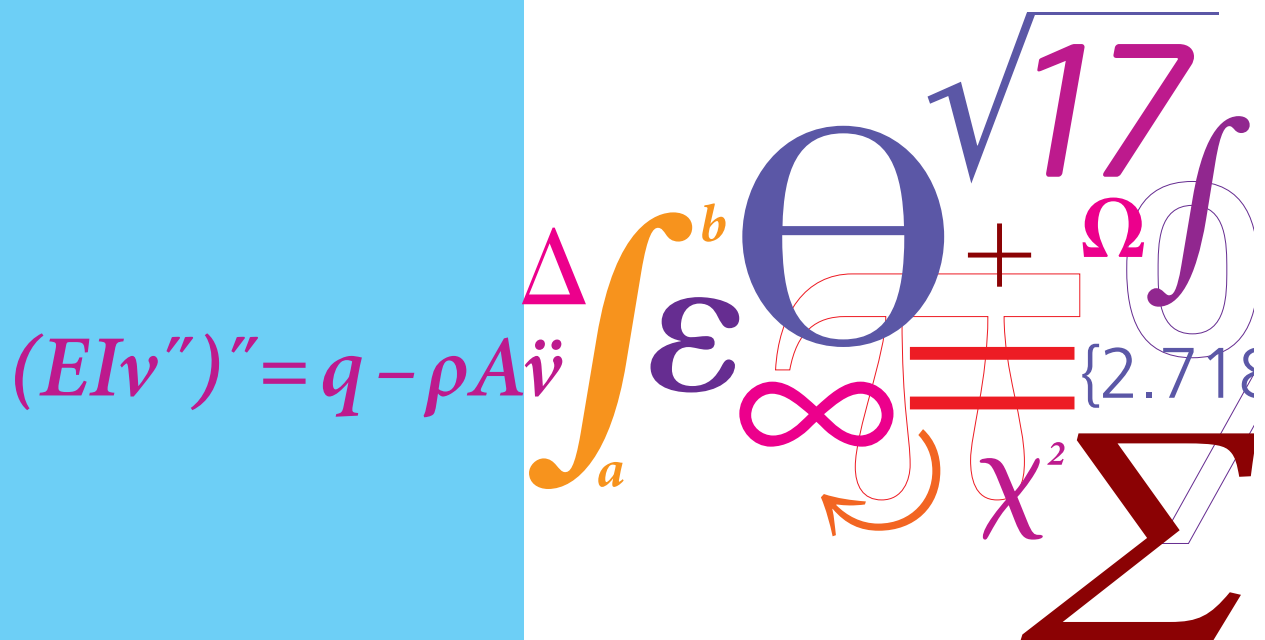
Copyright and moral rights for the publications made accessible in the public portal are retained by the authors and/or other copyright owners and it is a condition of accessing publications that users recognise and abide by the legal requirements associated with these rights.

- Users may download and print one copy of any publication from the public portal for the purpose of private study or research.
- You may not further distribute the material or use it for any profit-making activity or commercial gain
- You may freely distribute the URL identifying the publication in the public portal

If you believe that this document breaches copyright please contact us providing details, and we will remove access to the work immediately and investigate your claim.

Tsunami-Seabed Interactions

PhD Thesis



Bjarke Eltard Larsen
 April 2018

Tsunami-Seabed Interactions

Bjarke Eltard Larsen
DTU Mechanical Engineering
Section of Fluid Mechanics, Coastal and Maritime Engineering
Technical University of Denmark

Main supervisor: Associate Professor David R. Fuhrman
Co-supervisors: Professor Erik Damgaard Christensen
Professor B. Mutlu Sumer

April 2018

Preface

The present thesis *Tsunami-Seabed Interactions* is submitted as one of the requirements for obtaining the degree of Ph.D. from the Technical University of Denmark. The work was performed at the department of Mechanical Engineering, Section of Fluid Mechanics, Coastal and Maritime Engineering with main supervisor Associate Professor David R. Fuhrman and co-supervisors Professor Erik Damgaard Christensen and Professor B. Mutlu Sumer. A thanks go out to all the supervisors. Special thanks to my main supervisor David R. Fuhrman for continued sparring throughout the project. It has been greatly appreciated, and has improved me as an academic.

The external research stay was conducted at Polytechnic University of Catalonia in Barcelona as part of the HYBRID project, which is a part of the H2020 Hydralab+ project. The project was lead by project leader Senior Lecturer Ming Li and principal investigator Lecturer Dominic A. van der A. During the research I took part in both planning and executing the experiments, and have subsequently been involved in the data processing and article writing. Thank you to Ming Li and Dominic A. van der A. for inviting DTU to be part of project, and thank you your guidance during the project. Also thank you to Joep van der Zanden for our collaboration during and after this project. I hope that we will continue the cooperation in the future.

I would also like to thank to Lasse Kærgaard Arbøll and Sarah Frigaard Kristoffersen who conducted the experiments, presented in Chapter 3, as part of their Master thesis. You did an impressive experimental work.

I am also thankful for the cooperation with Johan Roenby who provided me with his newly implemented code and also co-authored Chapter 4.

A thanks goes out to Xerxes Mandviwalla and Niels Gjøøl Jacobsen for sparring on, especially, `openFOAM` related issues. Many implementations would have taken significantly longer, were it not for you. Thanks also to Associate Professor Stefan

Carstensen for continued discussions during the Ph.D.

Finally, thank you to my wife and kids for your support throughout the project. I am sure you now know more about tsunamis than the majority of the population.

The project was funded by the European Union project ASTARTE–Assessment, Strategy And Risk Reduction for Tsunamis in Europe, Grant no. 603839 (FP7-ENV-2013.6.4-3).

The research stay in Barcelona was supported by the European Communitys Horizon 2020 Programme through the grant to the budget of the Integrated Infrastructure Initiative HYDRALAB+, Contract no. 654110, and was conducted as part of the transnational access project HYBRID.

Bjarke Eltard Larsen

April 20, 2018

Contents

Preface	i
Abstract	v
Resume	viii
1 Introduction	1
1.1 Motivation	1
1.2 Background	5
1.3 Problem statement	21
1.4 Outline	23
2 Tsunami-induced scour around monopile foundations	27
3 Experimental study of tsunami-induced scour around a monopile foundation	42
4 Performance of interFoam on the simulation of progressive waves	56
5 On the over-production of turbulence beneath surface waves in RANS models	75
6 Full-scale CFD simulation of tsunamis. Part 1: Model validation and run-up	114
7 Full-scale CFD simulation of tsunamis. Part 2: Boundary layers and bed shear stresses	137
8 Conclusions	152

9 Appendix - Simulation of the Ting and Kirby (1994) plunging breakers experiment	163
References	170

Abstract

Tsunamis are long waves commonly caused by sudden motions of the seabed e.g. due to landslides or earthquakes. The potentially catastrophic impact of a tsunami is well known, and have recently been experienced, with the 2004 Indian Ocean tsunami and the 2011 Tohoku tsunami in Japan, responsible for 230,000 and 20,000 deaths, respectively. These tsunamis also caused severe damages to structures and buildings and eroded entire coastal regions.

While the run-up, inundation, and destructive potential of tsunami events have received considerable attention in the literature, the associated interaction with the sea bed i.e. boundary layer dynamics, induced sediment transport, and resultant sea bed morphology, have received comparably little specific attention. Such issues and processes are important, however, both in assessing potential larger scale deposition and erosion in affected coastal regions, as well as in understanding smaller scale erosion, such as tsunami-induced local scour around coastal and offshore structures. Furthermore, even though the run-up has received considerable attention in the past, detailed descriptions and understanding of how the tsunamis run-up is still lacking. Such an understanding can prove useful when evaluating potential tsunami hazards.

The lack of studies and understanding of the processes are probably due to, the long scales involved, which make it hard study experimentally. Furthermore, commonly used potential flow models do not resolve enough of the physics to provide the necessary insights.

Computational Fluid Dynamics models can, in principle, naturally handle wave propagation and dispersion, resolve both boundary layer dynamics and wave breaking, and could thus be used to study such processes. This present thesis aims at investigating, how primarily numerical but also experimental methods can be improved and used to ultimately increase fundamental knowledge about tsunami-seabed interactions. This involves local scour, run-up behaviour, tsunami-induced boundary layers, bed shear stresses and implications for the resulting sediment trans-

port. The present thesis further aims at using the gained knowledge to improve the prediction of such processes, either through simple empirical relations or the adaptation in "simpler" potential flow models.

The tsunami-induced scour process around offshore monopiles is studied both numerically and experimentally. The tsunamis were represented by time varying currents, which enabled the use of a rigid lid in the numerical simulations and a pump to drive the flow in the experiments. This approach thereby saved computational time and also made reasonably scaled experiments possible. Based on both the simulated and experimental results, details of the scour process is discussed, and a novel engineering approach, for predicting tsunami-induced scour around offshore monopiles is proposed.

To be able to simulate the run-up of tsunamis methodological developments are necessary. The widely used solver `interFoam`, is shown to have big challenges in accurately simulating free-surface waves. The effects of the temporal and spatial resolution on the solution is discussed, and the effects of the discretization practises and iterative solver settings are likewise documented. It is shown how these can be changed to improve the solution.

A previously described, though not well recognised, instability problem of two-equation turbulence closures is further analysed. It is shown that when this type of model is applied to potential flow waves, the instability problem cause the turbulent kinetic energy and eddy viscosity to increase exponentially. This has polluted many simulations of free-surface waves in the past, causing the waves to un-physically decay or arrive at the surf zone already polluted. It is then shown how two-equation turbulence models can be formally stabilized thereby solving this long standing problem.

Numerical simulations of full-scale tsunamis propagating on a flat bed before running up a constant slope region are presented. Both wave shapes and slopes are systematically varied, and the implications on the run-up heights are assessed. Furthermore, detailed descriptions of the run-up sequence for different scenarios are given, and it is discussed when the different run-up scenarios might occur. The importance of the shorter waves, sometimes riding at the front of the main tsunami wave, on the run-up height, inundation speed and local flow velocities, is likewise assessed.

From the same numerical simulations, detailed boundary layer dynamics, resulting shear stresses and implications for sediment transport are described and discussed.

The increased understanding of the tsunami-induced boundary layers, leads to the proposal of engineering approaches for predicting both boundary layer thickness and bed shear stresses beneath tsunami waves. These approaches are formulated such that they may easily be implemented in simpler numerical models, potentially improving their sediment transport predictive capabilities.

Resume

Tsunamier er lange bølger, normalt skabt af en pludselig forskydning af bunden, f.eks. et jordskred eller et jordskælv. Det potentielle katastrofale udfald af en tsunami er velkendt, og blev sidst oplevet med tsunamierne i Det Indiske Ocean i 2004 samt i Japan i 2011, som var skyld i henholdsvis 230.000 og 20.000 dødsfald. De to tsunamier var også skyld i massive skader på bygninger og konstruktioner samt eroderede hele kyststrækninger.

Mens bølgeopskyllet, samt det ødelæggende og dødelige potentiale af tsunamier, har modtaget anseelig opmærksomhed i litteraturen, har den tilhørende interaktion med havbunden (grænselagsdynamikker, sandtransport og resulterende morfologi) modtaget relativt lidt opmærksomhed. Disse problematikker og processer er til gengæld vigtige, både når erosion og aflejring i stork skala skal vurderes, men også i forståelsen af erosion i mindre skala, såsom tsunami-induceret bundudskæring omkring kystnære eller offshore konstruktioner. Selvom bølgeopskyllet har modtaget anseelig opmærksomhed, mangler der stadig en detaljeret beskrivelse- og forståelse af hvordan tsunamier løber op. Sådant en forståelse kan være meget vigtig når tsunamirisici skal vurderes.

Årsagen til disse mangler er til dels, at det er meget svært at studere. De lange skalaer involveret gør det svært at studere disse processer eksperimentelt, og de meget udbredte potentialstrømningsmodeller opløser ikke nok af fysikken til at give den nødvendig viden. Numerisk Fluid Mekanik kan, i princippet, opløse både tsunami bølgegrænselag og bølgebrydning, og kan således bruges til at studere disse processer. Denne afhandling sigter mod at undersøge, hvordan numeriske metoder kan forbedres og anvendes for at opnå fundamental viden om interaktioner mellem tsunamier og havbunden. Dette involverer lokal bundudskæring, bølgeopskylsopførsel, tsunami-inducerede grænselag og bundforskydningsspændinger. Denne afhandling sigter ydermere mod at bruge den opnåede viden til at forbedre evnen til at forudsige sådanne processer, enten gennem simple empiriske relationer eller gennem anven-

delse i potentialstrømningsmodeller.

Den tsunami-inducerede bundudskæringsproces omkring offshore monopæle bliver undersøgt både numerisk og ekseperimentelt. Tsunamierne blev repræsenteret af tidsvarierende strømninger, hvilket gjorde det muligt at bruge et stift låg i simuleringerne, og muliggjorde at bruge en pumpe til at drive strømmingen i eksperimenterne. Som resultat af denne tilgang blev beregningstiden mindre end ellers og det blev muligt at udføre et fornuftigt skaleret eksperiment. På baggrund af simuleringerne og eksperimenterne diskuteres detaljer af bundudskæringsprocessen, og en ny simpel metode til at forudsige tsunami-induceret bundudskæring foreslåes.

For at kunne simulere opløbet af tsunamier er det nødvendigt med metodisk udvikling. Det bliver vist at den meget udbredte model `interFoam` har store udfordringer med at simulere bølger præcist. Effekten af tidslig og rumlig opløsning på løsningen bliver diskuteret og effekten af diskretiseringsmetoder og iterative procedure dokumenteres. Det bliver vist, hvordan disse kan ændres så et bedre resultat opnås.

Et, tidligere beskrevet, om end ikke vel anerkendt, ustabilitets problem af to-lignings turbulens modeller bliver ydeligere analyseret. Når denne type modeller bliver anvendt på potentialstrømningsbølger, får ustabilitets problemet den turbulente kinetiske energi samt hvirvelviskositet til at stige eksponentielt. Dette har forurennet mange hidtidige simuleringer af bølger, og har været skyld i et ikke fysisk fald i bølgehøjder eller at bølger ankommer forurennet til brændingen. Det bliver herefter vist hvordan denne type modeller kan stabiliseres, og hermed bliver et problem som har stået uløst igennem mange år løst.

Fuldskala simuleringer af tsunamier som propagerer på en flad bund, før de løber op ad en konstant skrånende region bliver præsenteret. Både bølgeformer og hældninger varieres systematisk og effekten på opløbshøjde bliver vurderet. Detaljerede beskrivelser af forskellige opløbsscenarier bliver præsenteret, og det bliver diskuteret hvornår de forskellige scenarier opstår. Ydermere diskuteres betydningen af de korte bølger, som nogen gange rider på den meget længere hovedbølge, på bølgeopløbet.

På baggrund af resultater fra de samme simulering diskuteres detaljer af tsunami-grænselagsdynamikker, resulterende bundforskydningsspændinger og implikationer for sandtransporten. Den øgede forståelse af tsunami-induceret grænselag fører til et forslag til en simpel metode der kan bruges til at forudsige både grænselagstykkelse samt bundforskydningsspændinger under tsunamier. Denne metode er formuleret på en måde, så den nemt kan implementeres i simple numeriske modeller.

Chapter 1

Introduction

1.1 Motivation

One of the most catastrophic natural disasters in recent history is the Boxing Day Indian Ocean tsunami in 2004, where it was estimated that approximately 230,000 were killed (Suppasri et al., 2012). On December 26'th 2004, outside the western coast of Indonesia, an area about 1300 km long and 150 km wide moved up 5 m vertically and 11 m horizontally over a period of about 7 minutes (Song et al., 2005). This resulted in a large tsunami wave, propagating inside the bay of Bengal as well as across the Indian Ocean, causing damages all the way at the coasts of Somalia. Inside the Bay of Bengal, as well as on the coast of Indonesia, the destructions were naturally even more severe. This is illustrated in Figure 1.1, where satellite images of Lhoknga (Indonesia), taken before and after the tsunami hit, are shown. Here, it can clearly be seen that little remains of the city after the tsunami hit, and almost all trees and vegetation were washed away. Behind the town, a few kilometres inland, it can be seen that part of the area is still covered with water three days after the tsunami hit. In this area the coast locally retracted up to 200 m (Paris et al., 2009; Borrero et al., 2006). A study by Leone et al. (2011) reveal that from the coast of Banda Aceh (Indonesia) to approximately 2.7 km inland almost all buildings were destroyed, as a result of the Indian Ocean tsunami.

In addition to the Indian Ocean tsunami, many people probably remember the Tohoku tsunami in Japan in 2011, where, according to Suppasri et al. (2012), approximately 20,000 were killed. Two other "recent" tsunami events, with severe amounts of fatalities, were the Messina tsunami in 1908, where according to Billi et al. (2008) more than 60,000 were killed and the 1896 Sanriku tsunami in Japan, where Løvholt



December 29, 2004



January 10, 2003

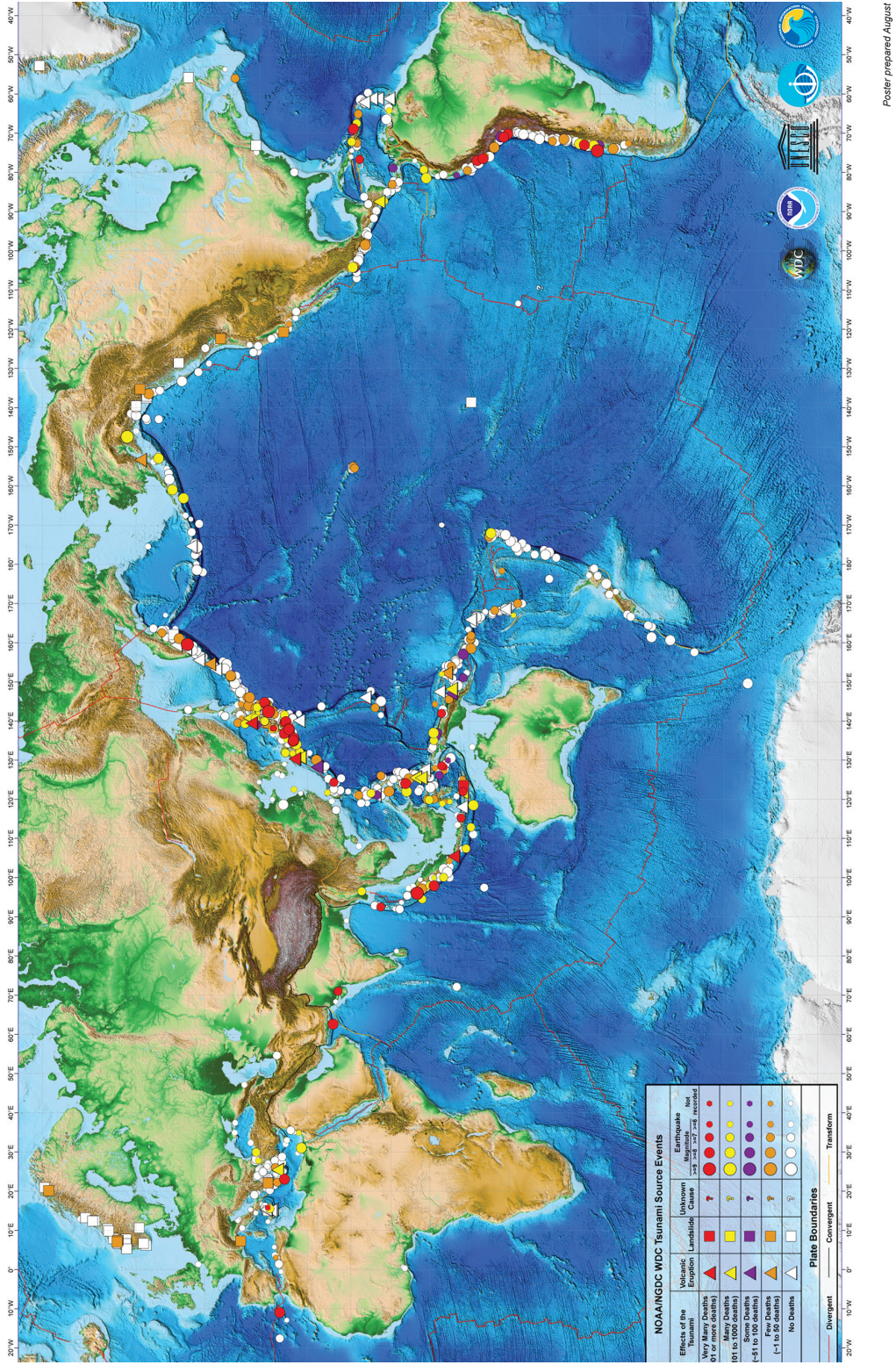
Figure 1.1: Before (bottom) and after (top) satellite images of Lhoknga, Indonesia. Image taken from NASA (2005)

et al. (2012) reported 27,000 fatalities. The four above tsunami events highlight the potential danger of the tsunamis, but also their relative frequent occurrence, four very large tsunamis (in terms of fatalities) within the last 130 years. These four were highlighted because of the large number of fatalities. There have been other

very large tsunamis with not nearly as many fatalities. One of the reasons for this is probably that tsunami warning systems and tsunami protection have improved. For instance, the 2011 Tohoku tsunami was a very large tsunami and many more could have died (not stating that the 20,000 fatalities from this tsunami are a small number). With the amount of tsunamis that have hit Japan in the past, however, Japan have taken a lot of measures to protect themselves against tsunamis, which probably saved a lot of human lives.

Tsunamis are even more frequent than suggested from the above. From 2000-2015, there have been 15 tsunamis, equivalent to one per year (Levin and Nosov, 2016). Of these, in addition to the Indian Ocean tsunami and the Tohoku tsunami, it is worth mentioning the 2006 Pangandaran tsunami near Indonesia, the 2009 Samoa tsunami, the 2010 Chilean tsunami and the 2010 tsunami near Sumatra. These were responsible for killing approximately 800, 200, 500 and 400 people respectively (Levin and Nosov, 2016). Although far from as destructive as the Boxing Day tsunami and the Tohoku tsunami, still catastrophic events. To further highlight the high frequency of tsunamis, Figure 1.2 shows the occurrence of Tsunamis ordered by death toll and tsunami source, covering a period from 1410 BC to 2011 AD. Here, it can be seen, that in addition to the four previously mentioned extreme tsunamis, the world has experienced 36 tsunamis with death tolls of more than 1,000 and 56 tsunamis with 101-1,000 fatalities. The high frequency and potential catastrophic impact of tsunamis show the importance of tsunami research both in terms of warning systems, impact assessments and risk analysis.

The fatalities are naturally the most horrifying of a tsunami event, but in addition, they have a potential large and long term effect on entire coastal regions, as can be seen from Figure 1.1. The tsunamis likewise destroy buildings and structures. Scouring was by Jayaratne et al. (2016) identified as the most frequent failure mechanism of buildings and structures in the 2011 Tohoku tsunami. Despite this, the associated interaction of the tsunami with the sea bed i.e. boundary layer dynamics, induced sediment transport, and resultant sea bed morphology, have received relatively little specific attention. These processes are important, however, both in assessing potential larger scale deposition and erosion in affected coastal regions, as well as in understanding smaller scale erosion, such as tsunami-induced local scour around coastal and offshore structures. Fundamental knowledge about tsunami-seabed interactions is thus still lacking, inspiring the present thesis.



Poster prepared August

Figure 1.2: Tsunami incidents ordered by death toll and tsunami source from 1410 BC to 2011. Image taken from NOAA (2011)

1.2 Background

This section will provide a general overview of tsunami physics and research, but with special focus on issues involving tsunami-seabed interactions, that is, how the seabed affect the tsunami wave and in turn how the tsunami wave affect the seabed.

Tsunamis are long waves primarily caused by a sudden motion of the seabed, e.g. an earthquake or a landslide, and according to van Dorn (1965), it means "Harbour wave" in Japanese. Following the generation, the tsunami propagates in deep water, often in the form of a leading wave, followed by several smaller trailing waves. The leading wave in deep water is very long, with the wave length (L) the order of hundreds of kilometres, but not very high, with wave heights (H) rarely exceeding one meter. Thus, in the deep ocean, these waves can hardly be detected if standing on a ship. When the tsunami enters shallow water, it shoals, and the wave length decreases while the wave height increases. Ultimately, the tsunami runs up the coast and finally draw down. The process from generation to run-up is illustrated in Figure 1.3. In this figure, the two terms run-up height and inundation distance are also illustrated. The run-up height marks the vertical height above sea level at the furthest point reached by the tsunami inland. The inundation distance is a measure of furthest horizontal point reached by the tsunami.

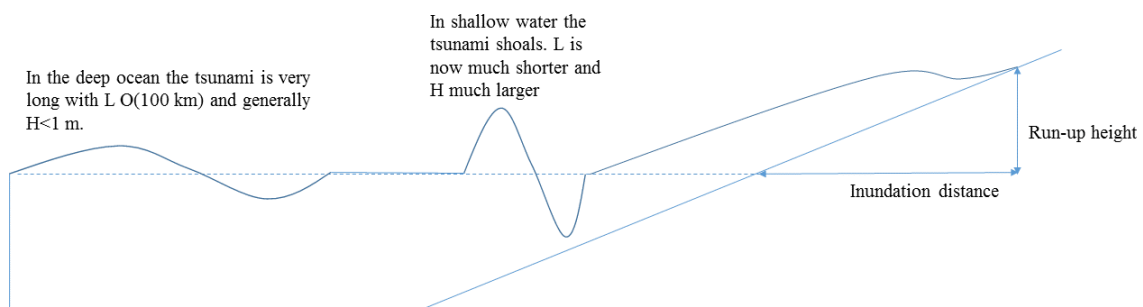


Figure 1.3: A conceptual drawing of the tsunami propagating from deep ocean to the shore.

While propagating, the tsunami might also be subject to refraction, where the part of the tsunami travelling in deeper water travels faster than the part in shallow water. This can turn and reshape the tsunami. When the tsunami encounter islands or peninsulas it can also be subject diffraction effects, spreading the tsunami.

The run-up stage is obviously the most destructive, but according to Fuhrman and Madsen (2009) as well as Levin and Nosov (2016), this process cannot be fully understood before the preceding stages, i.e. generation and propagation, are fully

understood. Naturally, the initial tsunami research was therefore focused on the generation and propagation of tsunamis. This background section will first introduce the research on generation, propagation and tsunami wave shapes. Then the research on run-up and inundation will be presented, followed by a section presenting the research on sediment transport and boundary layers. Many of the studies covered in this background chapter have contributed to more than one of these three themes, but this is a way to structure the review of the large amounts of tsunami literature. Other areas of the tsunami research, such as warning systems, protection systems, rebuilding after a tsunami attack, long and short term societal impacts, detailed studies on earthquakes and land slides, while being interesting and worth researching, will not be covered in this thesis.

Generation, propagation and wave shapes

In general, tsunamis are generated by a sudden displacement of large amounts of water. This could be the result of earthquakes, land slides, ice falls or volcanic eruptions. The most frequent tsunami source is earthquakes, which, according to Tang (2017), have caused 87 % of the generated tsunamis the last approximately 4,000 years.

The earliest work focused on tsunamis generated as an impulsive movement of the bed (similar to an earthquake). This was done using analytical studies by Kajura (1963), van Dorn (1965), Braddock et al. (1973) and according to Madsen and Schäffer (2010) in Carrier (1971). Tsunamis generated by an impulsive movement of the bed was also studied using both analytical and experimental methods by Hammack (1973), Segur (1973), Hammack and Segur (1974) and Hammack and Segur (1978). The latter four studies represent an important milestone in the tsunami research, as they found that a positive initial surface disturbance will eventually lead to the formation of solitons or solitary waves (Madsen et al., 2008). This finding, together with real tsunami observations of series of smaller waves hitting the coast, have resulted in many studies using the solitary wave as representative of the tsunami see e.g. Goring (1978), (Synolakis, 1986, 1987), Yeh et al. (1994), Briggs et al. (1995), Liu et al. (1995), Li (2000), (Li and Raichlen, 2001, 2002, 2003), Tonkin et al. (2003), and Kobayashi and Lawrence (2004). In the study by Madsen et al. (2008) the use of solitary waves as a representation of tsunamis was questioned. They showed that the scales involved with a solitary wave are not representative of actual field scales, and are more related to wind waves than actual tsunamis.

The problem is, that with the solitary wave, the wavelength cannot be determined independent of the wave height. This means that on the continental shelf, leading tsunami waves are much longer than solitary waves. Moreover, they showed that the propagation distance required for a solitary wave to develop were longer than the circumference of the earth, and therefore they concluded, that real tsunamis will not turn into solitary waves. Tsunamis can, however, turn into undular bores in shallow water, which has also been seen at many coasts. For a more in-depth discussion of the solitary wave paradigm for tsunami research, please see Madsen et al. (2008).

Although solitary waves cannot be viewed as representative of tsunamis, the research preformed is still valid for the physics of solitary waves, and the methods developed have also, to some degree, been used as an inspiration in more recent tsunami research. Furthermore, solitary waves can also be very useful in terms of model validation, something which will also be used in this thesis.

The process of tsunami generation and propagation is still being studied analytically. Clarisse et al. (1995) furthered the work of Kajura (1963) and developed uniform asymptotic solutions to the Cauchy-Poisson problem in both one and two dimensions. This was also done by Berry (2005) seemingly unaware of the earlier contribution by Clarisse et al. (1995) (Madsen et al., 2016). Very recently Madsen et al. (2016) generalized these solutions to work for arbitrary initial disturbances and also work for varying bathymetries. Their results compared extremely well with a high order Boussinesq model, and much better than a non linear shallow water (NLSW) model, in a controlled environment with the tsunami propagating on a flat bed. This is indeed an impressive result, as the semi-analytical approach by Madsen et al. (2016) is much faster than simulating the process with a NLSW model or a Boussinesq model. When comparing with real tsunami measurements, neither the analytical model nor the NLSW model performed particularly well. This was partly explained by the simple model not being able to handle refraction and diffraction effects, which are clearly present. It was further argued that the source used to generate the tsunami was perhaps not accurate enough, as the linear shallow water (LSW) model and Boussinesq model, employed by Løvholt et al. (2012) performed a lot better in the simulations of the same event. Despite the far from optimal comparison with real measurements, the good comparison in a controlled environment, shows that there is still room for analytical methods in research on tsunami propagation.

There have also been a lot of studies reporting field measurements of tsunami surface elevations. These measurements have in past primarily been done near the shore,

see e.g. van Dorn (1965). Recently, as highlighted by Bernard et al. (2006), reliable measurements of tsunami surface elevations in the deep ocean have also been performed. This is actually an impressive achievement as the tsunami wave heights in the deep ocean are small. One can easily imagine the difficulty of extracting a tsunami wave signal with a wave height $O(0.5\text{m})$ from the general sea-state, which naturally includes tidal changes and shorter but higher waves. In recent studies, (e.g. Synolakis and Kong (2006) and Kawai et al. (2013)) the spatial distribution of surface elevation measurements has become very high. The high spatial resolution of surface elevation measurements results in a much higher quality of real time tsunami forecasting, as shown in Titov et al. (2016).

The field studies enable a better understanding of the variety of realistic tsunami signals. In an analytical study on run-up Madsen and Schäffer (2010) suggested to represent the tsunamis either as long sinusoidal waves, single waves or N-waves. Single waves are similar in shape to the solitary waves, but the period and wave height can be determined independently, ensuring the possibility of obtaining proper scaling. The N-waves are the summation of a positive and negative single wave and can be used to characterise a leading depression or leading elevation tsunami. Chan and Liu (2012) were inspired by Madsen and Schäffer (2010) and showed that the summation of three single waves (either positive or negative) gave a realistic representation of the 2011 Tohoku tsunami. These studies are significant, as they show the variety of realistic tsunami signals, and also enable researchers to study tsunamis by purely considering the wave shape and not the (traditional) generation phase.

Disregarding the traditional generation phase, whether it be by earthquakes or landslides, and attempting to reproduce realistic tsunamis experimentally, have been done in a number of studies. Rossetto et al. (2011) showed that a properly scaled tsunami wave could be made using a pneumatic wave generator. Another approach was attempted by Goseberg et al. (2013), who used a pump to generate properly scaled long waves. Finally, Schimmels et al. (2016) and Sriram et al. (2016) were able to generate properly scaled tsunami signals in the large wave flume in Hannover, using a wave paddle. These studies were primarily concerned with showing that properly scaled tsunamis could be generated, but do show promise for the study of tsunamis in a laboratory setting. It should be said, however, that the required length of the flume, if wanting to house the entire length of the tsunami wave, is still extremely long. Of the above, only the approximately 300 m long flume in the studies by Schimmels et al. (2016) and Sriram et al. (2016) was long enough to

house the entire tsunami wave. Few other properly scaled experimental studies on tsunamis exists, and these will be discussed in more detail in the following subsection on run-up and inundation.

The generation and propagation of tsunami waves have also been studied numerically, primarily using NLSW models or Boussinesq models. These models come from a depth averaging of the Navier-Stokes equations. In the NLSW models, the pressure is assumed to be hydrostatic, whereas in the Boussinesq models, approximations to the non-hydrostatic pressure is kept, which enable these models to describe dispersion. According to Levin and Nosov (2016), the first attempt to model tsunami propagation was done by Aida (1974). Since then numerous NLSW models have been developed. One of these is the TUNAMI model by Goto and Ogawa (1997). Another is the Method Of Splitting Tsunami (MOST) model, originally developed by V. Titov and I. Gonzalez (1997) and Titov and Synolakis (1998). MOST is now being used for tsunami warning systems in conjunction with Deep-ocean Assessment and Reporting of Tsunamis (DART) buoys (Titov et al., 2016). Another widely used model for studying generation and propagation is COrnell Multigrid COupled Tsunami model (COMCOT) developed by Liu et al. (1998). In addition to the models mentioned above, there exist a substantial number of NLSW models, which have been used to simulate the generation and propagation of tsunamis. For a more in-depth review see Levin and Nosov (2016).

Despite not being able to handle dispersion, NLSW models have, as stated by Madsen et al. (2016), had reasonable success in simulating geophysical tsunamis. Over long propagation distances, however, a dispersive tail might evolve. Furthermore, at the steep tsunami wave front, where the undular bores might form, dispersion likewise become important. Dispersion can obviously be handled by Boussinesq models. Lynett and Liu (2002) and Lynett and Liu (2005) used Boussinesq models to simulate landslide generated tsunamis and Fuhrman and Madsen (2009) presented results using a high-order Boussinesq model, and showed that it was capable of simulating generation, subsequent propagation and run-up from both landslide and earthquake generated tsunamis. Glimsdal et al. (2013) also studied landslide generated tsunamis and discussed the importance of dispersion when simulating tsunami waves. They concluded, that for land slide generated tsunamis as well as smaller earthquakes, dispersive effects are important, whereas for larger earthquakes they are primarily important in the near-shore region where undular bores may show up. These findings have partly been backed up by Løvholt et al. (2012) and Grilli et al. (2013) who both simulated the earthquake generated Tohoku 2011 tsunami

using Boussinesq models. They showed that dispersive effects were small close to the generation. They also showed, however, that after travelling a sufficient distance dispersive effects accumulated and became important. Grue et al. (2008) studied the formation of undular bores in the strait of Malacca, and showed that if propagating sufficiently long in shallow water, the wave front will steepen and an undular bore will form. In straits like this, they argued, the effect of dispersion therefore cannot be neglected. Kim and Lynett (2011) studied, generally, the formation of undular bores and compared the ability of a NLSW model to that of a Boussinesq model. They concluded, in relation to tsunamis, that an undular might form, and that only the Boussinesq model was able to capture this. The NLSW model on the other hand under-predicted the surface elevations and velocities of the wave front.

Numerically the process can also be studied using computational fluid dynamics (CFD). CFD has been used to study tsunamis, but the research has mostly focused on run-up and inundation, and the studies using CFD, will therefore be discussed in the coming subsection.

Run-up and inundation

In this section the research on run-up and inundation will be reviewed. For an in-depth study of the history of tsunami hydrodynamic research until 2006, with a special focus on run-up, please see Synolakis and Bernard (2006). As already noted, the solitary waves do not properly represent the scales of real geophysical tsunamis, and therefore the present section will focus on run-up and inundation of non solitary waves.

Following a tsunami event, the run-up height and inundation distance are often surveyed, as was done with the 1992 Nicaragua tsunami (Baptista et al., 1993), the 1998 Papua New Guinea tsunami (Lynett et al., 2003), the 2004 Indian Ocean tsunami (Borrero et al., 2006; Synolakis and Kong, 2006; Shibayama, 2015) as well as the 2011 Tohoku tsunami (Mori et al., 2011), just to name a few. These field surveys provide valuable information on tsunami hazards and also provide useful benchmarks for numerical models. In addition to the field surveys, satellite images have provided detailed inundation maps and information of offshore wave heights. Comparing with run-up heights and inundation distances of such surveys have often been the goal of many NLSW models and Boussinesq models, see e.g. NLSW simulations by Titov et al. (2005) and Tang et al. (2012) or the Boussinesq simulations by Løvholt et al. (2012), Grilli et al. (2013), Park et al. (2015).

There have, however, also been a big interest in trying to get a more fundamental understanding of the run-up by using analytical methods, instead of merely reproducing past events. The analytical study on run-up of long waves dates back to Green (1838), who derived a solution for long linear waves propagating towards the shore on a constant slope. His solution was, however, not valid at the shoreline where the amplitude goes to infinity. The solution was extended by Lamb (1932), such that it was valid at the shoreline, but still only for a constant slope. Keller and Keller (1964) further extended the analysis and derived a solution for linear waves propagating on an initial flat bed before running a constant slope. Carrier and Greenspan (1958) derived the solution for non-linear waves propagating on a constant slope. Later, Synolakis (1987) combined the non-linear solution of Carrier and Greenspan (1958) with the linear solution of Keller and Keller (1964) at the toe of the slope. In 2008, Madsen and Fuhrman (2008) extended the work of Synolakis (1987), and formulated the solution for the run-up of sinusoidal waves in terms of the surf similarity parameter. This gave run-up elevations and inundation speeds as functions of the surf similarity parameter, and based on these expressions they were able to offer a suggestion to why some beaches were more devastated than others during the 2004 Indian Ocean tsunami. In a similar fashion Madsen and Schäffer (2010) derived analytical expressions for run-up elevations and inundation speeds of both single waves, N-waves and sinusoidal waves, expressed in terms of the surf similarity parameter. Their solutions assumed a linear wave at the toe of the slope and satisfied the NLSW equations at the slope. These expressions have been shown to be able to accurately predict run-up in tsunami experiments (see e.g. Goseberg (2013) and Drahne et al. (2016)). More recently, Chan and Liu (2012) expanded these solutions to work for other general wave shapes.

Experiments regarding tsunami run-up, not using solitary waves, have been done primarily using bores or with long wave experiments. Matsuyama et al. (2007) performed a properly scaled tsunami experiment in their 200 m long wave flume. The waves were sinusoidal and propagated first on a flat bed, before running up a constant 1/10 slope and then finally another constant slope region, with slopes ranging from 1/100–1/200. The waves, while propagating, developed into undular bores, which shoaled and ultimately broke. In this study, however, they did not focus on run-up height, but rather wave transformation, wave breaking and velocities during breaking. To my knowledge, this is the first experiment of its sort where undular bores show up in a run-up related tsunami experiment. Baldock et al. (2009) studied the run-up of breaking tsunami fronts (using breaking bores) and came up with a simple empirical relationship for the run-up height based solely on the bore height

at the still water level. Using the pump driven wave generation approach described in Goseberg et al. (2013), Goseberg (2013) studied the reduction in run-up heights due to beach front developments. He found that, without structures on the beach the analytical expression by Madsen and Schäffer (2010) matched well the experimental run-up heights. Furthermore, he found that buildings on the beach front could reduce run-up height as well as draw-down speed significantly. Drahe et al. (2016) also used the pump driven wave generation approach described in Goseberg et al. (2013). They were able to generate properly scaled sinusoidally looking waves, propagating on a constant depth running up different constant slope beaches. Their experimental results matched well with the analytical run-up expressions derived by Madsen and Schäffer (2010). Charvet et al. (2013) performed long wave experiments, using the method by Rossetto et al. (2011) to generate the waves. They argued that the submerged part of the beach was a more appropriate parameter than the water depth for the normalisation of the wavelength for wave classification. Furthermore, they found that the run-up scaled with \sqrt{A} for very long waves, where A is the amplitude of the incoming wave. In Schimmels et al. (2016) and Sriram et al. (2016) waves propagated on a flat bed, before running up a 1/6 slope. Here the run-up height was not measured, but they demonstrated the splitting of the wave front into shorter waves, similar to Matsuyama et al. (2007), and they also showed the wave reflection from the steep slope.

Numerically, NLSW models have been used a lot to simulate the run-up of tsunamis. Titov and Synolakis (1997) simulated 1993 Hokkaido-Nansei-Oki tsunami using a NLSW model, solving both horizontal directions. Their modelled inundation distances, run-up heights and inundation speeds matched well with field measurements. They thus showed the potential of NLSW models in modelling propagation and inundation of tsunamis. Arcas and Titov (2006) simulated the 2004 Indian Ocean Tsunami using the MOST code focusing on Sri Lanka. They demonstrated that the code showed good agreement with measured surface elevation in offshore regions. They were only able to show good agreement between modelled and surveyed arrival times in one of the three surveyed sites, however. In contrast, the wave heights in these sites still matched well. Tang et al. (2009) showed the ability to reproduce well propagation and run-up of fourteen historical tsunamis. In Tang et al. (2012) measurements from two DART buoys were used for quantifying tsunami energy and the modelled inundation distances compared well with the measured for the 2011 Tohoku tsunami. The above mentioned NLSW studies are by no means exhaustive and numerous additional studies exist (again see Levin and Nosov (2016)).

The run-up process have also been studied using Boussinesq models. Madsen and Fuhrman (2008) used the their high order Boussinesq model to simulate the run-up of long sinusoidally shaped waves, and their numerical results matched well their analytical solution. Løvholt et al. (2012) simulated the Tohoku tsunami, by trying to reconstruct the earthquake. They came up with four different earthquake scenarios, and found one of them to yield good comparison with field measurements, and concluded that the model could be used for a rapid hazard assessment, as the bathymetry used was rather coarse and based on freely available data.

Lynett and Liu (2005) studied landslide generated tsunami run-up process using a Boussinesq model and came up with empirical expressions for the run-up height as a function of non-dimensional slide thickness, front and back lengths of the slide, the steepness of the slide, the aspect ratio of the slide, the specific gravity of the slide material and finally the slope of the beach the tsunami is inundating.

Park et al. (2015) used the Boussinesq model COULWAVE by Lynett et al. (2002). They compared their modelled run-up height with the analytical solution from Madsen and Schäffer (2010). In the non-breaking region very good agreement between the modelled results and the analytical expression was achieved. They concluded, however, that the breaking criterion from Madsen and Schäffer (2010) was inaccurate, and that the predicted run-up height, using this expression, would lead underestimations of the run-up heights. They further argued, that the friction at the bed could have potential impact on the run-up height, especially in relation to when the waves would break. They showed that adding bed friction moved the breaking to higher surf-similarity parameters. Furthermore, they argued, that the idealistic case from Madsen and Schäffer (2010) was not realistic, and employed a compound setup, with a constant depth, followed by a constantly sloping offshore region as well as another constantly sloping onshore region. They derived a new empirical expression, which they showed compared well with field measurements from the Tohoku 2011 tsunami. They argued that these expressions could work well to estimate preliminary run-up heights, especially in situations where detailed topography is not available. Other studies using Boussinesq models to simulate tsunami run-up include Grilli et al. (2013) and Ioualalen et al. (2007)

CFD studies on tsunami run-up are few. Horrillo et al. (2006) simulated the propagation of the Indian Ocean tsunami using both a NLSW model, a Boussinesq model and a volume of fluid (VOF) - Reynolds-averaged Navier Stokes (RANS) model. They concluded that for many practical purposes the NLSW models was sufficiently accurate, but over long propagation distances dispersion became important, which

only the Boussinesq and the RANS model could handle. Horrillo et al. (2006), however, did not go into details regarding the simulated run-up with the RANS model. Biscarini (2010) first validated their VOF model against by comparing with video sequences from an experimental landslide generated tsunami. She was subsequently able to accurately predict the run-up height of the 1958 Lituya Bay (Alaska) landslide generated tsunami. Montagna et al. (2011) validated their CFD model (Flow 3D) with an experimental landslide generated tsunami. They concluded that the model was able to accurately reproduce surface elevations near the generation as well as in inundated areas, but did not proceed to simulate full-scale tsunami events. Tomita and Takahashi (2014) used the STOC-IC model, developed by Tomita et al. (2006). It solves the RANS equations, but the free-surface is solved for using the depth-averaged continuity equation. This means that this model cannot handle wave breaking, without a breaking criterion. They were able to accurately reproduce an experiment where undular bores showed up at the tsunami wave front. Finally, Qu et al. (2017) compared run-up of properly scaled tsunamis with those obtained using a solitary wave. They concluded, similar to many others, that there were great differences between the solitary waves and the properly scaled tsunami waves.

Sediment transport and Boundary Layers

This section will describe the literature on tsunami induced sediment transport and boundary layers. To structure the section, the processes are divided into local processes, large scale processes and boundary layer dynamics.

Local processes

When the tsunami interacts with a structure, there will be a changed flow pattern locally. Streamlines contract, there will be stagnation point in front of the structure, the structure can induce a down-flow and vortices can be shed from the structure. All these effects, have an influence on the local bed shear stress, and thus sediment transport, which can result in scouring around the structure. Scour is potentially damaging, and was rated the most common failure mechanism of coastal structures from the 2011 Tohoku tsunami event in the survey by Jayaratne et al. (2016). Other surveys have been conducted focusing on scour. Fraser et al. (2013) reported tsunami damages to coastal defences and buildings as a result of the 2011 Tohoku tsunami. They showed both the importance of high vertical buildings for evacuation and also showed large scouring around numerous buildings. Bricker et al. (2012) conducted a

field study of scour depths measured on the landward side of seawalls and floodwalls, as well as beside a building foundation footing, from the 2011 Tohoku tsunami. They concluded that existing methods were not capable of accurately predicting tsunami induced scour. Other field studies include Wilson et al. (2012), who studied scour and deposition within harbors, and concluded that the tsunami currents were magnified near the harbour entrance causing increased scouring. Around the edges of the erosive current, however, sediment deposited.

Tsunami-induced scouring has also been investigated using experimental methods. Chen et al. (2013) conducted an experimental study on tsunami-induced scour around coastal roadways, and concluded that roads positioned half the inundation distance were most vulnerable. Furthermore, they concluded that the largest scouring occurred at the seaward side. Chen et al. (2016) studied experimentally the scour around a breakwater, but used CFD to visualize the flow field. The incoming waves were solitary waves, but the authors acknowledged that these did not scale well. Wang et al. (2016) studied, both experimentally and numerically, tsunami induced scour behind a seawall. They used an incompressible smoothed particle hydrodynamics (ISPH) model, and coupled it with an erosion model. Their incoming flow was simply a continuous overflow. They found that their numerical model compared well with experiments and further concluded that there was a linear relationship between overflow depth and scour depth on the lee-side of the wall.

Tsunami-induced scour around monopiles is an interesting topic on its own, as monopiles can represent either bridge piers or offshore wind turbines. Tonkin et al. (2003) studied the scour promoted by incident solitary waves around a cylinder on a sloping beach, where the cylinder was mounted near the shoreline. They concluded that the scouring at the front side of the monopile could be explained by standard shear stress explanations, but that the rapid scouring on the backside was primarily caused by the pore-pressure gradient doing back flow. Nakamura et al. (2008) studied scour around a square pile induced by solitary and long waves. Here the monopile was likewise standing onshore, and the waves were both breaking and non-breaking. They concluded that the long waves resulted in significantly more scour than the shorter solitary waves. The experiments by Tonkin et al. (2003) were also simulated numerically using a NLSW model by Pan and Huang (2012), with the intent of simulating tsunami-induced scour around bridge piers. The tsunami-induced scour process around onshore monopiles has also been studied by Shafiei et al. (2015) and Lavictoire (2015) who used bores to represent the tsunamis and both produced empirical formula for the prediction of the scour depth.

As seen from the above, the number of studies on tsunami-induced scouring is relatively low and many of the studies have used solitary waves, which do not scale well. Furthermore, the above studies have all treated tsunami-induced scour around on-shore monopiles, and to my knowledge no studies on tsunami-induced scour around offshore monopiles exists.

Larger scale processes

As already mentioned, tsunamis can potentially course large scale beach erosion and have a long standing effect on entire coastal regions. Following the recent tsunami events, with the growth satellite images, estimating the impact of a tsunami event on coastlines have become easier. In addition to this, many coast are frequently being surveyed, and therefore knowledge about the pre tsunami coastal profile is available in many places. In the Takata Matsubara area (Japan) it was reported that 90 % of the beach disappeared during the Tohoku tsunami and it was estimated that the total volume of morphological change in this area was $1.9 \times 10^6 \text{ m}^3$ (Yamashita et al., 2016). Before and after satellite images of the beaches of Banda Aceh (Indonesia) from the 2004 Indian Ocean tsunami likewise show large scale erosion, with the coast locally retracting up to 200 m (Paris et al., 2009; Borrero et al., 2006). In Udo et al. (2016), changes in the topography before and after the Tohoku tsunami attack, was reported of the Rikuzen-Takata Coast. In some places more than 6 m of sand in the vertical was eroded. Additionally, their study showed, that sediment transported by the backwash of the tsunami, deposited on the shoreward side of the breakwaters, which then hindered transport further out to sea. Despite this natural beach recovery had not taken place to any significant degree, however. In Kuriyama et al. (2014) the beach profile change at Hasaki due to the Tohoku tsunami was recorded. Here, interestingly, the beach profile was measured a mere 6 hours before the tsunami hit, and likewise only three days after the tsunami. The beach profile change at Hasaki was not very significant, and this demonstrates the variety in effect the same tsunami can have on different beaches. Some surveys also focus on measuring sediment deposits left by the tsunami see e.g. Dawson and Shi (2000), Kato et al. (2012) or Paris et al. (2009).

There is large research branch focusing on estimating tsunami characteristics from sediment deposits, and for the remainder of this thesis, I will refer to this branch as paleo tsunami research. Establishing relationships between tsunami deposits and tsunami hydrodynamics can make it possible to better asses past tsunamis, both in terms of recurrence and strength. The paleo tsunami research generally focus

either on forward modelling or inverse modelling. With the forward models the hydrodynamics and resulting sediment transport is solved for, and the modelled deposits are then compared with measured deposits. The models used here, are often NLSW models, and the research related to these will be discussed later in this section. The inverse models, on the other hand, starts with the sediment deposits and attempts to reconstruct the tsunami. Many different inverse models exist, and for a more complete overview please see Sugawara et al. (2014a). The simplest inverse model, is probably the model by Moore et al. (2007). Here, the minimum friction velocity required to move the largest grains in the deposit is first determined. Second, by assuming that the particles travel in suspension, are not re-suspended and that the large particles are present near the surface, an equation for the travel time of a particle is derived. This together with "law of the wall" equation gives two equations with two unknowns, namely the water depth and the mean velocity. Another model was proposed by Soulsby et al. (2007). In this model it is assumed that there is a linear relationship between the decreasing mean grain size of the tsunami deposits and the increasing distance inland (normally referred to as inland fining). In this model all particles likewise travel in suspension, and re-suspension of particles are not possible. Jaffe and Gelfenbuam (2007) developed a model, which was based on the observation that deposits normally fine upwards (i.e. smaller grain sizes in the upper layers of the deposit). Their idea was that sediment in suspension is in equilibrium with the tsunami hydrodynamics, and when the tsunami slows, the sediment deposits. This model uses expressions for turbulence profiles, sediment distribution profiles and further assumes no sediment transport during the tsunami backwash. Such models described above have been used to some degree, and with reasonable success, to predict tsunami characteristics of recent tsunamis, see e.g. Jaffe and Gelfenbuam (2007), Spiske et al. (2010) and Sugawara et al. (2014a).

Experiments involving tsunami induced sediment transport on beaches are few. Chen et al. (2012) studied the beach profile change made by N-waves. Their waves were, however, as also recognized by the authors themselves, too short. They concluded that no significant erosion occurred during wave breaking and run-up, but rather during draw-down. Yamaguchi and Sekiguchi (2015) studied experimentally sediment deposits using different size tsunamis and different topographies. They concluded that the total amount of sediment deposited, depended on the tsunami magnitude, but that the thickness of the deposit, in any one given spot, did not show the same dependence. This illustrates the difficulty in extracting information of the tsunami kinematics from a sediment deposit. In an attempt to contribute to the paleo tsunami research, Johnson et al. (2016) studied deposits left by a breaking

bore and concluded that an existing advection-settling model was able to predict flow depths within a factor two and velocities within a factor 1.5, thus showing a reasonable performance of one of the paleo tsunami inverse models. Yoshii et al. (2017) studied experimentally tsunami deposits in their 205 m long flume. They concluded that the majority of the deposits came from the onshore flow. The return flow created seaward fining, something contrary to many paleo tsunami inverse models, a point also made by Paris et al. (2012).

In addition to the field surveys, the majority of the research, involving tsunami-induced sediment transport, at a larger scale, have been made using NLSW models. The accurate modelling of tsunami-induced sediment transport and morphology seem to have two different end goals (though they are naturally related). One is to better be able to predict sediment deposits, which in turn will improve the ability to estimate wave characteristics of historic tsunamis based on sediment deposits (i.e. the forward models of the paleo tsunami research). The second is, to be able to better predict the impact of a tsunami attack on the coast. The NLSW models can either be depth-averaged (this is most common), in this case they are referred to as two-dimensional horizontal models (2DH) or they can be three dimensional, by resolving the vertical with a number of layers. To save computational time, however, often these three dimensional models are used only two dimensionally and become two-dimensional vertical (2DV) models.

Li et al. (2012b) coupled the the 2DH COMCOT model from Liu et al. (1998), traditionally used for tsunami simulations, with the sediment transport module of the open source code XBeach. The sediment transport was based on the depth averaged advection-diffusion equation and it seems that bed load transport in their study was neglected. The estimated bed shear stress was based on a spatially varying Manning coefficient. They demonstrated, that their new coupled model, COMCOT-SED, gave quantitative similar predictions on sediment deposits to measured data from the 2004 Indian Ocean tsunami. Using the same model, Li et al. (2012a) studied six different rupture scenarios, focusing on the impact of different ruptures on inundation as well as tsunami-induced sediment transport and morphology, for the city of Painan (Indonesia). Considering specifically two scenarios, they showed that a positive leading wave would cause erosion near the shore and create a large sandbar offshore. Furthermore, the positive leading wave was shown to deposit some sand inland. A leading depression tsunami, on the other hand, would cause a sandbar even further offshore, due to the back flow of the leading depression, and not deposit significant amounts of sand inland. They concluded that these findings

could potentially be useful for the paleo tsunami research community. Ontowirjo et al. (2013) also used the base COMCOT code from Liu et al. (1998), and coupled it with sediment transport calculations to estimate coastal erosion and deposition in Lhoknga (Indonesia) during the Indian Ocean tsunami. Their sediment transport calculations included both bed load and suspended load formulations. The latter was solved through the advection-diffusion equation for sediment concentration. In general, their computed deposit thickness, compared well with measured deposits from Paris et al. (2009). They further concluded that a majority of the deposit came from bed load, which might challenge some of the most well known inverse models only focusing on suspended load.

Sugawara et al. (2014b) used the 2DH TUNAMI-N2 code by Goto and Ogawa (1997) coupled with a sediment transport model, to simulate sediment transport by the Tohoku tsunami at Sendai. The sediment transport consisted of bed load and suspended load formulations, and the suspended load was calculated using a depth-averaged advection equation. Similar to other studies, Sugawara et al. (2014b) used a Manning coefficient for the calculation of the bed shear stress. They concluded that the simulated deposits corresponded well with the measured. They further concluded that the sediment transport and deposition was very dependent on structures such as dikes or roads. Yamashita et al. (2016) also used the TUNAMI-N2 code, this time to simulate large scale sediment transport caused by the Tohoku tsunami inside the Hirota Bay. They concluded that their model was able to give similar results for erosion and deposition as the field survey by Kato et al. (2012). In addition, they compared their computed suspended sediment transport fields with aerial videos of the tsunami. Here, large sediment clouds were clearly visible, and the modelled results showed good qualitative agreement with the videos. This is an innovative and interesting way of comparing the numerical results with actual tsunami events. Interestingly, they also found that the instantaneous change in morphology affected the run-up process. They showed that with morphological modelling the dikes were eroded, causing the tsunami to inundate further, compared to a model not computing sediment transport and morphology.

In Kuriyama et al. (2014) the one layer hydrostatic version of the STOC code was used to simulate the morphological development at Hasaki from the Tohoku tsunami in 2011, and modelled results were compared with detailed field measurements. The profile change here was, as already mentioned, not large, and the model in general predicted profile changes of the right order of magnitude. In many cross shore positions the sign, i.e. erosion versus deposition, was wrong, however.

Apotsos et al. (2011a) validated that the Delft3D model could be used to simulate tsunami induced sediment transport processes. The Delft3D model was used as a 2DV model, and the vertical was divided into 10 layers. Furthermore, the model used a $k - \epsilon$ turbulence model for closure. Their model included both bed load and suspended load formulations, it included hindering settling due to high concentrations as well as the possibility of using several different grain sizes. This model thus includes more relevant physical processes than many of the previous models. Their results generally compared within a factor two of measured deposit thickness at Kuala Meurisi (Indonesia), which can be considered a reasonable success in my opinion. Apotsos et al. (2011c) used the same model and studied sediment transport and morphology using both a measured topography as well as idealized topographies. They concluded, that some sediment is eroded by the wave front, but that majority of sediment transport occur due to the long backwash. This is in contrast to one of the main assumptions of the inverse models. They further found that deposited sediment fines landward as well as upward within the deposit. Finally, again using Delft3D, Apotsos et al. (2011b) compared simulated results with field measurements in Fagafue Bay on American Samoa and concluded that sediment supply and steep onshore topography limited the sediment deposits. This, they stated, has not been accounted for in previous paleo tsunami research studies.

The numerical models above, have all used the assumption of logarithmic velocity profiles or a Manning coefficient, to calculate the bed shear stress, which drives the sediment transport. Furthermore, the suspended load has in most of the studies been based either on a depth averaged equation or idealised suspended sediment transport profiles extending all the way to the free-surface. Due to the very limited number of studies on tsunami-induced boundary layers, it is however not known how well these approximations work, in such instances.

Boundary layers

Research on the actual physics of tsunami-induced boundary layers are, to the best of my knowledge, limited to the field measurement by Lacy et al. (2012), the numerical study by Williams and Fuhrman (2016) and the numerical study by Tanaka et al. (2016).

Lacy et al. (2012) showed that the tsunami induced boundary layers of the 2010 Chilean tsunami did not span the entire depth though spanning significantly more than standard wave-induced boundary layers. The velocity profiles inside the bound-

ary layer were shown to be reasonably captured by a logarithmic distribution during peak flow. In Lacy et al. (2012)'s results the velocities led the surface elevations with 90° , something that was explained by friction terms effect on the momentum balance. This explanation does not fully convince me, however. Furthermore, it was demonstrated that the tsunami was able to move sediment, although it did not have a huge influence on suspended sediment transport, as the wind waves present where larger than the tsunami.

In a one dimensional vertical (1DV) RANS model Williams and Fuhrman (2016) simulated a series of tsunami-scale boundary layers. Their study, was limited to the offshore region to prevent the boundary layer being depth limited, and the driving tsunami signal was treated as a time varying current. Williams and Fuhrman (2016) simulated the boundary layers beneath three types of idealized tsunami signals, namely single waves, N-waves and sinusoidal waves. They performed simulations for a wide range of roughnesses and tsunami amplitudes and proposed formulas for predicting boundary layer thicknesses and friction factors. They emphasized that the tsunami-induced boundary layers are both current-like due to their long duration, but also wave-like, in the sense that they are unsteady and that the boundary layer may not span the entire water depth, similar to that observed by Lacy et al. (2012).

In an attempt to combat the uncertainties of the NLSW models regarding the bed-shear stress, Tanaka et al. (2016) simulated tsunami run-up with a NLSW model coupled with a RANS model for describing the boundary layer. They showed this gave different shear stress approximations compared to those predicted using a Manning coefficient. Only the coupled model was able to capture the high stress related to the tsunami front. It is, however, unclear how they coupled the NLSW model and the RANS model. Despite this, it is an interesting attempt to remedy some of the uncertainties with the NLSW models in regards to bed shear stresses.

1.3 Problem statement

As could be gathered from the description of the literature on tsunami research, the generation, propagation, run-up and inundation of tsunamis, have received considerable attention in the past. The resulting interaction with the seabed, i.e. boundary layer dynamics, local scour, large scale erosion and deposition, have received considerably less attention. This is natural and warranted, since the run-up stage can potentially results in a large number of fatalities. As a result of the limited amount of

research, however, present understanding of how a tsunami interacts with the seabed can still be improved. Furthermore, each of the commonly used methods described in the previous section have challenges or shortcomings in filling this knowledge gap.

Experimentally, the largest challenge is the large scales involved. The full-scale tsunami wave lengths span several kilometres and the periods are in the order of minutes to hours rather than seconds. These scales are very difficult to reproduce in a properly scaled experiment. As Jiang et al. (2015) even stated: "both the length and time scales of an actual tsunami wave cannot be down-scaled in wave flume experiments according to the Froude similarity law." This is a rather bold statement, as some properly scaled experiments do exist. These studies, however, still suffer from spatial limitations. The studies by Schimmels et al. (2016) and Sriram et al. (2016) could only employ a steep 1/6 slope if the flume should contain the entire wave length. Their flume, approximately 300 m long, is much longer than typical wave flumes. In the studies using a pump to drive the flow the flumes were too short to house the entire tsunami, thus making it difficult to study the e.g. interaction between incoming and reflected waves.

Surveys, in general, have provided very useful knowledge on the effect of a tsunami, but provide little in understanding of the detailed physics of the tsunami. Furthermore, these surveys are primarily carried out inland, and therefore there is no knowledge on e.g. scouring around offshore structures.

As an alternative to experiments and surveys, NLSW models and Boussinesq models have been used. These, in general do a good job on tsunami propagation but, as already mentioned the NLSW models cannot handle dispersion, and both types of models rely on breaking criteria, as well as simple assumptions in relation to boundary layers and bed shear stresses. These assumptions might work well, but until detailed knowledge of the tsunami-induced boundary layers is gained, this cannot be known.

With the increased computational power, CFD models can, potentially, be used to study tsunami-seabed interactions. Such models have the ability to resolve the tsunami-induced boundary layers and solve for the resulting sediment transport, and can likewise describe physical dispersion and properly resolve wave breaking. CFD models can therefore be used to create fundamental new insights, which are otherwise very difficult to obtain. Simulating either local scour processes or the entire run-up process is, however, still computationally very heavy, and therefore it is imperative that simpler models be developed, either as simple empirical relations

or through the adaptation in simpler less computationally heavy numerical models. This has prompted the following overall research question:

How can numerical and experimental methods be improved and used to increase fundamental knowledge about tsunami-seabed interactions involving local scour, run-up behaviour, boundary layers and bed shear stresses, enabling an improved ability to predict these processes through simple empirical relations or the adaptation in potential flow models?

This overall research question will be answered through four specific research questions:

RQ 1) How can tsunami-induced scour around offshore monopile foundations be studied, characterized and predicted?

RQ 2) How can current VOF and RANS models be used and modified to enable accurate simulations of the run-up of a tsunami event?

RQ 3) What characterizes the tsunami run-up processes, and what is the importance of the "shorter" waves, sometimes riding on the tsunami front, on run-up height, inundation speed and local flow velocities?

RQ 4) What are the characteristics of tsunami-induced boundary layers, bed shear stresses and resulting sediment transport beneath shoaling, inundating and retreating tsunamis and how can the boundary layer thickness and bed shear stress be predicted as well as included in potential flow models?

1.4 Outline

This thesis is presented as a collection of papers. Each following chapter is therefore a paper in its own. The status of each paper is indicated on title page before each chapter.

The first two papers (Larsen et al., 2017, 2018a), presented in Chapters 2 and 3, both involve tsunami-induced scour around offshore monopile foundations and are targeting directly *RQ1*. Chapter 2 is a purely numerical study, whereas Chapter 3 is primarily experimental.

In Chapter 2, the `sediMorph` code, originally developed by Jacobsen et al. (2014), is used. This code is implemented in the open source software `OpenFOAM` and is a

fully coupled, hydrodynamic, sediment transport and morphologic model. It is well validated and well tested. It has been used to simulate breaker bar development by Jacobsen et al. (2014), pipeline scour processes by Fuhrman et al. (2014), Larsen et al. (2016) and Bayraktar et al. (2016) as well as monopile scour processes by Baykal et al. (2015) and Baykal et al. (2017).

Building on the study by Williams and Fuhrman (2016) describing tsunami-induced boundary layers as both current-like and wave-like, the tsunami scour process is studied by treating the tsunami as a sinusoidally time varying current. This approach enables saving computational power, as the effects associated with the free-surface can be neglected, and the scour process is studied entirely from a near-bed perspective. In this paper the details of the tsunami-induced scour process are discussed. Based on the simulated results, a simple engineering model, capable of predicting the time varying tsunami-induced scour depth, is proposed.

In Chapter 3, the tsunami-induced scour process is studied experimentally. Here, similar to the previous chapter, the tsunami is treated as a time varying current. This enables the use of a pump to drive the flow. In this paper a single wave is used, rather than the sinusoidal wave used in the previous chapter. Final bed profiles are obtained by scanning the bed around monopile, and the time varying scour development is captured by a camera mounted inside the monopile. Detailed knowledge of the scour process obtained from the experiments are compared to the findings from the first paper (Chapter 2), and the simple engineering model for predicting tsunami-induced scour, previously proposed, is further generalized.

Papers three and four (Larsen et al., 2018b; Larsen and Fuhrman, 2018c), presented in Chapters 4 and 5, both target *RQ2*. The findings from these papers are not directly limited to tsunami research, but can rather be seen as methodological contributions to VOF and RANS models' general ability to simulate free-surface waves.

In Chapter, 4 the simulations are purely laminar, and the ability of the widely used `OpenFOAM` solver, `interFoam`, to accurately simulate propagating waves, is assessed. The simulations are performed using a laminar model, as it can be considered a prerequisite for any numerical model to be able to accurately simulate laminar waves, before solving the more complex turbulent situations like wave-induced boundary layers or wave breaking. It is shown that with the standard set-up, `interFoam` does not do a particularly good job in accurately propagating waves. In this chapter, the effects of spatial and temporal resolution, as well as discretization practises are discussed in detail, and it is shown, that the performance of `interFoam` can be improved

significantly. Furthermore, the performance the new solver, `interFlow`, is also compared to `interFoam`. `interFlow` is based on the algorithm `isoAdvector`, developed by Roenby et al. (2016). Despite a slightly better performance, `interFlow` is not used in the subsequent chapters. There are two reasons for this. First, `interFlow` only performed significantly better than `interFoam` when the discretization schemes were carefully tuned to give, what is referred to in the chapter as, "a diffusive balance". As stated in the chapter, it is not known how well this diffusive balance will work in a more complex situation involving e.g. wave breaking. Second, `interFlow` cannot handle moving meshes, and will therefore not be able to be used for morphological simulations. Though morphological simulations using `interFoam` were not performed in the present thesis, it was originally a goal, and is likewise a target for future research. Therefore, ensuring best possible performance of `interFoam` is desirable and continuing with `interFoam` was preferred.

In Chapter 5, a long-standing instability problem originally described by Mayer and Madsen (2000) for two-equations RANS models, when applied to free-surface waves, is solved. In past RANS simulations of free-surface waves, both breaking and non-breaking, there have been a collective tendency to overestimate turbulence levels. This tendency has often been most pronounced prior to breaking. This is most probably due to the instability problem, identified by Mayer and Madsen (2000), which cause un-physical production of turbulence and eddy viscosity beneath potential flow waves. The problem is treated analytically, and the unstable growth rates of commonly used turbulence models are derived. In this paper we show how standard turbulence closures can be stabilized. We demonstrate that only the stabilized versions of the turbulence models are able to propagate waves over long distances without a non-physical decay in the wave heights, otherwise experienced with standard turbulence closures. Initially non-breaking waves are considered, as it can be considered a pre-requisite for any turbulence model used to simulate waves, that it can handle the simple non-breaking propagating waves. In this chapter the performance of the stabilized and standard turbulence models are subsequently compared to a breaking wave experiment, and it is shown that only the stabilized models can predict low levels of turbulence pre-breaking, and maintain a correct undertow profile from the pre-breaking region to the outer surf zone.

Chapters 4 and 5 can be considered necessary methodological developments before accurate tsunami run-up simulations could be performed using a VOF-RANS model. These chapters can also be considered additional validation cases for Chapters 6 and 7, though these chapters contained separate validation cases.

To supplement, Chapter 5, at the end of the thesis an appendix is added (Chapter 9). This includes the simulated results of the plunging breakers experiment of Ting and Kirby (1994). In Chapter 5, the modelled results were only compared to the spilling breakers experiment of Ting and Kirby (1994). The reason for this was, that an additional case, would not add anything new in relation to the instability problem. For the present thesis, the simulation of the plunging breakers can, however, be used to further qualify the chosen value of one of the turbulence model's stress limiters.

Paper five (Larsen and Fuhrman, 2018a), presented in Chapter 6, directly targets *RQ3*. This paper presents numerical simulations of full-scale tsunamis propagating on a flat bed before running up a constant slope region. In this paper both single waves and N-waves are considered, and the slopes are systematically varied. Three previously observed run-up types are identified in the simulations, and an additional run-up types is likewise identified. The detailed physics of each of these run-up types are discussed, and it is likewise discussed in which situations the different run-up types might occur. Additionally the influence of the smaller waves, riding on the much longer main wave, on the run-up height, inundation speed and flow velocity is discussed.

Paper six (Larsen and Fuhrman, 2018b), presented in Chapter 7, directly answers *RQ 4*. This paper presents result from the same simulations as Chapter 6, but with a special focus on the boundary layer dynamics, resulting bed shear stresses and implications for sediment transport. By studying spatial distribution of Shields parameters and Rouse numbers conclusion regarding sediment transport are made, and some of the assumptions of the inverse paleo tsunami models are discussed. Additionally, a detailed discussion of the tsunami-induced boundary layers beneath both shoaling and inundating tsunami is performed. A formula for predicting the tsunami-induced time varying boundary layer thickness is proposed and an engineering model for predicting time varying friction velocity beneath tsunamis is likewise proposed. Both the engineering model for the friction velocity and the expression for predicting the boundary layer thickness are formulated such that they can easily be implemented in potential flow models.

Finally, in Chapter 8 the conclusions of the thesis is presented, and answers to each of the specific research questions are given.

Chapter 2

Tsunami-induced scour around monopile foundations

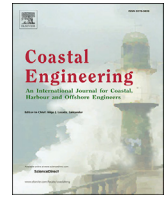
This Chapter has been published as:

Larsen, B. E., Fuhrman, D. R., Baykal, C., Sumer, B. M. (2017). *Tsunami-induced scour around monopile foundations*. Coastal Engineering **129**: 36-49. doi: 10.1016/j.coastaleng.2017.08.002.



Contents lists available at ScienceDirect

Coastal Engineering

journal homepage: www.elsevier.com/locate/coastaleng

Tsunami-induced scour around monopile foundations

Bjarke Eltard Larsen^{a,*}, David R. Fuhrman^a, Cüneyt Baykal^b, B. Mutlu Sumer^{a,1}^a Technical University of Denmark, Department of Mechanical Engineering, Section of Fluid Mechanics, Coastal and Maritime Engineering, DK-2800, Kgs. Lyngby, Denmark^b Middle East Technical University, Department of Civil Engineering, Ocean Engineering Research Center, Dumlupınar Blvd., 06800, Cankaya, Ankara, Turkey

ARTICLE INFO

Keywords:

Tsunamis
Scour
Monopiles
Morphology
Computational Fluid Dynamics
Turbulence modelling

ABSTRACT

A fully-coupled (hydrodynamic and morphologic) numerical model is presented, and utilized for the simulation of tsunami-induced scour around a monopile structure, representative of those commonly utilized as offshore wind turbine foundations at moderate depths i.e. for depths less than 30 m. The model is based on solutions to Reynolds-averaged Navier-Stokes equations, coupled with two-equation $k - \omega$ turbulence closure, with additional bed and suspended load descriptions forming the basis for sea bed morphology. The model is first validated for flow, bed shear stresses, and scour within a steady current, where a generally excellent match with experimentally-based results is found. A methodology for maintaining and assessing hydrodynamic and morphologic similarity between field and (laboratory) model-scale tsunami events is then presented, combining diameter-based Froude number similarity with that based on the dimensionless wave boundary layer thickness-to-monopile diameter ratio. This methodology is utilized directly in the selection of governing tsunami wave parameters (i.e. velocity magnitude and period) used for subsequent simulation within the numerical model, with the tsunami-induced flow modelled as a long sinusoidally-varying current. The flow, sediment transport, and scour processes beneath up to ten tsunami waves are simulated in succession. These illustrate a generally accumulative scour process i.e. a relatively rapid scour induced by the leading wave, with an additional build-up of the scour depth during additional trailing waves. The resulting scour seems to approach an equilibrium value after sufficient time duration, which corresponds reasonably to that predicted by existing steady-current scour depth expressions, after accounting for the finite boundary layer thickness induced by the unsteady tsunami wave, i.e. it is important to incorporate both current-like, as well as wave-like aspects of the long tsunami event. Based on the simulated results, a simple methodology for predicting the tsunami-induced scour depth in engineering practice is finally developed. This methodology is demonstrated to match the predicted scour development for all of the simulated flows considered, ranging from the series of transient tsunami waves to the steady-current limit.

1. Introduction

Tsunamis are long waves, typically having periods the order of minutes to hours, that are generated by sudden motions of the sea bed e.g. due to undersea earthquakes or landslides. When such waves approach and/or reach the shoreline, they are potentially catastrophic, as has been well documented e.g. in the recent tsunami event that occurred in the Indian Ocean (2004), as well as in the Tohoku tsunami off the coast of Japan (2011).

While the run-up, inundation, and destructive potential of tsunami events has received considerable attention in the literature, the associated interaction with the sea bed i.e. boundary layer dynamics, induced sediment transport, and resultant sea bed morphology, have received

relatively little specific attention. Such issues and processes are important, however, both in assessing potential larger scale deposition and erosion in affected coastal regions, as well as in understanding smaller scale erosion, such as tsunami-induced local scour around coastal and offshore structures (e.g. monopiles, piers, pipelines, and breakwaters), which can potentially contribute to their failure. (Williams and Fuhrman, 2016) simulated a series of tsunami-scale boundary layers, emphasizing that they may be both current-like due to their long durations, but also wave-like, in the sense that they are unsteady and that the boundary layer may not span the entire water depth. This assertion is likewise consistent with field measurements of (Lacy et al., 2012). Studies investigating tsunami-induced scouring around coastal and offshore structures in any context are few, but include e.g. (Wilson et al., 2012), who studied

* Corresponding author.

E-mail address: bjelt@mek.dtu.dk (B.E. Larsen).¹ Present address: BM SUMER Consultancy & Research, Istanbul Technical University, ARI Teknokent 3, B110, 34467 Maslak, Istanbul, Turkey.

sediment scour and deposition within harbors; (Chen et al., 2013), who studied tsunami-induced scour at coastal roadways; and (Bricker et al., 2012), who conducted a field study of scour depths measured on the landward side of seawalls and floodwalls, as well as beside a building foundation footing, from the 2011 Tohoku tsunami. Experimental investigations on the tsunami-induced scour specifically around monopiles are seemingly limited to that of (Tonkin et al., 2003), who studied the scour promoted by incident solitary waves around a cylinder on a sloping beach, where the cylinder was mounted near the shoreline and to (Nakamura et al., 2008) who studied scour around a square pile induced by solitary and long waves. The experiments by (Tonkin et al., 2003) were also simulated numerically using a nonlinear shallow water model by (Pan and Huang, 2012), with the intent of simulating tsunami-induced scour around bridge piers. At this point it is worth emphasizing that studying tsunamis as solitary waves does not allow for their effective period and wave amplitude to be determined independently, and as a result the solitary wave duration is likely too short to represent geophysical tsunami events (see e.g. the discussion of (Madsen et al., 2008)).

As seen from the above, most of the works considering the general topic of tsunami-induced scour have only recently been published i.e. in the past few years. Hence, a detailed understanding of the underlying processes, as well as general structure vulnerability, is presently lacking. The present study aims to further the understanding of tsunami-induced scour, by numerically investigating tsunami-induced flow and scour processes around a monopile structure, representative of those commonly utilized as offshore wind turbine foundations.

While the scour around monopiles due e.g. to waves and tidal currents has been extensively studied (see e.g. (Sumer and Fredsøe, 2002)), the potential scour around offshore wind turbine foundations induced by tsunami attack has not been previously studied, either experimentally or numerically. To ensure proper design, it is therefore important that a detailed understanding of the potential tsunami-induced scour around such structures be improved.

2. Hydrodynamic and turbulence model description

In this section the hydrodynamic model is presented. The flow is simulated by solving the incompressible Reynolds-averaged Navier-Stokes equations (RANS) and the continuity equation, coupled with a two-equation k - ω turbulence model for closure. The continuity equation and the RANS equations are, respectively, given in (1) and (2):

$$\frac{\partial u_i}{\partial x_i} = 0, \quad (1)$$

$$\frac{\partial u_i}{\partial t} + u_j \frac{\partial u_i}{\partial x_j} = -\frac{1}{\rho} \frac{\partial p}{\partial x_i} + \frac{\partial}{\partial x_j} \left(2\nu S_{ij} + \frac{\tau_{ij}}{\rho} \right), \quad (2)$$

where u_i are the mean components of the velocities, x_i are the Cartesian coordinates, p is the pressure, t is the time, S_{ij} is the mean strain rate tensor given by

$$S_{ij} = \frac{1}{2} \left(\frac{\partial u_i}{\partial x_j} + \frac{\partial u_j}{\partial x_i} \right), \quad (3)$$

and τ_{ij} is the Reynolds stress tensor, which is expressed according to the Boussinesq approximation

$$\tau_{ij} = -\overline{u'_i u'_j} = 2\nu_T S_{ij} - \frac{2}{3} k \delta_{ij}. \quad (4)$$

Here the overbar signifies time (ensemble) averaging, ν_T is the eddy viscosity, δ_{ij} is the Kronecker delta, and

$$k = \frac{1}{2} \overline{u'_i u'_i} \quad (5)$$

is the turbulent kinetic energy density. In the above a prime superscript denotes turbulent (fluctuating) velocity components. To achieve closure, the k - ω turbulence model by (Wilcox, 2006, 2008) will be utilized. This model includes the following transport equations for the turbulent kinetic energy density k and the specific dissipation rate ω :

$$\frac{\partial k}{\partial t} + u_j \frac{\partial k}{\partial x_j} = \tau_{ij} \frac{u_i}{x_j} - \beta^* k \omega + \frac{\partial}{\partial x_j} \left[\left(\nu + \sigma^* \frac{k}{\omega} \right) \frac{\partial k}{\partial x_j} \right], \quad (6)$$

$$\frac{\partial \omega}{\partial t} + u_j \frac{\partial \omega}{\partial x_j} = \alpha \frac{\omega}{k} \tau_{ij} \frac{\partial u_i}{\partial x_j} - \beta \omega^2 + \frac{\sigma_d}{\omega} \frac{\partial k}{\partial x_j} \frac{\partial \omega}{\partial x_j} + \frac{\partial}{\partial x_j} \left[\left(\nu + \sigma \frac{k}{\omega} \right) \frac{\partial \omega}{\partial x_j} \right]. \quad (7)$$

The closure coefficients are given as $\alpha = 0.52$, $\beta = 0.078$, $\beta^* = 0.09$, $\sigma = 0.5$, $\sigma^* = 0.6$, $\sigma_{do} = 0.125$, and

$$\sigma_d = H \left(\frac{\partial k}{\partial x_j} \frac{\partial \omega}{\partial x_j} \right) \sigma_{do} \quad (8)$$

where $H(\cdot)$ is the Heaviside step function, which takes a value of unity if the argument is positive and zero otherwise.

In this model the eddy viscosity, which is present in the Reynolds stress tensor via the Boussinesq approximation, is given by

$$\nu_T = \frac{k}{\bar{\omega}}, \quad (9)$$

with $\bar{\omega}$ defined according to:

$$\bar{\omega} = \max \left[\omega, C_{lim} \sqrt{\frac{2S_{ij}S_{ij}}{\beta^*}} \right], \quad (10)$$

where the second part of the expression is a stress limiting feature, with $C_{lim} = 7/8$.

The computational domain is discretized into finite volumes of quadrilateral blocks in varying shapes and dimensions. Fig. 1 shows an example computational mesh typical of that used for the forthcoming scour simulations, which consist of two steady current validation simulations and two tsunami scour simulations. The computational domain, unless stated otherwise, has the following dimensions: length, $l = 20D$, width, $w = 15D$, and height, $h = 2D$, in which D is the monopile diameter. The total number of cells comprising the computational domains utilized is 170,496 with the near-bed cells having a height $O(d)$, in which d is the grain size. The monopile is located at the center of the domain $(x, y) = (0, 0)$. It is emphasized that considerable effort has been put into optimizing the computational mesh for convergence while at the same time keeping the computational time affordable. The length of $20D$ for the tsunami simulations is justifiable as is it sufficient to simulate steady current scour, which can be viewed as the infinite period limit for waves, see the forthcoming validation in Section 5.

2.1. Boundary conditions

The boundary conditions for the hydrodynamic model are as follows: The friction wall boundaries, that is the monopile and the seabed, will have a no-slip condition imposed such that velocities are zero. The top boundary will be modelled as a frictionless lid meaning that vertical velocities are set to zero, and horizontal velocities and scalar hydrodynamic quantities have zero vertical gradient. This means that the top boundary does not represent the free surface of tsunami waves and the simulations are performed as single-phase simulations. As described in (Roulund et al., 2005) this is reasonable provided that the depth based Froude number Fr_h is sufficiently small. In the simulated tsunami cases $Fr_h = U_m / \sqrt{gh} \leq 0.2$, where U_m is the velocity magnitude beneath the tsunami waves. In the two steady current validation cases to be shown later $Fr = U / \sqrt{gh} = O(0.4)$ which is slightly larger, but not radically different, than $O(0.2)$ where (Roulund et al., 2005) showed that there

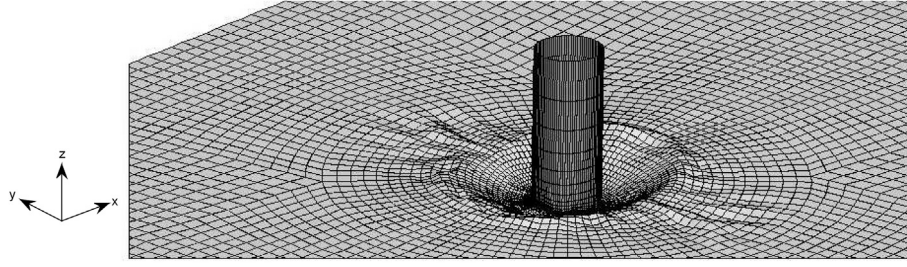


Fig. 1. Example of the mesh in the vicinity of the monopile used in the scour simulations.

was negligible free surface effect. Similar conditions were considered by (Baykal et al., 2015). Therefore the flows considered will be fairly well represented in the lid simulations although some variations can occur in the two steady current cases such as the absence of a flow in the radial direction, caused, otherwise, by the head difference between the surface elevation in front and at the side edge of the monopile. It is emphasized that the two steady current cases are performed primarily to validate the model's ability to capture the isolated effect of the limited boundary layer thickness on the scour depth, which is ideally accomplished using the rigid lid.

The bottom and the monopile surface are modelled utilizing a generalized wall function approach. The friction velocity is determined from the tangential velocity at the nearest cell center, based on the profile of (Cebeci and Chang, 1978):

$$\frac{u}{U_f} = 2 \int_0^{y_c^+} \frac{dy^+}{1 + [1 + 4\kappa^2 (y^+ + \Delta y_{cc}^+)^2 C]^{1/2}}, \quad (11)$$

$$C = [1 - \exp(-(y^+ + \Delta y_{cc}^+)/25)]^2, \quad (12)$$

$$\Delta y_{cc}^+ = 0.9 \left[\sqrt{k_s^+} - k_s^+ \exp\left(-\frac{k_s^+}{6}\right) \right], \quad (13)$$

who generalized the van Driest (van Driest, 1956) profile to incorporate potential roughness effects, with $y_c = \Delta y/2$ being the normal distance from the wall to the cell center, where Δy is the thickness of the near wall cell, $k_s = 2.5d$ is Nikuradse's equivalent sand roughness and $y_c^+ = y_c U_f / \nu$. The boundary conditions for k and ω are then as described by (Fuhrman et al., 2014)

$$\frac{k}{U_f^2} = \min \left\{ A \Delta y_c^{+2}, \frac{1}{\sqrt{\beta^*}} \right\}, \quad (14)$$

$$\frac{\omega \nu}{U_f^2} = \max \left\{ \frac{B}{\Delta y_c^{+2}}, \frac{1}{\sqrt{\beta^*} \kappa \Delta y_c^+} \right\}. \quad (15)$$

The first arguments in these functions ensure that these variables follow their proper scaling $k \sim y^2$ and $\omega \sim 1/y^2$ for near wall cells within the viscous sub-layer (see e.g. (Wilcox, 2006)). The values $A = 1/(\delta^{+2} \sqrt{\beta^*}) = 0.02466$ and $B = \delta^+ / (\sqrt{\beta^*} \kappa) = 96.885$ are utilized, which ensure a continuous transition to the (fully-turbulent) second arguments at $\Delta y_c^+ = \delta^+$, where $\delta^+ = 11.626$ is taken as the viscous sub-layer thickness (in dimensionless wall coordinates). At the bottom and the monopile surface the eddy viscosity is not calculated from (9), but is instead calculated from

$$U_f^2 = \frac{\tau_b}{\rho} = (\nu + \nu_T) \frac{dU}{dz}. \quad (16)$$

Following (Larsen et al., 2016), the flow is driven by a Dirichlet condition i.e. the velocity is specified at the left-hand inlet boundary,

which comes from a separate one-dimensional vertical (1DV) pure boundary layer simulation, made utilizing the same model as described above. In this boundary layer simulation the flow is driven by a body force which will be specified in the description of the simulated cases. From here the velocity profile, as well as the profiles for k and ω , are sampled and utilized as inlet boundary conditions within the scour simulations. Through this approach the special characteristics of the tsunami boundary layer are incorporated directly within the driving inlet flow.

3. Sediment transport and morphological models

In this section the sediment transport and morphological models are described. The description will only include the most essential details since the implementation of the models have already been described and discussed by (Jacobsen, 2011), as well as in the recent publication of (Jacobsen et al., 2014).

The model for the bed load transport corresponds to that of (Roulund et al., 2005), who extended the model of (Engelund and Fredsøe, 1976) to also include three dimensional effects as well as bed slope modifications to the Shields parameter.

The suspended load is calculated by solving the advection-diffusion equation for the concentration [see e.g. 21, p. 238]:

$$\frac{\partial c}{\partial t} + (u_j - w_s \delta_{j3}) \frac{\partial c}{\partial x_j} = \frac{\partial}{\partial x_j} \left[(\nu + \beta_s \nu_T) \frac{\partial c}{\partial x_j} \right], \quad (17)$$

where c is the suspended sediment concentration, w_s is the settling velocity, and $\beta_s = 1$ is utilized meaning that the sediment diffusivity takes the same value as the eddy viscosity. The settling velocity is calculated by the approach given in (Fredsøe and Deigaard, 1992), which is based on the drag coefficient of the falling sediment grains.

Equation (17) is solved on a sub-set of the main computational mesh where the near-bed cells below a given reference level b are removed. At this reference level a reference concentration, c_b , boundary condition is imposed. There are several formulations of c_b but here the one by (Engelund and Fredsøe, 1976) is utilized. The concentration at the reference level is given by

$$c_b(\theta) = \frac{c_0}{(1 + 1/\lambda_b)^3}, \quad (18)$$

in which $c_0 = 0.6$ is the maximum value for the concentration, and the linear concentration λ_b is

$$\lambda_b^2 = \frac{\kappa^2 \alpha_1^2}{0.013 s \theta} \left(\theta - \theta_c - \frac{\pi \mu_d}{6} p_{EF} \right), \quad (19)$$

where

$$p_{EF} = \left[1 + \left(\frac{\pi \mu_d}{6(\theta - \theta_c)} \right)^4 \right]^{-1/4} \quad (20)$$

and

$$\theta = \frac{\tau_b}{\rho g(s-1)d} = \frac{U_f^2}{(s-1)gd} \quad (21)$$

is the Shields parameter. Throughout the present work the coefficient of dynamic friction is set to $\mu_d = 0.51$ and the critical Shields parameter θ_c is computed from a base value $\theta_{c0} = 0.05$, accounting for bed-slope effects as in (Roulund et al., 2005).

Following (Fuhrman et al., 2014), a reference level of $b = \alpha_1 d = 3.5d$ is utilized. This is quite similar to the value $b = 3.6d$ utilized by (Liang and Cheng, 2005). To prevent un-physical "overloading" conditions i.e. where the concentration just above the bed exceeds c_b calculated from the reference concentration formula, the solution suggested by (Justesen et al., 1986) is invoked. That is, if the concentration close to the bed exceeds the reference concentration, the value is in practice taken from the cell adjacent to the boundary. At the top and monopile boundaries a zero-flux condition for c is utilized.

3.1. Morphological model

The morphological updating routine is based on the sediment continuity (Exner) equation

$$\frac{\partial h}{\partial t} = \frac{1}{1-n} \left[-\frac{\partial q_{Bi}}{\partial x_i} + D + E \right], \quad i = 1, 2 \quad (22)$$

where $n = 0.4$ is the bed porosity and

$$D = (w_s - u_3)c_b, \quad E = (\nu + \beta_s \nu_T) \frac{\partial c}{\partial x_3} \Big|_{x_3=b} \quad (23)$$

are the deposition and erosion coming from the suspended sediment model. The Exner equation is based on instantaneous sediment transport fields and therefore the morphological and hydrodynamic times are equivalent. To ensure that the bed slopes do not exceed the angle of repose the sand slide model described in detail by (Roulund et al., 2005) is implemented. In the present work, this model is activated at positions where the local bed angle exceeds the angle of repose $\phi_s = 32^\circ$, and is de-activated once the local bed angle has been reduced to 31.9° .

The equations comprising the fully-coupled model outlined above are solved numerically using the open-source CFD toolbox OpenFOAM[®], version 1.6-ext, making use of a finite volume spatial discretization with a collocated variable arrangement, in conjunction with a standard PIMPLE algorithm. Again, for further details see (Jacobsen et al., 2014). The fully-coupled model presented above has also been utilized recently by (Baykal et al., 2015) who simulated the current-induced scour process around a vertical monopile cylinder, by (Baykal et al., 2017) who simulated scour and backfilling around piles in waves as well as by (Fuhrman et al., 2014) (Larsen et al., 2016), and (Bayraktar et al., 2016) in the simulation of wave-induced and wave-plus-current-induced scour and/or backfilling processes beneath submarine pipelines.

4. Re-analysis of existing research

Before proceeding with validation of the model, some of existing research on scour around monopiles will first be revisited, with particular focus on the effects of a finite boundary layer thickness, which turns out to be highly important to the understanding of tsunami-induced scour processes around offshore monopiles. The reason for this is two-fold. First, while data exists, there is not currently available a closed-form expression for predicting the equilibrium scour depth accounting for the finite boundary layer thickness. Second, the existing formula for the time scale of the scour development, will give rise to some extremely small time scales when extrapolating to full scale. Therefore the experimental data is revisited and a new expression for the time scale

is proposed.

According to (Sumer and Fredsøe, 2002) and (Melville and Sutherland, 1988) the non dimensional equilibrium scour depth, S_e/D is a function of θ , the sediment gradation, the boundary layer thickness to pile size ratio δ/D , the sediment to pile-size ratio, the shape factor and the alignment factor. For the present simulations, with uniform sediment distribution and a circular pile, however the scour depth becomes only a function of θ and δ/D . If the situation is in the live-bed regime the influence of θ is rather small, and effectively the scour depth is primarily a function of δ/D . In Fig. 2 experimental data compiled by (Melville and Sutherland, 1988) (also reproduced in (Sumer and Fredsøe, 2002)) is shown together with a new line representing the following expression

$$\frac{S_e}{S_0} = 1 - \exp\left(-0.9 \frac{\delta}{D}\right), \quad (24)$$

where $S_0/D = 1.3$ is the widely-accepted equilibrium current induced scour value around a circular pile (without depth limitation), see (Sumer and Fredsøe, 2002). This expression is a fit to the data which will be used later in estimating equilibrium scour depths. Included in the figure are also results involving steady current scour from the present study as well as one result from the numerical study (using the same model) by (Baykal et al., 2015). These results will be compared and discussed in forthcoming sections. It can be seen that equation (24) gives a quite good approximation to the experimental results even though the experiments show some scatter (the standard deviation on S_e/S_0 from the expression is 0.11). There is a tendency for smaller scour depths as the boundary layer thickness to pile diameter reduces. The reason for this is that the decreased boundary layer thickness in turn decreases the size of the horseshoe vortex and thus reduces the scouring capacity.

Based on a series of steady current scour experiments (Sumer et al., 1992a), likewise proposed the following regression equation for estimating the scour time scale:

$$T_s^* = \frac{\sqrt{g(s-1)d^3}}{D^2} T_s = \frac{1}{2000} \frac{\delta}{D} \theta^{-2.2}, \quad (25)$$

which can be interpreted as the time it takes for significant scour to occur. Here T_s is the dimensional time scale and T_s^* is the non-dimensional time scale. It is important to emphasize, however, that (25) is based on experiments spanning the parametric range $0.039 \leq \delta/D \leq 10$ and $0.062 \leq \theta \leq 0.29$. Care must therefore be taken when extrapolating this expression to field conditions e.g. where Shields parameters $\theta = O(1)$ may be reached, see Tables 2 and 3 in section 6. Based on a re-investigation of the experimental data set of (Sumer et al., 1992a),

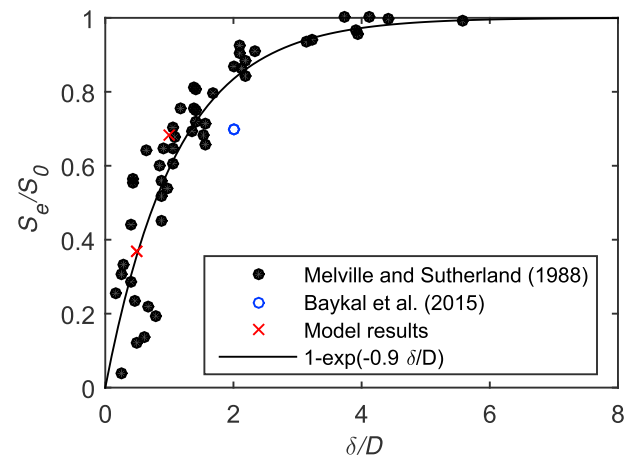


Fig. 2. Effect of boundary layer thickness on equilibrium scour depth. Experimental results compiled by (Melville and Sutherland, 1988) (also reproduced by (Sumer and Fredsøe, 2002)).

we propose a slightly modified expression:

$$T_s^* = \frac{1}{400} \left(\frac{\delta}{D} \right)^{0.7} \theta^{-1.5}. \quad (26)$$

The fit of the original experimental data set to both expressions (25) and (26) is shown in Fig. 3. Included in the figure are also the two time scales calculated from the forthcoming simulations. From this figure it is seen that the new expression (26), shown in Fig. 3b, slightly improves clustering of the data compared to the original expression (25), shown in Fig. 3a, though both expressions yield similar time scale predictions within the parametric range of the data. Due to the lower magnitude exponent on the Shields parameter θ , i.e. power -1.5 rather than -2.2 , it is felt that the modified expression (26) will be less prone to extrapolation errors at field scales. The reduced power of θ also makes sense on the following physical grounds. The time scale of the scour process should be proportional to the volume of the scour hole, $\Psi \propto D^3$, divided by the product of sediment transport rate, q_T , and width of the scour hole $\propto D$:

$$T_s \propto \frac{\Psi}{q_T D} \propto \frac{D^3}{q_T D} = \frac{D^2}{q_T}. \quad (27)$$

Inserting this into the expression for the non-dimensional time scale (25) gives

$$T_s^* = \frac{\sqrt{g(s-1)d^3}}{D^2} T_s \propto \frac{\sqrt{g(s-1)d^3}}{q_T} = \Phi_T^{-1} \propto \theta^{-3/2} \quad (28)$$

where Φ_T is the non-dimensional transport rate and is assumed to scale as $\theta^{3/2}$, common to many sediment transport formulae, see e.g. (Fredsoe and Deigaard, 1992). Based on these considerations, the scour time scale will therefore be estimated from the modified expression (26) in what follows.

5. Model validation

In this section, the numerical model described above will be validated for scour around a vertical cylindrical pile mounted on a horizontal plane soil bed, subjected to a steady current. Given the generally long periods (spanning several minutes to hours) typical of tsunamis, validation based on steady current flows can be considered more relevant than e.g. based on experiments using typical wind wave scales. Given the large computational costs of advanced CFD models such as those utilized in the present paper, simulations are necessarily limited to laboratory spatial and temporal scales. This model has already been used to simulate both detailed flow structures, bed shear stresses as well as scour around a wall mounted monopile by (Baykal et al., 2015) and it has therefore been partly validated for the purpose of this study. In addition two more steady scour cases are simulated here to further validate the models ability to correctly capture the relationship between S_e/D and δ/D , as well as the temporal scour development and thus the time scale of the scour process. In Table 1 the setup of the two additional cases is given where the boundary layer height δ is taken as the flow depth. The flow will be driven via the inlet by prescribing the horizontal velocity u , the turbulent kinetic energy density k , and the specific dissipation rate ω . As described in Section 3 the profiles for the three quantities comes from a separate

Table 1
Set-up of the two additional validation cases with $d = 0.17$ mm and $D = 0.1$ m.

Test	δ (m)	U (m/s)	U_f (cm/s)	δ/D	θ	Fr
1	0.05	0.246	1.28	0.5	0.06	0.35
2	0.10	0.430	1.89	1.0	0.13	0.43

1DV simulation which is driven by a body force given by

$$F = \frac{U_f^2}{\delta} \quad (29)$$

where U_f is chosen to give the desired Shields parameter.

In Fig. 4 the computed non-dimensional scour depth is plotted as a function of non-dimensional time. Included in the plots (dashed lines) is also the well known expression for the temporal development of the scour process as given by (Sumer and Fredsøe, 2002)

$$\frac{S}{D} = \frac{S_e}{D} \left(1 - \exp\left(-\frac{t^*}{T_s^*}\right) \right) \quad (30)$$

where t^* is the non-dimensional time given by

$$t^* = \frac{\sqrt{g(s-1)d^3}}{D^2} t. \quad (31)$$

The non-dimensional time scale has been calculated by equation (26) and the equilibrium scour depth by equation (24), both of which are experimentally based. As expected it can be seen that an initial phase of extensive scouring is followed by a longer phase of limited scouring, slowly approaching the equilibrium scour depth. The scour process of the two cases follows equation (30) quite well, although in both cases the initial scour phase in the model is a bit more rapid. The simulated and predicted equilibrium scour depths in both cases are quite similar, especially recalling the scatter from Figs. 2 and 3.

That the equilibrium scour depth is predicted well by the model can also be seen by re-inspection of Fig. 2. Here it can be seen that the model successfully captures the reduced scour depths due to the finite boundary layer thickness. The model also captures the time scale of the scour process which can be seen by inspection of Fig. 3. Here the modelled time scales are compared with the experimental as well as equation (26). The modelled time scales are calculated by integrating the scour curve according to

$$T_s^* = \int_0^{t_{max}^*} \frac{S_{max} - S}{S_{max}} dt^*, \quad (32)$$

where S_{max} is the maximum scour depth at any given time and t_{max}^* is the time at which the maximum scour occurs.

In Fig. 5 the equilibrium bed profile, in the near-pile region, from Test 2 is shown. Here some of the characteristic features of the steady current scour around a monopile can be seen. Upstream of the monopile the expected semi-circular shape of the scour hole with bed slopes equal to the angle of repose is clearly visible, whereas the slope downstream of the monopile is more gentle and the shape of the hole cannot be characterized as semi-circular. Further, downstream of the monopile bed material is deposited along the edges of the scour hole as a result of small-scale counter-rotating stream-wise phase-averaged vortices close to the bed and further downstream deposited material moves towards the center forming a bar as a result of large-scale counter-rotating streamwise phase-averaged vortices, as discussed in detail by (Baykal et al., 2015) see their Fig. 12a and by (Petersen, 2014). It can also be seen that the surrounding bed contains ripples. At full field scales, sheet flow conditions may in fact be reached and hence, the small scale ripple features developing in the present (model scale) result may in fact be related to scale effects. The presence of the ripples do not seem to influence the scour process, as no ripples are present in the neighbourhood of the pile where the flow field is disturbed and ripple formation prevented.

6. Similarity of tsunami field and model scales

As noted in the previous section, due to the large computational expenses associated with advanced CFD models, it is presently only feasible to simulate such scour processes around a monopile at model

(laboratory) spatial and temporal scales. The reason for this is that while much of the mesh might follow a standard length scaling, the near bed mesh does not, as the utilized model and field scale grain sizes are very similar. This would of course increase the needed number of cells but more importantly the small near bed cells combined with much higher full scale velocities would require the time step to be substantially smaller to ensure typical Courant number based restrictions. Therefore, prior to conducting such numerical simulations involving tsunami-induced scour, it is necessary to first establish a methodology for maintaining similarity of model and full field scales, in terms of properly chosen dimensionless quantities. In this section such a methodology for establishing hydrodynamic and morphodynamic similarity within an unsteady tsunami-induced scouring process will be introduced and described. This methodology will then be utilized to determine parameters used for numerical simulation at model scales in the subsequent section.

As inspiration for obtaining typical full tsunami scales, we will now consider a well-known measurement of the 2004 Indian Ocean tsunami event from the yacht Mercator, taken at a water depth $h = 14$ m, which is depicted in Fig. 6. Based on this signal (Madsen and Fuhrman, 2008), estimated that the leading wave of this tsunami could be reasonably represented as sinusoidal, with a wave period $T = 13$ min and surface elevation amplitude $A = 2.5$ m. Based on these parameters, the velocity magnitude U_m beneath such an event can be readily estimated, as a first approximation, based on linear shallow water theory

Table 2

Case 1: Comparison of resulting dimensional (above horizontal line) and dimensionless (below horizontal line) quantities at selected field and simulated model conditions. Dimensionless quantities maintained at both scales are highlighted in bold.

	Full scale	Model scale
D	5 m	0.1 m
d	0.3 mm	0.17 mm
T	13 min = 780 s	52.9 s
U_m	2.1 m/s	0.297 m/s
U_f	0.0745 m/s	0.0146 m/s
δ	2.36 m	0.047 m
T_s	1449 s	76.4 s
S	2.25 m	0.045 m
<hr/>		
s	2.65	2.65
Fr_D	0.30	0.30
δ/D	0.47	0.47
KC	328	157
$Re_D = U_m D/\nu$	10^7	$3 \cdot 10^4$
θ_m	1.1	0.078
T/T_s	0.54	0.69
S/D	0.45	0.45

Table 3

Case 2: Comparison of resulting dimensional (above horizontal line) and dimensionless (below horizontal line) quantities at selected field and simulated model conditions. Dimensionless quantities maintained at both scales are highlighted in bold.

	Full scale	Model scale
D	2.5 m	0.1 m
d	0.3 mm	0.17 mm
T	13 min = 780 s	87.2 s
U_m	2.1 m/s	0.42 m/s
U_f	0.0745 m/s	0.0190 m/s
δ	2.36 m	0.094 m
T_s	589 s	57 s
S	1.86 m	0.074 m
<hr/>		
s	2.65	2.65
Fr_D	0.42	0.42
δ/D	0.94	0.94
KC	655	366
$Re_D = U_m D/\nu$	$5.3 \cdot 10^6$	$4.2 \cdot 10^4$
θ_m	1.1	0.13
T/T_s	1.33	1.53
S/D	0.74	0.74

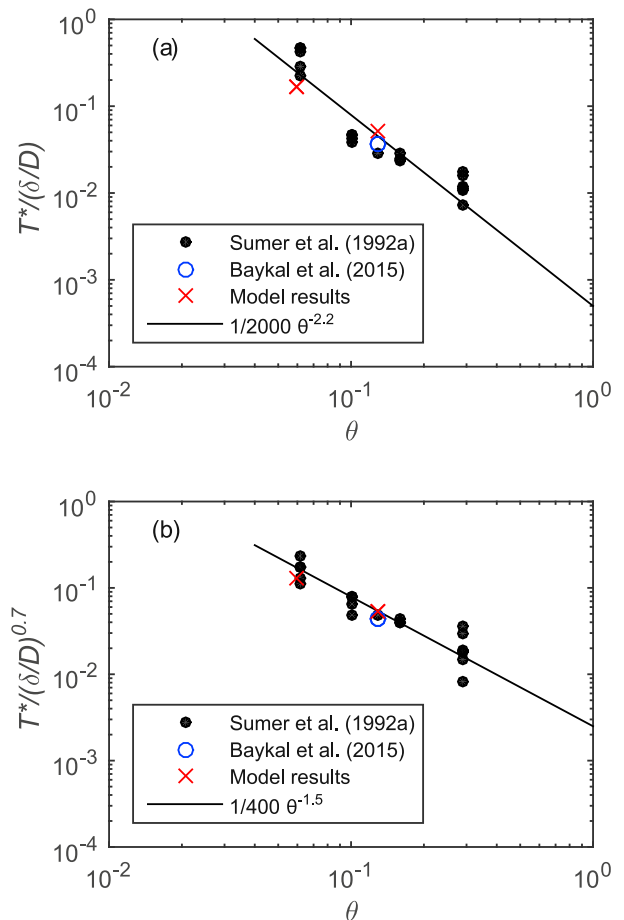


Fig. 3. Comparison of two regression equations: (a) (25) and (b) (26) for predicting the time scale of scour, based on the experimental data set of (Sumer et al., 1992a).

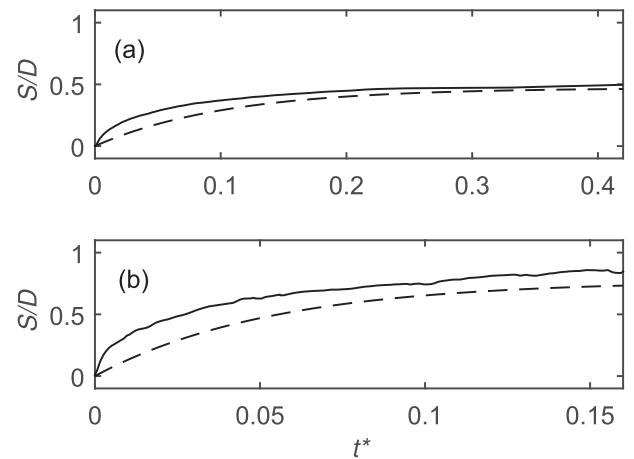


Fig. 4. Computed temporal evolution of the scour depth under steady current conditions (full lines) of a) Test 1 and b) Test 2. Also shown (dashed lines) is that from (30) after invoking (24) and (26).

$$U_m = A \sqrt{\frac{g}{h}} \tag{33}$$

yielding $U_m = 2.1$ m/s. This follows a similar methodology as also utilized in the tsunami-scale boundary layer simulations of (Williams and Fuhrman, 2016). It can be noted that a sinusoidal description for this tsunami event can be considered a much closer approximation than

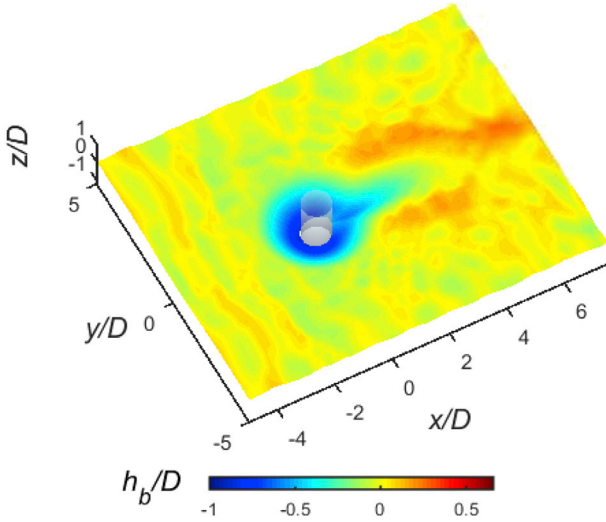


Fig. 5. Equilibrium near-pile bed profile of Test 2.

would e.g. a signal based on a solitary wave description, which would only include positive surface displacement, and which would not allow for the effective period and wave amplitude to be determined independently (see e.g. the discussion of (Madsen et al., 2008)). Note also that, based on records of free surface fluctuations at several locations during the 2011 Japan Tohoku tsunami, (Chan and Liu, 2012) have likewise concluded that the leading tsunami waves, in both near-field and far field regions, can be characterized as small amplitude long waves i.e. consistent with the linear shallow water description utilized above. The previously mentioned velocity magnitude U_m and period T will be utilized in what follows as characteristic values, representative of tsunamis at full scale, though obviously precise values may differ from these for other specific events and/or locations. Note that the corresponding water depth ($h = 14$ m) for this signal is conveniently appropriate for the present considerations, as monopile foundations are commonly utilized within offshore wind turbines out to depths no larger than about 30 m. Additionally, for the purposes of our discussion, a full-scale monopile diameter of $D = 5$ m will be considered, which is typical for offshore wind turbine foundations. Finally, for the sake of our discussion, bed sediments at full scale will be considered to have a typical grain size $d = 0.30$ mm i.e. corresponding to medium-fine sand.

Based on the values above, the following important hydrodynamic quantities can be estimated using widely-utilized dimensionally-correct expressions from the literature. The wave boundary layer thickness δ can be estimated based e.g. on the well-known expression of (Fredsoe and Deigaard, 1992)

$$\frac{\delta}{D} = \frac{k_s}{D} 0.09 \left(\frac{a}{k_s} \right)^{0.82} \quad (34)$$

where $k_s = 2.5d = 0.75$ mm and $a = U_m T / (2\pi) = 261$ m is the amplitude

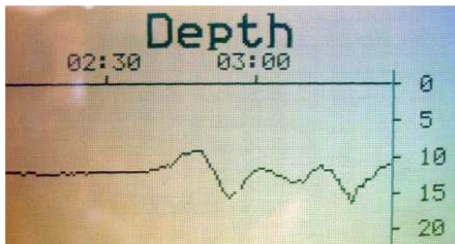


Fig. 6. Sound-meter registration of the Indian Ocean tsunami on December 26, 2004 from the yacht Mercator in the bay of Nai Ham, at the southwestern tip of Phuket, Thailand. The vertical axis measures depth in meters (from the keel i.e. 2 m below mean water level); The horizontal axis measures time in hours. Source Thomas Siffer (www.thomassiffer.be).

of the free stream orbital motion. Utilizing these yields the estimate $\delta = 2.36$ m for the parameters considered. The value has additionally been confirmed from tsunami-scale boundary layer simulations by (Williams and Fuhrman, 2016), which is based on the one-dimension vertical turbulent boundary layer model of (Fuhrman et al., 2013). Notice that, though expectedly much larger than typical wind wave boundary layer thicknesses of up to say 10 cm, the estimated boundary layer thickness is still only a fraction of the water depth, $h = 14$ m, in this example. The depth-based Froude number $Fr_h = U_m / (gh)^{0.5} = 0.18$ is also relatively small (< 0.2). Hence, for the conditions considered, the effects associated with the physical water depth h can be considered small, with associated length scales then based entirely on the monopile diameter D . Accordingly, we define a dimensionless Froude number as follows:

$$Fr_D = \frac{U_m}{\sqrt{gD}} \quad (35)$$

As discussed previously, due to their generally long periods, it is expected that the instantaneous flow and resulting scour process around a monopile during a tsunami event will more closely resemble those under steady flow conditions, rather than those beneath wind waves. Therefore, to achieve hydrodynamic similarity we will select the flow parameters U_m and T such that we maintain similarity in terms of the diameter-based Froude number (35), as well as the boundary layer thickness-to-diameter ratio δ/D , based on (34). Equating the Froude number (35) ensures that the adverse pressure gradient induced by the presence of the structure itself will be similar at both model and field scales, i.e. that the ratio of the excess stagnation pressure head in front of the monopile $U_m^2 / (2g)$ -to-pile diameter D will be maintained. Similarly, by maintaining similarity in δ/D , we ensure that the relative size of the horseshoe vortex, which is expected to largely govern the scouring process, will be similar at both model and full scales. Also of interest, is the so-called Keulegan-Carpenter number

$$KC = \frac{U_m T}{D} \quad (36)$$

which governs the formation and relative extension of the wake pattern in oscillatory motion. Additionally, it is likewise of interest to estimate the time scale of the expected scour process. Under both current and wave conditions, this is widely known to depend on the Shields parameter. For waves this can be defined as

$$\theta_m = \frac{U_{fm}^2}{(s-1)gd'} \quad (37)$$

where the maximum value of the friction velocity U_{fm} can be estimated from

$$U_{fm} = \sqrt{\frac{f_w}{2}} U_m, \quad (38)$$

where the rough-bed wave friction factor f_w expression from (Fuhrman et al., 2013) is utilized

$$f_w = \exp \left(5.5 \left(\frac{a}{k_s} \right)^{-0.16} - 6.7 \right). \quad (39)$$

This is likewise consistent with the general findings of (Williams and Fuhrman, 2016), who found that this expression maintained reasonable accuracy, even when extrapolated to full tsunami-scale. With an estimation of the Shields parameter the time scale of scour T_s can now be estimated. Due to the long durations typical of tsunamis, this time scale will be based on existing steady current scour research, equation (26), but invoking the expected tsunami-induced wave boundary layer thickness from (34). Hence, both current-like and wave-like features of tsunami-induced flows will be accounted for. In a similar fashion the

equilibrium scour depth can be estimated by invoking the same boundary layer thickness in equation (24), again utilizing $S_0 = 1.3$.

Choosing a scaling factor of $\lambda = 50$ and maintaining similarity in terms of the Froude number as well as the boundary layer thickness to pile diameter ratio results in a model scale wave period $T = 52.9$ s, and a velocity magnitude $U_m = 0.297$ m/s. It can be noted that, consistent with the notion that tsunamis are much longer than wind waves, the resulting period is significantly longer than those typically used in model-scale scour experiments involving wind waves, which would typically involve periods $T = O(1)$ s.

The resulting values, based on the presently described parameterization, are summarized in Table 2, under the full scale column. Both dimensional, as well as dimensionless, quantities are tabulated. Importantly, it can now be ascertained that the full scale tsunami period-to-scour time scale ratio $T/T_s = 0.54 = O(1)$ i.e. typical tsunami periods can be expected to be the same order of magnitude as expected scour time scales. This is an important recognition, and implies that the scouring process induced by tsunami events may, or may not, be of sufficient duration to reach equilibrium scour conditions. Either scenario seems realistic, as equilibrium scour conditions can require several scour time scales to be reached.

The resulting dimensional and dimensionless parameters based on the discussed model scale are likewise summarized in Table 2, where the sediment grain diameter $d = 0.17$ mm utilized in the previously discussed model validation is maintained. The dimensionless quantities maintained at both full and model scales are highlighted in bold. The methodology described herein is designed to yield hydrodynamic similarity at model and full scales. However, as can be seen from Table 2, it does not yield precise similarity in all other dimensionless parameters. As is well-known, the Reynolds number is obviously not maintained, though this is not expected to greatly influence the scour process, as the Reynolds number does not play an important role in the formation of the horseshoe vortex. Additionally, e.g. the expected Shields parameter at model scale is an order of magnitude below that expected at full scale. Both are above critical, however, hence both conditions can be considered as effectively in the live bed scour regime which is necessary for scour similarity, see e.g. Fig. 3.24 in (Sumer and Fredsøe, 2002). These differences are also accounted for, at least in part, in the dimensionless period-to-scour time scale ratio T/T_s , which while not identical (0.54 versus 0.69), is quite close at both full and model scales. Hence, the morphological process occurring over an individual wave period at model scale will represent a similar portion of the scour process as expected at full scale. This case will be denoted Case 1.

In addition to the case just described, to extend the parametric range considered one more case will likewise be simulated. Here the full scale monopile is assumed to have half the diameter, i.e. $D = 2.5$ m (in this case the scaling factor is $\lambda = 25$ such that the mesh can conveniently be reused). The full scale and model scale quantities, calculated utilizing the same similarity approach, for this case are similarly summarized in Table 3. Note that in this case $\delta/D = 0.94$, nearly double that of Case 1. This will be denoted Case 2.

7. Simulation of tsunami-induced scour

Based on the preceding section, we will now simulate the tsunami-induced scour process around a monopile using the previously described and validated fully-coupled CFD numerical model. The idealized flow induced by our prototypical tsunami event will be introduced via the inlet (left hand) boundary by prescribing the horizontal velocity u , the turbulent kinetic energy density k , and the specific dissipation rate ω . The profiles for the three quantities comes from a separate 1DV simulations which were driven by a body force given by

$$F = U_m \frac{2\pi}{T} \cos\left(\frac{2\pi}{T} t\right). \quad (40)$$

For the purposes of our numerical model experiment, the model scale parameters presented previously in Tables 2 and 3 (i.e. $U_m = 0.297$ m/s and $T = 52.9$ s as well as $U_m = 0.42$ m/s and $T = 87.2$ s) will be utilized to drive the simulations. For Case 1 ten and Case 2 four, full tsunami periods will be simulated in succession. The motivation for considering multiple periods is four-fold: First, a real-life tsunami may well consist of a leading wave, in addition to several trailing waves; Second, consideration of the successive periods will shed light on tsunami-induced scour in the presence of pre-existing scour holes; Third, this will increase the effective total scour time, and hence can be considered relevant e.g. for other tsunami events having longer period than those specifically being considered herein; Fourth, it will shed light on whether the our understanding of the physical process, and therefore also our estimation of the equilibrium scour depth, is correct. As an indication of computational time for the present simulations, each successive model-scale period requires approximately 10 days of CPU time, when simulated in parallel on eight modern processors i.e. the full simulations require up to approximately four months to complete.

The simulated time series of the scour depth for Case 1, taken at both the front and back face of the monopile, are first presented in Fig. 7. It is seen from Fig. 7 that the first half-cycle (flow going rightward) expectedly produces significant scour at the front (left) side, which is then followed by a similar scouring process on the back (right) side during the second half-cycle (flow going leftward). These scouring processes can be mainly attributed to separate horseshoe vortices forming on opposite sides during the two successive half cycles. This is illustrated in Fig. 8 where instantaneous coherent vortical structures, identified by the so-called Q-criterion, around the monopile is depicted. The Q-criterion was originally formulated by (Hunt et al., 1988) and is defined as

$$Q = \frac{1}{2} (|\Omega_{ij}|^2 - |S_{ij}|^2) > \Pi_E \quad (41)$$

where $\Omega_{ij} = 1/2(\partial u_i/\partial x_j - \partial u_j/\partial x_i)$ is the mean rotation tensor and Π_E is a threshold used to define eddy containing zones. In Fig. 8 a horseshoe vortex is clearly seen in front of the monopile and further down stream the lee-wake vortices are clearly visible. This confirms the previous explanation, that the instantaneous flow and scour processes beneath a tsunami can be taken as resembling a current, but with finite boundary layer thickness limited by the growth duration. It may be noted that the Q-criterion has been extensively used in conjunction with scour and backfilling around piles in waves by (Baykal et al., 2017).

Due to the relatively long times involved, the processes occurring during the two half cycles of the tsunami seem to be largely independent of one another. It should be noted that, in the present scenario, the first half-cycle may be taken as either representing a leading elevation or

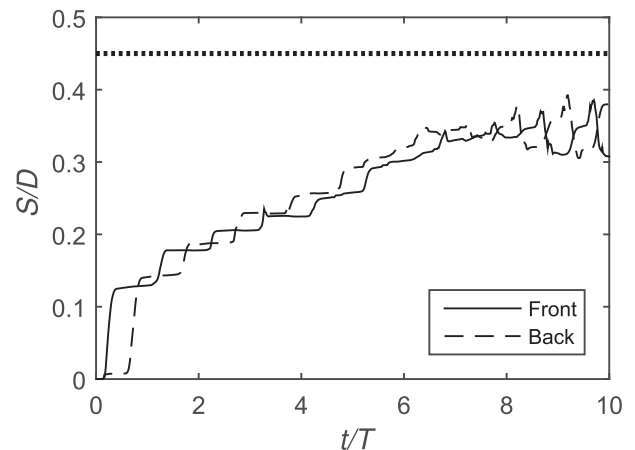


Fig. 7. Computed time series of scour depth at the front and back face of the monopile for Case 1. The horizontal dashed line represents the equilibrium scour depth estimated from (24).

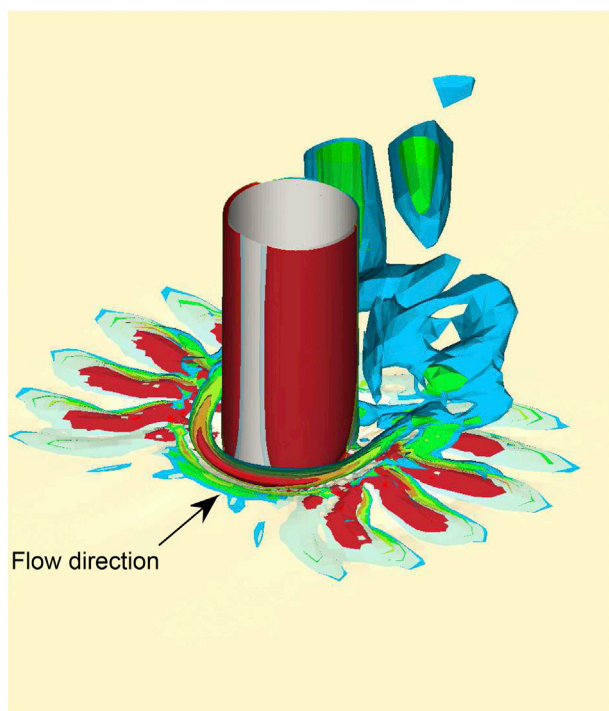


Fig. 8. 3D view of instantaneous vortical structures around the monopile at $t = 1.25T$ and a threshold of $Q = 2 \text{ s}^{-2}$.

leading depression tsunami wave, depending on the orientation adopted. Beyond the first period, it is seen that the scour deepens at both front and back sides during the successive wave periods in a loosely stepwise fashion i.e. the observed scour process can be characterized as largely cumulative. In the final periods some backfilling is observed each time the flow reverses. This is interpreted as the scour hole finally being so large that most of the sand being removed from one side of the monopile cannot escape the hole but instead is being deposited at the other side of the monopile. As a reference value, the equilibrium scour depth predicted by (24), after invoking (34), yields $S_e/D = 0.45$. This value is also depicted in Fig. 7 as the horizontal dashed line. As seen, after several periods of accumulation the resulting scour on both sides of the monopile seems to be gradually approaching this equilibrium value. Note that the relatively moderate equilibrium scour (at least in dimensionless terms i.e. $S_e/D < 0.5$) predicted in the present case, is again due to the finite boundary layer thickness-to-diameter ratio $\delta/D = 0.47$, which limits the relative size of the formed horseshoe vortices. Invoking the full scale monopile diameter $D = 5 \text{ m}$, however, this still correspond to considerable scour i.e. up to approximately $S = 2.25 \text{ m}$ for the full scale conditions considered. Based on the cumulative nature of the present results, it is reasonable to expect that the scour around a monopile will continue to build over the duration of a given tsunami event, ceasing when equilibrium scour depths are reached, which will occur only if the event is sufficiently long. Additionally, the effects on the scour associated with finite boundary layer thickness seem to be reasonably accounted for by the steady current expression (24), after invoking the tsunami wave boundary layer thickness from (34).

In Fig. 9 the time series of the scour depth, taken at both the front and the back face of the monopile, for the Case 2 (corresponding to a full scale diameter of $D = 2.5 \text{ m}$) is shown. The development of the scour depth in this case is similar to that of Case 1 in that the first half-cycle produces significant scour at the front side and the second produces significant scour at the back side. Further, beyond the first period the scour hole deepened in a stepwise cumulative fashion, and the depth is gradually approaching the equilibrium value calculated by invoking the boundary layer thickness in (24). The present case however exhibits one feature

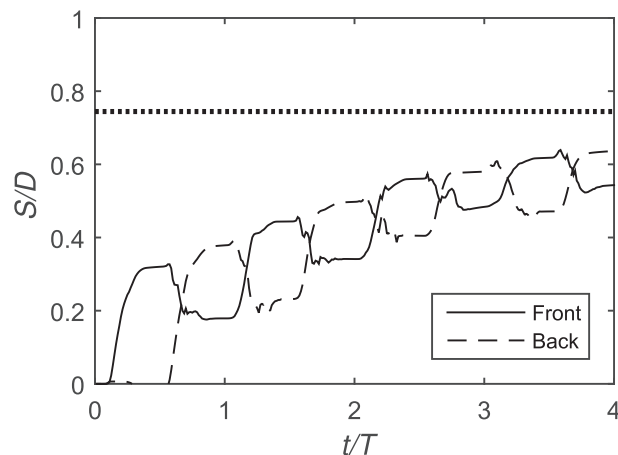


Fig. 9. Computed time series of scour depth at the front and back face of the monopile for Case 2. The horizontal dashed line represents the equilibrium scour depth estimated from (24).

quite different from Case 1. Already in the first period, after the flow reversal sediment is being transported from the back-side, backfilling into the front-side of the monopile. This process is then repeated when the flow re-reverses. This can be explained by the expected period to time scale ratio of this case being substantially larger than in Case 1, and thus within a half period there is sufficient time to transport substantial sediment all the way from one side of the monopile to the other.

Snapshots of the computed scour holes at selected times when the flow is leftward ($t = 0.4T, 1.4T$, and $2.4T$) as well as rightward ($t = 0.9T, 1.9T$, and $2.9T$) are additionally depicted in Fig. 10 (Case 1) and 11 (Case 2). These figures likewise illustrate the generally stepwise buildup of scour on the two opposing sides of the monopile during each successive half-cycle of the simulated tsunami (see again Fig. 7). In addition to the scour occurring on the front and back faces of the monopile, small scale ripple-like features are also seen develop. For Case 1 the ripples appear first to the transverse sides of the monopile, and then alternatively to the front and back of the monopile as time progresses, and they are more pronounced than in Case 2. Such features tend to initially form during the flow reversal, due to settling of suspended sediments. For Case 2 the bed profile has more current-like features than Case 1. This can be explained by the period to time-scale ratio being larger in the slim diameter case, and thus each period represents a larger portion of the scouring process towards equilibrium.

The computed scour profiles along the model centerline ($y = 0$), taken at the same instances as depicted in Figs. 10 and 11, are similarly depicted in Fig. 12 (Case 1) and 13 (Case 2). To ease comparison, these have been divided into times when the flow is leftward (Figs. 12a and 13a, corresponding to the left-hand subplots of Figs. 10 and 11) and rightward (Figs. 12b and 13b, corresponding to the right-hand subplots on Figs. 10 and 11). Inspection of the scour profiles, as a whole, demonstrates that reasonable symmetry is maintained throughout the scour process, consistent with the symmetric nature of the idealized (sinusoidal) flow description utilized. The asymmetry observed at any particular time is primarily due to the directionality of the flow (i.e. rightward or leftward directed) just experienced.

Based on the present results, in real (less idealized) tsunami events the asymmetry of the scour profile can be expected to depend strongly on the asymmetric nature of individual tsunami waves, which can of course vary widely from event to event. Considering the present results at half- and full-period intervals should provide a reasonable first indication regarding expected scour asymmetry, however.

8. Practical model for predicting tsunami-induced scour

As it is not always feasible in practice to perform advanced fully-

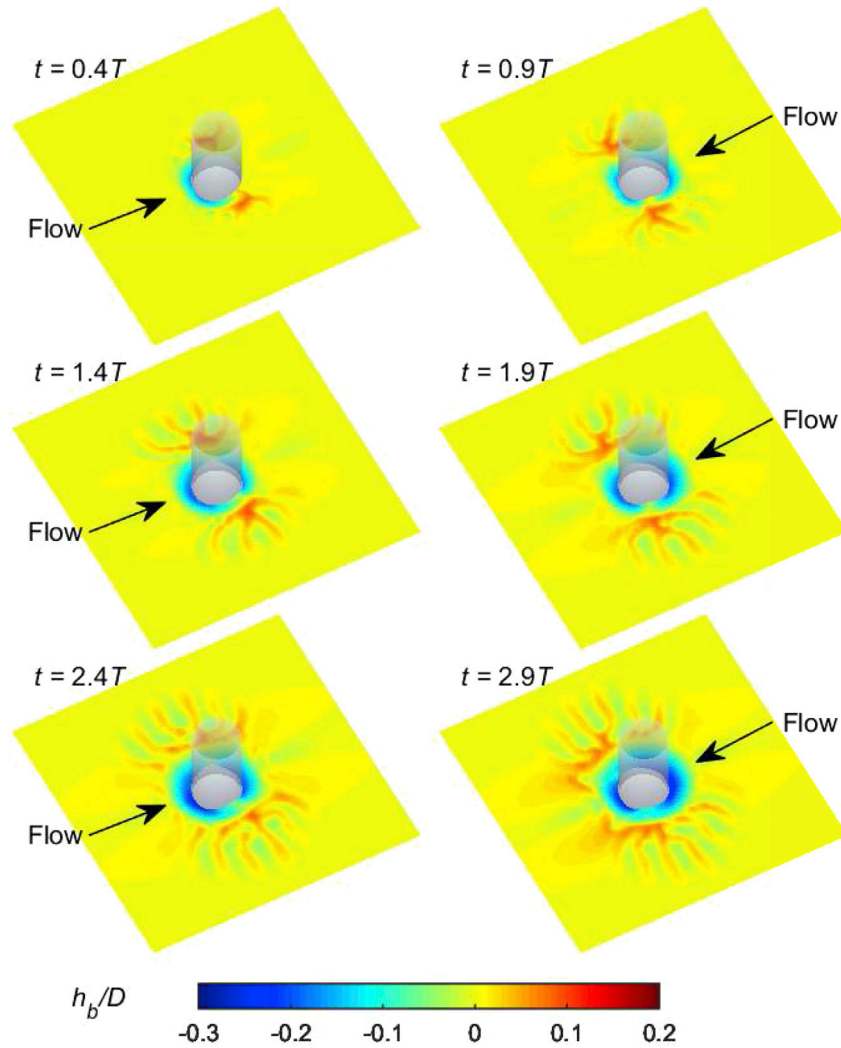


Fig. 10. Bed profiles around the monopile for Case 1 for three different periods.

coupled CFD simulations of tsunami-induced scour processes (even at model scales), especially for a large number of scenarios, it is of major importance that simpler methods be developed for predicting the tsunami-induced scour around monopile foundations in engineering practice. Such a simple practical method will be developed in the present section, which will utilize existing physical scour process knowledge, while also incorporating additional insight gained from the numerical simulation of the scour process presented in Section 7.

To begin making a practical assessment on the expected tsunami-induced scour around a monopile foundation, it is convenient to first estimate the maximum expected equilibrium scour that would be expected to occur at infinite time i.e. if a given tsunami event was repeated indefinitely. Taking into account the effect of a (potentially finite) boundary layer thickness-to-pile diameter ratio δ/D , this equilibrium scour S_e can be reasonably estimated according to (24) where the tsunami wave boundary layer thickness δ can be estimated directly from (34), and where the maximum potential current-induced scour (for large boundary layer thickness) may be taken as

$$\frac{S_0}{D} = 1.3 \pm \sigma_{S/D}. \quad (42)$$

Here $\sigma_{S/D} = 0.7$ is the standard deviation of expected scour, as presented by (Sumer et al., 1992b), which can be accounted for in practice to adjust for a desired level of conservativeness. In what follows, we aim to predict the mean expected scour, hence this standard deviation will be neglected

i.e. we simply utilize $S_0/D = 1.3$ in (24). Now, as emphasized previously, typical tsunami periods can be expected to be the same order of magnitude as expected scour time scales. This, again, implies that true equilibrium scour depths may, or may not, be reached, depending on the duration of a given tsunami event, since reaching equilibrium can require several scour time scales. It is therefore important to take the expected time development of the scour process into account when making tsunami-induced scour predictions. Utilizing a scour time scale T_s estimated from (26), this temporal variation can then be described according to the following expression

$$\frac{S}{D} = \frac{S_e}{D} \left(1 - \exp\left(-\frac{t_s}{T_s}\right) \right), \quad t_s = n\psi T. \quad (43)$$

This resembles (30), which is commonly used to characterize typical time development of scour processes. In the equation above t_s represents the effective scour time, and n represents the integer number of successive waves characterizing a given tsunami i.e. $n = 1$ can be utilized to predict the maximum scour occurring during the leading tsunami wave, with $n = 2, 3, \dots$ utilized for predicting the accumulated scour induced by any successive waves. The additional factor $\psi \leq 1$ can be taken to represent the effective scouring fraction of a period. Based on the stepwise fashion in which the scour hole deepens and the relative independence of the two half cycles, it is expected to be at least $\psi < 1/2$ (if a sinusoidal tsunami description is utilized as herein). In fact it can be expected to be somewhat lower than $1/2$ since θ is not at a maximum throughout the entire

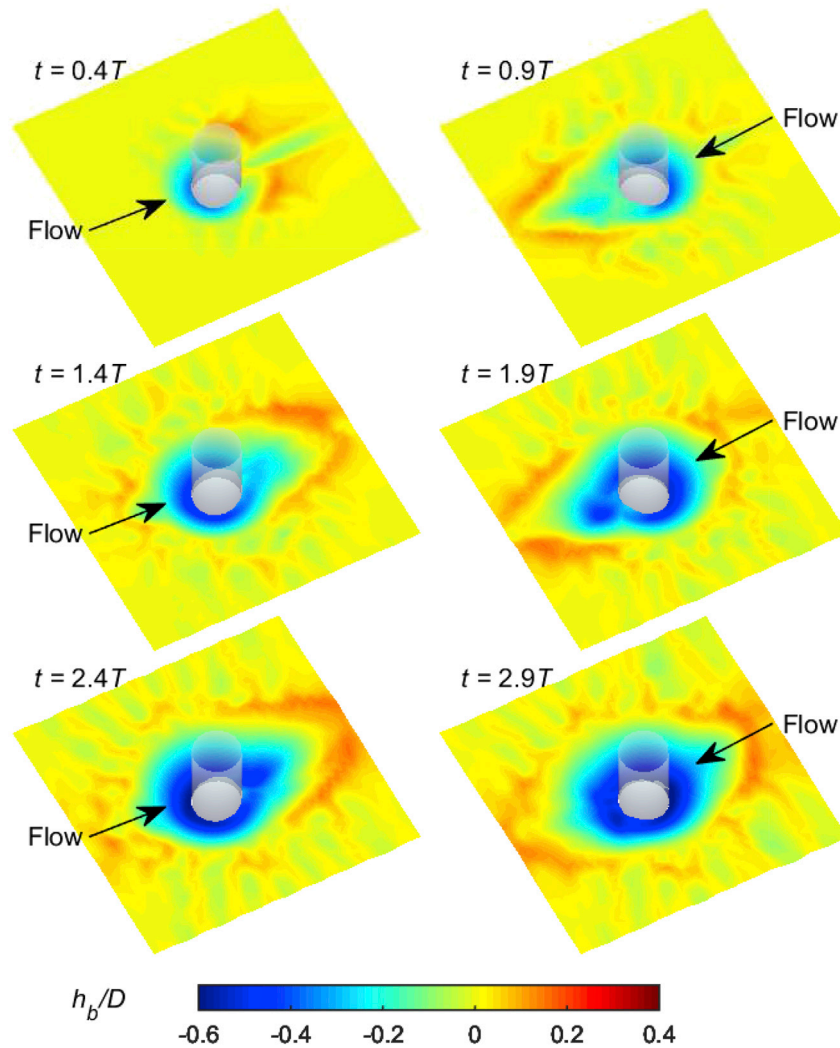


Fig. 11. Bed profiles around the monopile for Case 2 for three different periods.

period. Therefore a value of $\psi = 1/3$ has been chosen for use in what follows as it is in line with the previous arguments and is seen to match the simulations well. Note that for large t_s , (43) will simply lead to equilibrium scour i.e. $S = S_e$.

To test the validity of the simple practical model described above, the predicted scour from the practical approach leading to (43) will be compared directly with the numerical scour results presented in Section 7. In Figs. 14 and 15 the simulated scour process is shown together with scour curves obtained utilizing equation (43) invoking the tsunami boundary layer thickness for the calculation of S_e and T_s . Included in the figure is also the steady current estimate obtained by invoking the flow depth as the boundary layer thickness and setting $\psi = 1$. As can be seen, the simple predictive model proposed above does a consistently good job of predicting the scour observed within the numerical simulations, as it follows quite well the maximum scour depth within each period. The estimate is not exact, but recalling the scatter in the experimental results, leading to equation (24) on which the engineering model is built, the estimate is satisfactory. As expected the steady current estimate is somewhat higher, especially for Case 1, and this illustrates the importance of invoking the expected effect of the limited tsunami boundary layer thickness. It is emphasized that the approach proposed above is conveniently founded upon existing experimentally-based expressions for use in steady current scour, but invoking the boundary layer thickness and Shields parameter expected from tsunami wave events i.e. it effectively combines both current-like and wave-like properties of tsunamis.

As such, at the infinite period limit, the practical model proposed is fully consistent with existing methodology for predicting equilibrium scour under steady current conditions. It is finally important to emphasize that the steady current limit can be considered quite physically relevant for scenarios involving tsunami-induced scour in some circumstances, at least as an upper bound. In particular, this limit would seem particularly relevant for tsunamis having very long duration (i.e. large T/T_s), for scour occurring at shallower water depths (where the boundary layer thickness δ can be taken as equivalent to the water depth h), or for tsunami-induced scour around smaller monopile diameters (i.e. where the boundary layer thickness-to-pile diameter ratio becomes large i.e. $\delta/D > 4$) e.g. those more typical of bridge piers.

To further highlight the predictive capability of the simple model, accumulated scour results from each of the successive wave periods in the simulations (see Figs. 7 and 9) will be considered separately, with the results corresponding to the maximum scour occurring during a given period of interest. Results at both the front and back face of the monopile will be considered separately, for completeness. A plot summarizing the computed versus predicted (utilizing the present simple practical approach) maximum scour is depicted in Fig. 16. For completeness the computed and predicted equilibrium value for the simulated current-induced scour Section 5, previously considered as model validation, is also shown (\times) in Fig. 16, as is the steady current result from (Baykal et al., 2015) which again was simulated utilizing the same model. As can be seen, the simple predictive model proposed above does a

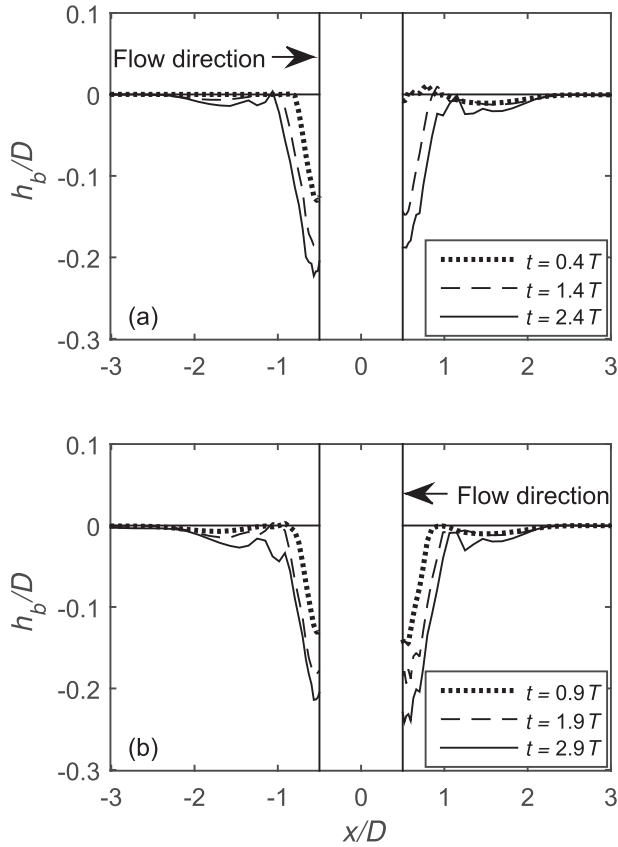


Fig. 12. Computed scour profiles along the centerline for Case 1 for three consecutive periods.

consistently good job of predicting the scour observed within the numerical simulations, with all results reasonably near the line of perfect agreement (full line) in Fig. 16. This conclusion holds for the full range of flows considered: For the transient tsunami cases, though the simple model cannot predict all details, such as the momentary lee-side back-filling episodes observed on the front face, it adequately predicts the accumulative maximum scour occurring over all successive simulated tsunami periods. As discussed previously, relatively moderate S/D values are found for the tsunami scenarios considered, owing to effects associated with the finite boundary layer thickness, which seem to be properly accounted for. Such effects become less important at the steady current limit, leading to the larger S/D , which is also adequately captured by the proposed simple approach.

9. Conclusions

This paper presents a numerical assessment for tsunami-induced scour around a monopile structure, as commonly utilized in practice as offshore wind turbine foundations. The basis of the numerical model is the advanced fully-coupled hydrodynamic and morphological CFD model presented in (Jacobsen et al., 2014), and utilized specifically for simulating scour processes by (Baykal et al., 2015; Fuhrman et al., 2014) and (Larsen et al., 2016). The model hydrodynamics are based on Reynolds-averaged Navier-Stokes (RANS) equations, coupled with two-equation $k - \omega$ turbulence closure. These are then coupled with both bed and suspended sediment transport descriptions, which drive resultant morphology of the sea bed. Simulations of the scour process in steady current has been performed as model validation, complementing previous validation made by (Baykal et al., 2015).

Due to computational expense, it is only feasible at present to simulate scour processes at model (laboratory) spatial and temporal scales. Therefore, prior to making any simulations, a methodology has been

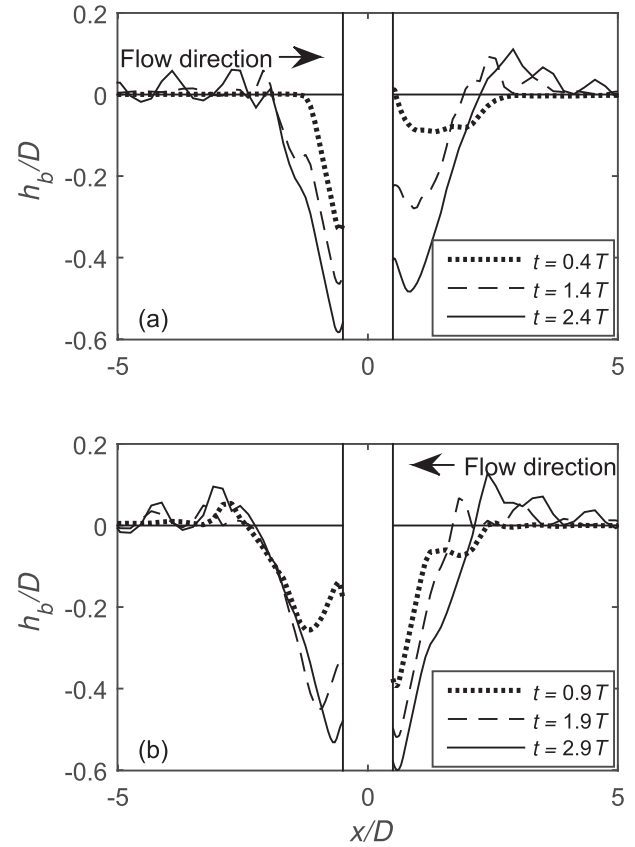


Fig. 13. Computed scour profiles along the centerline for Case 2 for three consecutive periods.

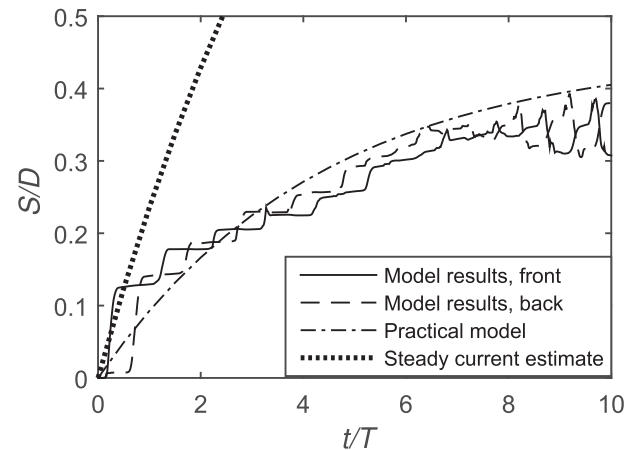


Fig. 14. Comparison between the predicted and simulated scour depths for Case 1.

developed for establishing similarity (based on dimensionless numbers) between full tsunami and model scales, in precisely the same fashion as in hydraulic scale model experiments in which similarity is established between full scale real life and the hydraulic scale model. This methodology is based on a diameter-based Froude number, coupled with the dimensionless ratio of the expected boundary layer thickness-to-monopile diameter δ/D . The Froude similarity ensures similarity in the adverse pressure gradients induced by the presence of the structure itself, whereas the δ/D similarity ensures equivalent relative size of the horseshoe vortex in front of the monopile. Reasonable morphologic similarity of the scour process is also maintained, by ensuring that the dimensionless tsunami period-to-scour time scale ratios are similar. It is

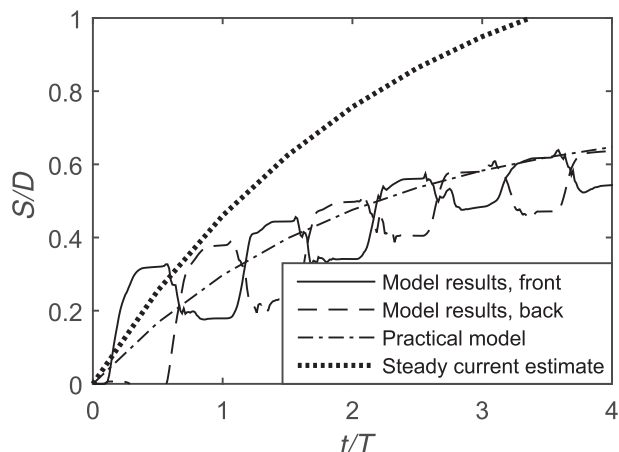


Fig. 15. Comparison between the predicted and simulated scour depths for Case 2.

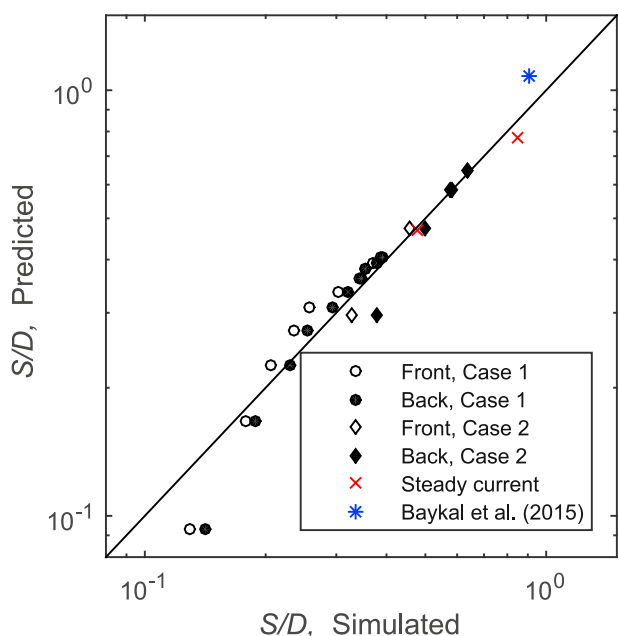


Fig. 16. Comparison between the predicted and simulated scour depths.

demonstrated that typical tsunami periods can be expected to be the same order of magnitude as expected scour time scales in real life. This implies that equilibrium scour conditions may, or may not, be reached, depending on the total duration of a given tsunami event.

Taking a well-known tsunami measurement from the 2004 Indian Ocean tsunami as a typical event at full scale (in terms of its surface amplitude and approximate period), input parameters are found based on the similarity principles described above. These are then utilized within simulations of the tsunami-induced scour process around a monopile foundation. The results generally demonstrate that, consistent with physical expectations due to their long periods, the tsunami-induced scour process reasonably resembles that under steady current conditions. Unlike steady current scour, however, the tsunami-induced scour process, under the conditions considered, can be limited by finite wave boundary layer thickness, rather than the flow depth. Hence, it is important to take into account both the current-like (due to their long periods), as well as their wave-like (unsteady) properties, to fully understand and assess the tsunami-induced scour process. This is consistent with the findings of tsunami-scale wave boundary layer simulations of (Williams and Fuhrman, 2016).

Based on existing scour knowledge, combined with the insight gained from the advanced CFD simulations, a simple methodology has been developed for predicting tsunami-induced scour around monopiles in practice. The method takes into account the time variation of the scour process as well as finite boundary layer thickness effect, and can hence be applied to predict the cumulative tsunami-induced scour under successive periods i.e. it is not limited to simply a leading wave description. The practical method makes modified use of existing experimentally-based expressions for predicting steady current scour and time scales, and hence is fully-consistent with these at this (infinite period) limit. The practical method is demonstrated to accurately predict all of the simulated scour depths considered in the present paper i.e. ranging from the simulated transient tsunami events to those induced by steady current flows.

Acknowledgements

The authors acknowledge support from the European Union project ASTARTE–Assessment, Strategy And Risk Reduction for Tsunamis in Europe, Grant no. 603839 (FP7-ENV-2013.6.4-3). The third and fourth author additionally acknowledges Innovative Multi-purpose Offshore Platforms: Planning, Design and Operation (MERMAID), 20122016, Grant Agreement No. 288710 of European Commission, 7th Framework Programme for Research.

References

- Baykal, C., Sumer, B.M., Fuhrman, D.R., Jacobsen, N.G., Fredsøe, J., 2015. Numerical investigation of flow and scour around a vertical circular cylinder. *Phil. Trans. Roy. Soc. A* 373. Article no. 20140104.
- Baykal, C., Sumer, B.M., Fuhrman, D.R., Jacobsen, N.G., Fredsøe, J., 2017. Numerical simulation of scour and backfilling processes around a circular pile in waves. *Coast. Eng.* 122, 87–107.
- Bayraktar, D., Ahmad, J., Eltard Larsen, B., Carstensen, S., Fuhrman, D.R., 2016. Experimental and numerical study of wave-induced backfilling beneath submarine pipelines. *Coast. Eng.* 118, 63–75.
- Bricker, J.D., Francis, M., Nakayama, A., 2012. Scour depths near coastal structures due to the 2011 tohoku tsunami. *J. Hydraul. Res.* 50 (6), 637–641.
- Cebeci, T., Chang, K.C., 1978. Calculation of incompressible rough-wall boundary-layer flows. *AIAA J.* 16, 730–735.
- Chan, I.-C., Liu, P.L.F., 2012. On the runup of long waves on a plane beach. *J. Geophys. Res.* - Oceans 117 (8), 1–17. <http://dx.doi.org/10.1029/2012JC007994>.
- Chen, J., Huang, Z., Jiang, C., Deng, B., Long, Y., 2013. Tsunami-induced scour at coastal roadways: a laboratory study. *Nat. Hazards* 69 (1), 655–674. <http://dx.doi.org/10.1007/s11069-013-0727-6>.
- Engelund, F., Fredsøe, J., 1976. A sediment transport model for straight alluvial channels. *Nord. Hydrol.* 7, 293–306.
- Fredsøe, J., Deigaard, R., 1992. *Mechanics of Coastal Sediment Transport*. World Scientific, Singapore.
- Fuhrman, D.R., Schløer, S., Sterner, J., 2013. RANS-based simulation of turbulent wave boundary layer and sheet-flow sediment transport processes. *Coast. Eng.* 73, 151–166. <http://dx.doi.org/10.1016/j.coastaleng.2012.11.001>.
- Fuhrman, D.R., Baykal, C., Sumer, B.M., Jacobsen, N.G., Fredsøe, J., 2014. Numerical simulation of wave-induced scour and backfilling processes beneath submarine pipelines. *Coast. Eng.* 94, 10–22.
- Hunt, J.C.R., Wray, A.A., Moin, P., 1988. Eddies, streams, and convergence zones in turbulent flows, Center for Turbulence Research. *Proceedings of the Summer Program*.
- Jacobsen, N.G., 2011. A Full Hydro- and Morphodynamic Description of Breaker Bar Development. Ph.D. thesis. Technical University of Denmark, Kgs. Lyngby.
- Jacobsen, N.G., Fredsøe, J., Jensen, J.H., 2014. Formation and development of a breaker bar under regular waves. Part 1: model description and hydrodynamics. *Coast. Eng.* 88, 182–193.
- Justesen, P., Fredsøe, J., Deigaard, R., 1986. The bottleneck problem for turbulence in relation to suspended sediment in the surf zone. In: *Proc. 20th Int. Conf. on Coastal Engineering*, pp. 1225–1239.
- Lacy, J.R., Rubin, D.M., Buscombe, D., 2012. Currents, drag and sediment transport induced by a tsunami. *J. Geophys. Res.* - Oceans 117 (9), C09028.
- Larsen, B.E., Fuhrman, D.R., Sumer, B.M., 2016. Simulation of wave-plus-current scour beneath submarine pipelines. *J. Waterw. Port. C-ASCE* 142 (5), 08216001. [http://dx.doi.org/10.1061/\(ASCE\)WW.1943-5460.0000338](http://dx.doi.org/10.1061/(ASCE)WW.1943-5460.0000338).
- Liang, D., Cheng, L., 2005. Numerical model for wave-induced scour below a submarine pipeline. *J. Waterw. Port. C-ASCE* 131, 193–202.
- Madsen, P.A., Fuhrman, D.R., 2008. Run-up of tsunamis and long waves in terms of surf-similarity. *Coast. Eng.* 55, 209–223.
- Madsen, P.A., Fuhrman, D.R., Schäffer, H.A., 2008. On the solitary wave paradigm for tsunamis. *J. Geophys. Res.* 113 <http://dx.doi.org/10.1029/2008JC004932>. Article no. C12012.

- Melville, B., Sutherland, A., 1988. Design method for local scour at bridge piers. *J. Hydraul. Eng. ASCE* 114 (10), 1210–1226.
- Nakamura, T., Kuramitsu, Y., Mizutani, N., 2008. Tsunami scour around a square structure. *Coast. Eng. J.* 50 (2), 209–246.
- Pan, C., Huang, W., 2012. Numerical modeling of tsunami wave run-up and effects on sediment scour around a cylindrical pier. *J. Eng. Mech. - ASCE* 138 (10), 1224–1235. [http://dx.doi.org/10.1061/\(ASCE\)EM.1943-7889.0000406](http://dx.doi.org/10.1061/(ASCE)EM.1943-7889.0000406).
- Petersen, T.U., 2014. Scour Around Offshore Wind Turbine Foundations. Ph.D. thesis. Technical University of Denmark. Department of Mechanical Engineering, Kgs. Lyngby, Denmark.
- Roulund, A., Sumer, B.M., Fredsøe, J., Michelsen, J., 2005. Numerical and experimental investigation of flow and scour around a circular pile. *J. Fluid Mech.* 534, 351–401.
- Sumer, B.M., Fredsøe, J., 2002. *The Mechanics of Scour in the Marine Environment*. World Scientific, Singapore.
- Sumer, B.M., Christiansen, N., Fredsøe, J., 1992a. Time scale of scour around a vertical pile. In: *Proc. Of the Second International Offshore and Polar Engineering Conference*, vol. 3, pp. 308–315.
- Sumer, B.M., Christiansen, N., Fredsøe, J., 1992b. Scour around a vertical pile in waves. *J. Waterw. Port. C-ASCE* 118, 15–31.
- Tonkin, S., Yeh, H., Kato, F., Sato, S., 2003. Tsunami scour around a cylinder. *J. Fluid Mech.* 496 (496), 165–192.
- van Driest, E.R., 1956. On turbulent flow near a wall. *J. Aeronaut. Sci.* 23, 1007–1011, 1036.
- Wilcox, D.C., 2006. *Turbulence Modeling for CFD*, third ed. DCW Industries, Inc., La Canada, California.
- Wilcox, D.C., 2008. Formulation of the $k-\omega$ turbulence model revisited. *AIAA J.* 46, 2823–2838.
- Williams, I.A., Fuhrman, D.R., 2016. Numerical simulation of tsunami-scale wave boundary layers. *Coast. Eng.* 110, 17–31.
- Wilson, R., Davenport, C., Jaffe, B., 2012. Sediment scour and deposition within harbors in California (USA), caused by the march 11, 2011 tohoku-oki tsunami. *Sediment. Geol.* 282, 228–240. <http://dx.doi.org/10.1016/j.sedgeo.2012.06.001>.

Chapter 3

Experimental study of tsunami-induced scour around a monopile foundation

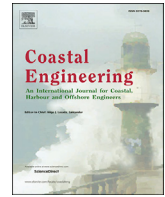
This Chapter has been published as:

Larsen, B. E., Arbøll L. K., Kristoffersen, S. F., Carstensen, S., Fuhrman, D. R. (2018). *Experimental study of tsunami-induced scour around a monopile foundation*. Coastal Engineering **138**: 9-21. doi:10.1016/j.coastaleng.2018.04.007



Contents lists available at ScienceDirect

Coastal Engineering

journal homepage: www.elsevier.com/locate/coastaleng

Experimental study of tsunami-induced scour around a monopile foundation

Bjarke Eltard Larsen^{*}, Lasse Kærgaard Arbøll, Sarah Frigaard Kristoffersen, Stefan Carstensen, David R. Fuhrman

Technical University of Denmark, Department of Mechanical Engineering, DK-2800, Kgs. Lyngby, Denmark



ARTICLE INFO

Keywords:

Tsunamis
Boundary layers
Scour
Morphology
Monopiles
Computational fluid dynamics

ABSTRACT

This paper presents an experimental study of the tsunami-induced scour process around a monopile foundation, representative of those commonly used for offshore wind farms. The scour process is studied by subjecting the monopile to a time varying current, which enables a properly down-scaled experiment from the boundary layer and scour perspective. It is shown how the scaled experiments corresponds to real life idealized tsunami cases with periods ranging from 10 to 40 min. It is then shown that the boundary layers of the model tsunami are well described by recently developed empirical relations for tsunami boundary layers. By subjecting the monopile to several successive tsunami waves the scour process is shown to occur in a stepwise cumulative fashion, with the final equilibrium scour depth tending to the depth limited steady current limit. It is shown that the entire scour development can reasonably be predicted by a recently developed simple engineering model. Finally, the experimental results are compared to a fully coupled hydrodynamic and morphologic CFD model and a good correspondence is obtained.

1. Introduction

Tsunamis are long waves, typically having periods the order of minutes to hours, that are commonly caused by sudden motions of the bed e.g. due to landslides or earthquakes. Tsunami research has been carried out using many different approaches. Tsunami deposits have been gathered to get an idea of prehistoric tsunamis, see. e.g. Dawson and Shi (2000) for an overview. Tsunamis have also been studied by conducting surveys and actual field measurements, see Lacy et al. (2012), Bricker et al. (2012), Kuriyama et al. (2014), Fu et al. (2013), Udo et al. (2016) and Jayaratne et al. (2016). A few analytical studies exists e.g. Madsen et al. (2008) and Yeh and Mason (2014). Numerically, most tsunami research has focused on solving the non-linear shallow water equations or simulating the tsunami with a Boussinesq model see e.g. Madsen and Fuhrman (2008), Fuhrman and Madsen (2009), Apotsos et al. (2011a), Apotsos et al. (2011c), Apotsos et al. (2011b), Cheng and Weiss (2013), Sugawara et al. (2014a), Sugawara et al. (2014b). Recently, more computationally heavy numerical studies have been performed by solving the Reynolds-Averaged-Navier-Stokes (RANS) equations by Douglas and Nistor (2015) and Jiang et al. (2015), or with the Smoothed Particle Hydrodynamics Method (SPH) by Wei et al. (2016). Experimentally, tsunamis have often been attempted to be studied using solitary waves. However, when scaled up, these waves resemble more wind wave than

tsunami scales, as their flow durations are far too short, and their relevance to real-world-geophysical tsunamis is questionable (see Madsen et al. (2008) and Chan and Liu (2012)). Schimmels et al. (2016) have succeeded in producing properly-scaled tsunamis and the same experimental facility was used to study tsunami propagation by Sriram et al. (2016), where the feasibility of studying tsunami run-up was also discussed. Onshore tsunamis have also been studied as bores see. e.g. Lavioctoire (2015) or Douglas and Nistor (2015). However, as noted by Sriram et al. (2016), the undular or breaking bores are just two realizations of tsunami run-up, and one cannot generalize a particular tsunami case, as even the same tsunami event can have very different manifestations at different locations. Also, when studying tsunamis as bores, scaling considerations are still important, as the duration of the experimental bore should be sufficiently long. As discussed by Schimmels et al. (2016), a typical full scale tsunami event with a duration of 1000 s, corresponds to 100 s at model scale using a scaling factor of 100 using a standard Froude scaling approach. This is a much longer duration than most model-scale tsunami experiments.

Studies investigating tsunami-induced scour around coastal and offshore structures (the focus of the present work) are rather limited. From surveys, Wilson et al. (2012) studied the sediment scour and deposition within harbours in California as a result of the 2011 Tohoku tsunami. Experimentally, Chen et al. (2013) studied the tsunami-induced

^{*} Corresponding author.

E-mail address: bjelt@mek.dtu.dk (B.E. Larsen).

<https://doi.org/10.1016/j.coastaleng.2018.04.007>

Received 21 September 2017; Received in revised form 19 March 2018; Accepted 5 April 2018

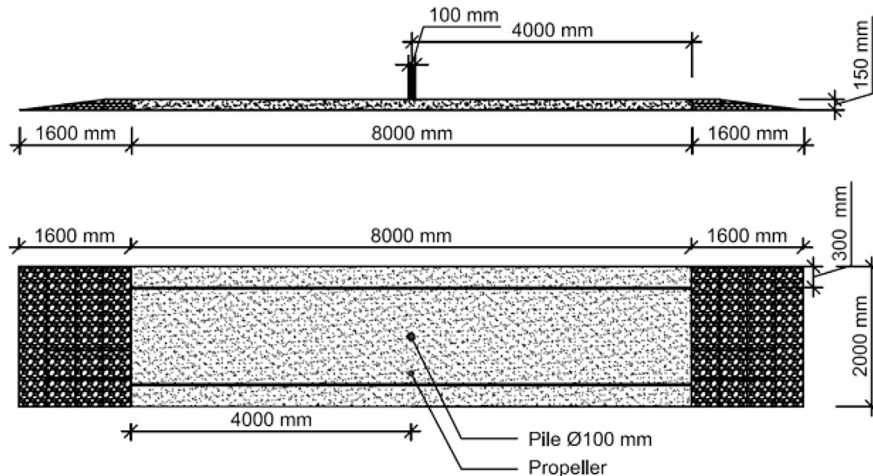


Fig. 1. Schematic view of the test set-up. A pile with a outer diameter of 0.1 m is placed in the middle of a 8 m long, 2 m wide and 0.15 m deep sand bed. A 1:8 slope is placed at both ends of the sand bed.

scour at coastal roadways. Also, [Bricker et al. \(2012\)](#) conducted a field study of scour depths measured on the landward side of seawalls and floodwalls, as well as beside a building foundation footing, from the 2011 Tohoku tsunami. Experimental investigations on the tsunami-induced scour specifically around monopiles are seemingly limited to those of [Tonkin et al. \(2003\)](#), who studied the scour promoted by incident solitary waves around a cylinder on a sloping beach, where the cylinder was mounted near the shoreline, [Nakamura et al. \(2008\)](#) who studied scour around a square pile induced by solitary and long waves, as well as by [Shafiei et al. \(2015\)](#) and [Lavictoire \(2015\)](#) who studied the bore-induced local scour around a circular structure. It is again emphasized that the temporal duration using solitary waves are far less than would be typical of model scale geophysical tsunamis.

While the behaviour and evolution of tsunami waves is indeed difficult to reproduce experimentally due to the long durations, the offshore near-bed processes can be studied by viewing the tsunami as a time varying current, which is justifiable provided that the Froude number is sufficiently small. This has been done by [Williams and Fuhrman \(2016\)](#), who simulated a series of tsunami-scale boundary layers, emphasizing that they are both current like and wave like. The boundary layers resemble steady currents due to their long duration. They also resemble waves, as they are unsteady and the boundary layer may not span the entire water depth. This assertion is likewise consistent with field measurements of [Lacy et al. \(2012\)](#). [Larsen et al. \(2017\)](#) simulated the tsunami-induced scour at model scale by also approximating the tsunami-induced flow as a time varying current within a

CFD approach. They developed a procedure for properly scaling tsunami-induced scour and came up with a practical engineering model for predicting the scour development beneath successive tsunami waves.

The two afore mentioned studies approximating tsunami-induced boundary layers and scour are both numerical in nature. However, representing a tsunami via a time varying current is also experimentally attractive, as it enables the study of offshore tsunami-induced boundary layers and scour to be performed using a pump-driven flow, rather than more traditional wave paddles. It can be noted that the scour process beneath a time varying current has also been studied previously by [Link et al. \(2017\)](#), though with the intent to study flood wave-induced scour around bridge piers. The present paper aims to extend knowledge on tsunami-induced scour around off-shore monopile foundations by studying the scour process induced by the pump-driven flow that would be expected beneath long properly-scaled tsunami waves. This approach also means that the effect of variation in pore pressure gradients on the scour process as described by [Tonkin et al. \(2003\)](#) and [Nakamura et al. \(2008\)](#) are not accounted for the current setup. This is reasonable if the monopile is standing off-shore and the Froude number is small. The paper also aims to strengthen the link to the practical engineering models developed in the purely numerical studies by [Williams and Fuhrman \(2016\)](#) and [Larsen et al. \(2017\)](#). The numerical models employed in these studies have therefore also been used in the present study to simulate the boundary layers and scour process of selected cases.



Fig. 2. An image of the set-up in the flume. The carriage used when recording the bed topology is in this image over the upstream end of the sand bed.



Fig. 3. A close-up of the monopile and propeller.

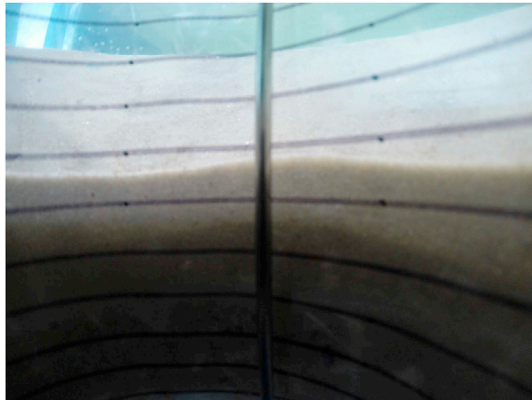


Fig. 4. Image from inside the monopile.

2. Experimental methods and equipment

The present experiments have been conducted within the hydraulics laboratory at DTU in a flume which is 35 m long, 2 m wide and 0.5 m deep. The flume has glass side walls, providing a good view of the flow and scour process. The water depth in all the experiments was $h = 0.27$ m. A sand bed spanning 8 m was placed with its center at the center of the flume, and the sand had a grain size of $d_{50} = 0.18$ mm. The sand bed spanned the entire width of the flume and the thickness of the bed was 0.15 m, which ensured that the bottom of the flume was not reached during the scour process. A transparent circular pile made from an acrylic tube with an outer diameter $D = 0.1$ m was placed at the center of the sand bed. At the ends of the sand bed a slope of 1:8 was made of tiles ($0.4 \text{ m} \times 0.4 \text{ m}$), in order to keep the sand in place. These tiles were covered by stones with sieve diameters ranging from 1.6 cm to 3.2 cm, to create an even slope. A H33-1 Armfield micropropeller velocity meter was placed between the sidewall and the pile. Furthermore, the device was positioned far enough from the bed so it measured the free-stream velocity of the incoming flow. The lower limit of the measuring range of the H33-1 micropropeller is specified as 0.05 m/s. Velocities below this limit have therefore been omitted in the results. Fig. 1 shows a schematic view of the test set-up including the location of the micropropeller and in Fig. 2 an image of the set-up is shown. Finally, Fig. 3 shows a close-up image of the micropropeller and monopile. The flow in the flume was created by a pump which could be controlled by sending in a time varying control signal. The initial program for controlling the pump was not optimal, and therefore an effort was made to improve the

Table 1

Dimensional and non-dimensional quantities for each case, where the boundary layer thickness δ is estimated as the minimum of that predicted from (2) and the water depth h . For Case 1–9 the mean, μ , and standard deviation, σ , of the amplitude of the velocity U_m is shown. The mean velocity is used as the reference value. The effective scouring fraction, ψ is calculated from (16). Case 1–3 were generated using Program 1 and Case 4–12 were generated using Program 2.

Case	T [s]	U_m [m/s]		S_c/D	δ/h	θ_m	N_{waves}	ψ
		μ	σ					
1	177	0.32	0.011	0.76	0.52	0.07	89	–
2	161	0.34	0.007	0.89	0.50	0.07	62	–
3	146	0.40	0.020	0.89	0.53	0.10	66	–
4	72	0.42	0.020	0.83	0.28	0.12	48	0.10
5	79	0.45	0.023	0.87	0.33	0.13	44	0.09
6	97	0.40	0.022	0.86	0.36	0.10	55	0.15
7	123	0.45	0.014	1.00	0.50	0.13	58	0.12
8	147	0.42	0.013	0.98	0.56	0.11	52	0.11
9	479	0.42	0.008	1.08	1.00	0.09	40	0.07
10	79	0.49	–	–	0.36	0.15	–	–
11	123	0.51	–	–	0.56	0.15	–	–
12	479	0.49	–	–	1.00	0.12	–	–
13	–	0.41	–	1.23	1.00	0.12	–	–
14	–	0.25	–	0.82	1.00	0.04	–	–

control signals. In what follows the signals produced with the initial control program will be referred to as Program 1, whereas signals produced with the improved method will be referred to as Program 2. The initial and final bed levels were measured with a laser distance meter (optoNCDT ILR 1182-30) mounted on a carriage with two degrees of freedom. Another laser distance meter recorded the position of the carriage in the stream-wise direction, while a draw-wire encoder (Kübler D5.3501.A221) recorded the transverse position. The output from the distance sensors were connected to a data acquisition system (NI-USB-6218). Post processing of the point measurements gave the bed topology around the pile. The measurements of the temporal scour variation were performed using a GoPro Hero3+ camera. The camera was placed inside the cylinder along with a chart with equally spaced grid lines of 1 cm. Fig. 4 shows an example of the view from inside the monopile.

In Williams and Fuhrman (2016) three different realizations for idealized tsunami events were considered: a single (elongated soliton) wave, a so-called N-wave and a sinusoidal wave. For this study a single wave was utilized as a representation of a tsunami, with the free stream velocity given by

$$u_0 = U_m \text{sech}^2(\Omega t), \quad (1)$$

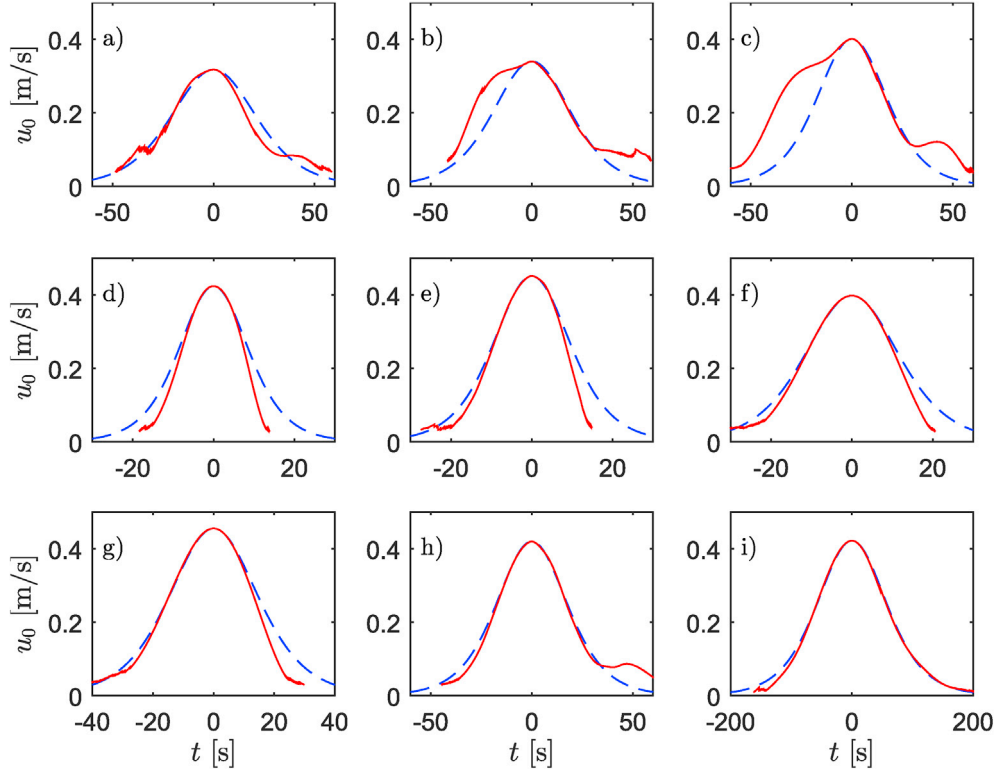


Fig. 5. Comparison between measured (–) and fitted (– –) velocity signals for a) Case 1, b) Case2, c) Case 3, d) Case 4, e) Case 5, f) Case 6, g) Case 7, h) Case 8, i) Case 9.

where u_0 is the free stream velocity, U_m is the maximum free stream velocity, $\Omega = 2\pi/T$ where T can be interpreted as a characteristic period of motion corresponding to the time duration where the free stream flow exceeds $0.007 U_m$. It should be noted that, although solitary-like in shape, the period and velocity magnitude can be chosen independently, thus allowing their individual proper scaling. The single wave was chosen in part because a uni-directional velocity signal could be better controlled than an oscillating signal, and in part because it enabled the study of the scour process using a new generic signal. In contrast, Larsen et al. (2017) studied the tsunami-induced scour process by utilizing a sinusoidal flow as a generic tsunami signal.

Table 1 lists the maximum free stream velocity, the period, the non-dimensional equilibrium scour depth (S_e/D), the boundary layer thickness to water depth ratio (δ/h) and the maximum Shields parameter (θ_m). Cases 1–9 are intended as tsunami scour experiments. Cases 10–12 are intended as pure tsunami boundary layer experiments. In these test the undisturbed velocity profile were measured by pitot tubes placed at varying distances from the bed. Finally, Cases 13–14 correspond to steady current scour measurements, which can be regarded as the infinite period limit.

The boundary layer thickness is calculated utilizing expressions provided by Williams and Fuhrman (2016). Specifically, for hydraulically smooth conditions they suggested:

$$\frac{\delta}{a} = 0.044Re^{-0.07} \quad (2)$$

where $a = U_m/\Omega$ is a characteristic length scale and $Re = aU_m/\nu$ is the Reynolds number. The hydraulically smooth expression was used for all the model scale experiment calculations since $k_s^+ = k_s U_f/\nu$ never exceeds 10, where U_f is the friction velocity and ν the kinematic viscosity. Alternatively, for hydraulically rough condition (used when calculating the full scale equivalents of the model scale experiments) they suggested:

$$\frac{\delta}{a} = 0.05 \left(\frac{a}{k_s} \right)^{-0.11} \quad (3)$$

where $k_s = 2.5d_{50}$ is Nikuradse's equivalent sand roughness. Furthermore, the Shields parameter was calculated by

$$\theta_m = \frac{U_{fm}^2}{(s-1)gd_{50}} \quad (4)$$

where $s = 2.65$ is the relative density of the grains, g is gravitational acceleration, and U_{fm} is the maximum friction velocity calculated from

$$U_{fm} = \sqrt{\frac{f_w}{2}} U_m \quad (5)$$

where the friction factor is given by

$$f_w = 0.04Re^{-0.16} \quad (6)$$

and

$$f_w = \exp\left(5.5 \left(\frac{a}{k_s}\right)^{-0.16} - 6.7\right) \quad (7)$$

for the hydraulically smooth and rough conditions, respectively. These friction factor expressions come from Fuhrman et al. (2013) and were shown by Williams and Fuhrman (2016) to give reasonable friction factor estimates for the simulated tsunami cases.

Due to the inability of the propeller to measure small velocities, the period of the incoming flow could not be determined directly. The period is therefore found by minimizing the error between the measured and the analytical velocity (see equation (1)) at $u_0 > 0.95U_m$ for Case 1–3 and $u_0 > 0.8U_m$ for Case 4–12. Fig. 5 shows the measured free-stream velocity and the fit utilized for the period for 6 of the cases, as typical examples. It is readily apparent that the measured velocity variations fit

better with the sech^2 profile for Cases 6–9 than for Cases 2 and 3. This is due to the fact that Cases 1–3 utilized an early program for controlling the pump, which was subsequently improved upon in Cases 4–12. Nevertheless, though the fit with the idealized signal is not as good, the actual velocity variations are as realistic for the tsunami-induced flow as in the other cases, and therefore the results will still be presented.

The given equilibrium scour depth is not taken after just one tsunami wave, but after several waves (up to 89) in succession. While a real life tsunami attack would not likely consist of 89 successive waves, there have been reports of a leading wave followed by several trailing waves, and it is therefore relevant to continue the scour process more than just one wave. Furthermore, continuing until equilibrium is reached will reveal whether the authors' physical understanding of the problem is correct. Similar to the suggestion in the numerical study by Larsen et al. (2017), the authors argue that the scour process resembles that within a steady current scour, with the equilibrium scour depth tending to the steady current scour depth limit after taking into account the finite wave boundary layer thickness.

3. Hydrodynamic and morphological similitude

Before continuing to the experimental results, considerations regarding the hydrodynamic and morphological similitude to full scale conditions will be presented. The scaling utilized follows the approach presented in Larsen et al. (2017). It is not possible to achieve complete similarity. However, as shown by Roulund et al. (2005), if the Froude number is $O(0.2)$ then the effects of the free-surface become negligible, and the scour process can be viewed entirely from a boundary layer perspective. In this case, tsunami induced scour can be studied using a time varying current. In the present study the experimental cases had $Fr = 0.20\text{--}0.31$ and the full scale cases, which are derived in what follows, have $Fr = 0.14\text{--}0.21$, i.e. both in experiments and full scale equivalents the Froude numbers are $O(0.2)$, hence the effects of the free-surface can be considered small.

Kinematic similarity, and thus geometric similarity, for the scour process is achieved by similarity in $U_m^2/(gD)$ and δ/D . Similarity in $U_m^2/(gD)$ ensures that the adverse pressure gradient induced by the presence of the structure itself will be similar at both model and field scales, i.e. that the ratio of the excess stagnation pressure head in front of the monopile $U_m^2/(2g)$ -to-pile diameter D will be maintained.

The main driver of the scour process is the horseshoe vortex, whose size and strength is largely determined by the boundary layer thickness-to-diameter ratio δ/D and the adverse pressure gradient. Achieving similarity in both $U_m^2/(gD)$ and δ/D is therefore of utmost importance from the scour perspective. As the boundary layer thickness is governed by the amplitude of the orbital motion, a , and thus the period of the motion, then similarity in boundary layer thickness-to-monopile diameter ratio determines the scaling of the flow period. The above approach

Table 2
Corresponding full scale wave parameters for the nine (1–9) scour cases and three (10–12) velocity profile cases.

Case	T [s]	U_m [m/s]	H [m]	D [m]	d [mm]	h [m]	θ_m
1	1528	2.02	5.8	4	0.3	20	0.99
2	1372	2.15	6.1	4	0.3	20	1.12
3	1240	2.53	7.2	4	0.3	20	1.54
4	592	2.63	7.5	4	0.3	20	1.80
5	650	2.85	8.1	4	0.3	20	2.07
6	809	2.52	7.2	4	0.3	20	1.60
7	1032	2.87	8.1	4	0.3	20	2.00
8	1247	2.66	7.6	4	0.3	20	1.69
9	2416	2.66	7.6	4	0.3	20	1.59
10	648	3.10	8.85	4	0.3	20	2.43
11	1028	3.23	9.21	4	0.3	20	2.50
12	2071	3.10	8.85	4	0.3	20	2.16

ensures the best possible similarity in the hydrodynamics inducing the scour process. Furthermore, to ensure reasonable similarity in the scouring rate relative to the period, the sediment grain size at full scale is chosen to give scour time scale-to-period ratios that are of the same order of magnitude at both model and field scale. To calculate the time scale, the modified time scale for steady current scour presented in Larsen et al. (2017), is utilized:

$$T_s^* = \frac{\sqrt{g(s-1)d^3}}{D^2} T_s = \frac{1}{400} \left(\frac{\delta}{D}\right)^{0.7} \theta^{-1.5} \quad (8)$$

where T_s^* is the non-dimensional scour time scale, T_s is the dimensional scour time scale, δ is the wave boundary layer thickness and θ is found via equations (4)–(7). The actual time scale of the tsunami-induced scour will be somewhat larger, as the flow is only near maximum for a fraction of the period, but keeping the time scale-to-period ratio approximately the same at both model and full scale will ensure that the morphological time is similar at model and full scale.

At full scale a monopile diameter of $D_{full} = 4$ m, a water depth of $h_{full} = 20$ m and a grain size of $d_{full} = 0.3$ mm can be considered typical of

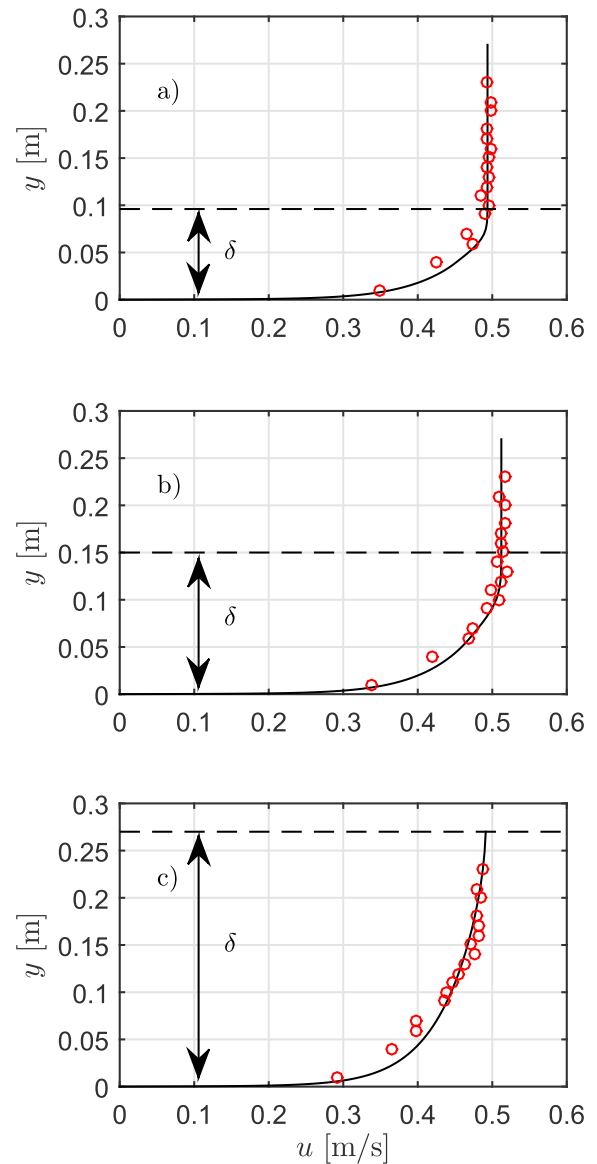


Fig. 6. Measured ensemble average velocity profiles at peak flow ($t=0$) (o) together with the model results using MatRANS (–) and the boundary layer thickness from (2) (– –). a) Case 10, b) Case 11 and c) Case 12.

conditions at offshore wind turbines. The resulting full scale maximum free-stream velocity is obtained through similarity in $U_m^2/(gD)$. The corresponding full scale period is then found by achieving similarity in δ/D by the use of equation (3). Finally the full-scale wave height has been found from linear shallow water theory:

$$U_m = \frac{H}{2} \sqrt{\frac{g}{h}} \quad (9)$$

The resulting full scale wave parameters are shown in Table 2. As seen from Table 2, the cases considered are representative of full scale tsunamis having periods ranging from about 10 min up to 40 min and wave heights of 5–8 m at a water depth of 20 m. The full-scale Shields parameter, θ , is of course significantly larger than the model scale θ , but as mentioned, with scour time scale-to-period ratio similar at both model and full scales, the non-dimensional scour depth should be similar during the scour process.

It is again emphasized that the above scaling procedure does not follow standard Froude scaling, but is made to ensure best possible similarity between model and field scale in relation to flow inducing the scour process.

4. Tsunami-induced boundary layers

In this section the tsunami-induced boundary layers will be shown and discussed. To accurately predict sediment transport, morphology and scour processes a detailed understanding of the boundary layer is essential. Due to their long yet unsteady and transient nature, tsunami scale boundary layers are difficult to produce experimentally, and as a result tsunami scale boundary layers have received relatively little attention in the literature. Williams and Fuhrman (2016) investigated full scale tsunami induced boundary layers utilizing a numerical one-dimensional vertical (1DV) Reynolds-Averaged Navier-Stokes (RANS) model coupled with $k - \omega$ turbulence closure. Their simulations suggested that the boundary layer of a tsunami will typically not be limited by the water depth at locations sufficiently offshore, and this in turn means that the tsunami-generated boundary layer flow can be considered as both current-like due to their long duration and wave-like due to their unsteady boundary layers which do not necessarily span the entire water column. To show that this is also the case in the present experiments the velocity profiles were measured for three different velocity signals (Cases 10–12). Fig. 6 shows the velocity profile at the peak ($t = 0$). Included in the figure is also the velocity profile obtained by simulating the flow with the MatRANS model utilized in Williams and Fuhrman (2016), as well as the boundary layer thickness obtained from equation (2). For more details of the model, the reader is referred to Williams and Fuhrman (2016) and Fuhrman et al. (2013) which contains the original description of the model.

Fig. 6 illustrates that the boundary layer of the experimental tsunami signal does indeed not necessarily span the entire water depth, as seen in Cases 10 and 11. In contrast, in Case 12, the boundary layer extends all the way to the surface, but it should be noted that the period in this case is also extremely long compared to the two other cases. Thus, this tsunami is more current-like than wave-like by the time peak flow is reached. The calculated boundary layer thickness is actually larger than the flow depth, and hence we instead use $\delta = h$ for this case. Furthermore, Fig. 6 also illustrates that the MatRANS model captures the behaviour of the transient boundary layer quite well, as a generally excellent match in the predicted velocity profiles is achieved. Finally, and naturally taking into account the good match with the MatRANS model, the predicted boundary layer thickness based on equation (2) also yields a good estimate.

Based on the three measured boundary layers, the previously estimated Shields parameters, which together with the boundary layer thickness, is the governing parameter for the scour depth, can also be compared to the experiments. This is done utilizing the measured ve-

locity closest to the bed to estimate U_{fm} , which then can be converted into a Shields parameter utilizing equation (4). U_{fm} is found by assuming a profile of the following form

$$U_m = \frac{1}{\kappa} U_{fm} \ln \frac{y_0}{k_s g(k_s^+)} \quad (10)$$

where $y_0 = 0.01$ m is the measurement point closest to the bed, $\kappa = 0.4$ is the von Karman constant and

$$g(k_s^+) = \frac{1}{9k_s^+} + \frac{1}{30} \exp\left(-140(k_s^+ + 6)^{-1.7}\right) \quad (11)$$

to take into account that the wall is transitional. The proposed function for $g(k_s^+)$ above comes from an approximation which has been fit to data from Nikuradse (1933) and joins the smooth (12) and rough (13) expressions given in Monin and Yaglom (1973):

$$g(k_s^+) = \frac{1}{9k_s^+} \quad (12)$$

$$g(k_s^+) = \frac{1}{30} \quad (13)$$

The data and the fit to the data is shown in Fig. 7. The shape of the function looks very similar to that found in Schlichting and Gersten (2003), originally taken from Tani (1988).

From equation (10) U_{fm} is found iteratively and inserted into equation (4) to give $\theta = [0.14, 0.13, 0.1]$ for Case 10, 11 and 12, respectively. It can be seen that the Shields parameters calculated based on the experiments are very similar to those obtained utilizing the friction factor given in (6), see Table 1 (Case 10–12). Thus, it can be concluded that the estimates for both boundary layer thicknesses as well as Shields parameters presented in Table 1 are indeed representative of the experiments and suitable for further scour predictions.

5. Tsunami-induced scour

In this section the tsunami-induced scour will be presented. First, the short term scour development will be presented, followed by a presentation of the long term scour development as well as equilibrium scour depths and profiles. After this the results of the predictive engineering model proposed by Larsen et al. (2017) will be compared to the experimental results.

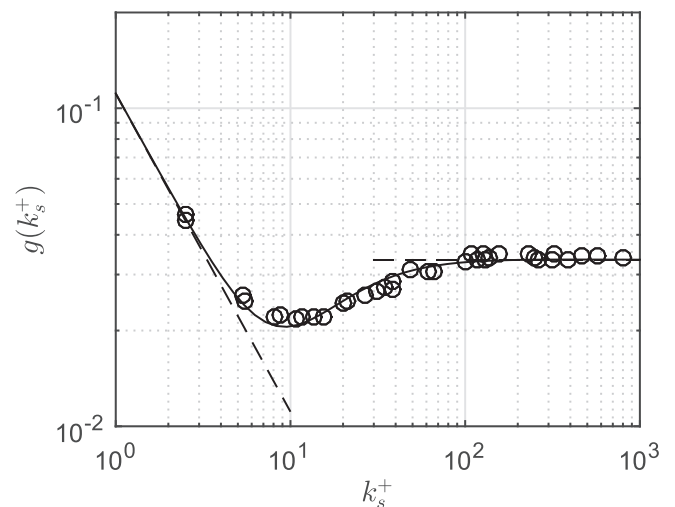


Fig. 7. Comparison of equation (11) (–), data (o) Nikuradse (1933) reproduced from Monin and Yaglom (1973) as well as smooth (12) and rough (13) expressions from Monin and Yaglom (1973) (- -).

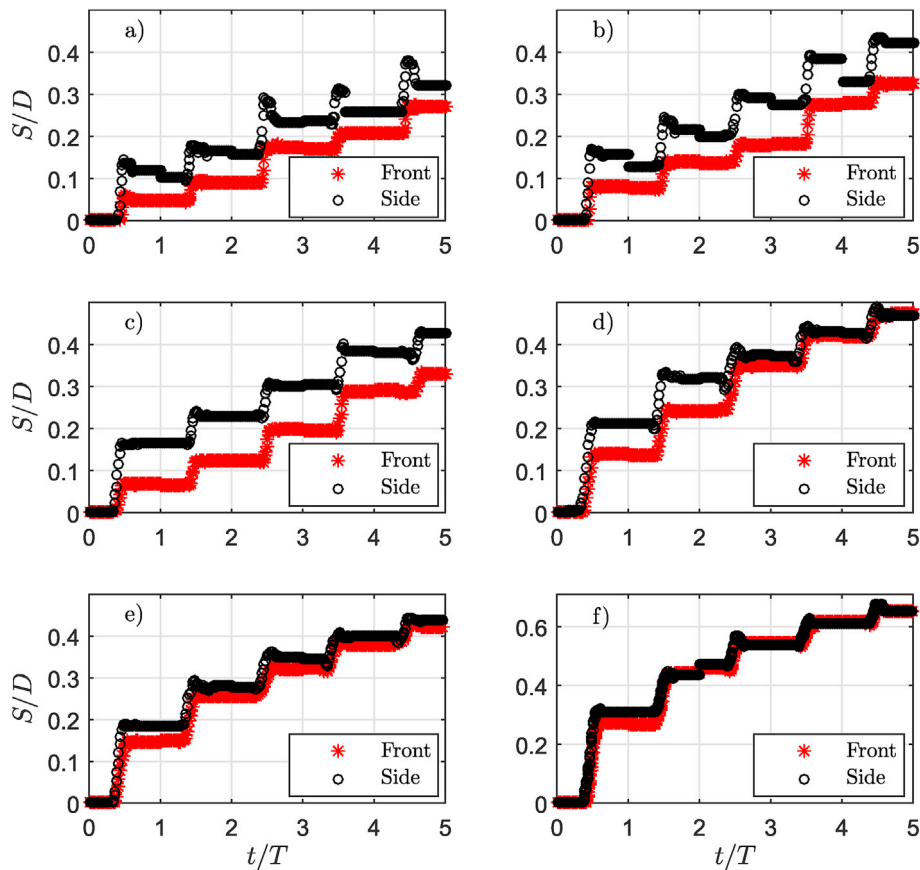


Fig. 8. Temporal scour development of the first five periods. a) Case 4, b) Case 5, c) Case 6, d) Case 7, e) Case 8, f) Case 9.

Fig. 8 shows the observed temporal scour variation during the first five periods in front of and at the front-side of the monopile for the six of the nine cases (the only six that recorded the detailed scour process). The front-side of the monopile is located approximately 30° from the centerline and will for the rest of the present paper be referred to as the side.

The scour hole is seen to deepen in a stepwise-cumulative way, with the majority of the scouring happening in the few first periods. The actual scouring is limited to a small fraction of the period. This is very similar to the computed results shown in Larsen et al. (2017). It can also be seen that in all the cases, the scour rate at the side of the monopile is faster than the scour rate at the front. This is interpreted as the bending of the streamlines creating large amplification of the bed shear stress at the front side of the monopile. This is very similar to that observed in experiments by Hjorth (1975) and the numerical study by Baykal et al. (2015). After some time the amplification of the bed shear stress at the sides reduces and the main driver of the scour process is no longer the contracted streamlines, but the horseshoe vortex, which evens out the difference in scour depth at the front and the front side of the monopile (this is even more evident in Fig. 9 where the entire scour development is shown, spanning up to nearly 60 events in succession). Some backfilling at the front sides can be observed, most noticeably in Case 4, 5 and 7 (Fig. 8a, b and 8d). The backfilling occurs at three different instances of the scour process, and it will now be explained for each. First, just before continued scouring a small decrease in scour depth can be seen, most evident in Case 7 (Fig. 8d), but also present in Case 6, 8 and 9 (Fig. 8c, e, and 8f). From qualitative assessment of the video sequence it can be seen that the backfilling occurs because sand is sliding into the hole. This can be interpreted as the horseshoe vortex not yet attaining its full size, but the free-stream Shields parameter exceeding its critical value. When this happens sand is starting to move, and once it reaches the scour hole, where the bottom slope is at the angle of repose, it slides into the hole. Second, right after scouring a decrease in scour depth can also be seen,

most noticeable in Case 4 (Fig. 8a), but also present to a lesser degree in Cases 5–9 (Fig. 8b–f). In this case, also based on qualitative assessment of the video, sand is likewise sliding into the scour hole, and the physical interpretation is the same, namely that the horseshoe vortex has weakened and the critical shields parameter is still exceeded outside the scour hole, pushing sand into the hole. Third, a discontinuous jump in the scour depth can be seen in-between periods. This is most evident in Case 5 (Fig. 8b) at $t/T = 1, 2, 3, 4$. The reason for this is reflected flow in the flume transporting some sand from the back of the monopile to the front. The jump is discontinuous in the figure because the reflection occurs after the duration of a full period. However, in most cases the backfilling from the reflected flow was rather limited, and does not seem to affect the overall scouring process too much, except perhaps slowing it down a bit compared to the case without reflection. The stepwise cumulative scouring shown in Fig. 9 is very similar to Series C from Link et al. (2017) (see their Fig. 4c), although their experiments were conducted solely in the clear-water regime.

To further shed light on the physics of the process and also to investigate the possible effects of tsunami scouring in the case of a pre-existing scour hole, the experiments were continued beyond the first five periods until equilibrium or almost equilibrium scour depth was reached. Here we define equilibrium scour depth as a depth that does not change over time. In reality small changes occur with minor scouring and backfilling, but the mean scour depth over a period of time should remain constant. Fig. 9 shows the temporal development in the scour depth, with measurements being taken once per period. It can be seen that the depth of the scour holes are increasing rapidly during the first few periods, and thereafter the increase gets slower and slower, and the scour depth is gradually approaching an equilibrium value. It is recognized that final equilibria have not been reached in Case 4, Case 7 and Case 9. Based on the very limited change from period to period in these cases, the scour depths are, however, not expected to increase much beyond what is

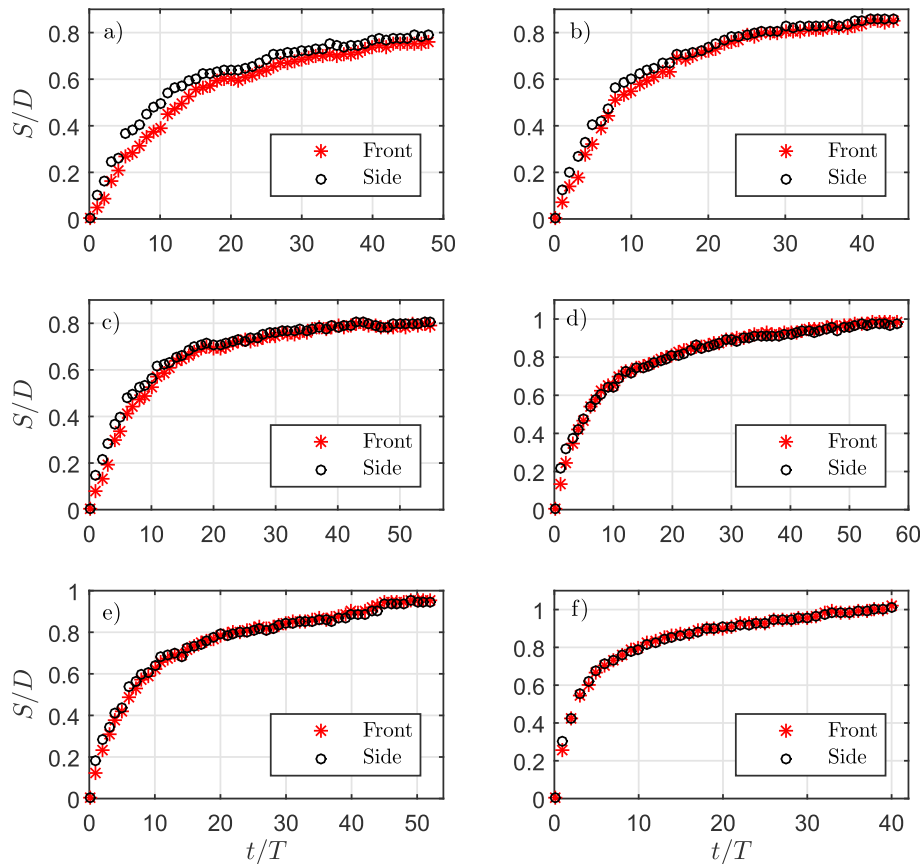


Fig. 9. Temporal scour development of the entire experiment at integer values of t/T (i.e. after each tsunami). a) Case 4, b) Case 5, c) Case 6, d) Case 7, e) Case 8, f) Case 9.

shown in Fig. 9. Again, it can also be seen that the scour depth is increasing faster at the front side of the monopile compared to the front center in the first periods. However, after sufficient time the scour depth at the front side and the front center are more or less equal.

Fig. 10 shows the final bed topography of all nine tsunami cases (Fig. 10a–i) as well as the final bed from the live-bed steady current experiment (Fig. 10j). The bed topography from the nine tsunami cases look rather similar, with a semi-circular hole forming around the monopile, and sand deposited behind the monopile. The upstream bed of Cases 1 and 2 (Fig. 10a and b) are clear of bed forms and could thus be interpreted as being in the clear-water regime. All cases are in the clear-water regime in parts of the periods, but the live-bed regime period is generally long enough to develop bed forms. The cases with bed forms bear some resemblance to the steady current scour hole (Fig. 10j) although the extend of the hole in the steady current case is somewhat larger. This is probably due to (1) the tsunami cases perhaps not reaching full equilibrium, and probably more importantly, due to (2) the boundary layer thickness not spanning the entire depth in the tsunami flows, which will limit the relative size of the horseshoe vortex.

In Larsen et al. (2017) it was argued that the tsunami-induced scour depth, should (if given enough time) tend to the current-induced equilibrium scour depth, after taking into account the finite boundary layer thickness, and that this could be predicted utilizing

$$\frac{S_e}{S_0} = 1 - \exp\left(-0.9 \frac{\delta}{D}\right) \quad (14)$$

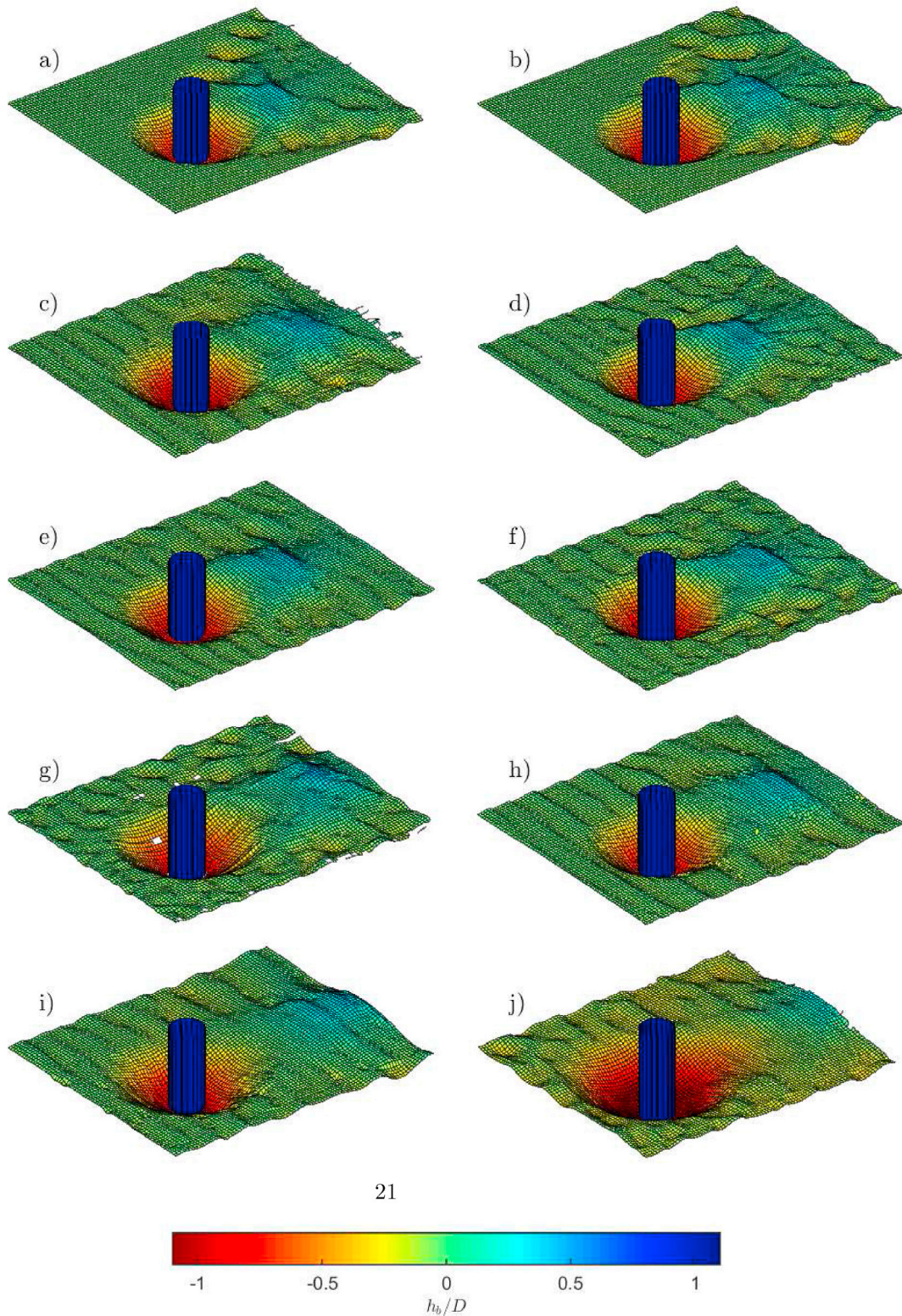
where $S_0/D = 1.3$ is the widely-accepted equilibrium current induced scour value around a circular pile (without depth limitation). In Fig. 11 the equilibrium scour depths are shown as a function of the boundary layer thickness to diameter ratio and compared to equation (14). The

scour depths are not taken from the video, but rather as the maximum depth from the scanned bed. However the estimates from the video do not differ significantly from the bed scan. Included in the figure are also the results from the MSc thesis of Lavictoire (2015) who studied the bore induced scour around a circular cylinder standing on a dry beach, as well as the results for the bore induced scour around a circular cylinder by Shafiei et al. (2015). We have taken the height of the approaching bore as the boundary layer thickness for these latter two studies. It may be seen that the tsunami-induced equilibrium scour depth can reasonably be predicted by equation (14). There is, of course, some scatter, but this scatter is of the same order of magnitude as the scatter of the current induced scour depth, see Larsen et al. (2017) where the relationship in Equation (14) was proposed. It can also be seen that equation (14) provides a good estimate of the equilibrium scour depth in the case where the cylinder is standing in-land and is subjected to a bore, as equation (14) also captures well the experimental results by Lavictoire (2015) and Shafiei et al. (2015).

As seen from Figs. 8 and 9 the equilibrium scour depths in the experiments are not reached after one or two tsunami waves, but rather after approximately 50 tsunami waves, and therefore the scour depth predicted from equation (14) may not be appropriate for estimating the scour depth of a tsunami attack. In some cases it will, but this will depend entirely of the time scale of the scour process and the boundary layer thickness. Therefore, the temporal evolution should likewise generally be taken into account. In Larsen et al. (2017) the following expression was suggested for the temporal evolution of the tsunami induced scour depth

$$\frac{S}{D} = \frac{S_e}{D} \left(1 - \exp\left(-\frac{t_s}{T_s}\right) \right), t_s = n\psi T. \quad (15)$$

where S_e is the equilibrium scour depth predicted by equation (14). This



21

Fig. 10. Equilibrium bed profiles of a) Case 1, b) Case 2, c) Case 3, d) Case 4, e) Case 5, f) Case 6, g) Case 7, h) Case 8, i) Case 9, j) Case 13 (Steady scour).

resembles the commonly used expression to characterize typical time development of scour processes, see [Sumer and Fredsøe \(2002\)](#). In the equation above t_s represents the effective scour time, and n represents the integer number of successive waves characterizing a given tsunami i.e. $n = 1$ can be utilized to predict the maximum scour occurring during the leading tsunami wave, with $n = 2, 3, \dots$ utilized for predicting the accumulated scour induced by any successive waves. The additional factor

$\psi \leq 1$ represent the effective scouring fraction of a period. In [Larsen et al. \(2017\)](#) the tsunami was represented by a sinusoidal flow and $\psi = 1/3$ was chosen. This value is, however, not appropriate for the present situation where the flow is unidirectional. Instead, we have chosen to predict the value by estimating the ratio of the predicted volume of sediment transported by the tsunami wave relative to the predicted volume of sediment transported by a steady current having the same θ as

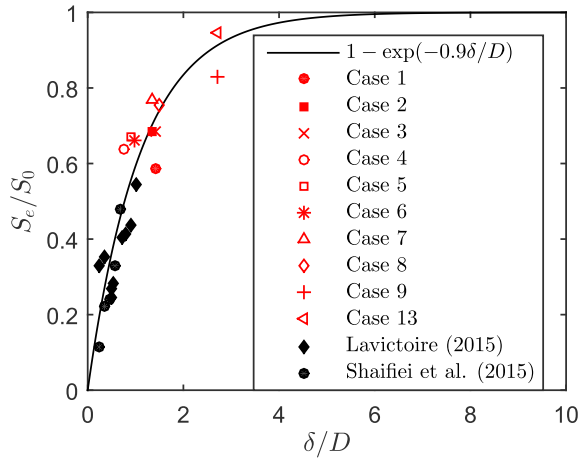


Fig. 11. Equilibrium measured scour depth as function of predicted boundary layer thickness.

θ_m of the tsunami, i.e.

$$\psi = \frac{\int_0^T \theta(\theta > \theta_c)^{3/2} dt}{\int_0^T \theta_m^{3/2} dt} \quad (16)$$

where θ is the predicted instantaneous value of Shields parameter of the tsunami, $\theta_c = 0.05$ is the critical Shields parameter, and θ_m is the maximum Shields parameter of the tsunami predicted by equation (4). θ is calculated by equations (4), (5) and (7), maintaining a constant friction factor but substituting U_m with $u_0 = U_m \text{sech}^2(\Omega t)$. In the above formulation θ is raised to 3/2 as many sediment transport formulae scale with

$\theta^{3/2}$, see e.g. Fredsøe and Deigaard (1992). The resulting values of ψ can be seen in Table 1. It should be noted that equation (16) does not give $\psi = 1/3$ integrating one half-cycle of the sinusoidal flow from Larsen et al. (2017). However, ψ estimates for these sinusoidal wave signals using equation (16) are not significantly different from $\psi = 1/3$ hence using equation (16) in this case (only integrating for one half cycle) would still give reasonable scour predictions.

Utilizing the estimated values of ψ the predicted scour evolution of Cases 4–9 are plotted in Fig. 12 together with the measured scour depths. As can be seen, the simple predictive model proposed above does a good job of predicting the scour observed within the experiments, especially during the first tsunami waves. Further taking into account the scatter in the experimental results leading to equation (14) (on which the engineering model is built), the estimate is satisfactory. The worst prediction is Case 9 where the predicted scour depth is approximately 20% more than from the experiment, but still well within normal scatter in scour experiments.

6. Model-experiment comparison

In this section Cases 6–8 will be simulated with the same model used in the previous numerical study by Larsen et al. (2017) on tsunami induced scour around monopile foundations where the tsunami was there represented by a sinusoidal velocity signal. This is done to strengthen the validity of the simple predictive engineering model. In Larsen et al. (2017) the engineering model was suggested based purely on numerical results, and a good comparison with the current experiments will further validate the accuracy of the numerical model and thus also the predictive engineering model for tsunamis represented, not only as single waves, but also as sinusoidal waves.

The simulations are performed using the sediMorph model, implemented in OpenFOAM-1.6-ext, originally developed by Jacobsen

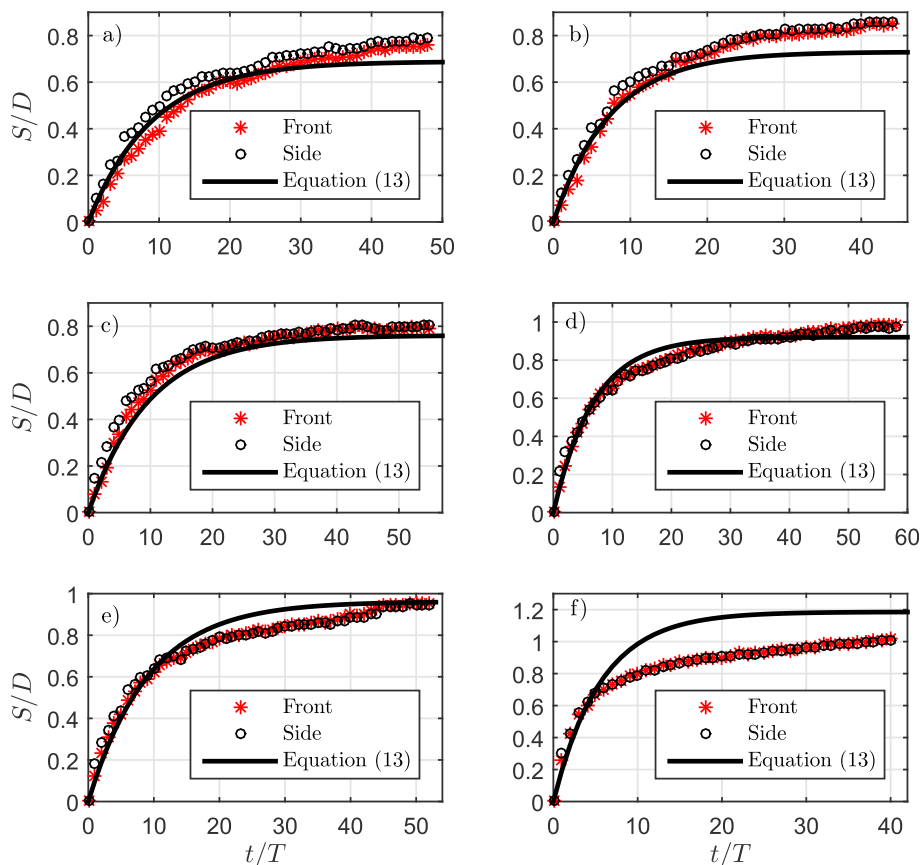


Fig. 12. Predicted and measured temporal scour development of the entire experiment. a) Case 4, b) Case 5, c) Case 6, d) Case 7, e) Case 8, f) Case 9.

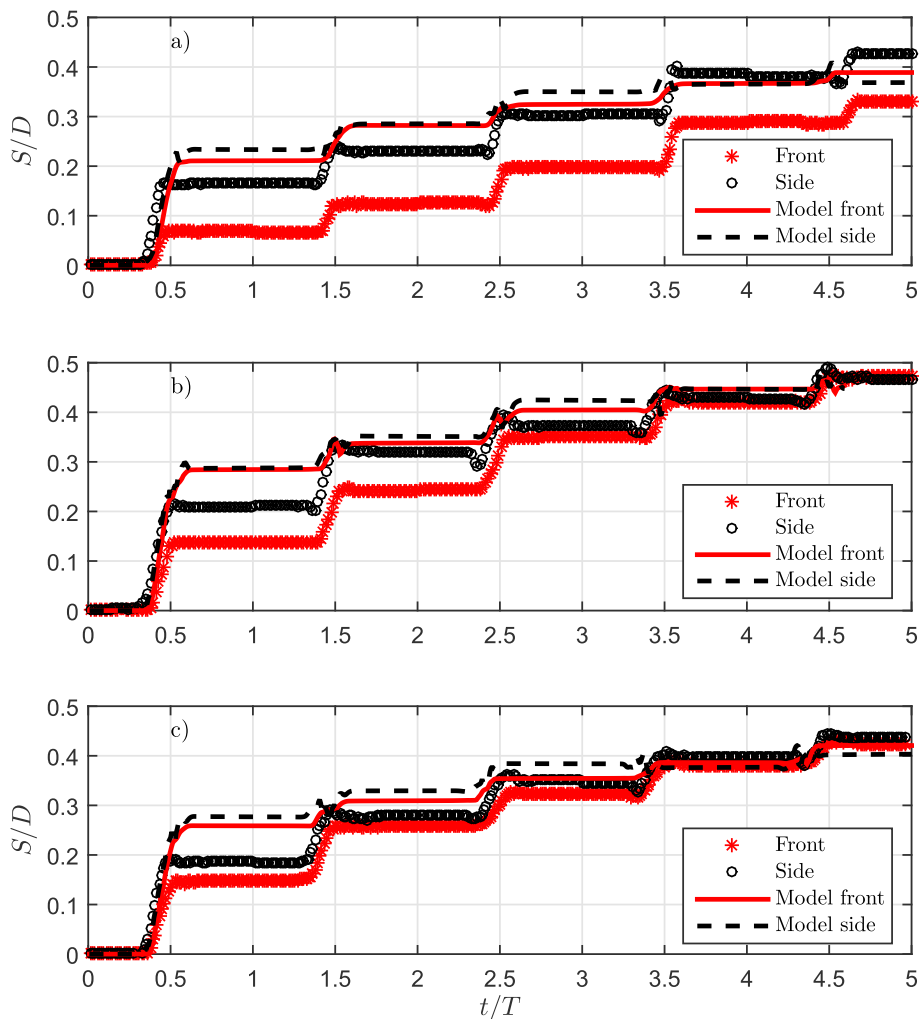


Fig. 13. Comparison between modelled and experimental scour development.

(2011) and Jacobsen et al. (2014). The model is a fully coupled RANS model, with $k - \omega$ turbulence closure, bed load transport, suspended load transport and morphology. The model is very well validated and has been used to simulate breaker bar development by Jacobsen et al. (2014), current, wave and wave-plus-current induced scour and backfilling beneath submarine pipelines by Fuhrman et al. (2014), Larsen et al. (2016) and Bayraktar et al. (2016) as well as current, wave and tsunami induced scour around a monopile by Baykal et al. (2015), Baykal et al. (2017) and Larsen et al. (2017). For more details on the model implementation the reader is referred to Jacobsen et al. (2014).

The computational domain is discretized into finite volumes of quadrilateral blocks in varying shapes and dimensions and the computational domain has the following dimensions: length, $l = 20D$, width, $w = 15D$, and height, $h = 2D$, in which D is the monopile diameter. The total number of cells comprising the computational domains utilized is 170,496 with the near-bed cells having a height $O(d)$, in which d is the grain size. The monopile is located at the center of the domain $(x,y) = (0, 0)$. This mesh and boundary conditions are exactly the same as used in Larsen et al. (2017) who simulated steady current induced scour as well as tsunami induced scour and the reader is referred to this study for more details of the model set-up.

Fig. 13 shows the detailed scour development of Cases 6–8 of both the experiment and the numerical model. It can be seen that the model, similar to the experiments, predicts the scour occurring in a stepwise fashion, with the scour rate at the side being slightly larger than the

center. The model over-predicts the scour in the first period, but after that the agreement between the model and the experiments improves. The reason for the over-predicted scour depth in the first period could be that all sediment transport formulae within the model build on the assumption of rough-turbulent flow at the bed. In reality the grain Reynolds number $U_f d/\nu \approx 3$. In this region the critical Shields parameter θ_c is slightly larger than $\theta_c = 0.05$ which is utilized in the model. Another explanation could be that even though the bed was levelled between each experiment, it was not completely flat, as in the simulation. Small bed forms could thus give extra flow resistance and thus lower the bed shear stress compared to the model. After simulating a few waves the modelled cases also contain some bed forms, and the scour development is more similar. The gradual development of bed forms can also be seen in Fig. 14 where the simulated bed profile of Case 7 is shown after one, three and five periods. After one period the bed is almost free of bed forms. After three periods small ripples have developed on the side and finally after five periods the bed forms have spread to the front of the monopile. The gradual deepening and widening of the scour hole in time is also quite clear, and the bed profile after five periods is starting to show resemblance with the equilibrium profile of Case 7 (Fig. 10h).

Despite the difference between the initial scour depths of the model and the experiment, we still find this comparison satisfactory. This further validates the sediMorph model as well as the predictive engineering formula for tsunami induced scour beneath sinusoidally varying velocity signals.

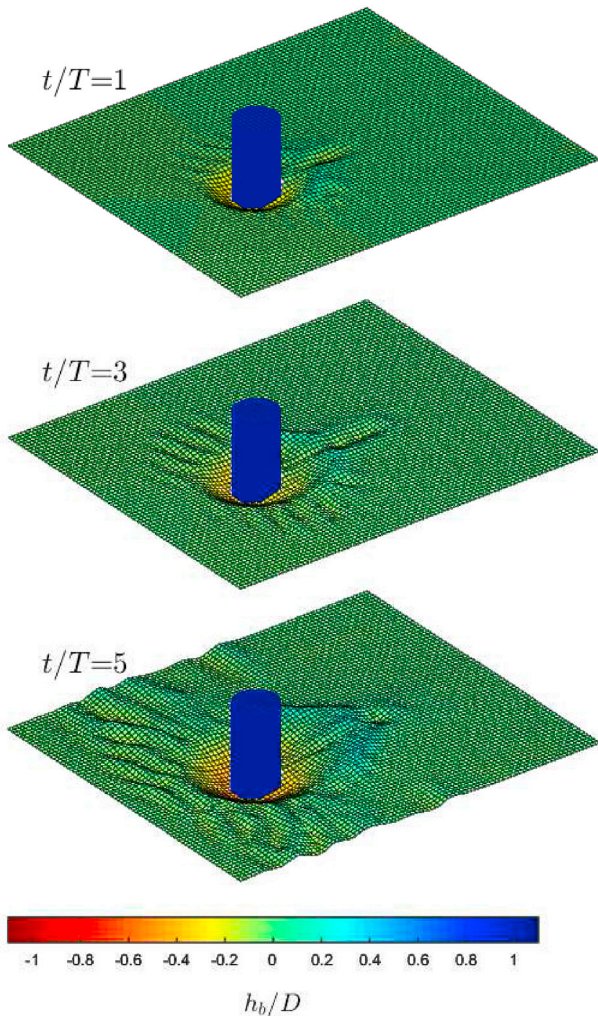


Fig. 14. Simulated bed profiles of Case 7 at $t/T = 1$, $t/T = 3$ and $t/T = 5$.

7. Conclusions

This paper presents an experimental analysis of tsunami-induced scour around monopiles representative of offshore wind turbine foundations. The offshore scour process has been studied by treating the incoming tsunami as a time varying current which enabled properly scaled experiments. To complement a previous (entirely numerical) study by Larsen et al. (2017) using a sinusoidal velocity signal, a “single wave” (elongated soliton) formulation has been used as a synthetic tsunami signal, which has been repeated in succession.

Based on a recently developed method for maintaining similarity between model and full scale tsunami-induced scour it is shown that the nine cases considered corresponds to real-life tsunamis having periods from 10 min to 40 min and wave heights of 5 m–8 m at a water depth of 20 m. The boundary layer beneath the model tsunami signal is shown to be accurately predicted by the MatRANS model (Fuhrman et al. (2013)) as well as by recently developed formula for boundary layer thickness and friction factors beneath tsunami waves (Williams and Fuhrman (2016)).

The scour development is shown to occur in a stepwise cumulative fashion, with the equilibrium scour depth tending to that predicted by existing steady current scour depth expressions after accounting for the finite boundary layer thickness induced by the unsteady flow.

It is shown that the temporal development can reasonably be predicted by the practical engineering model developed by Larsen et al. (2017) with a small change in the parameter ψ (representing the effective scouring

duration within a period), which is now found analytically as the ratio of the volume sediment transported by one tsunami wave relative to volume of sediment transported by a steady current having the same Shields parameter as the maximum Shields parameter of the tsunami. The practical engineering model thus only requires use of existing experimentally-based expressions for predicting steady current scour and time scales as wells as analytical calculations of the parameter ψ .

Finally, three cases were simulated by a fully coupled hydrodynamic and morphologic CFD-model and a good correspondence was obtained. These results add to the validation of the sediMorph model (Jacobsen (2011)), and hence give further confidence in the previous purely-numerical study of tsunami-induced scour conducted by Larsen et al. (2017).

Acknowledgements

The first and last author acknowledge support from the European Union project ASTARTE–Assessment, Strategy And Risk Reduction for Tsunamis in Europe, Grant no. 603839 (FP7-ENV-2013.6.4-3).

References

- Apotsos, A., Buckley, M., Gelfenbaum, G., Jaffe, B., Vatvani, D., 2011a. Nearshore tsunami inundation model validation: toward sediment transport applications. *Pure Appl. Geophys.* 168 (11), 2097–2119.
- Apotsos, A., Gelfenbaum, G., Jaffe, B., 2011b. Process-based modeling of tsunami inundation and sediment transport. *J. Geophys. Res.* 116 (1).
- Apotsos, A., Gelfenbaum, G., Jaffe, B., Watt, S., Peck, B., Buckley, M., Stevens, A., 2011c. Tsunami inundation and sediment transport in a sediment-limited embayment on American Samoa. *Earth Sci. Rev.* 107 (1–2), 1–11.
- Baykal, C., Sumer, B.M., Fuhrman, D.R., Jacobsen, N.G., Fredsøe, J., 2015. Numerical investigation of flow and scour around a vertical circular cylinder. *Phil. Trans. Roy. Soc. A* 373 article no. 20140104.
- Baykal, C., Sumer, B.M., Fuhrman, D.R., Jacobsen, N.G., Fredsøe, J., 2017. Numerical simulation of scour and backfilling processes around a circular pile in waves. *Coast. Eng.* 122, 87–107.
- Bayraktar, D., Ahmad, J., Larsen, B.E., Carstensen, S., Fuhrman, D.R., 2016. Experimental and numerical study of wave-induced backfilling beneath submarine pipelines. *Coast. Eng.* 118, 63–75.
- Bricker, J.D., Francis, M., Nakayama, A., 2012. Scour depths near coastal structures due to the 2011 Tohoku tsunami. *J. Hydraul. Res.* 50 (6), 637–641.
- Chan, I.-C., Liu, P.L.F., 2012. On the runup of long waves on a plane beach. *J. Geophys. Res. - Oceans* 117 (8), 1–17.
- Chen, J., Huang, Z., Jiang, C., Deng, B., Long, Y., 2013. Tsunami-induced scour at coastal roadways: a laboratory study. *Nat. Hazards* 69 (1), 655–674.
- Cheng, W., Weiss, R., 2013. On sediment extent and runup of tsunami waves. *Earth Planet Sci. Lett.* 362, 305–309.
- Dawson, A.G., Shi, S., 2000. Tsunami deposits. *Pure Appl. Geophys.* 157 (6–8), 875–897.
- Douglas, S., Nistor, I., 2015. On the effect of bed condition on the development of tsunami-induced loading on structures using openfoam. *Nat. Hazards* 76 (2), 1335–1356.
- Fredsøe, J., Deigaard, R., 1992. *Mechanics of Coastal Sediment Transport*. World Scientific, Singapore.
- Fu, L., Kosa, K., Sasaki, T., 2013. Tsunami damage evaluation of Utatsu bridge by video and 2-d simulation analyses. *J. Struct. Eng.* 59a, 428–438.
- Fuhrman, D.R., Baykal, C., Sumer, B.M., Jacobsen, N.G., Fredsøe, J., 2014. Numerical simulation of wave-induced scour and backfilling processes beneath submarine pipelines. *Coast. Eng.* 94, 10–22.
- Fuhrman, D.R., Madsen, P.A., 2009. Tsunami generation, propagation, and run-up with a high-order boussinesq model. *Coast. Eng.* 56 (7), 747–758.
- Fuhrman, D.R., Schløer, S., Sterner, J., 2013. RANS-based simulation of turbulent wave boundary layer and sheet-flow sediment transport processes. *Coast. Eng.* 73, 151–166.
- Hjorth, P., 1975. *Studies on the Nature of Local Scour*. Lund Institute of Technology. University of Lund. Bulletin Series A 46.
- Jacobsen, N.G., 2011. *A Full Hydro- and Morphodynamic Description of Breaker Bar Development*. Ph.D. thesis. Technical University of Denmark, Kgs. Lyngby.
- Jacobsen, N.G., Fredsøe, J., Jensen, J.H., 2014. Formation and development of a breaker bar under regular waves. Part 1: model description and hydrodynamics. *Coast. Eng.* 88, 182–193.
- Jayarathne, M.P.R., Premaratne, B., Adewale, A., Mikami, T., Matsuba, S., Shibayama, T., Esteban, M., Nistor, I., 2016. Failure mechanisms and local scour at coastal structures induced by tsunami. *C. Eng. J.* 58 (4), 1640017.
- Jiang, C., Chen, J., Yao, Y., Liu, J., Deng, Y., 2015. Study on threshold motion of sediment and bedload transport by tsunami waves. *Ocean Eng.* 100, 97–106.
- Kuriyama, Y., Takahashi, K., Yanagishima, S., Tomita, T., 2014. Beach profile change at Hasaki, Japan, caused by 5-m-high tsunami due to the 2011 off the Pacific coast of Tohoku earthquake. *Mar. Geol.* 355, 234–243.
- Lacy, J.R., Rubin, D.M., Buscombe, D., 2012. Currents, drag, and sediment transport induced by a tsunami. *J. Geophys. Res. - Oceans* 117 (9).

- Larsen, B.E., Fuhrman, D.R., Baykal, C., Sumer, B.M., 2017. Tsunami-induced scour around monopile foundations. *Coast. Eng.* 129, 36–49.
- Larsen, B.E., Fuhrman, D.R., Sumer, B.M., 2016. Simulation of wave-plus-current scour beneath submarine pipelines. *J. Waterw. Port C-ASCE* 142 (5) article no. 08216001.
- Lavictoire, A., 2015. Bore-induced Local Scour Around a Circular Structure. University of Ottawa, Canada.
- Link, O., Castillo, C., Pizarro, A., Rojas, A., Ettmer, B., Escauriaza, C., Manfreda, S., 2017. A model of bridge pier scour during flood waves. *J. Hydraul. Res.* 55 (3), 310–323.
- Madsen, P.A., Fuhrman, D.R., 2008. Run-up of tsunamis and long waves in terms of surf-similarity. *Coast. Eng.* 55, 209–223.
- Madsen, P.A., Fuhrman, D.R., Schäffer, H.A., 2008. On the solitary wave paradigm for tsunamis. *J. Geophys. Res.* 113 article no. C12012.
- Monin, A., Yaglom, A., 1973. *Statistical Fluid Mechanics: Mechanics of Turbulence*. MIT Press.
- Nakamura, T., Kuramitsu, Y., Mizutani, N., 2008. Tsunami scour around a square structure. *Coast. Eng. J.* 50 (2), 209–246.
- Nikuradse, J., 1933. *Stroemungsgesetze in rauhen rohren*. Forschung 4.
- Roulund, A., Sumer, B.M., Fredsoe, J., Michelsen, J., 2005. Numerical and experimental investigation of flow and scour around a circular pile. *J. Fluid Mech.* 534, 351–401.
- Schimmels, S., Sriram, V., Didenkulova, I., 2016. Tsunami generation in a large scale experimental facility. *Coast. Eng.* 110, 32–41.
- Schlichting, H., Gersten, K., 2003. *Boundary-layer Theory*. Springer.
- Shafiei, S., Melville, B.W., Shamseldin, A.Y., Watts, M.J.H., Hoffman, T.G., 2015. Experimental investigation of tsunami bore induced scour around structures. In: *Australian Coasts and Ports 2015 Conference*, pp. 807–813.
- Sriram, V., Didenkulova, I., Sergeeva, A., Schimmels, S., 2016. Tsunami evolution and run-up in a large scale experimental facility. *Coast. Eng.* 111, 1–12.
- Sugawara, D., Goto, K., Jaffe, B.E., 2014a. Numerical models of tsunami sediment transport - current understanding and future directions. *Mar. Geol.* 352, 295–320.
- Sugawara, D., Takahashi, T., Imamura, F., 2014b. Sediment transport due to the 2011 Tohoku-Oki tsunami at Sendai: results from numerical modeling. *Mar. Geol.* 358, 18–37. <https://doi.org/10.1016/j.margeo.2014.05.005>.
- Sumer, B.M., Fredsoe, J., 2002. *The Mechanics of Scour in the Marine Environment*. World Scientific, Singapore.
- Tani, I., 1988. Drag reduction by ribble viewed as roughness problem. *Proc. Jpn. Acade. B. Phys. Biol. Sci.* 64 (2), 21–24.
- Tonkin, S., Yeh, H., Kato, F., Sato, S., 2003. Tsunami scour around a cylinder. *J. Fluid Mech.* 496 (496), 165–192.
- Udo, K., Takeda, Y., Tanaka, H., 2016. Coastal morphology change before and after 2011 off the Pacific coast of Tohoku earthquake tsunami at Tikuzen-Takata coast. *Coast. Eng. J.* 58 (4), 1640016.
- Wei, Z., Dalrymple, R.A., Rustico, E., Heralut, A., Bilotta, G., 2016. Simulation of nearshore tsunami breaking by smoothed particle hydrodynamics method. *J. Waterw. Port C-ASCE* 142 (4), 05016001.
- Williams, I.A., Fuhrman, D.R., 2016. Numerical simulation of tsunami-scale wave boundary layers. *Coast. Eng.* 110, 17–31.
- Wilson, R., Davenport, C., Jaffe, B., 2012. Sediment scour and deposition within harbors in California (USA), caused by the march 11, 2011 tohoku-oki tsunami. *Sediment. Geol.* 282, 228–240.
- Yeh, H., Mason, H.B., 2014. Sediment response to tsunami loading: mechanisms and estimates. *Geotechnique* 64 (2), 131–143.

Chapter 4

Performance of interFoam on the simulation of progressive waves

This Chapter is under preparation as:

Larsen, B. E., Fuhrman, D. R., Roenby, J. (2018). *Performance of interFoam on the simulation of progressive waves.*

Performance of interFoam on the simulation of progressive waves

Bjarke Eltard Larsen^{a,*}, David R. Fuhrman^a, Johan Roenby^b

^aTechnical University of Denmark, Department of Mechanical Engineering, Section of Fluid Mechanics, Coastal and Maritime Engineering, DK-2800 Kgs. Lyngby, Denmark

^bDHI, Department of Port & Offshore Technology, Agern Allé 5, 2970 Hørsholm

Abstract

The performance of `interFoam` (a widely-used solver within the popular open source CFD package `OpenFOAM`) in simulating the propagation of a nonlinear (stream function solution) regular wave is investigated in this work, with the aim of systematically documenting its accuracy. It is demonstrated that over time there is a tendency for surface elevations to increase, wiggles to appear in the free surface, and crest velocities to become (severely) over estimated. It is shown that increasing the temporal and spatial resolution can mitigate these undesirable effects, but that a relatively small Courant number is required. It is further demonstrated that the choice of discretization schemes and solver settings (often treated as a "black box" by users) can have a major impact on the results. This impact is documented, and it is shown that obtaining a "diffusive balance" is crucial to accurately propagate a surface wave over long distances without requiring exceedingly high temporal and spatial resolutions. Finally, the new code `isoAdvector` is compared to `interFoam`, which is demonstrated to produce comparably accurate results, while maintaining a sharper surface. It is hoped that the systematic documentation of the performance of the `interFoam` solver will enable its more accurate and optimal use, as well as increase awareness of potential shortcomings, by CFD researchers interested in the general CFD simulation of free surface waves.

Keywords: `interFoam`, waves, discretization practises, `isoAdvector`

1. Introduction

As a tool to simulate waves `interFoam`, in the widely-used CFD package `OpenFOAM` (or other solvers build on `interFoam`, e.g. `waves2Foam` developed by Jacobsen et al. (2012)) are becoming increasingly popular. As examples, `interFoam` has been utilized to simulate breaking waves by e.g. Jacobsen et al. (2012); Brown et al. (2016); Jacobsen et al. (2014); Lupieri and Contento (2015); Higuera et al. (2013). It has also been used to simulate wave-structure interaction by e.g. Higuera et al. (2013); Chen et al. (2014); Paulsen et al. (2014); Hu et al. (2016); Jacobsen et al. (2015); Schmitt and Elsaesser (2015).

Wave breaking and wave-structure interaction are both very complex phenomena, but `interFoam` has also been utilized to simulate more simple cases, such as the progression of a solitary wave by Wroniszewski et al. (2014), which was suggested as a benchmark to compare to other CFD codes. The study by Wroniszewski et al. (2014) highlighted a problem, that to our knowledge, has gone largely unnoticed in the formal journal literature, namely that the velocity at the crest of the wave is over-predicted relative to the analytical solutions. This was also highlighted in conference paper Roenby et al. (2017b), the MSC thesis of Afshar (2010) and the PhD thesis Tomaselli (2016). A second problem was highlighted in the study by Paulsen et al. (2014), where it was shown that `interFoam` is not capable of

maintaining a constant wave height for long propagation distances. They also mentioned, though not going into great detail, that the choice of convection scheme affected this behaviour. The choice of convection scheme was also briefly touched upon by Wroniszewski et al. (2014), who, like Paulsen et al. (2014), utilized an upwind scheme, chosen for stability reasons. A third (again not well described in the literature) problem is the appearance of wiggles in the air-water interface, as documented by Afshar (2010). A fourth problem, which has received considerable attention (though not in the context of waves), is the growth of spurious velocities in low density fluid near the interface; see e.g. Francois et al. (2006); Meier et al. (2002); Rudman (1997); Popinet and Zaleski (1999); Shirani et al. (2005); Menard et al. (2007); Tanguy et al. (2007); Galusinski and Vigneaux (2008); Hysing (2006). The previous mentioned studies all related the growth of spurious velocities to the surface tension. More recently, however, it should be noted that Vukcevic (2016); Vukcevic et al. (2016); Wemmenhove et al. (2015) demonstrated development of spurious velocities in situations without surface tension.

While a benchmark case as presented in Wroniszewski et al. (2014) is, in principal, a good idea many relevant details of the `interFoam` setup were not presented, and this is typically the case in many of the previous mentioned studies. Such details are quite important, at least from the perspective of benchmarking, as it turns out that the performance of `interFoam` is quite sensitive to the setup (briefly touched upon in Paulsen et al. (2014) and Wroniszewski et al. (2014) in the choice of con-

*Corresponding author

Email address: bje1t@mek.dtu.dk (Bjarke Eltard Larsen)

vection scheme). Hence, prior to benchmarking `interFoam` or other CFD solvers, it is imperative that an "optimal" (or at least reasonably so) settings be known and utilized.

As the intended audience of the present paper is OpenFOAM users, a working knowledge of this software is assumed throughout. To shed light on the general CFD simulation of surface gravity waves, the present study will systematically investigate the performance of `interFoam` on a canonical case involving a simple, intermediately deep, progressive regular wave train. It will demonstrate that taking `interFoam` "out of the box," i.e. utilizing the standard setup from one of the popular tutorials, will yield quite poor results. After showing the default performance of `interFoam` the sensitivity of `interFoam` to different settings will be investigated. First, a standard sensitive analysis is conducted with respect to the Courant number and mesh resolution. This is done specifically to highlight that commonly-used Courant numbers may not be sufficiently small to accurately simulate gravity waves. Then, utilizing a lower Courant number, different `interFoam` settings will be systematically tested, and finally combined to form a reasonably optimal set up. More general set up considerations will also be discussed. The recently developed code `isoAdvector` will finally be coupled with `interFoam`, and the performance of `interFoam` (utilizing `isoAdvector` instead of MULES) will be compared to the performance of the standard `interFoam` solver.

2. Model description

2.1. Hydrodynamics

The flow is simulated by solving the continuity equation coupled with momentum equations, respectively given in (1) and (2):

$$\frac{\partial u_i}{\partial x_i} = 0, \quad (1)$$

$$\frac{\partial \rho u_i}{\partial t} + u_j \frac{\partial \rho u_i}{\partial x_j} = -\frac{\partial p^*}{\partial x_i} - g_j x_j \frac{\partial \rho}{\partial x_i} + \frac{\partial}{\partial x_j} (2\mu S_{ij}) + \sigma_T \kappa \frac{\partial \alpha}{\partial x_i}, \quad (2)$$

Here u_i are the mean components of the velocities, x_i are the Cartesian coordinates, ρ is the fluid density (which takes the constant value ρ_{water} in the water and jumps at the interface to the constant value ρ_{air} in the air phase), p^* is the pressure minus the hydrostatic potential $\rho g_j x_j$, g_j is the gravitational acceleration, $\mu = \rho \nu$ is the dynamic molecular viscosity (ν being the kinematic viscosity), and S_{ij} is the mean strain rate tensor given by

$$S_{ij} = \frac{1}{2} \left(\frac{\partial u_i}{\partial x_j} + \frac{\partial u_j}{\partial x_i} \right). \quad (3)$$

The last term in equation (2) accounts for the effect of surface tension, σ_T , where κ is the local surface curvature and α is the so-called indicator field introduced for convenience, which takes value 0 in air and 1 in water. It can be defined in terms of the density as

$$\alpha = \frac{\rho - \rho_{\text{air}}}{\rho_{\text{water}} - \rho_{\text{air}}}. \quad (4)$$

We assume that any intrinsic fluid property, Φ , can be expressed in terms of α as

$$\Phi = \alpha \Phi_{\text{water}} + (1 - \alpha) \Phi_{\text{air}}. \quad (5)$$

The evolution of α is determined by the continuity equation, which in terms of α reads

$$\frac{\partial \alpha}{\partial t} + \frac{\partial \alpha u_j}{\partial x_j} = 0. \quad (6)$$

In `interFoam` the numerical challenge of keeping the interface sharp is addressed using a numerical interface compression method and limiting the phase fluxes based on the "Multidimensional universal limiter with explicit solution" (MULES) limiter. Numerical interface compression is obtained by adding a purely heuristic term to equation (6), such that it attains the form

$$\frac{\partial \alpha}{\partial t} + \frac{\partial \alpha u_j}{\partial x_j} + \frac{\partial}{\partial x_j} (\alpha(1 - \alpha)u'_j) = 0. \quad (7)$$

Here u'_j is a modelled relative velocity used to compress the interface. For more details on the numerical implementation, the reader is referred to Deshpande et al. (2012).

All simulations are performed utilizing OpenFOAM version `foam-extend 3.2`. The authors are aware of a "new" MULES algorithm (not present in the extend versions) in newer versions from OpenFOAM-2.3.0, and also of the new commit support for Crank-Nicolson on the time integration of α . Therefore the base case to be presented later, was also simulated utilizing a newer version of the standard OpenFOAM, namely OpenFOAM-3.0.1. We were unable to produce significantly different results with these newer versions as compared to our simulations with `foam-extend 3.2`, hence the base performance demonstrated in what follows is likewise expected to be representative of newer versions.

2.2. Boundary and initial conditions

For this study a simple base case of a regular propagating wave will be simulated with various numerical settings. The quality of the simulated wave will be assessed through comparison with the analytical solution in terms of surface elevations and velocity profiles. We use a so-called stream function wave from Rienecker and Fenton (1981), initialized with `waves2Foam` developed by Jacobsen et al. (2012), with a period $T = 2$ s and wave height $H = 0.125$ m at a water depth of $h = 0.4$ m. This gives $kh = 0.66$ and $H/h = 0.31$, which indicates that the simulated wave is non-linear and at intermediate depth, with k being the wave number. The stream function solution can be considered as a numerically exact wave solution based on nonlinear potential flow equations. The properties have been selected to correspond to the incoming wave in the well-known spilling breaker experiment of Ting and Kirby (1994). For all simulations the wave will be propagated through a domain which is exactly one wave length long and two water depths high with cyclic periodic boundary conditions on the sides. Unless stated otherwise the domain is discretised into cells having an aspect ratio of 1 with the number of cells

per wave height $N = H/\Delta y = 12.5$, resulting in cells with $\Delta x = \Delta y = 0.01$ m. This results in a two dimensional domain with 379×80 cells. At the bed a slip condition is utilized in accordance with potential flow theory. At the top the `pressureInletOutletVelocity` is used. This means that there is a zero gradient condition except on the tangential component which has a value of zero.

3. interFoam settings

In this section the default numerical settings for our simulations, as well as a general description of OpenFOAM's discretization practices, are presented. Our base numerical settings will be those found in the popular `damBreak` tutorial shipped with `foam-extend-3.2`. With this starting point we will change various settings to investigate their effect on the quality of the numerical solution. More specifically, we copy the `controlDict`, `fvSchemes` and `fvSolution` files directly from the `damBreak` tutorial. In the `constant` directory the mesh and the physical parameters of the case are specified: $\rho_{\text{water}} = 1000 \text{ kg/m}^3$, $\rho_{\text{air}} = 1.2 \text{ kg/m}^3$, $\nu_{\text{water}} = 1 \cdot 10^{-6} \text{ m}^2/\text{s}$, $\nu_{\text{air}} = 1.45 \cdot 10^{-5} \text{ m}^2/\text{s}$, and $\sigma_T = 0.0 \text{ N/m}$ (i.e. no surface tension). We note that the analytic stream function solution does not take into account the presence of air, nor the effect of viscosity or surface tension. With the chosen wave parameters and boundary conditions (e.g. no slip at the bed) the physics are dominated by inertia and gravity. With a density ratio of $\rho_{\text{water}}/\rho_{\text{air}} \sim 833$, the air will behave like a "slave fluid" moving passively out of the way for the water close to the surface. To confirm the insignificance of the physical viscosity in our setup, we have compared simulations with these set to their physical values and to zero, and confirmed that this had no effect on our results. We have also performed simulations with $\rho_{\text{air}} = 0.1 \text{ kg/m}^3$ and $\rho_{\text{air}} = 10 \text{ kg/m}^3$. This had almost no effect in the short term, but had some effect for long propagation distances. Increasing the density made the air behave less like a "slave fluid" and slowed the propagation of the wave. Decreasing the density created larger air velocities, but did not alter the wave kinematics significantly. We have confirmed that switching the surface tension between zero and its physical value ($\sigma_T = 0.07 \text{ N/m}$) had next to no effect on our simulation results, as expected in the gravity wave regime. Finally, the simulations are performed without turbulence, as the results are intended to be compared with the idealized stream function (potential flow) solution.

The OpenFOAM case setup is contained in a file called `controlDict` which, among others things, controls the time stepping method. The schemes used to discretize the different terms in the governing equations are specified in the `fvSchemes` file, and the file `fvSolution` contains various settings for the linear solvers and for the solution algorithm. In Table 1 the essential parameters for the base set up from these three files are indicated. The most important details of the scheme and solver choices presented in Table 1 will be described in the following. For descriptions of the remaining settings, the reader is referred to the OpenFOAM user guide and programmers guides in Greenshields (2015, 2016).

3.1. controlDict

In this subsection the most important `controlDict` settings are presented. The time step can be specified either as fixed, such that the user defines the size of the time step, or as adjustable. In the latter case the time step is adjusted such that a maximum Courant number $Co = u_i \Delta t / \Delta x_i$ or a maximum `AlphaCo` (The Courant number in interface cells) is maintained at all times. In the `damBreak` tutorial an adjustable time step is used with $Co = 0.5$, hence this value will be utilized initially.

3.2. fvSchemes

In this subsection some of the discretisation schemes are presented to aid in the understanding of the forthcoming analysis. The `ddt` scheme specifies how the time derivative $\partial/\partial t$ is handled in the momentum equations. Available in OpenFOAM are: `steadyState`, `Euler`, `Backwards` and `CrankNicolson`. In this study, `steadyState` is naturally disregarded as the simulations are unsteady. The `Euler` scheme corresponds to the first-order forward Euler scheme, whereas `Backward` corresponds to a second-order, OpenFOAM implemented time discretization scheme, which utilizes the current and two previous time steps. The `CrankNicolson` (CN) scheme includes a blending factor ψ , where $\psi = 1$ corresponds to pure (second-order accurate) CN and $\psi = 0$ corresponds to pure `Euler`. This blending factor is introduced to give increased stability and robustness to the CN scheme.

In the finite volume approach used in OpenFOAM, the convective terms in the mass (7) and momentum (2) equations are integrated over a control volume, and afterwards the Gauss theorem is applied to convert the integral into a surface integral:

$$\int_V \nabla \cdot (\phi u) dV = \oint_S \phi (n \cdot u) dS \approx \sum_f \phi_f F_f, \quad (8)$$

where $\phi(x, t)$ is the field variable, ϕ_f is an approximation of the face averaged field value and $F_f = s_f \cdot u_f$ is the face flux, with s_f being the face area vector normal to the face pointing out of the cell. ϕ_f can be determined by interpolation, e.g. using central or upwind differencing. Central differencing schemes are second order accurate, but can cause oscillations in the solution. Upwind differencing schemes are first order accurate, cause no oscillations, but can be very diffusive.

OpenFOAM includes a variety of total variation diminishing (TVD) and normalized variable diagram (NVD) schemes aimed at achieving good accuracy while maintaining boundedness. TVD schemes calculate the face value ϕ_f by utilizing combined upwind and central differencing schemes according to

$$\phi_f = (1 - \Gamma)\phi_{f,UD} + \Gamma\phi_{f,CD} \quad (9)$$

where $\phi_{f,UD}$ is the upwind estimate of ϕ_f , $\phi_{f,CD}$ is the central differencing estimate of ϕ_f . Γ is a blending factor, which is a function of the variable r representing the ratio of successive gradients,

$$r = 2 \frac{d \cdot (\nabla \phi)_P}{\phi_N - \phi_P}. \quad (10)$$

Table 1: Base setup from the damBreak tutorial

controlDict	Scheme/Value
adjustTimeStep	true
maxCo	0.5
maxAlphaCo	0.5
fvSchemes	
ddt	Euler
grad	Gauss Linear
div(rho*phi,U)	Gauss LimitedLinearV 1
div(phi,alpha1)	Gauss VanLeer01
div(phiIr,b,alpha1)	Gauss interfaceCompression
laplacian	Gauss linear corrected
interpolation	linear
snGrad	corrected
fvSolution	
pcorr(solver,prec,tol,relTol)	PCG, DIC, 1e-10, 0
pd(solver,prec,tol,relTol)	PCG, DIC, 1e-07, 0.05
pdFinal(solver,prec,tol,relTol)	PCG, DIC, 1e-07, 0
U(solver,prec,tol,relTol)	PBiCG, DILU, 1e-06, 0
cAlpha	1
momentumPredictor	yes
nOuterCorrectors	1
nCorrectors	4
nNonOrthogonalCorrectors	0
nAlphaCorr	1
nAlphaSubCycles	2

Here d is the vector connecting the cell centre P and the neighbour cell centre N . In NVD-type schemes the limiter is formulated in a slightly different way. In the damBreak tutorial base setup the TVD scheme is utilized by specifying the keyword `limitedLinearV 1` for the momentum flux, `div(rho*phi,U)`, and `vanLeer01` for the mass flux, `div(phi,alpha1)`, where the keyword `phi` means face flux. With the `limitedLinear` scheme $\Gamma = \max[\min(2r/k, 1), 0]$, where k is an input given by the user, in this case $k = 1$. When using the scheme for vector fields a "V" can be added to the TVD schemes, which changes the calculation of r to take into account the direction of the steepest gradients. The `vanLeer` scheme calculates the blending factor as $\Gamma = (r + |r|)/(1 + |r|)$. The 01 added after the TVD scheme name means that Γ is set to zero if it goes out of the bounds 0 and 1, thus going to a pure upwind scheme to stabilize the solution. The other available TVD/NVD schemes differ in their definition of Γ and resulting degree of diffusivity. Since r depends on the numerically calculated gradient of ϕ , the choice of gradient scheme can also play an important role. In general the gradients are calculated utilizing a Gauss linear scheme, but this might lead to unbounded face values, and therefore gradient limiting can be applied. As an example the gradient scheme can be specified as `Gauss faceMDLimited`. The keyword `face` or `cell` specifies whether the gradient should be limited base on cell values or face values and the keyword `MD` specifies that it should be the gradient normal to the faces. In addition to the linear choice of gradient schemes there also exists a least square scheme as well

as a fourth order scheme.

The `laplacian` scheme specifies how the Laplacian in the pressure correction equation within the PISO algorithm, as well the third term on the right hand side of equation (2), should be discretized. It requires both an interpolation scheme for the dynamic viscosity, μ , and a surface normal gradient scheme `snGrad` for ∇u . Often a linear scheme is used for the interpolation of μ and the proper choice of surface normal gradient scheme depends on the orthogonality of the mesh. Besides being used in the Laplacian, the `snGrad` is also used to evaluate the second and fourth term on the right hand side of equation (2). Often a linear scheme will be used, with or without orthogonality correction. Another option is to use a fourth order surface normal gradient approximation. Finally, the interpolation scheme determines how values are interpolated from cell centres to face centres.

3.3. fvSolution

In the `fvSolutions` file the iterative solvers, solution tolerances and algorithm settings are specified. The available iterative solvers are preconditioned (bi-)conjugate gradient solvers denoted `PCG/PBiCG`, a `smoothSolver`, generalised geometric-algebraic multi-grid, denoted `GAMG`, and a diagonal solver. Each solver can be applied with different preconditioners and the smooth solver also has several smoothing options. The `GAMG` solver works by generating a quick solution on a coarse mesh consisting of agglomerated cells, and then mapping this solution as the initial guess on finer meshes to finally obtain an

accurate solution on the simulation mesh. The different preconditioners and smoothers will not be discussed here, but Green Shields (2015, 2016) can be consulted for additional details.

In addition to the solver choices the PISO, PIMPLE and SIMPLE controls are also given in the `fvSolution` file. The `cAlpha` keyword controls the magnitude of the numerical interface compression term in equation (7). `cAlpha` is usually set to 1 corresponding to a “compression velocity” of the same size as the flow velocity at the interface. The `momentumPredictor` is a switch specifying enabling activation/deactivation of the predictor step in the PISO algorithm. The parameter, `nOuterCorrectors` is the number of outer correctors used by the PIMPLE algorithm and specifies how many times the entire system of equations should be solved within one time step. To run the solver in “PISO mode” we set `nOuterCorrectors` to 1. The parameter `nCorrectors` is the number of pressure corrector iterations in the PISO loop. The parameter `nAlphaSubCycles` enables splitting of the time step into `nAlphaSubCycles` in the solution of the α equation (7). Finally, the parameter `nAlphaCorr`, specifies how many times the α field should be solved within a time step, meaning that first the α field is solved for, and this new solution is then used in solving for the α field again.

4. Results and discussion

In this section the simulated results involving the propagation of the regular stream function wave will be presented and discussed for various settings.

4.1. Performance of `interFoam` utilizing the `damBreak` settings

First, the “default” performance of `interFoam` in the progression of the stream function wave is presented, utilizing the settings from the `damBreak` tutorial. The setup utilized here will be considered as the base setup, and the remainder of the simulations in this study will utilize this base setup with minor adjustments.

Starting from the analytical stream function solution imposed as an initial condition (utilizing the `waves2Foam` toolbox of Jacobsen et al. (2012)), the simulation is performed for 200 s (corresponding to 100 periods). This is sufficiently long to highlight certain strengths and problems of `interFoam`. Results are sampled at the cyclic boundary 20 times per period. In Figure 1 the surface elevation time series is shown. Quite noticeably, even though the depth is constant, the wave height immediately starts to increase, and this continues until the wave at some point (approximately at $t = 20T$) breaks. This rather surprising result demonstrates the potentially poor performance of `interFoam`, as the wave does not come close to maintaining a constant form. A similar result has been shown in Afshar (2010). A feature that seems to contribute, though is not solely responsible for, the un-physical steepening of the wave, is small “wiggles” on the interface. These are illustrated in Figure 2 where a snapshot of the wave is seen after approximately five and 16 periods. The vertical axes are exaggerated to highlight the presence of the wiggles. As the wave propagates these wiggles emerge, continue to grow and sometimes merge, hence contributing to the

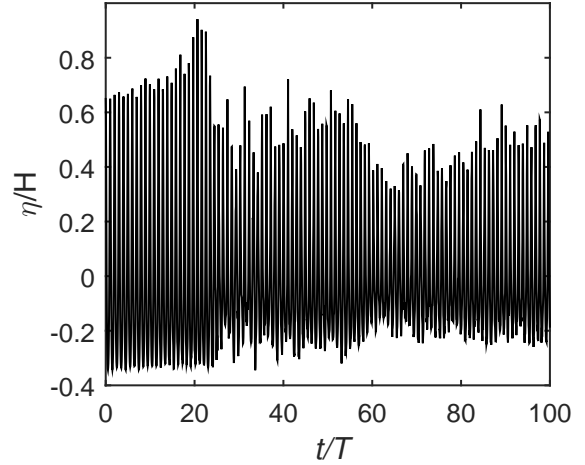


Figure 1: Surface elevation for the propagating wave utilizing the `damBreak` setup

steepening of the wave, which ultimately breaks. The cause of the wiggle feature will be discussed in Section 4.4.

While propagating, in addition to steepening, the celerity is also increasing compared to the analytical stream function solution, resulting in a phase error. To demonstrate this the surface elevation for the first 20 periods is compared with the stream function solution in Figure 3. Here it is quite evident that significant phase errors occur after approximately propagating for 10 periods, where the simulated results start to lead the analytical solution. This corresponds approximately to the time where over-steepening is apparent, hence the phase error may be attributed to the un-physical increase in the nonlinearity of the wave.

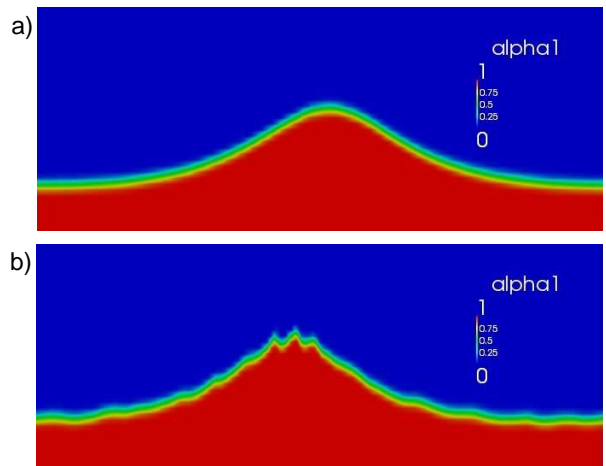


Figure 2: Snapshot at a) $t = 5.5T$ and b) $t = 16.25T$, illustrating the appearance of small wiggles in the crest after sufficiently long propagation

Also of great interest is the velocity profile beneath the propagating wave, as velocity kinematics often form the basis for force calculations on coastal or offshore structures, while also influencing e.g. bed shear stresses and hence sediment transport predictions (in simulations where the boundary layer is also resolved). In Figure 4 the velocity profile directly beneath the

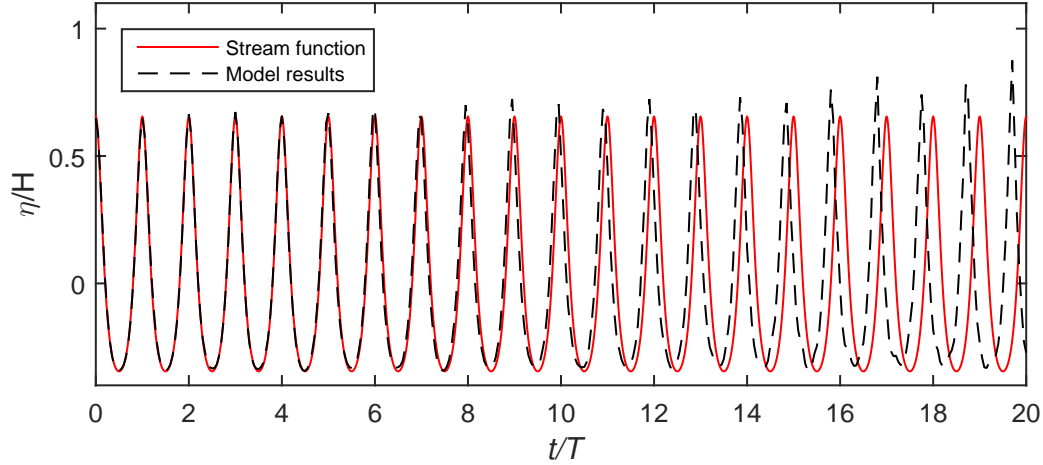


Figure 3: Surface elevation for the propagating wave utilizing the damBreak setup

crest of the wave after five periods is shown together with the analytical stream function solution. It should be noted that the velocity here, and in future results, is taken as $U = u_1\alpha$, and it is only shown from the bed until the height where it reaches its maximum value. This is done to capture the velocity all the way to the crest of the wave and not merely to a predefined height (as just shown, the wave height increases). Furthermore, this formulation also includes the velocities at cells containing a mixture of air and water, which is desirable, as some diffusion of the interface is seen.

As seen in Figure 4, the velocity beneath the crest is underestimated close to the bed and, especially near the free surface, is severely overestimated. This is despite the fact that the wave has still reasonably maintained its shape up to this time, see Figure 2a and 3. This over-predicted crest velocity, in addition to the steepening of the wave, also likely contributes to the wave breaking. The overestimation of crest velocities in regular waves by *interFoam* has, to our knowledge, gone almost un-recognized in the journal literature. It is recorded in Wroniszewski et al. (2014) in the propagation of a solitary wave and in Roenby et al. (2017b) as well as in the MSc thesis of Afshar (2010) and the PhD thesis of Tomaselli (2016). The overestimation of the crest velocity is believed to arise from an imbalance in the discretized momentum equation near the interface. As the wave propagates the increase in crest velocity becomes continually worse, and in addition to the imbalance in the momentum equation near the free surface, the steepening of the wave also contributes to this increase.

Finally, though not shown herein for brevity, we note that regions of high air velocities were seen to develop just above the free surface and in the mixture cells. Such spurious velocities have elsewhere been attributed to surface tension effects, see e.g. Deshpande et al. (2012), but the spurious velocities found in these simulation are clearly of a different nature as the surface tension is turned off. The main challenge leading to this behavior is that when the water/air density ratio is high, even small erroneous transfers of momentum across the interface from the heavy to the light fluid will cause a large acceleration of the light fluid, as also discussed by Vukcevic (2016);

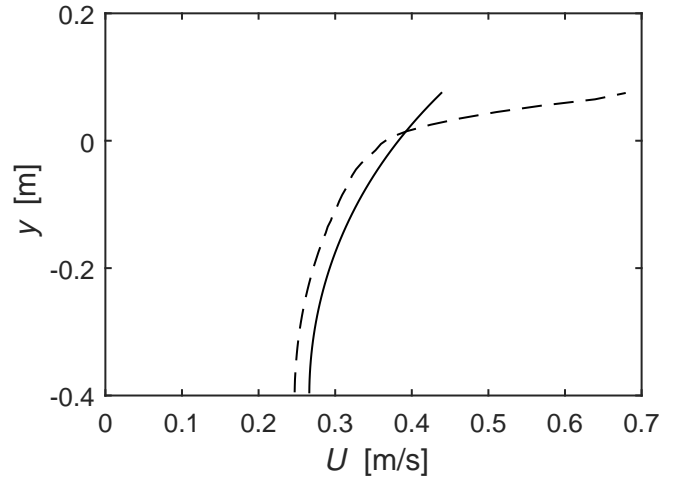


Figure 4: Modelled velocity distribution beneath the crest (- -) and stream function solution, (-) at $t = 5T$.

Vukcevic et al. (2016); Wemmenhove et al. (2015). The resulting large air velocities may then be subsequently diffused back across the interface into the water, the degree to which will be discussed in Section 4.4.

4.2. Effect of the Courant number, Co

With the poor performance previously shown using the default *damBreak* settings, two natural places to attempt improvement in the solution would be in the temporal and spatial resolutions. In this section the effect of the temporal resolution will be investigated by varying Co .

Figure 5 shows the surface elevation as a function of time for six different values of Co . From this it is evident that lowering Co has a significant impact on *interFoam*'s performance. However, even with $Co = 0.02$ *interFoam* it is not capable of keeping the wave shape for 100 periods as the wave heights are still seen to increase. Up until 20 wave periods the wave height is close to constant when using $Co \leq 0.15$. The wave is still leading the analytical stream function solution and in general

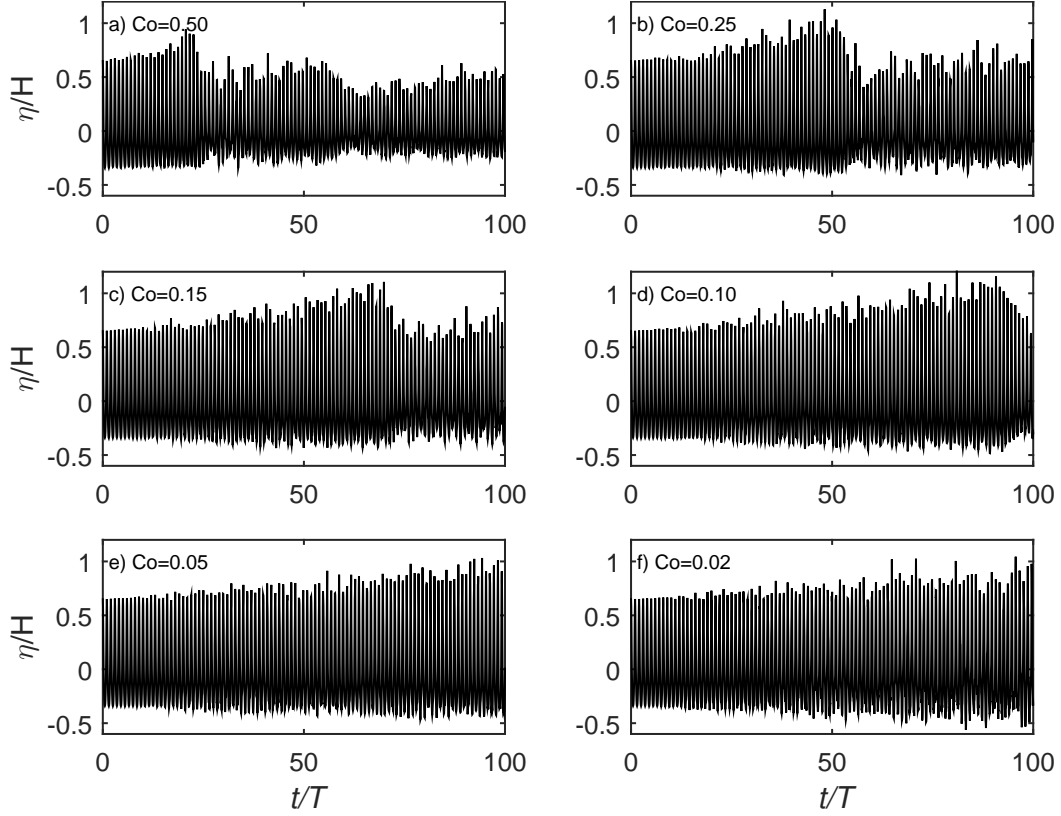


Figure 5: Simulated surface elevation as a function of time for six different Courant numbers (Main fixed parameters: $N = 12.5$, ddt-Euler, grad-Gauss Linear, div(rho*phi,U)- Gauss LimitedLinearV 1, laplacian-Gauss linear corrected, $c_\alpha = 1$).

lowering Co reduces the overestimation of the wave celerity as can be seen in table 2 where the phase-shift at $t = 25T$ is shown for the six different values of Co . The phase shift is calculated as $\phi_{shift} = (t_{peak} - t_{analytical})/T \cdot 360^\circ$, where t_{peak} is the time where the crest of the wave passes the sampling position, and $t_{analytical}$ is the time where the stream function solution should have passed the sampling position.

Co	0.02	0.05	0.10	0.15	0.25	0.50
$\phi_{shift} [^\circ]$	0.0	0.0	-18	-36	-72	-198

Figure 6 shows the velocity profiles beneath the crest at $t = 5T$ for the six different values of Co together with the stream function solution, similar to Figure 4. It can be seen that as Co is lowered the simulated velocity profiles become closer to the analytical solution. The reason for this is probably two-fold. First, lowering Co delays the presence and growth of the interface wiggles and thus also the steepening of the wave. Second, any inconsistent treatment of the force balance near the free surface is substantially limited by the small time step as it reduces e.g. the error committed in linearising the convective term $u_j(\partial\rho u_i/\partial x_j)$. The importance of keeping a low time step in `interFoam` when doing two-phase simulations has also been highlighted by Deshpande et al. (2012) in the context of surface tension dominated flows, where it was shown that a small time step is crucial for limiting the growth of spurious velocities.

Even though the present inertia dominated situation is different from the analysis of Deshpande et al. (2012), the solution to minimize the interface imbalance by limiting the time step still seems to hold.

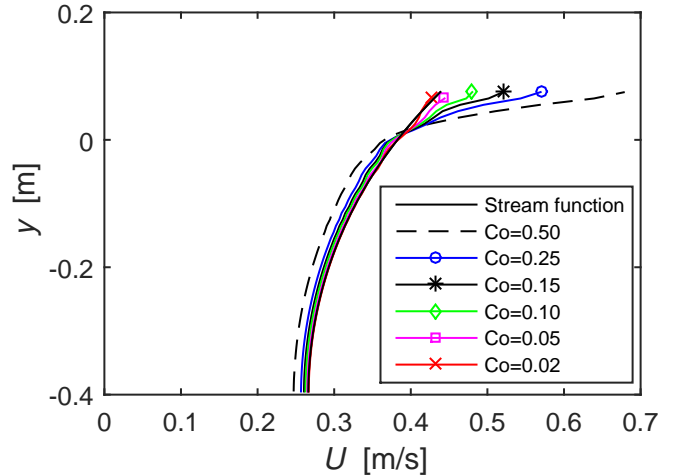


Figure 6: Velocity distribution beneath the crest at $t = 5T$ for various Courant numbers (Main fixed parameters: $N = 12.5$, ddt-Euler, grad-Gauss Linear, div(rho*phi,U)- Gauss LimitedLinearV 1, laplacian-Gauss linear corrected $c_\alpha = 1$).

In addition to the velocity profiles depicted in Figure 6, it

is also of interest to see how the overestimation of the crest velocity evolves in time. Therefore, in Figure 7 the error in the crest velocity calculated as

$$\Delta E = \frac{\max(U) - U_{\text{analytical}}}{U_{\text{analytical}}} \quad (11)$$

is shown for each of the six values of Co considered. Regardless

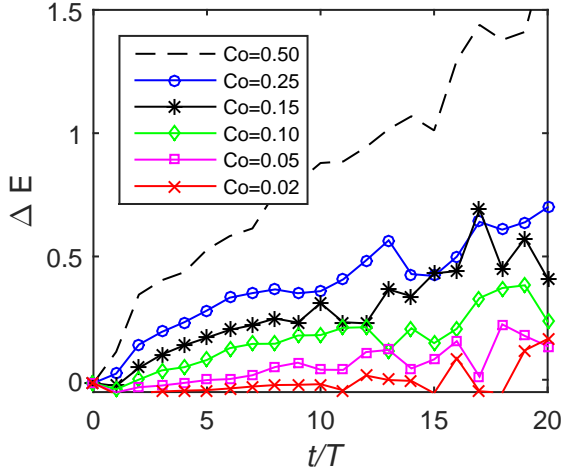


Figure 7: Error in the maximum crest velocity as a function of periods (Main fixed parameters: $N = 12.5$, ddt-Euler, grad-Gauss Linear, div(rho*phi,U)-Gauss LimitedLinearV 1, laplacian-Gauss linear corrected $c_\alpha = 1$).

of Co , the overestimation of the crest velocity is apparent and grows in time. From Figure 7 it can be seen that even with a relatively small Co , e.g. $Co = 0.15$, after only propagating five periods, the crest velocity is approximately 17% larger than the analytical. It thus seems that, what is generally viewed as a rather "low" Co , is still not sufficiently small to accurately simulate surface waves. In contrast, the error in the crest velocity for the case with $Co = 0.05$ is only 0.1% after five periods, thus this value seems like a proper Co for the accurate simulation of this wave.

4.3. The effect of mesh resolution

Having checked the effect of the temporal resolution, it now seems natural to check the effect of varying the spatial resolution. However, as the solution with $Co = 0.5$ from the damBreak tutorial was poor, the rest of the forthcoming analysis will be continued with $Co = 0.15$, with the hope of further improving the previous results. In Jacobsen et al. (2012) it was noted that interFoam performed best with cell aspect ratios, defined as $\Delta x/\Delta y$, of 1, and this ratio will be maintained throughout the analysis. In the previous cases $N = 12.5$, and now three additional simulations will be performed with $N = 50$, $N = 25$ and $N = 6.25$ respectively. Figure 8 shows the surface elevations as a function of time for the four different resolutions. Similar to increasing the temporal resolution (i.e. lowering Co) it can be seen that increasing the number of cells per wave height greatly improves the solution when considering the ability to propagate the wave while maintaining constant form.

Before continuing, it is also worth commenting on the shape of the air–water interface in the different resolutions, which is illustrated in Figure 9 for $N = 6.25$ and $N = 25$. As expected

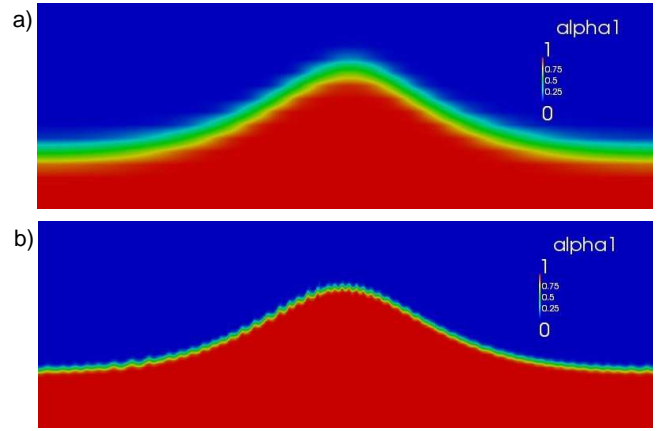


Figure 9: Snapshot at $t = 5.5T$ for a) $N = 6.25$ and b) $N = 25$ (Main fixed parameters: $Co = 0.15$, ddt-Euler, grad-Gauss Linear, div(rho*phi,U)-Gauss LimitedLinearV 1, laplacian-Gauss linear corrected $c_\alpha = 1$).

with $N = 6.25$ the interface looks smeared and is not well captured. With $N = 12.5$ (not shown here for brevity) the interface looks similar to Figure 2a, but the wave gradually steepens in time as previously explained. With $N = 25$ and also $N = 50$ the interface is even sharper and with $N = 25$ the wave heights were also seen to increase, but somewhat slower. This is probably related to the size of the wiggles being much smaller with the finer mesh. In these cases the wiggles were not only present in the top of the crest, but also along the whole wave surface. They also appeared at an earlier time, as seen in Figure 9b.

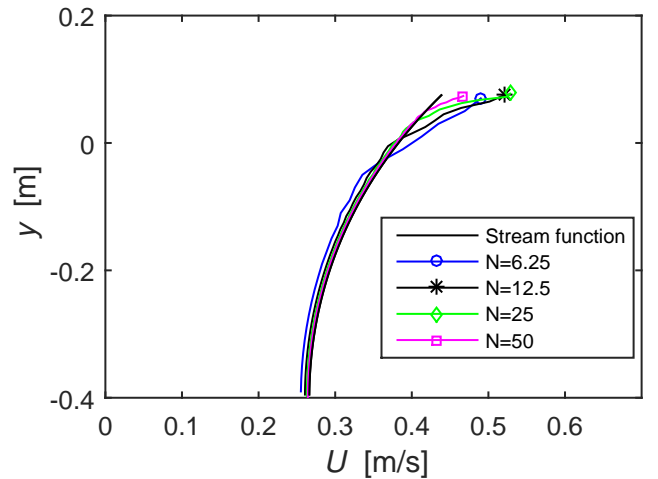


Figure 10: Velocity distribution beneath the crest at $t = 5T$ for various mesh resolutions (Main fixed parameters: $Co = 0.15$, ddt-Euler, grad-Gauss Linear, div(rho*phi,U)-Gauss LimitedLinearV 1, laplacian-Gauss linear corrected $c_\alpha = 1$).

In Figure 10 the velocity profiles beneath the crest at $t = 5T$ are shown for the four different spatial resolutions together with the analytical stream function solution. In general, it can be

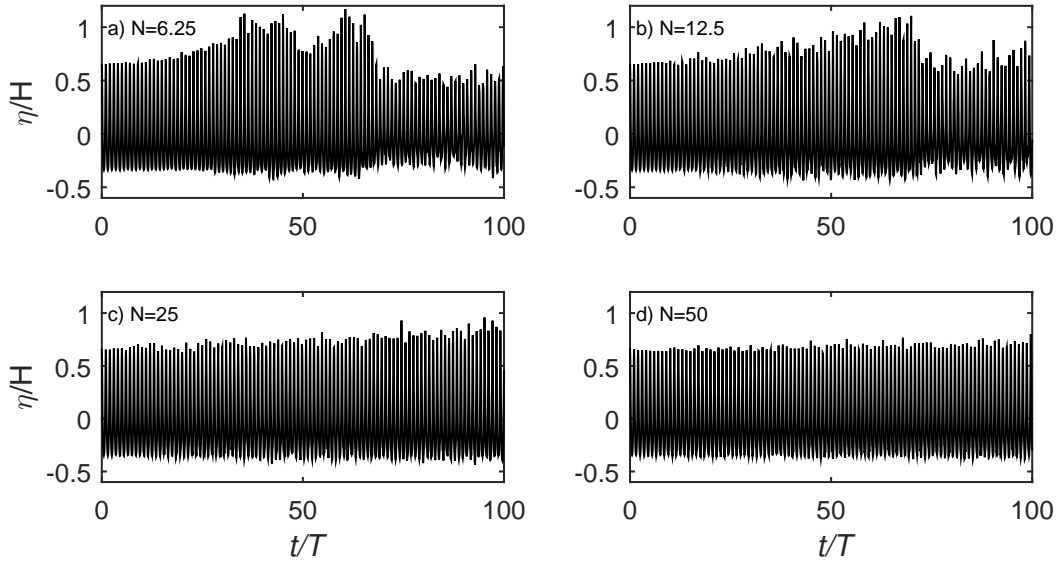


Figure 8: Simulated surface elevation as a function of time for four different mesh resolutions (Main fixed parameters: $Co = 0.15$, ddt-Euler, grad-Gauss Linear, div(rho*phi,U)-Gauss LimitedLinearV 1, laplacian-Gauss linear corrected $c_\alpha = 1$).

seen that, improving the spatial resolution improves the solution. However, for the case with $N = 25$ the crest velocity is as high as in the coarser resolved cases. This can be explained by the afore mentioned wiggles. At the crest of such a surface wiggles, the velocity is much higher compared to the rest of the wave. This is not seen to the same degree with $N = 50$ where the surface wiggles are much smaller. When propagating the wave longer than the five periods, it was experienced that the case with $N = 25$ had crest velocities closer to the analytical solution than the two coarser resolved cases. From the above results it is worth noting that increasing the spatial resolution was not able to produce as good results for the velocity profiles as increasing the temporal resolution, see Figures 6 and 10. From a computational point of view decreasing Co seem to be a more efficient alternative to increase accuracy, than increasing the mesh resolution. This is especially true considering that increasing the mesh resolution, will also make the time step decrease to maintain a given Co . However, in terms of keeping the wave height constant for the entire simulation, increasing the spatial resolution does seem to yield better results compared to simply increasing the temporal resolution.

4.4. fvSchemes and fvSolution settings

Thus far increasing the temporal and spatial resolution have been attempted, and unsurprisingly, these improved the solution. For the rest of this study $Co = 0.15$ and $N = 12.5$ will be maintained for the sake of balancing computational costs and accuracy, and the additional effects of changing schemes and solution settings will be investigated. As quite a few schemes are available, not all results of our investigations will be shown. Our findings will be summarized and figures will be included when found to be most relevant. Later, we will combine some of the investigated schemes to improve the overall solution quality.

It has been shown that the interface between air and water in time develop wiggles, which in time grow and sometimes lead to breaking. First, the additional effects of modifying c_α (with default value $c_\alpha = 1$), which controls the size of the compression velocity, will be investigated. It was experienced that increasing c_α causes the wiggles to appear earlier and grow faster. Reducing c_α reduces the wiggles and at the same time causes the interface to smear out over more cells. This strongly indicates that the wiggles are caused by the numerical interface compression method.

To illustrate the effect of c_α , the surface elevations are shown for four different values in Figure 11. In this figure, to demonstrate the effect of c_α on the interface, we also plot the $\alpha = 0.99$ and $\alpha = 0.01$ contours for the crest and the trough for each period. The reduction in wave height seen in the case with $c_\alpha = 0$ (Figure 11a), is the effect of a very heavy diffusion of the interface. This can be seen even more clearly when looking at the $\alpha = 0.99$ and $\alpha = 0.01$ contours. It can be seen that after 20 periods the 0.99 contour at the crest is actually positioned lower than the trough level and the 0.01 contour at the trough is almost at the crest level. The distance between the 0.01 contour and 0.99 contour is approximately four cells with $c_\alpha = 0.5$ (Figure 11b), whereas it only spans approximately three cells for $c_\alpha = 1$ (Figure 11c) and $c_\alpha = 1.5$ (Figure 11d). This shows that increasing c_α does compress the interface, but that the interface will span more than one cell, even with a high value of c_α .

In addition to the c_α value, various other settings affect the size and behaviour of the wiggles, and in the following $c_\alpha = 1$ will be maintained, for the sake of comparison. The effect of the time discretization scheme on the surface elevations is shown in Figure 12. Changing the time discretization scheme from Euler (first order) to CN (second order) exacerbates the wiggle feature, causing them to develop earlier and extend throughout the surface. Contrary to results utilizing the Euler scheme, the

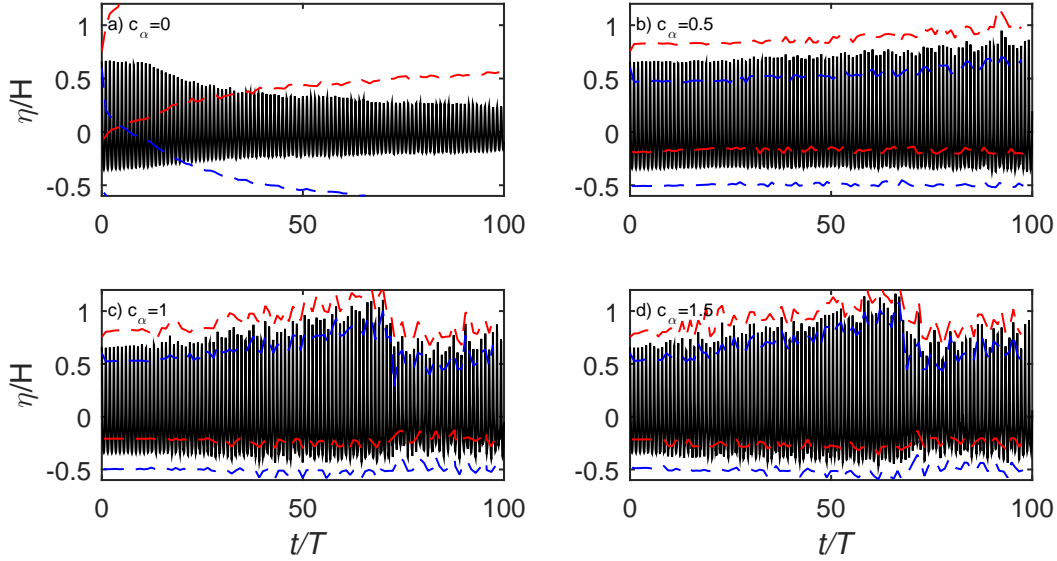


Figure 11: Simulated surface elevations (-) as a function of time for different values of c_α together with the $\alpha = 0.99$ and $\alpha = 0.01$ contours (- -) (Main fixed parameters: $Co = 0.15$, $N = 12.5$, ddt-Euler, grad-Gauss Linear, div(rho*phi,U)-Gauss LimitedLinearV 1, laplacian-Gauss linear corrected).

wiggles do not cause the wave to steepen to the same extent. The wiggles grow in size, but they often break on top of the wave before merging, and therefore the wave does not steepen as much as with the Euler scheme. It is believed that the wig-

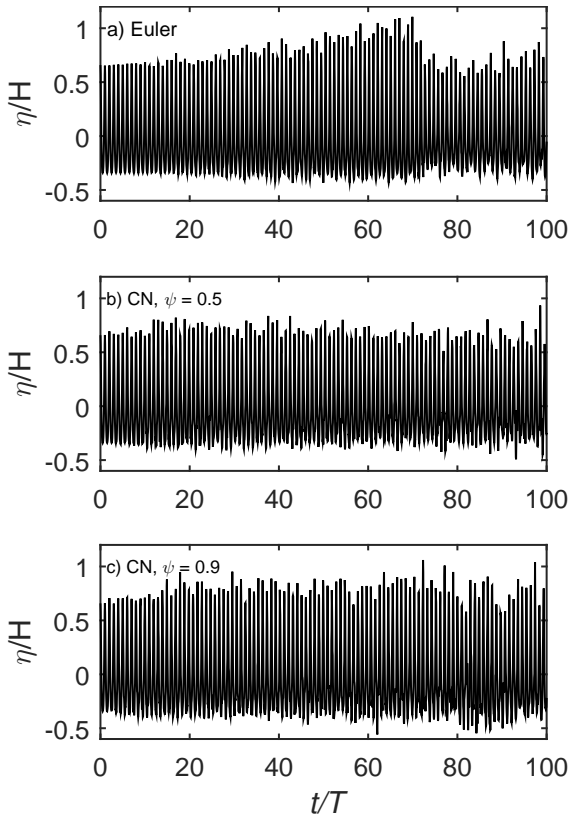


Figure 12: Simulated surface elevation as a function of time for different time discretization schemes (Main fixed parameters: $Co = 0.15$, $N = 12.5$, grad-Gauss Linear, div(rho*phi,U)-Gauss LimitedLinearV 1, laplacian-Gauss linear corrected, $c_\alpha = 1$).

gle feature is more pronounced with the CN scheme simply because the scheme is less diffusive than the Euler scheme. The artificial compression term, as just shown, adds some erratic behaviour to the interface, and this is diffused by numerical damping when using the Euler scheme, but less so when using CN.

The reduction or complete removal of wiggles is also seen utilizing other more diffusive schemes, e.g. when using the upwind scheme for the convection of the α field or using the upwind scheme for the convection of momentum. In the case of utilizing the upwind scheme for the convection of the α field the solution is very similar to that seen when setting $c_\alpha = 0$ (Figure 11a), with the interface experiencing heavy diffusion and the resulting wave height decaying rapidly. Utilizing an upwind scheme for the convection of momentum also causes the wave height to decay, but at a much slower rate, and is not accompanied by the same degree of interface diffusion. However, utilizing a pure upwind scheme is generally not recommended due to excessive smearing of the solution.

Thus far it has been shown that c_α and the time discretization scheme have a significant impact on the surface elevation and interface. However, regarding the velocity profile beneath the crest (not shown here for brevity), the impact is very small, except for the case with $c_\alpha = 0$, which made the velocities throughout the water column beneath the crest too low. This is probably due to heavy diffusion of the interface (see Figure 11a).

As mentioned, the wiggles can be limited by choosing more diffusive schemes, but it still needs to be determined how these schemes affect the general propagation of the wave and the underlying velocity profile. Figure 13 shows the surface elevation for four different convection schemes (div(rho*phi,U)), and the influence of the choice on convection scheme is readily apparent. The most diffusive among the four schemes, the upwind scheme, makes the wave decay in a quite stable fashion (Figure 13b). The SFCD scheme (Figure 13c) is slightly more diffusive

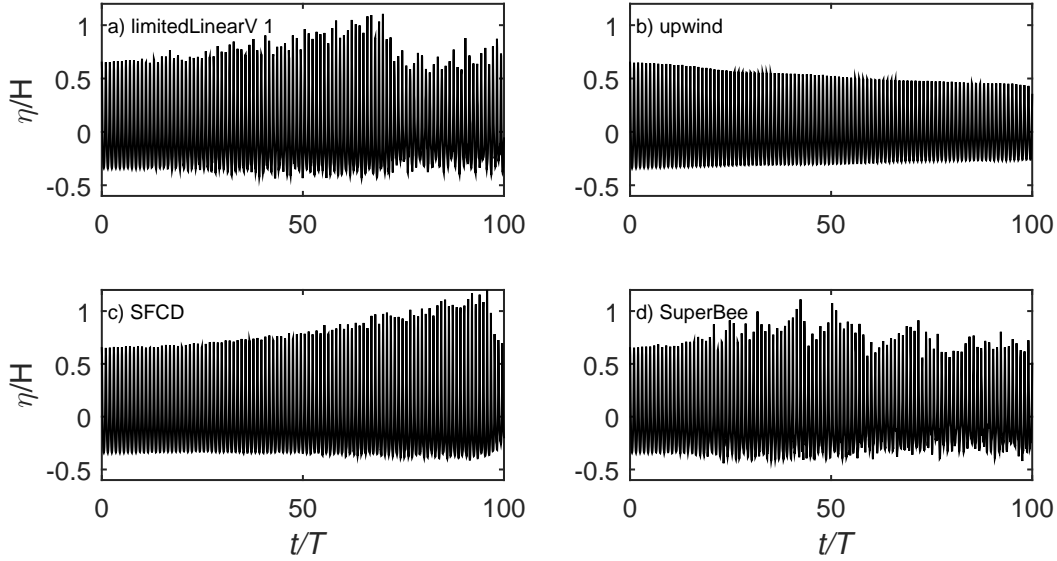


Figure 13: Simulated surface elevation as a function of time for different convection schemes (Main fixed parameters: $Co = 0.15$, $N = 12.5$, ddt-Euler, grad-Gauss Linear, laplacian-Gauss linear corrected, $c_\alpha = 1$).

than the `limitedLinearV 1` scheme (Figure 13a), and is seen to limit the growth in the wave height. The wave height still increases as time progresses but the increase is delayed and the simulation is less erratic. The fourth scheme is the `SuperBee` scheme (Figure 13d). This scheme is also within the TVD family, but it is much more erratic, and almost immediately the wave heights start to increase.

The velocity profiles beneath the crest for the four convection schemes are likewise shown at $t = 5T$ in Figure 14, and once again the importance of the convection scheme is quite clear. The `upwind` scheme limits the error in the velocity at the top crest whereas it underestimates the velocity closer to the bed. The `SFCD` scheme behaves slightly better than the `limitedLinearV 1` scheme, and the `SuperBee` scheme performs the worst. When propagating further the `SuperBee` scheme has oscillations in the velocity profile beneath the crest, which can also be seen to a smaller degree in Figure 14.

A range of other convection schemes have also been attempted. None of them, however, show significantly different results than those shown here, which have been selected to demonstrate the effect of convection scheme diffusivity on the propagation of the wave and velocity profile beneath the crest. While the convection schemes have been shown to have a great effect on both the ability to maintain a constant wave height, limit the wiggle feature in the interface and predict the velocity profile, it is not directly evident which scheme performs the best overall. The `upwind` scheme limits the error in the crest velocity the most, which would be beneficial when e.g. doing loads on structures, but due to the diffusivity of the scheme might not be able to capture e.g. vortex shedding around such a structure. The `SFCD` scheme improves the ability to maintain a constant wave height and limits the growth in the crest velocity compared to the `limitedLinearV 1` scheme from the `damBreak` tutorial, but the crest velocity is still severely overestimated.

We will now turn our attention to the gradient (grad)

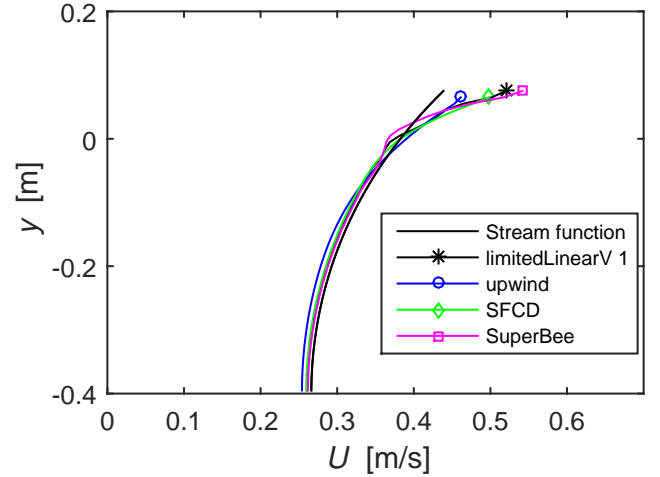


Figure 14: Velocity distribution beneath the crest at $t = 5T$ for various convection schemes (Main fixed parameters: $Co = 0.15$, $N = 12.5$, ddt-Euler, grad-Gauss Linear, laplacian-Gauss linear corrected, $c_\alpha = 1$).

schemes. These effects (relative to the default `Gauss Linear` scheme in Figures 5c and 6) on the wave propagation and velocity profile will be described, but for brevity no additional figures will be included. The fourth-order scheme (`fourth`) improves the propagation and delays the increase in wave heights, similar to the behaviour seen with the `SFCD` convective scheme (Figure 13c), which is more diffusive than the standard `limitedLinearV 1` scheme. The fourth scheme is however not more diffusive than the `Gauss Linear` scheme, and the delayed increase in wave height is probably due to the scheme having higher-order accuracy. The velocity profile beneath the crest, on the other hand, is not improved relative to the `Gauss Linear` scheme (Figure 6, $Co=0.15$). The `faceMDLimited Gauss Linear 1` gradient scheme has also

been tested, and behaves very similar to the upwind convection scheme (Figure 13b), in the sense that the wave heights decrease with time. The reason for this is probably that the gradient limiter, coupled with the `limitedLinearV 1` convection scheme, effectively makes the convection scheme an upwind scheme. With respect to the velocities the `faceMDLimited` gradient scheme produced a velocity profile very similar to that from the upwind scheme (Figure 14). That the limited gradient scheme can produce results similar to the upwind convection scheme was also observed by Liu and Hinrichsen (2014), who studied the effect of convection and gradient schemes on bubbling fluidized beds using OpenFOAM.

We will now describe how changing the Laplacian scheme effects the solution, relative to the default setting (`Gauss linear corrected`). As previously mentioned the Laplacian scheme requires keywords for both interpolation and `snGrad`, but the inputs for the stand alone interpolation and `snGrad` schemes are not changed. For the Laplacian scheme, combining the `Gauss linear` interpolation with the fourth `snGrad` scheme, resulting in the Laplacian scheme `Gauss Linear fourth`, gave improved results, both in terms of the ability to maintain constant wave heights and in terms of the velocity profile beneath the crest. However switching to the fourth-order scheme (`fourth`), resulted in very high spurious velocities in the air region above the wave, and hence (due to the Co -controlled time step) leads to reductions in the time steps used during the simulation. In this way changing to a fourth-order `snGrad` schemes in the Laplacian is effectively similar to lowering Co . To check whether the fourth-order `snGrad` scheme in the Laplacian really improved the solution, or if it is merely a result of a reduced time step, two additional simulations, now utilizing a fixed time step $dt=0.0025$ m/s, have been performed, with both `corrected` and `fourth` `snGrad` scheme in the Laplacian. The resulting velocity profiles at $t = 5T$, together with the result from a simulation with $\rho_{air} = 0.1$ kg/m³ (also utilizing the same fixed time step), are shown in Figure 15. The three simulations show similar results in the water phase, but rather different velocities in the air phase. These results indicate that, while being an un-physical and undesirable phenomenon, the spurious velocities in the air do not seem to effect the wave significantly. The case with a fourth-order `snGrad` scheme had approximately twice as high air velocities as the standard set up, but similar (actually slightly lower) crest velocities. The case with lower density also has higher air velocities, but very similar water velocities to the standard case. To summarize: Even though the fourth-order Laplacian scheme is able to produce better wave kinematics, caution must be taken as it produces large spurious velocities. These will, utilizing a variable time step, lead to very low time steps. Alternatively, a fixed time step may result in an unstable Courant number.

Before conducting the present study it was expected that the discretization schemes would have an effect on the solution, but it was also expected that in particular the choice of iterative solvers for the pressure would not have an effect, at least if the tolerances were sufficiently low. It turns out, however, that the iterative solver settings in `fvSolution` also affect the wave propagation. For the pressure equations (`pcorr`, `pd` and

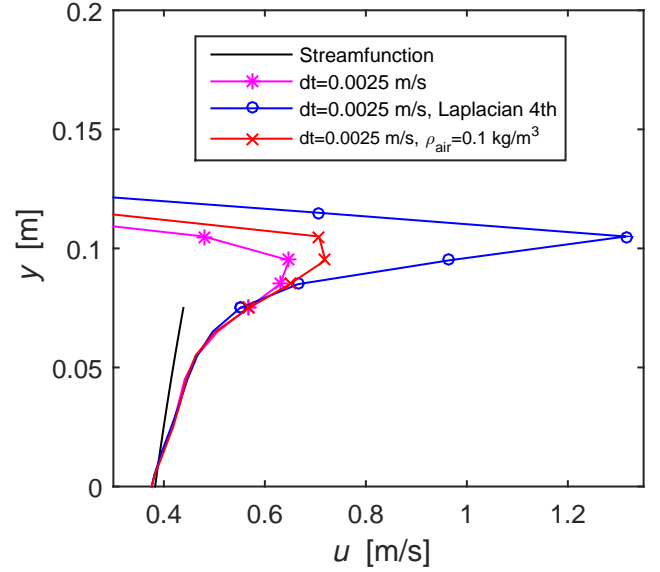


Figure 15: Velocity distribution beneath the crest at $t = 5T$ with a fixed time step utilizing the standard setup as well as 4th order Laplacian and $\rho_{air} = 0.1$ kg/m³. Full lines represent the velocities in pure water and the lines with symbols represent the velocities in the air or mixture cells (Main fixed parameters: $N = 12.5$, `ddt-Euler`, `grad-Gauss Linear`, `div(rho*phi,U)-Gauss LimitedLinearV 1`, $c_\alpha = 1$)

`pdFinal`) switching from PCG to GAMG made the simulations more erratic as the wave broke much earlier (however the simulation time was much lower), whereas switching to a smooth solver (`smoothSolver`) did not affect the quality of the solution, but took much longer time. It was also attempted to lower the tolerance by a factor 1000 on both the pressure and the velocity, but hardly any difference in the solution was seen. For the controls of the solution algorithm increasing the number of alpha correctors, `nAlphaCorr`, as well as alpha subcycles, `nAlphaSubCycles`, improved, though not dramatically, the propagation of the wave in terms of it maintaining its' shape, whereas increasing the number of correctors, `nCorrectors` did not change anything. Increasing the number of outer correctors, `nOuterCorrectors` (`nOCorr`), effectively making it into the PIMPLE algorithm, surprisingly made the wave height decrease very rapidly. This behaviour was also seen in Weber (2016) and will be investigated further in the forthcoming section.

The choice of iterative solvers could also potentially effect the velocity profile. The GAMG solver produced much higher crest velocities (close to that seen with $Co = 0.5$ in Figure 4). The `SmoothSolver`, which was a lot slower, produced an almost identical velocity profile to the PCG solver (Figure 6, $Co = 0.15$). Lowering the tolerances by a factor 1000 had almost no effect on the surface elevation, and the effect on the velocity profile was also negligible. Changing the number of α subcycles (`nAlphaSubCycles`), α correctors (`nAlphaCorr`) and number of correctors (`nCorrectors`) did not influence the crest velocity in any significant way, and raising the number of α correctors actually worsened the result closer to the bed.

It has now been shown that the discretization schemes and

solution procedures have a potentially large impact in the solution, both in terms of the wave height and velocity profile, as well as the wiggles in the interface and the spurious air velocities. Using more diffusive schemes than the base setup from the `damBreak` tutorial has been shown to limit or remove the growth of the wiggles, limit the overestimation of the crest velocity, and also limit the growth of the wave heights. However, the more diffusive schemes were seen to smear the interface, and could potentially be more inaccurate for other situations.

4.5. Combined schemes

It would be ideal to achieve a setup capable of propagating a wave for 100 periods, while keeping a relatively large time step and at the same time maintaining both its shape and the correct velocities. Changing one single scheme has not achieved that. It was however shown that adding some diffusion in some of the schemes could mitigate both the increase in wave height as well as the increased near-crest velocities.

To test whether a combination of schemes can improve the solution further, the upwind scheme on the convection of momentum, which was actually seen to cause the wave to decay (Figure 13b), will be combined with the slightly less diffusive blended CN scheme (Figure 12c). It is also attempted to increase the artificial compression, by increasing c_α while picking a more diffusive scheme for the gradient, namely `faceMDLimited` which also caused the wave height to decrease. Finally, the outer correctors are increased to two and combined with the blended CN scheme, together with the SFCD scheme for the momentum flux.

The surface elevations for three such combinations are seen in Figure 16b–d. Here it can be seen that by combining the diffusive upwind scheme for the convection of momentum and shifting from the more diffusive Euler scheme to a less diffusive CN scheme (Figure 16b) can maintain the wave height for the entire 100 periods. The same can be done by increasing the compression factor c_α while maintaining a more diffusive gradient scheme (Figure 16c, although in this case the wave heights actually decayed a bit), and also by increasing the number of outer correctors together with the CN scheme (Figure 16d). The latter results in slightly more variations in the wave height, but also utilized a much higher blending value in the CN scheme, which can cause oscillations in the solution and, as previously shown, excite wiggles in the free surface. All three cases show a great improvement compared to the original default case, repeated as Figure 16a to ease comparison. It should also be stated that the balance obtained for the case with the outer correctors is particularly delicate. First it was attempted to run with two outer correctors and a blended CN scheme, while maintaining the `limitedLinearV 1` scheme on the momentum flux. This however caused wiggles in the interface, as also previously described, and therefore the SFCD scheme was chosen to counteract the wiggles. The wiggles were not removed altogether with the SFCD scheme, but their presence was significantly delayed. Further, the best result was obtained with CN, $\psi = 0.625$, but lowering the blending factor to $\psi = 0.6$ made the wave height decrease slightly over the 100 periods,

and raising it to $\psi = 0.65$ made it increase slightly and caused more wiggles.

The resulting velocity profiles beneath the crest at $t = 5T$ for the three cases shown in Figure 16b–d are shown in Figure 17, together with the velocity profile obtained utilizing the base settings. Here it is evident that all three combinations give lower

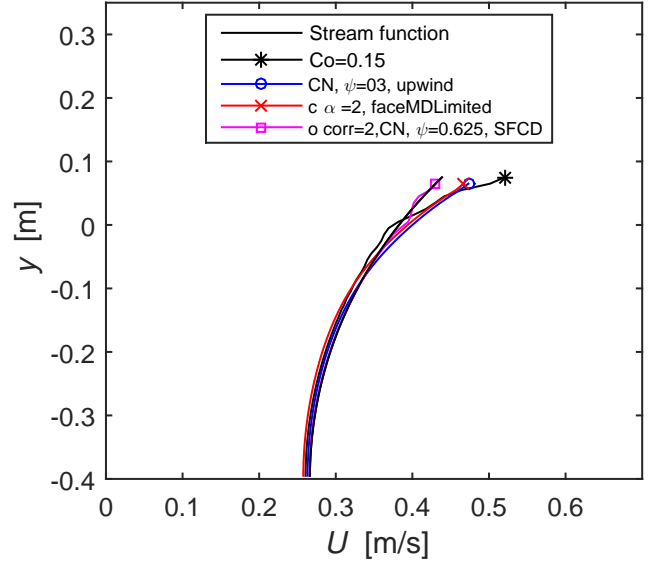


Figure 17: Velocity distribution beneath the crest at $t = 5T$ for various combined schemes (Main fixed parameters: $Co = 0.15$, $N = 12.5$, laplacian-Gauss linear corrected).

velocities in the crest than the standard setting. However the standard setup shows a slightly better comparison with the analytical result closer to the bottom than the case utilizing upwind for the momentum flux together with CN as well as the case utilizing $c_\alpha = 2$ together with the `faceMDLimited` gradient scheme. The final combination, utilizing two outer correctors together with a blended CN scheme and a SFCD scheme shows a significantly better result, and is very similar to the analytical profile. It can be seen that there are small odd oscillations in the profile of this case, and these oscillations actually become larger as the wave propagates. Nevertheless, this significant improvement is achieved with minimal increase in computational expense, especially compared to the results obtained utilizing the settings from the `damBreak` tutorial. The improvement in the velocity profile with the outer correctors is interpreted as the outer correctors ensuring a better coupling between velocity, pressure and the free-surface.

It has now been shown that it is possible to achieve a "diffusive balance" in the schemes, that enables `interFoam` to progress the wave while maintaining its shape. The same diffusive balance is also shown to limit, but (except for the case utilizing outer correctors) not eliminate, the overestimation of the velocity in the crest. This diffusive balance is, however, not universal. What seems a proper amount of diffusion in the case of $Co = 0.15$ is not so with a lower Co where the error in velocity of the crest is much smaller, and more diffusive schemes would actually worsen the solution. Also, what gives the best balance for this wave, might not give the best balance

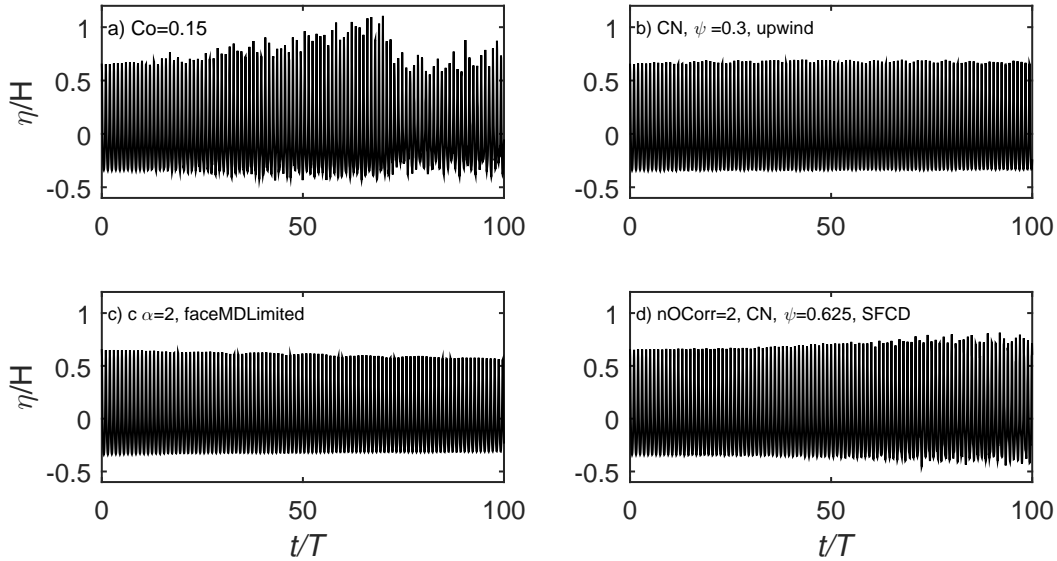


Figure 16: Simulated surface elevation as a function of time for different schemes (Main fixed parameters: $Co = 0.15$, $N = 12.5$, laplacian-Gauss linear corrected).

for a wave with another shape, but the present study reveals a generic strategy that can be fine tuned for individual cases. Interestingly, this implies that for variable depth problems, where waves would not maintain a constant form, there may not be a globally optimal combination. Nevertheless, it is still hoped that better-than-default accuracy can be achieved with the combinations suggested herein.

4.6. Summary of experience using *interFoam*

To summarize our experience using *interFoam* from this section: The safest way to get a good and stable solution is by using a small Courant number. If the time step is low enough, *interFoam* is capable of producing quite good results. However, due to limited time or computational resources, this solution may often not be realistic in practice.

If wishing to use larger time steps, alternatively, it is advised to try to obtain a diffusive balance. The best choice can then be determined on a case by case basis, though it is hoped that the examples utilized above may be a good starting point for more general situations. If looking to simulate e.g. wave breaking, the incoming waves could first be simulated in a cyclic domain, as done herein, prior to doing the actual larger-scale simulation. In this smaller simulation, the proper balance between, diffusivity, time step, computational expense and solution accuracy could be determined, before doing more advanced simulations. This should help ensure that reasonable accuracy in the initial propagation is maintained, which is important as this will affect the initial breaking point and hence the subsequent surf zone processes.

The present results have focused on a rather demanding task of simulating long-time CFD wave propagation over 100 periods, though the problem with the overestimation of crest velocities show up much earlier (see again Figure 4). To underline that *interFoam* is capable of producing a good result for most practical applications involving shorter propagation horizons,

without having to resort to a diffusive balance strategy, Figure 18 shows the surface elevations for the first five periods, as well as the velocity profile beneath the crest at $t = 5T$ using a small $Co = 0.05$. Here a good match with the analytical stream function solution is achieved. A similar improvement in the prediction of the crest velocities, with reduction of Courant number, were shown in Roenby et al. (2017b), and this thus seems to be a robust and generally viable strategy.

5. *interFoam* coupled with *isoAdvector*: *interFlow*

One of the problems with *interFoam* is that the surface gets smeared over several cells, as demonstrated in Section 4.4. This is mitigated by the artificial compression term, which makes the surface sharper, but (as shown herein, Figure 11) also produces some undesired effects. In this section we will finally test the results using *interFoam* coupled with the *isoAdvector* algorithm, recently developed by Roenby et al. (2016), which is also available in the newest version of OpenFOAM (OpenFOAM-v1706). The *isoAdvector* version in OpenFOAM-v1706 has a slightly different implementation of the outer correctors than the version used in the present study, see Roenby et al. (2017a) for details. With *isoAdvector* the equation for α (6) is not solved directly. Instead the surface is identified by an iso-line, similar to those shown for $\alpha = 0.99$ and $\alpha = 0.01$ in Figure 11. After identifying the exact position of the surface, it is then advected in a geometric manner. For more details on the implementation of *isoAdvector* the reader is referred to Roenby et al. (2016).

The new *isoAdvector* algorithm, coupled with *interFoam* will for the remainder of this study be named *interFlow*. As a first case, *interFlow* and *interFoam* will be compared for the previously well-tested case with the *damBreak* settings and $Co = 0.15$. It should be stated however, that *interFlow* was not able to propagate the wave with the settings used in

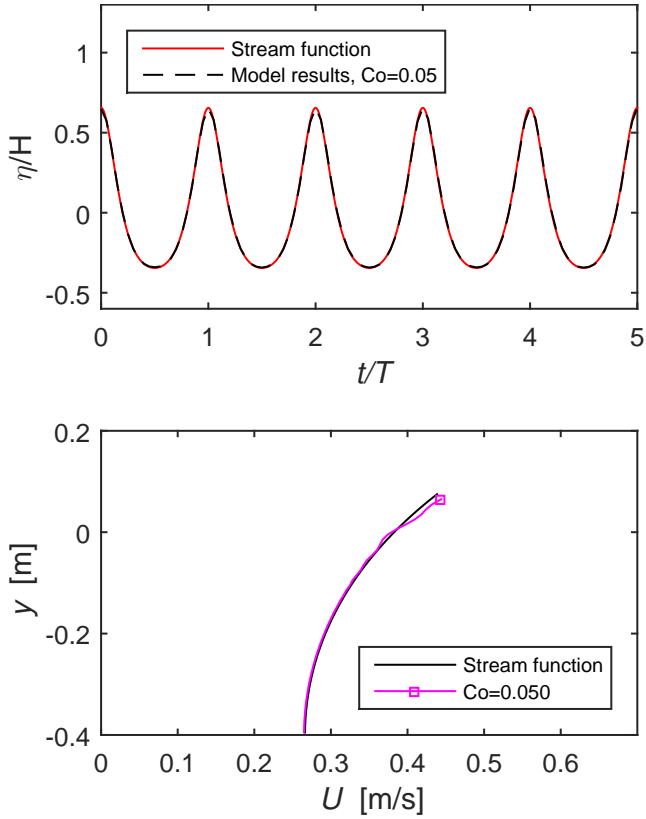


Figure 18: Surface elevations and velocity distribution beneath the crest at $t = 5T$ for $Co = 0.05$ (Main fixed parameters: $N = 12.5$, ddt-Euler, grad-Gauss Linear, div($\rho \cdot \phi, U$)-Gauss LimitedLinearV 1, laplacian-Gauss linear corrected, $c_\alpha = 1$).

interFoam. The tolerances on p^* (pd) needed to be reduced by a factor 100 and the tolerances on U (U) by a factor 10. Comparing the performance of the two is, however, still justified as interFlow actually, even with the decreased tolerances, performed the simulation slightly faster than interFoam. Moreover, the simulations with interFoam did not improve when lowering the tolerances with a factor 1000 as shown in Section 4.4. The speed-up in computational time was not due to larger time steps, but rather to the algorithm moving the free surface faster.

Figure 19 shows the surface elevations obtained utilizing the two different solvers. It is quite noticeable that, while with interFoam the wave heights start to increase, with interFlow the wave heights decrease mildly. Also shown are the contours for $\alpha = 0.99$ and $\alpha = 0.01$ for the crest and trough for each period. Here it can be seen that the two contours are substantially closer with interFlow. They are constantly separated by less than two cell heights meaning that there is actually only one interface cell in the vertical direction. This is a substantial improvement of the surface representation compared to interFoam. Since equation (7) is not solved, there is no artificial compression term, and the interface wiggles previously observed are gone altogether. This is likewise a desirable improvement. The artificial compression term has been shown to

have undesired effects, as it cause wiggles in the interface, in the simple propagation of a stream-function wave over sufficiently long propagation times. How these wiggles might behave in more complex situation like e.g. wave breaking is an open question, but one can imagine a greater effect in such a more chaotic situation.

In Figure 20 the velocity profile beneath the crest at $t = 5T$ is shown utilizing both interFoam and interFlow. Here it is quite clear that interFlow, with the current settings is not improving the velocity profile. The crest velocity is slightly larger than the interFoam solution, and closer to the bed, the velocity is underestimated. This underestimation of velocity is probably due to the decrease in wave height. That interFlow

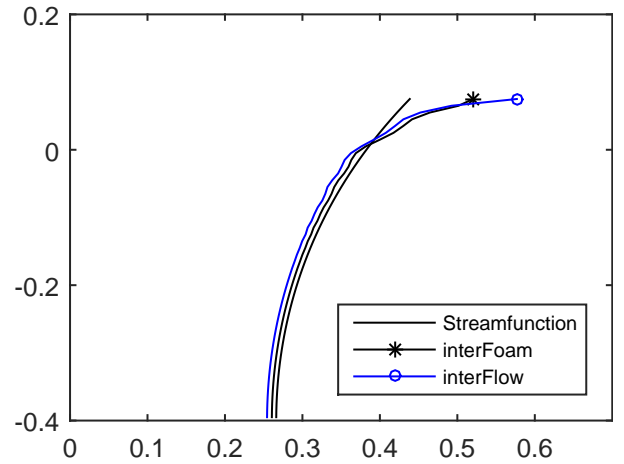


Figure 20: Velocity distribution beneath the crest at $t = 5T$ utilizing interFoam and interFlow (Main fixed parameters: $Co = 0.15$, $N = 12.5$, ddt-Euler, grad-Gauss Linear, div($\rho \cdot \phi, U$)-Gauss LimitedLinearV 1, laplacian-Gauss linear corrected).

gets an even larger error in the velocity in the top of the crest is probably due to the sharper interface, creating larger gradients, and any imbalance in the momentum equation near the interface may then be increased.

As shown with interFoam, interFlow is also sensitive to the setup, and the same diffusive balance that could be achieved with interFoam can also be achieved with interFlow. In Figure 21 the simulated surface elevations utilizing interFoam and interFlow respectively are once again compared, this time utilizing schemes to achieve a diffusive balance. It can be seen that interFlow, like interFoam, is capable of propagating the stream function wave for 100 periods, and that interFlow throughout the simulation keeps a sharper interface as the $\alpha = 0.01$ and $\alpha = 0.99$ contours are much closer. It can also be seen that interFlow does not have the same erratic surface elevation when utilizing two outer correctors together with a blended CN scheme, which can be explained by interFlow not having an artificial compression term, and therefore the CN scheme does not excite any erratic behaviour near the free surface. However like interFoam, interFlow is also very sensitive to the exact value of the blended CN scheme, and lowering the blending factor, i.e. going more towards the Euler scheme made the wave heights decay, and raising it towards more pure

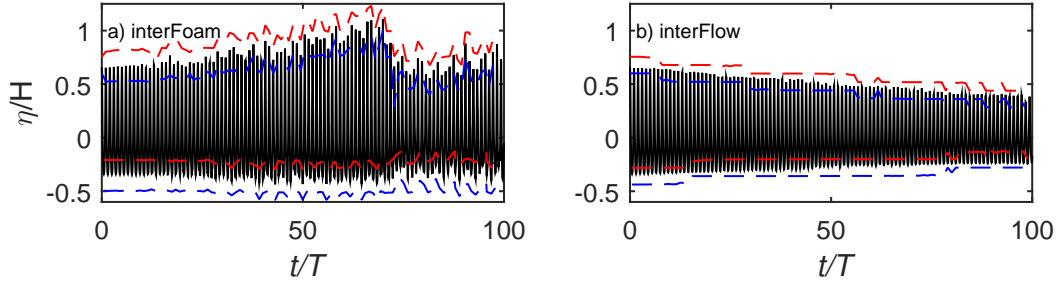


Figure 19: Simulated surface elevations (-) as a function of time utilizing interFoam and interFlow together with the $\alpha = 0.99$ and $\alpha = 0.01$ (- -) contours (Main fixed parameters: $Co = 0.15$, $N = 12.5$, ddt-Euler, grad-Gauss Linear, div(rho*phi,U)-Gauss LimitedLinearV 1, laplacian-Gauss linear corrected).

CN made the wave heights increase.

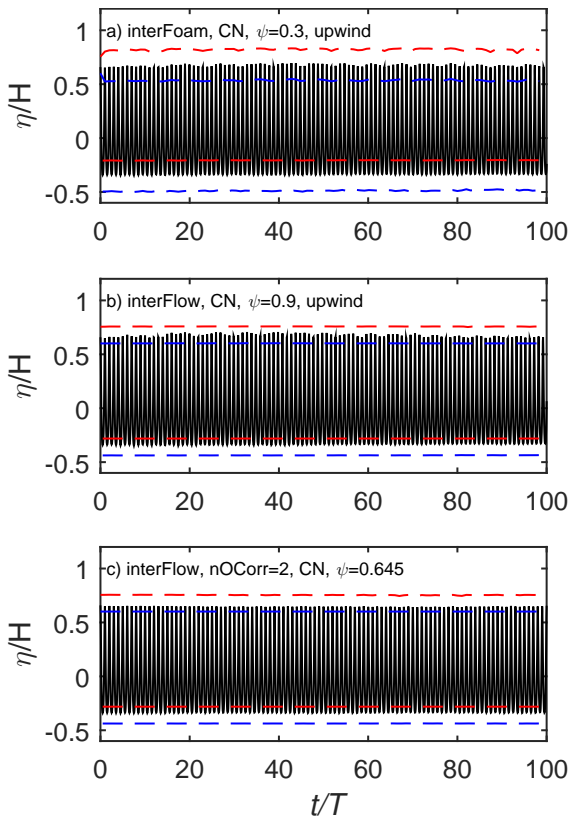


Figure 21: Simulated surface elevations (-) as a function of time utilizing interFoam and interFlow together with the $\alpha = 0.99$ and $\alpha = 0.01$ (- -) contours (Main fixed parameters: $Co = 0.15$, $N = 12.5$, grad-Gauss Linear, laplacian-Gauss linear corrected).

The resulting velocity profiles are shown in Figure 22. Here it can be seen that the two solvers perform quite similarly when utilizing an upwind scheme together with a blended CN scheme, and that the overestimation of the velocity near the crest is reduced. Furthermore, it can be seen that interFlow also shows a significantly improved velocity profile when switching to two outer correctors, together with a blended CN scheme and that interFlow does not suffer, to the same degree, from oscillations in the velocity profile as did interFoam.

To further underline the impressive performance of

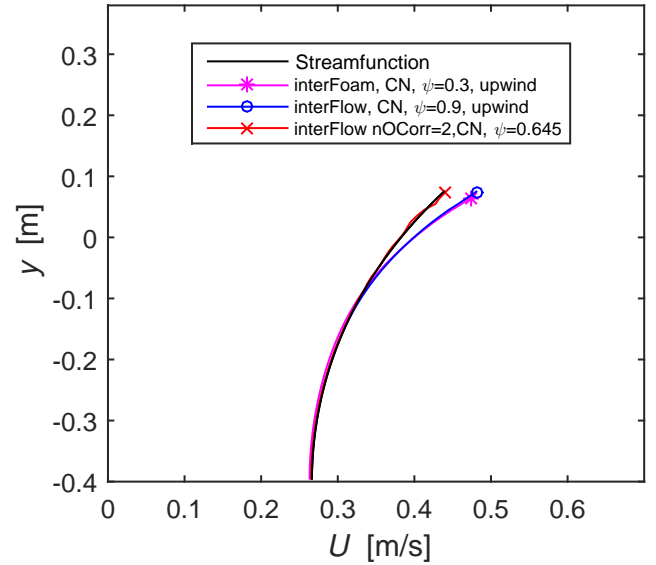


Figure 22: Velocity distribution beneath the crest at $t = 5T$ utilizing an upwind scheme for the convection for interFoam with CN($\psi=0.3$) as well as interFlow with CN($\psi=0.9$) and two outer correctors with CN($\psi=0.645$) (Main fixed parameters: $Co = 0.15$, $N = 12.5$, grad-Gauss Linear, laplacian-Gauss linear corrected).

interFlow when utilizing a balanced setup, Figure 23 shows the surface elevation from the 95th to the 100th period together with the velocity profile beneath the crest at $t = 100T$. Here it can be seen that even after propagating the nonlinear wave for 100 periods interFlow still follows the analytical stream function solution. The surface elevations are of the right magnitude, and there are no significant phase differences. Furthermore, it can be seen that the velocity profile is likewise quite close to the analytical result, though it suffers from minor oscillations.

6. Conclusions

In this study the performance of interFoam (a widely used solver in OpenFOAM in the simulation of progressive regular gravity waves (having intermediate depth and moderate nonlinearity) has been systematically documented. It has been shown that utilizing the basic settings of the popular interFoam tutorial damBreak will yield quite poor results, resulting in increasing wave heights, a wiggled interface, spurious air velocities,

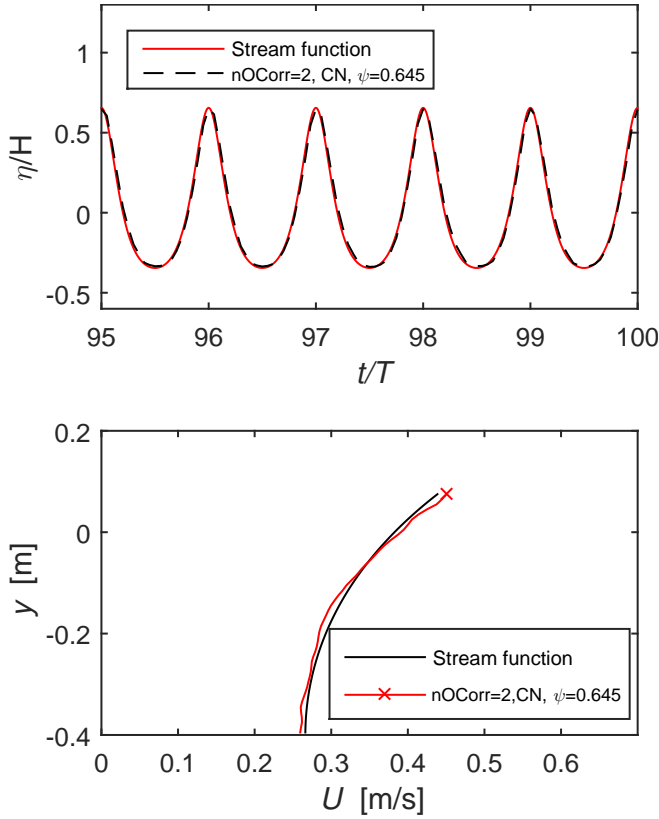


Figure 23: Surface elevations and velocity distribution beneath the crest after 100 periods utilizing *interFlow*.

and severely overestimated velocities near the crest. These four problems can be reduced substantially by lowering the time step and increasing the spatial resolution. It has been shown that a rather small time step, corresponding to a Courant number $Co \approx 0.05$ is needed to give a good solution when propagating a wave even short distances of around five wave lengths.

To test whether an improved solution could be achieved without (drastically) lowering the time step and increasing the spatial resolution, a set of simulation have been performed, where the discretization schemes and iterative solution procedures were changed one at a time. By gradually increasing and lowering the artificial compression term (c_α), it was identified as root of the interface wiggles, which was exacerbated when increasing the c_α and damped or completely removed when lowering c_α . It was also shown how changing from first-order forward Euler time discretization scheme to the (almost) second order, and less diffusive, blended Crank-Nicolson scheme caused the wiggles to appear earlier and cover a larger part of the interface. The convection schemes was shown to affect not only the interface wiggles, but also the development of the wave heights as well as the velocities beneath the crest. More diffusive convection schemes removed the interface wiggles and delayed the increase in wave heights or in fact, when using an upwind scheme, caused the wave heights to decrease. Furthermore, the more diffusive schemes also reduced the overestimation of the crest velocities. In general the effect of the gradient schemes was not as large as the convection

schemes, but the fourth scheme improved the solution, and the *faceMDLimited* scheme behaved very similar to the upwind convection scheme. Finally changing the *snGrad* scheme in the Laplacian created large spurious velocities in the air phase directly above the wave. These high velocities however did not seem to influence the wave kinematics. This was further backed by simulations done with a fixed time step, which clearly indicated that the spurious air velocities, while being an unwanted and un-physical phenomenon, do not have a large impact on the wave kinematics. By combining more or less diffusive schemes it was shown that a "diffusive balance" could be reached, where it was possible to propagate the wave a full 100 wave lengths while maintaining its shape. One of these balanced settings also showed a significant improvement in the velocity profile beneath the crest.

The new open source solver *interFlow* was subsequently applied, and it was shown that *interFlow* was capable of propagating the wave for 100 periods. The wave decreased slightly in time, but the interface was a lot sharper, and the wiggles in surface disappeared. Regarding the velocity profile *interFlow* performed slightly worse than *interFoam* with the base settings. Finally it was shown that *interFlow* could achieve the same kind of diffusive balance which enabled the solver to propagate the wave for 100 periods while maintaining its shape and also maintaining a good match with the analytical velocity profile.

Given its rapidly growing popularity among scientists and engineers, it is hoped that the present systematic study will raise awareness and enable users to more properly simulate a wide variety of problems involving the general propagation of surface waves within the open-source CFD package *OpenFOAM*. While the present study has focused on the canonical situation involving progressive non-breaking waves, the experience presented herein is expected to be widely relevant to other, more general, problems e.g. involving wave-structure interactions, propagation to breaking and resulting surf zone dynamics, as well as boundary layer and sediment transport processes that result beneath surface waves, all of which fundamentally rely on an accurate description of surface waves and their underlying velocity kinematics.

7. Acknowledgements

The first two authors acknowledge support from the European Union project *ASTARTE-Assessment, Strategy And Risk Reduction for Tsunamis in Europe*, Grant no. 603839 (FP7-ENV-2013.6.4-3). The third author additionally acknowledges: *Sapere Aude: DFF-Research Talent* grant from The Danish Council for Independent Research — Technology and Production Sciences (Grant-ID: DFF - 1337-00118). The third author also enjoys partial funding through the *GTS* grant to DHI from the Danish Agency for Science, Technology and Innovation. We would like to express our sincere gratitude for this support.

References

- Afshar, M. A., 2010. Numerical Wave Generation in OpenFOAM. MSc Thesis, Chalmers University of Technology Gotheburg, Sweden.
- Brown, S. A., Greaves, D. M., Magar, V., Conley, D. C., 2016. Evaluation of turbulence closure models under spilling and plunging breakers in the surf zone. *Coast. Eng.* 114, 177–193.
- Chen, L. F., Zang, J., Hillis, A. J., Morgan, G. C. J., Plummer, A. R., 2014. Numerical investigation of wave-structure interaction using OpenFOAM. *Ocean Eng.* 88, 91–109.
- Deshpande, S. S., Anumolu, L., Trujillo, M. F., 2012. Evaluating the performance of the two-phase flow solver interFoam. *Comput. Sci. Discov.* 5 (1), article no. 014016.
- Francois, M. M., Cummins, S. J., Dendy, E. D., Kothe, D. B., Sicilian, J. M., Williams, M. W., 2006. A balanced-force algorithm for continuous and sharp interfacial surface tension models within a volume tracking framework. *J. Comp. Phys.* 213 (1), 141–173.
- Galusinski, C., Vigneaux, P., 2008. On stability condition for bifluid flows with surface tension: Application to microfluidics. *J. Comp. Phys.* 227 (12), 6140–6164.
- Greenshields, C. J., 2015. OpenFOAM, The Open Source CFD Toolbox, Programmer's Guide. Version 3.0.1. OpenFOAM Foundation Ltd.
- Greenshields, C. J., 2016. OpenFOAM, The Open Source CFD Toolbox, User's Guide. Version 4.0. OpenFOAM Foundation Ltd.
- Higuera, P., Lara, J. L., Losada, I. J., 2013. Simulating coastal engineering processes with OpenFOAM (R). *Coast. Eng.* 71, 119–134.
- Hu, Z. Z., Greaves, D., Raby, A., 2016. Numerical wave tank study of extreme waves and wave-structure interaction using OpenFoam (R). *Ocean Eng.* 126, 329–342.
- Hysing, S., 2006. A new implicit surface tension implementation for interfacial flows. *Int.l J. Numer. Meth. Fluids* 51 (6), 659–672.
- Jacobsen, N. G., Fredsøe, J., Jensen, J. H., 2014. Formation and development of a breaker bar under regular waves. Part 1: Model description and hydrodynamics. *Coast. Eng.* 88, 182–193.
- Jacobsen, N. G., Fuhrman, D. R., Fredsøe, J., 2012. A wave generation toolbox for the open-source CFD library: OpenFOAM (R). *Int. J. Numer. Meth. Fluids* 70, 1073–1088.
- Jacobsen, N. G., van Gent, M. R. A., Wolters, G., 2015. Numerical analysis of the interaction of irregular waves with two dimensional permeable coastal structures. *Coast. Eng.* 102, 13–29.
- Liu, Y., Hinrichsen, O., 2014. CFD modeling of bubbling fluidized beds using OpenFOAM (R) : Model validation and comparison of TVD differencing schemes. *Computers and Chem. Eng.* 69, 75–88.
- Lupieri, G., Contento, G., 2015. Numerical simulations of 2-d steady and unsteady breaking waves. *Ocean Eng.* 106, 298–316.
- Meier, M., Yadigaroglu, G., Smith, B. L., 2002. A novel technique for including surface tension in plic-vof methods. *European J. Mech. B-fluids* 21 (1), 61–73.
- Menard, T., Tanguy, S., Berlemont, A., 2007. Coupling level set/VOF/ghost fluid methods: Validation and application to 3D simulation of the primary break-up of a liquid jet. *Int. J. Multiphase Flow* 33 (5), 510–524.
- Paulsen, B. T., Bredmose, H., Bingham, H. B., Jacobsen, N. G., 2014. Forcing of a bottom-mounted circular cylinder by steep regular water waves at finite depth. *J. Fluid Mech.* 755, 1–34.
- Popinet, S., Zaleski, S., 1999. A front-tracking algorithm for accurate representation of surface tension. *Int. J. Numer. Meth. in Fluids* 30 (6), 775–793.
- Rienecker, M., Fenton, J., 1981. A fourier approximation method for steady water-waves. *J. Fluid Mech.* 104 (MAR), 119–137.
- Roenby, J., Bredmose, H., Jasak, H., 2016. A computational method for sharp interface advection. *Royal Society Open Science* 3 (11), 160405.
- Roenby, J., Bredmose, H., Jasak, H., 2017a. Isoadvector: Geometric VOF on general meshes. In: 11th OpenFOAM Workshop. 11th OpenFOAM Workshop. Springer Nature. Status: Accepted.
- Roenby, J., Larsen, B. E., Bredmose, H., Jasak, H., 2017b. A new volume-of-fluid method in OpenFOAM. In: 7th Int. Conf. Comput. Methods Marine Eng. 7th Int. Conf. Comput. Methods Marine Eng. Nantes, France, pp. 1–12.
- Rudman, M., 1997. Volume-tracking methods for interfacial flow calculations. *Int.l J. Numer. Meth. Fluids* 24 (7), 671–691.
- Schmitt, P., Elsaesser, B., 2015. On the use of OpenFOAM to model oscillating wave surge converters. *Ocean Eng.* 108, 98–104.
- Shirani, E., Ashgriz, N., Mostaghimi, J., 2005. Interface pressure calculation based on conservation of momentum for front capturing methods. *J. Comp. Phys.* 203 (1), 154–175.
- Tanguy, S., Menard, T., Berlemont, A., 2007. A level set method for vaporizing two-phase flows. *J. Comp. Phys.* 221 (2), 837–853.
- Ting, F. C. K., Kirby, J. T., 1994. Observation of undertow and turbulence in a laboratory surf zone. *Coast. Eng.* 24 (1-2), 51–80.
- Tomaselli, P., 2016. Detailed analyses of breaking wave dynamics interaction with nearshore and offshore structures. Ph.D. thesis, . Technical University of Denmark., Kgs. Lyngby, Denmark.
- Vukcevic, V., 2016. Numerical modelling of coupled potential and viscous flow for marine applications. Ph.D. thesis, University of Zagreb, Zagreb, Croatia.
- Vukcevic, V., Jasak, H., Malenica, S., 2016. Decomposition model for naval hydrodynamic applications, part i: Computational method. *Ocean Eng.* 121, 37–46.
- Weber, J., 2016. Numerical Investigation on the Damping of Water Waves in a Towing Tank. BSc. Thesis.Thechnical University of Berlin, Berlin, Germany. .
- Wemmenhove, R., Luppens, R., Veldman, A. E. P., Bunnik, T., 2015. Numerical simulation of hydrodynamic wave loading by a compressible two-phase flow method. *Computers and Fluids* 114, 218–231.
- Wroniszewski, P. A., Verschaeve, J. C. G., Pedersen, G. K., 2014. Benchmarking of navier-stokes codes for free surface simulations by means of a solitary wave. *Coast. Eng.* 91, 1–17.

Chapter 5

On the over-production of turbulence beneath surface waves in RANS models

This Chapter is a revised version under review for publication as:

Larsen, B. E., Fuhrman, D. R. (2018). *On the over-production of turbulence beneath surface waves in RANS models*. Journal of Fluid Mechanics (In review)

On the over-production of turbulence beneath surface waves in RANS models

Bjarke Eltard Larsen¹†, and David R. Fuhrman¹

¹Technical University of Denmark, Department of Mechanical Engineering, Section of Fluid Mechanics, Coastal and Maritime Engineering, DK-2800 Kgs. Lyngby, Denmark

(Received 18-12-2017; revised 28-03-2018; accepted xx)

In previous computational fluid dynamics studies of breaking waves, there has been a marked tendency to severely overestimate turbulence levels, both pre- and post-breaking. This problem is most likely related to the previously described (though not sufficiently well recognized) conditional instability of widely-used turbulence models when used to close Reynolds-Averaged Navier-Stokes (RANS) equations in regions of nearly potential flow with finite strain, resulting in exponential growth of the turbulent kinetic energy and eddy viscosity. While this problem has been known for nearly 20 years, a suitable and fundamentally sound solution has yet to be developed. In this work it is demonstrated that virtually all commonly-used two-equation turbulence closure models are unconditionally, rather than conditionally, unstable in such regions. A new formulation of the k - ω closure is developed which elegantly stabilizes the model in nearly-potential flow regions, with the modifications remaining passive in sheared flow regions, thus solving this long-standing problem. Computed results involving non-breaking waves demonstrate that the new stabilized closure enables nearly constant-form wave propagation over long durations, avoiding the exponential growth of the eddy viscosity and inevitable wave decay exhibited by standard closures. Additional applications on breaking waves demonstrate that the new stabilized model avoids the unphysical generation of pre-breaking turbulence which widely plagues existing closures. The new model is demonstrated to be capable of predicting accurate pre- and post-breaking surface elevations, as well as turbulence and undertow velocity profiles, especially during transition from pre-breaking to the outer surf zone. Results in the inner surf zone are similar to standard closures. Similar methods for formally stabilizing other widely-used closure models (k - ω and k - ϵ variants) are likewise developed, and it is recommended that these be utilized in future RANS simulations of surface waves.

1. Introduction

Among the most ubiquitous phenomena seen in natural aquatic environments, coastal or otherwise, are free surface waves. Such waves give rise to a highly diverse range of complexity in terms of their fluid mechanics, with the bulk region beneath non-breaking waves corresponding to nearly-potential flow, bordered by a thin (usually turbulent) boundary layer at the bottom, and often a highly complicated multi-phase (air and water) turbulent surf zone further shoreward. With the growth of computer power, computational fluid dynamics (CFD) is increasingly being used to study various free-surface wave processes, though the range of complexity mentioned above can complicate applications with a single model. Problems involving the computational study of surface waves commonly include their simple propagation (e.g. Paulsen *et al.* 2014; Devolder

† Email address for correspondence: bjelt@mek.dtu.dk

et al. 2017), their interaction with structures (e.g. Higuera *et al.* 2013; Chen *et al.* 2014; Paulsen *et al.* 2014; Jacobsen *et al.* 2015; Schmitt & Elsaesser 2015; Hu *et al.* 2016), or the highly complex of phenomena of breaking waves and surf zone dynamics.

Some of the earliest studies involving the computational study of breaking waves include Sakai *et al.* (1986), who used the marker-and-cell (MAC) method developed by Harlow & Welch (1965), and Lemos (1992), who was among the first to apply the volume of fluid method (VOF), originally developed by Hirt & Nichols (1981). Perhaps the most modelled experiments are the spilling and plunging breaking cases of Ting & Kirby (1994, 1996). These have been widely used as validation for large eddy simulation (LES) models (e.g. Watanabe & Saeki 1999; Hieu *et al.* 2004; Christensen 2006), smooth particle hydrodynamics (SPH) models (e.g. Shao 2006; Makris *et al.* 2016), as well as those based on Reynolds-averaged Navier-Stokes (RANS) equations coupled with various two-equation turbulence closure models, the focus of the present study. Such studies include those utilizing closures within both the $k-\epsilon$ (e.g. Lin & Liu 1998; Bradford 2000; Xie 2013; Hsu *et al.* 2015; Brown *et al.* 2016) and $k-\omega$ (e.g. Mayer & Madsen 2000; Jacobsen *et al.* 2012, 2014; Brown *et al.* 2016) families.

In the RANS model studies of breaking waves mentioned above, there has been a marked and collective tendency to predict turbulence levels that are much higher than have been measured. Such over-predicted turbulence is often even most apparent prior to breaking, where (in contrast to experimental findings and intuition) computed turbulent kinetic energy levels can be the same order of magnitude as within the surf zone (see e.g. Lin & Liu 1998; Bradford 2000; Hsu *et al.* 2015; Brown *et al.* 2016). These effects can potentially cause pre-mature wave decay, and such discrepancies can carry over well into the outer surf zone, thus affecting the computed sub-surface kinematics and subsequent surf zone dynamics as a whole. The widespread over-production of turbulence in RANS modelling of surface waves, especially prior to breaking, represents a significant and fundamental problem to their computational study. It implies that such commonly-used CFD models cannot even manage the relatively simple task of long-term wave propagation without un-physical dissipation, which should seemingly be a pre-requisite to their application on more complicated surf zone processes. Moreover, it implies that in many computational studies of the surf zone, the results have most likely been polluted even prior to the onset of the breaking process, which has usually been the very focus of study.

The underlying cause of this problem seems to not be sufficiently well recognized. For example, following long time simulations, Hsu *et al.* (2002) found unrealistically high turbulence in the what they characterized as supposed low turbulence regions, hence being among the first to recognize this problem. They suspected that this was “due to the convection and diffusion mechanism, which transports the turbulence from the high turbulence region (e.g., the surf zone) to the low turbulence region”. To combat this they included a damping mechanism on the eddy viscosity, which effectively reduced the turbulence to acceptable levels. Bradford (2011) used a $k-l$ model and somewhat similarly found that limiting the mixing length to be less than or equal to the local flow depth maintained model stability. In a study of breaking waves using several different two-equation closures Brown *et al.* (2016) found that nearly all of their simulations of spilling breakers resulted in significantly over-produced turbulence prior to breaking. While they did not offer any explanation as to the underlying cause, they did recognize the detrimental effect on the local undertow profiles through comparison with results where no closure was utilized. Devolder *et al.* (2017) also recognized the problem of over-predicted turbulence levels beneath computed surface waves (and the related unphysical decay in the wave heights), and attributed this to turbulence from the air penetrating

into the water. To combat this they included a buoyancy production term directly in the k -equation. While this term should likely be included in two-phase models, and it limited the excessive production of turbulence to some degree, it does not solve the fundamental problem; This can clearly be seen from their figure 7, where the computed eddy viscosity is still many orders of magnitude larger than the kinematic fluid viscosity.

Rather, the more likely explanation for the widespread over-prediction of turbulence in RANS models of surface waves was provided prior to the studies mentioned just above by Mayer & Madsen (2000). They specifically showed through analysis that the standard k - ω model of Wilcox (1988) can become unstable when applied to a region of potential flow beneath surface waves, leading to exponential growth of both the turbulent kinetic energy and eddy viscosity. Although they did not specifically analyze the k - ϵ model, they stated that it too suffers from similar issues. Mayer & Madsen (2000) also made an ad-hoc attempt to solve the problem by using the mean rotation, rather than the strain rate, in their production terms. This, indeed, greatly reduced the growth of the eddy viscosity and hence improved predictions of the wave breaking point relative to their unmodified model. However, (as will be discussed herein) there are several fundamental deficiencies with this ad-hoc modification, and it has not been widely adopted (seemingly only by Jacobsen *et al.* 2012, 2014); Indeed, Mayer & Madsen (2000) did not recommend this change as a final solution, but instead suggested further research into the problem.

Motivated largely by their suggestion, and especially by a desire to ultimately solve this long-standing problem in a more fundamentally satisfying and definitive way, the present work will re-visit the two-equation closure instability problem identified by Mayer & Madsen (2000), who strictly proved conditional instability of the k - ω closure model. Their analysis will be briefly reviewed and extended to prove that this model is, in fact, unconditionally unstable for the conditions they considered, with a predictable asymptotic exponential growth rate when applied to a region of nearly-potential flow having finite strain. Building directly on the analysis, we will likewise demonstrate how such models can be simply and elegantly stabilized, in a manner that will importantly remain passive in other sheared regions of interest. The significant advantages to utilizing the new stabilized closure model will be demonstrated directly through examples involving simulations of non-breaking and breaking waves.

The present paper is organized as follows: Stability analysis of several RANS turbulence closure models will be performed in Section 2, including a review of the work of Mayer & Madsen (2000). The analysis in the main text will focus on k - ω closure models, including the standard model of Wilcox (1988), the ad-hoc modification of Mayer & Madsen (2000), as well as the more recent version presented by Wilcox (2006). Building further from the analysis, this will subsequently lead to development of a new and formally stable k - ω closure model that is otherwise compatible with these earlier versions. The significant advantages of utilizing the stabilized model will be demonstrated in Section 3, for problems involving simple surface wave propagation, as well as the simulation of the spilling breaking wave experiment of Ting & Kirby (1994), where the problem of over-production of turbulence leading up to breaking is known to be especially pronounced.

Similar analysis of several other widely-utilized two-equation turbulence closure models (k - ω SST, standard k - ϵ , and RNG k - ϵ models) is provided in Appendix A for completeness. The analysis therein demonstrates that these models are likewise unconditionally unstable in the same sense as are those considered in the main text. Furthermore, we demonstrate that they too can be formally stabilized with similar, relatively simple, modifications.

2. Stability analysis of RANS turbulence closure models beneath nearly-potential flow waves

2.1. Turbulence closure model

For many problems in fluid mechanics, it is neither practical nor computationally feasible, to resolve all necessary scales for direct numerical simulation (DNS) or even large eddy simulation (LES), both of which inevitably require high resolution of three spatial dimensions. As an alternative, it is often necessary to instead work within the confines of Reynolds-averaged Navier-Stokes (RANS) equations, thereby necessitating a separate closure model for describing the effects of turbulence on the mean flow. As a suitable description of turbulence for the present purposes, we will adopt a generalized version of the widely-used k - ω model, comprised of the following transport equations for the turbulent kinetic energy density $k = 1/2(\overline{u'_i u'_i})$:

$$\frac{\partial \rho k}{\partial t} + u_j \frac{\partial \rho k}{\partial x_j} = \rho P_k - \rho P_b - \rho \beta^* k \omega + \frac{\partial}{\partial x_j} \left[\left(\mu + \rho \sigma^* \frac{k}{\omega} \right) \frac{\partial k}{\partial x_j} \right] \quad (2.1)$$

and the specific dissipation rate ω :

$$\frac{\partial \rho \omega}{\partial t} + u_j \frac{\partial \rho \omega}{\partial x_j} = \rho P_\omega - \rho \beta \omega^2 + \rho \frac{\sigma_d}{\omega} \frac{\partial k}{\partial x_j} \frac{\partial \omega}{\partial x_j} + \frac{\partial}{\partial x_j} \left[\left(\mu + \rho \sigma \frac{k}{\omega} \right) \frac{\partial \omega}{\partial x_j} \right]. \quad (2.2)$$

Here u_i are the mean components of the velocity, x_j are the Cartesian coordinates, $\mu = \rho \nu$ is the dynamic molecular viscosity, ν is the kinematic viscosity, ρ is the density, t is time, and

$$\tau_{ij} = -\overline{u'_i u'_j} = 2\nu_T S_{ij} - \frac{2}{3} k \delta_{ij} \quad (2.3)$$

is the Reynolds stress tensor, expressed in accordance with the Boussinesq approximation. Here the overbar signifies time (ensemble) averaging, a prime superscript denotes turbulent (fluctuating) components, δ_{ij} is the Kronecker delta,

$$S_{ij} = \frac{1}{2} \left(\frac{\partial u_i}{\partial x_j} + \frac{\partial u_j}{\partial x_i} \right) \quad (2.4)$$

is the mean strain rate tensor, and

$$\nu_T = \frac{k}{\tilde{\omega}} \quad (2.5)$$

is the eddy viscosity. The shear production term for k is

$$P_k = \tau_{ij} \frac{\partial u_i}{\partial x_j} = p_0 \nu_T, \quad p_0 = 2S_{ij} S_{ij}. \quad (2.6)$$

Similarly, the buoyancy production for k is formulated as

$$P_b = -\frac{g_i}{\rho} \overline{\rho' u'_i} = p_b \nu_T, \quad p_b = \alpha_b^* N^2, \quad N^2 = \frac{g_i}{\rho} \frac{\partial \rho}{\partial x_i}, \quad (2.7)$$

where $(g_1, g_2, g_3) = (0, 0, -g)$ is gravitational acceleration and N is the the Brunt-Vaisala frequency. The production of ω is likewise taken as

$$P_\omega = \alpha \frac{\omega}{k} \frac{\tilde{\omega}}{\tilde{\omega}} P_k = \alpha \frac{\omega}{\tilde{\omega}} p_0. \quad (2.8)$$

It is emphasized that the basic form of the shear turbulence production term (i.e. $P_k = \tau_{ij} \partial u_i / \partial x_j$) should be considered sacred, as it can be theoretically derived through the Reynolds-averaging process; As the Reynolds stress τ_{ij} appears both here, as well as

in the governing RANS equations, it is imperative that they be kept identical. The production of the specific dissipation rate P_ω , on the other hand, is essentially empirical in nature (based on dimensional analysis, hence necessitating the closure coefficient α on this term). It is hence not theoretically tied to the RANS equations, and may therefore be treated with considerably more freedom.

The equations above can be considered a generalized form of the Wilcox (2006) turbulence closure model. In addition to his basic model, we have specifically added the previously defined buoyancy production term P_b in (2.1) for potential application to two-phase (air-water) flows. A similar term was implemented for the k - ϵ model by e.g. Rodi (1987) and Burchard (2002), for the k - ω model by e.g. Umlauf *et al.* (2003) and Fuhrman *et al.* (2013) as well as for the k - ω SST model by Devolder *et al.* (2017). We have likewise incorporated additional freedom via the introduction of two (rather than the usual one) utility variables $\tilde{\omega}$ and $\tilde{\tilde{\omega}}$ within (2.5) and (2.8). These represent potential stress limited versions of ω , to be determined and taken advantage of in what follows. The generalized form presented above is convenient, as it can be reduced to a number of common variations of the k - ω model in the literature, with suitable selections of $\tilde{\omega}$, $\tilde{\tilde{\omega}}$, and closure coefficients. Throughout the present work (unless noted otherwise) we will adopt the closure coefficients of Wilcox (2006, 2008): $\alpha = 0.52$, $\beta = 0.0708$ (constant for two-dimensional flows), $\beta^* = 0.09$, $\sigma = 0.5$, $\sigma^* = 0.6$, $\sigma_{do} = 0.125$, with

$$\sigma_d = H \left(\frac{\partial k}{\partial x_j} \frac{\partial \omega}{\partial x_j} \right) \sigma_{do}, \quad (2.9)$$

where $H(\cdot)$ is the Heaviside step function, which takes a value of unity if the argument is positive and zero otherwise. Additionally, we adopt the value $\alpha_b^* = 1.36$, which is derived in Appendix B.

2.2. Turbulence production beneath potential flow waves

Let us now briefly review the production of turbulence beneath potential flow progressive waves, as originally described by Mayer & Madsen (2000). Following their work, and for the sake of simplicity, let us consider the velocity fields given by Stokes first-order wave theory, where $z = 0$ is measured from the bed:

$$u = \frac{H\sigma}{2} \frac{\cosh(k_w z)}{\sinh(k_w h)} \cos(k_w x - \sigma t), \quad (2.10)$$

$$w = \frac{H\sigma}{2} \frac{\sinh(k_w z)}{\sinh(k_w h)} \sin(k_w x - \sigma t). \quad (2.11)$$

Here σ is the angular frequency, k_w is the wave number, h is the water depth and H is the wave height. If these velocity fields are inserted into (2.6), after period-averaging, there will be turbulent kinetic energy production corresponding to:

$$\langle p_0 \rangle = \frac{k_w^2 H^2 \sigma^2}{2} \frac{\cosh(2k_w z)}{\sinh^2(k_w h)}. \quad (2.12)$$

Note that after further depth-averaging, this becomes

$$\langle p_0 \rangle = \frac{k_w^2 H^2 \sigma^2}{2k_w h \tanh(k_w h)}. \quad (2.13)$$

Hence, the above demonstrates that there will be a non-zero production of turbulent kinetic energy in a potential flow region beneath surface waves, provided that the eddy viscosity is finite.

2.3. Analysis of the standard Wilcox (1988) k - ω model

Having established that standard methods for achieving turbulence closure will potentially result in finite turbulence production in a region of potential flow, let us now conduct a formal stability analysis of several widely-used closure models. For this purpose, consider a region of nearly-potential flow, such that

$$p_\Omega = 2\Omega_{ij}\Omega_{ij} \ll p_0, \quad \Omega_{ij} = \frac{1}{2} \left(\frac{\partial u_i}{\partial x_j} - \frac{\partial u_j}{\partial x_i} \right) \quad (2.14)$$

in a fluid of constant density (hence $P_b = p_b = 0$), where Ω_{ij} is the mean rotation rate tensor and p_0 is assumed fixed at some finite value. Following Mayer & Madsen (2000), diffusive and convective terms will be neglected in the analysis for the sake of simplicity, which is justifiable in the region above the bottom boundary layer. In this case the governing generalized turbulence model equations (2.1) and (2.2) reduce to

$$\frac{\partial k}{\partial t} = \frac{k}{\tilde{\omega}} p_0 - \beta^* \omega k, \quad (2.15)$$

$$\frac{\partial \omega}{\partial t} = \alpha \frac{\omega}{\tilde{\omega}} p_0 - \beta \omega^2. \quad (2.16)$$

Let us begin by analyzing what will be deemed the standard (Wilcox 1988) k - ω model. This corresponds to setting $\omega = \tilde{\omega} = \tilde{\tilde{\omega}}$ in the above leading to the further reduced equations

$$\frac{\partial k}{\partial t} = \frac{k}{\omega} p_0 - \beta^* \omega k, \quad (2.17)$$

$$\frac{\partial \omega}{\partial t} = \alpha p_0 - \beta \omega^2. \quad (2.18)$$

This corresponds to the same form as considered by Mayer & Madsen (2000). (Note that the closure coefficients in the Wilcox (1988) model are slightly different from those used here, but have no qualitative influence on the analysis.) Mayer & Madsen (2000) proved conditional instability of this model, stating that if at any instant

$$\omega \leq \sqrt{\frac{1 - \alpha}{\beta^* - \beta}} p_0 = 5\sqrt{p_0} \quad (2.19)$$

then the turbulence model will become unstable, resulting in exponential growth of the eddy viscosity.

In what follows, we will extend their analysis, and formally prove that the simplified model, subject to the conditions described above, is in fact unconditionally unstable. Moreover, we will establish a methodology to analytically determine the asymptotic unstable growth rate. From inspection of (2.18), it is seen that this equation is de-coupled from the k equation (2.17). Hence, regardless of its initial value, ω will ultimately evolve to a constant such that $\partial\omega/\partial t = 0$, corresponding in this case to

$$\omega_\infty = \sqrt{\frac{p_0 \alpha}{\beta}} \approx 2.71\sqrt{p_0}. \quad (2.20)$$

As this satisfies the constraint (2.19), this slight extension thus proves that the model is, indeed, unconditionally unstable; This stronger finding has apparently also been arrived at independently by Mayer ca. 2001 (personal communication, October 31, 2017). Moreover, once the specific dissipation rate reaches its asymptotic value $\omega = \omega_\infty$, the k

equation effectively becomes linearised, ultimately leading to equations of the form

$$\frac{1}{k} \frac{\partial k}{\partial t} = \frac{1}{\nu_T} \frac{\partial \nu_T}{\partial t} = \Gamma_\infty, \quad (2.21)$$

having solutions such that $k \sim \nu_T \sim \exp(\Gamma_\infty t)$, where Γ_∞ is the asymptotic unstable growth rate. For the standard k - ω model under consideration this works out to be

$$\Gamma_\infty = (\beta - \alpha\beta^*) \sqrt{\frac{p_0}{\alpha\beta}} \approx 0.125\sqrt{p_0}. \quad (2.22)$$

As an independent check of the analysis above, we have performed several numerical simulations of (2.17) and (2.18). As a demonstration we will consider a case with initial conditions $\omega = \omega_0 = 100\sqrt{p_0}$, such that the turbulence scales are initially well separated from those of the mean flow, and $k = k_0 = 10\nu\sqrt{p_0}$ such that initially $\nu_T/\nu = 0.1$. Figure 1 shows the simulated temporal development of k/k_0 , $\omega/\sqrt{p_0}$ and ν_T/ν . Included in the figure as the dashed lines are the predicted asymptotic exponential growth rates for k and ν_T from the above analysis, as well as the predicted asymptotic value ω_∞ . As can be seen ω quickly tends towards ω_∞ , and once this occurs k and ν_T (which were initially declining) start growing exponentially at precisely the growth rate Γ_∞ predicted above.

2.4. Analysis of the modified Mayer & Madsen (2000) k - ω model

In an effort to combat the un-physical growth of turbulence in their CFD simulation of breaking waves, Mayer & Madsen (2000) made an ad-hoc modification of their production terms (P_k and P_ω , though they did not modify the eddy viscosity outside these terms) such that they were based on the vorticity, rather than the strain rate. They did not formally analyze the resulting turbulence closure model for stability, and this will therefore be investigated here. In the context of our simplified analysis, this ad-hoc modification is equivalent to setting

$$\tilde{\omega} = \tilde{\omega} = \frac{p_0}{p_\Omega} \omega \quad (2.23)$$

whence (2.15) and (2.16) become

$$\frac{\partial k}{\partial t} = \frac{k}{\omega} p_\Omega - \beta^* \omega k, \quad (2.24)$$

$$\frac{\partial \omega}{\partial t} = \alpha p_\Omega - \beta \omega^2. \quad (2.25)$$

These are identical to (2.17) and (2.18), but with p_0 now replaced by p_Ω . Hence, without requiring further analysis, it is evident that in this model ω will tend asymptotically to

$$\omega_\infty = \sqrt{\frac{p_\Omega \alpha}{\beta}} \approx 2.71\sqrt{p_\Omega} \quad (2.26)$$

at which point the unstable growth rate for k and ν_T will be

$$\Gamma_\infty = (\beta - \alpha\beta^*) \sqrt{\frac{p_\Omega}{\alpha\beta}} \approx 0.125\sqrt{p_\Omega}. \quad (2.27)$$

Thus, even with this alteration, since the vorticity would never be exactly zero in a CFD model involving surface waves (due to both numerical error and/or imposed boundary conditions) the resulting model is still formally unconditionally unstable, though the asymptotic growth rate would be significantly reduced compared to the standard k - ω model, since it is assumed that $p_\Omega \ll p_0$.

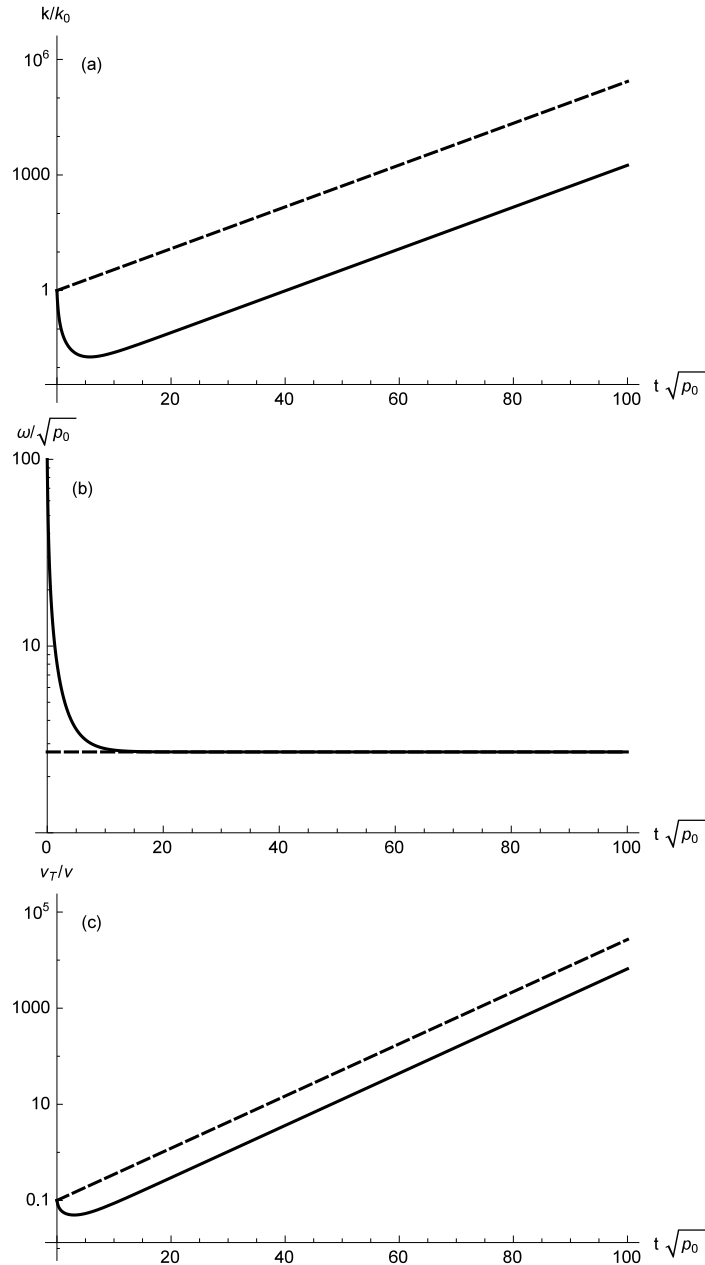


FIGURE 1. Simulated development (full lines) of (a) k/k_0 , (b) $\omega/\sqrt{p_0}$ and (c) ν_T/ν for the Wilcox (1988) closure model. Dashed lines indicate predicted asymptotic exponential growth rates in (a) k and (c) ν_T , as well as (b) the predicted asymptotic value $\omega = \omega_\infty$.

Independent confirmation of the analysis above is provided via numerical solution of the reduced governing equations, maintaining the same initial conditions as before and now with $p_\Omega/p_0 = 0.01$. The resulting evolution of the eddy viscosity is depicted in figure 2(a). Again this first declines, before ultimately growing exponentially at precisely the asymptotic rate predicted above.

The ad-hoc modification used by Mayer & Madsen (2000) represents an interesting first attempt to control the instability that they identified, and which was expanded upon in the preceding sub-section. Nevertheless, it cannot be considered a fundamentally viable solution for several reasons. First, though weaker, the model is still formally unconditionally unstable, as proved above. Second, Mayer & Madsen (2000) effectively utilized different $\tilde{\omega}$ in the production terms and in the eddy viscosity outside of these terms, which is in direct violation of the Boussinesq approximation (2.3); This is equivalent

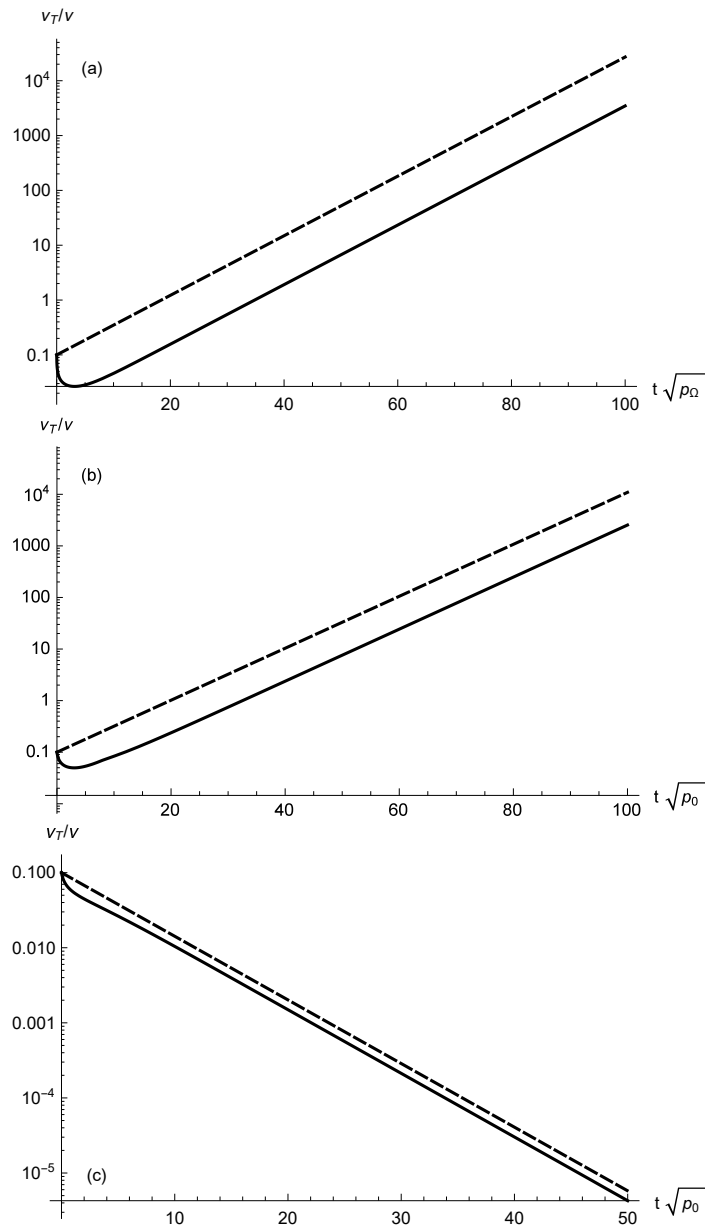


FIGURE 2. Simulated development of ν_T/ν (full lines) compared to the predicted asymptotic exponential growth (dashed lines) for the (a) Mayer & Madsen (2000) k - ω closure, (b) Wilcox (2006) k - ω closure, and (c) present k - ω closure with $\lambda_1 = 0$ and $\lambda_2 = 0.05$.

to simultaneously utilizing two different definitions of the Reynolds stress tensor τ_{ij} . Third, it is again emphasized that the turbulence production term is theoretical in nature (derived directly from Reynolds averaging), and hence rightly ought to be based on the strain rate rather than the vorticity, at least if the standard Boussinesq approximation is utilized. While in simple uniform boundary layer flows these may be equal, in more complex flows they can be quite different. (For example, in the forthcoming simulation of spilling breaking waves we have found that they can differ by a factor of 1–10 in most of the surf zone.) Hence, in the context of surface waves this modification must be considered intrusive, resulting in a significantly altered turbulence production term that is applied globally i.e. even in sheared flow regions of primary interest (e.g. the surf zone), where the original model should be maintained. This is evidenced directly by the work of Jacobsen, Fuhrman & Fredsøe (2012), who utilized the modified production terms of Mayer & Madsen (2000) to simulate spilling breaking waves, and found that it was necessary to alter one of the fundamental closure coefficients in isolation (from

$\alpha = 0.52$ to 0.4) to obtain reasonable undertow profiles. This is likewise problematic, since as shown e.g. in Wilcox (2006), the closure coefficients are carefully tuned, and are, among other things, related to the von Karman constant κ according to

$$\alpha = \frac{\beta}{\beta^*} - \sigma \frac{\kappa^2}{\sqrt{\beta^*}}. \quad (2.28)$$

Hence, the alteration just mentioned corresponds to a model yielding $\kappa \approx 0.482$ rather than the accepted $\kappa \approx 0.4$, and will therefore be inaccurate for simple steady uniform boundary layer flows. Indeed, it must be pointed out that (likely in recognition of some of the concerns presented above) Mayer & Madsen (2000) rightly concluded that "at this stage we do not recommend this modification as generally applicable and instead some new fundamental analysis and development seems necessary," largely inspiring the present work.

2.5. Analysis of the Wilcox (2006) k - ω model

As a third alternative, let us now similarly consider the stability of the Wilcox (2006) k - ω closure model. In this closure model Wilcox (2006) added, among other things, a stress limiting feature, such that

$$\tilde{\omega} = \tilde{\omega} = \max \left[\omega, \lambda_1 \sqrt{\frac{p_0}{\beta^*}} \right] \quad (2.29)$$

where he suggested $\lambda_1 = 7/8 = 0.875$. This feature essentially limits the resulting eddy viscosity in regions where turbulence production exceeds the dissipation, and has been shown to result in larger separation bubbles and greatly improve incompressible and transonic-flow predictions relative to models without this feature.

If the first argument in the limiter (2.29) dominates, then $\tilde{\omega} = \tilde{\omega} = \omega$ and the model becomes identical to that analyzed in §2.3, which was already proven to be unconditionally unstable in a nearly-potential flow with finite p_0 . Alternatively, if the second (stress limiting) argument dominates, then (2.15) and (2.16) become

$$\frac{\partial k}{\partial t} = \frac{k}{\lambda_1} \sqrt{\beta^* p_0} - \beta^* \omega k, \quad (2.30)$$

$$\frac{\partial \omega}{\partial t} = \frac{\alpha \omega}{\lambda_1} \sqrt{\beta^* p_0} - \beta \omega^2. \quad (2.31)$$

As before, setting the right-hand-side of (2.31) equal to zero, we now find that ω will tend to the asymptotic value

$$\omega_\infty = \frac{\alpha}{\lambda_1 \beta} \sqrt{\beta^* p_0} \approx 2.52 \sqrt{p_0}. \quad (2.32)$$

Inserting this value for ω back into (2.30) then leads directly to linearised expressions of the form (2.21), where the unstable growth rate is

$$\Gamma_\infty = \frac{(\beta - \alpha \beta^*)}{\lambda_1 \beta} \sqrt{\beta^* p_0} \approx 0.116 \sqrt{p_0}. \quad (2.33)$$

Hence, this model is likewise formally unconditionally unstable in the situation considered, though the stress limiter notably reduces the unstable growth rate slightly relative to the standard k - ω model.

Independent confirmation of the analysis above is provided via numerical solution of (2.15) and (2.16) while invoking (2.29), maintaining the same initial conditions for ω and ν_T as before. The resulting evolution of the eddy viscosity is depicted in figure 2(b). As

before, following the initial decline, the eddy viscosity grows exponentially at the rate predicted above.

2.6. Analysis of a new stabilized closure

In this section an elegant and simple solution to the instability considered above, which seems to widely plague most existing two-equation closure options (all that the authors have analyzed), will be presented. We seek a solution to this long-standing problem that will be otherwise un-intrusive i.e. such that the resulting model will default to an existing closure in sheared flow regions, while still formally curing the instability in regions of nearly-potential flow. At the same time the solution should remain true to the theoretically based terms in the k equation, maintain full consistency with the Boussinesq approximation, and not require alteration of any fundamental closure coefficients. We further aim for the solution to be readily adaptable to similarly stabilize other two-equation closures in wide use.

As just shown in §2.5, the stress limiting feature in the Wilcox (2006) model reduces the unstable growth rate, relative to the standard k - ω model. Working within this established feature is therefore a natural place to attempt to remedy this problem. To both formally stabilize the model and generally improve the CFD simulation of surface waves with RANS models, we propose the following modifications to the stress limiting features. First, we propose to generalize $\tilde{\omega}$ slightly such that:

$$\tilde{\omega} = \max \left[\omega, \lambda_1 \sqrt{\frac{p_0 - p_b}{\beta^*}} \right], \quad (2.34)$$

where we have included buoyancy production for potential two-phase (air and water) flow applications, for the sake of full consistency with (2.1). Obviously, this will not affect the formal stability of the model, as constant density (hence $p_b = 0$) is assumed in the analysis. Second (and much more importantly in the present context), to formally stabilize the instability considered at length above, we propose the following modification to $\tilde{\omega}$:

$$\tilde{\omega} = \max \left[\tilde{\omega}, \lambda_2 \frac{\beta}{\beta^* \alpha} \frac{p_0}{p_\Omega} \omega \right] \quad (2.35)$$

where $\lambda_2 \ll 1$ is an additional stress limiter coefficient, the physical meaning of which will be made explicitly clear in what follows. Note that the new addition to the limiter in (2.35) is, by design, un-intrusive, as it will become active only in a region of nearly-potential flow where $p_0 \gg p_\Omega$. Moreover, note that (for single-phase incompressible flows) if $\lambda_2 = 0$ the model becomes equivalent to the Wilcox (2006) model, whereas if $\lambda_1 = \lambda_2 = 0$ this model becomes equivalent to the standard k - ω model of Wilcox (1988). It is hence fully compatible with the other standard closures that have been specifically considered. (Note that to avoid any possibility of dividing by zero, the denominator in (2.35) can be implemented numerically as $p_\Omega + \xi$, where ξ is a small number near machine precision, though we strictly analyze the form above for the sake of elegance.)

To demonstrate the formal asymptotic stability of the proposed new model, let us first repeat the above analysis of the standard Wilcox (1988) model (momentarily setting $\lambda_1 = 0$, hence $\tilde{\omega} = \omega$), but now with the new limiter active in $\tilde{\omega}$. In this case, the k equation (2.15) becomes

$$\frac{\partial k}{\partial t} = \frac{\alpha \beta^*}{\lambda_2 \beta} \frac{k p_\Omega}{\omega} - \beta^* \omega k, \quad (2.36)$$

whereas the ω equation from (2.16) remains equivalent to (2.18), and hence ω will ultimately evolve to ω_∞ from (2.20). Inserting this value into (2.36) leads to linearized

expressions of the form (2.21), where the exponential growth rate is

$$\Gamma_\infty = \sqrt{\frac{p_0\alpha}{\beta}}\beta^* \left(\frac{p_\Omega}{\lambda_2 p_0} - 1 \right). \quad (2.37)$$

From this it can be seen that the new turbulence closure model will be formally stable (i.e. $\Gamma_\infty \leq 0$) provided that

$$\frac{p_\Omega}{p_0} \leq \lambda_2. \quad (2.38)$$

This hence provides a clear physical meaning for the added stress limiter coefficient λ_2 , as it defines the threshold of p_Ω/p_0 identifying a region as effectively potential flow. Note also that at the pure potential flow limit where $p_\Omega = 0$, the growth rate is $\Gamma_\infty = -\beta^* \sqrt{p_0\alpha/\beta} = -\beta^* \omega_\infty \approx -0.244\sqrt{p_0}$, and any turbulent kinetic energy will decay similar to how it would in a quiescent fluid.

If instead, we repeat the analysis of the Wilcox (2006) model (now retaining λ_1), then the k equation will remain equivalent to (2.36), whereas the ω equation will be equivalent to (2.31), and hence ω will tend towards ω_∞ in (2.32). Inserting this value as a constant within (2.36) then similarly leads to linearized expressions of the form (2.21), where the unstable growth rate is

$$\Gamma_\infty = \sqrt{p_0}\beta^* \left(\frac{p_\Omega\lambda_1}{p_0\lambda_2\sqrt{\beta^*}} - \frac{\alpha\sqrt{\beta^*}}{\lambda_1\beta} \right). \quad (2.39)$$

This will thus be stable provided that

$$\frac{p_\Omega}{p_0} \leq \lambda_2 \frac{\alpha\beta^*}{\lambda_1^2\beta} \approx 0.863\lambda_2, \quad (2.40)$$

where the standard coefficient values have been inserted. As the lead coefficient is near unity, it is seen that this further generalization does not greatly affect the previously mentioned physical interpretation of λ_2 . Note also that once $\omega = \omega_\infty$ if $\lambda_1 < \sqrt{\alpha\beta^*/\beta} \approx 0.813$ then the first argument will inevitably dominate in (2.34), and the threshold for stability will again be given by (2.38).

It should be noted that in uniform boundary layer flows $p_0 = p_\Omega$, and thus the new limiter will be completely inactive. Moreover, in other more complicated sheared flow regions (e.g. both in the surf-zone and the surface boundary layer region near the air-water interface) p_Ω and p_0 will typically be the same order of magnitude, and the new limiter will similarly remain inactive. Hence, the new closure will, by design, effectively reduce to a standard closure, except in a region of nearly-potential flow (clearly defined by the choice of λ_2), where such existing standard methods are inherently unconditionally unstable. The value of λ_2 should naturally be small, but also large enough to work for practical applications since p_Ω can always be expected to have a small, but finite, value in the discretized world. Throughout this work $\lambda_2 = 0.05$ is used to achieve such a balance.

The stabilization of the new model presented above has been confirmed via numerical simulation of (2.15) and (2.16) while invoking (2.34) and (2.35), maintaining the same initial conditions as before. An example (with $\lambda_1 = 0$ and $\lambda_2 = 0.05$) depicting the temporal evolution of the eddy viscosity is provided in figure 2(c). Consistent with the analysis above, exponential decay, rather than growth, is now observed. Thus, the new closure model should remain stable in a region of nearly-potential flow with finite strain, in contrast to all of the other models considered previously.

Model	Reference	$\approx \omega_\infty$	$\approx \Gamma_\infty$
Standard k - ω	Wilcox (1988)	2.71 $\sqrt{p_0}$	0.125 $\sqrt{p_0}$
k - ω	Mayer & Madsen (2000)	2.71 $\sqrt{p_\Omega}$	0.125 $\sqrt{p_\Omega}$
k - ω	Wilcox (2006)	2.52 $\sqrt{p_0}$	0.116 $\sqrt{p_0}$
k - ω SST	Menter (1994)	2.72 $\sqrt{p_0}$	0.066 $\sqrt{p_0}$
Standard k - ϵ	Launder & Sharma (1974)	2.31 $\sqrt{p_0}$	0.226 $\sqrt{p_0}$
RNG k - ϵ	Yakhot <i>et al.</i> (1991)	2.70 $\sqrt{p_0}$	0.142 $\sqrt{p_0}$

TABLE 1. Summary of asymptotic ω values (ω_∞) and unstable exponential growth rates (Γ_∞) for analyzed existing two-equation turbulence closures.

2.7. Analysis of other existing closure models

The formal asymptotic stability of several other widely-utilized two-equation turbulence closure models is similarly considered in Appendix A. These include: the k - ω SST model originally formulated by Menter (1994), the standard k - ϵ model of Launder & Sharma (1974), and the RNG k - ϵ model developed by Yakhot *et al.* (1991). It turns out that all of these basic two-equation models are similarly unconditionally unstable for the same conditions as analyzed above. This is demonstrated analytically, as well as via independent numerical simulations of the reduced governing equations. The resulting asymptotic values for ω_∞ and the unstable growth rates Γ_∞ for each of the pre-existing closure models analyzed in the present work are summarized in table 1.

Fortunately, and in line with the goals set forth above, these other widely-utilized closure models can also be formally stabilized via simple modifications to their stress limiting features, in a similar manner as presented in the preceding sub-section. The necessary modifications to stabilize each model are described in full detail in Appendix A. With these modifications, asymptotic exponential decay (rather than growth) in the turbulent kinetic energy and eddy viscosity is proved analytically, as well as independently demonstrated through numerical simulation of the reduced modified model equations, similar to the above.

To avoid the potential for excessive and un-physical over-production of turbulence in nearly-potential flow regions, it is recommended that these (or otherwise formally stabilized and un-intrusive) modified closure models be utilized in any future CFD simulations of surface waves with two-equation RANS closure models, the significant and fundamental benefits of which will be demonstrated in the next section.

3. Numerical simulation of surface waves

The advantages of utilizing a formally stable closure model will now be demonstrated directly through the CFD simulation of surface water waves. Essential details of the computational model are provided in the next sub-section, which will be followed by test cases involving the simulation of both non-breaking and breaking waves.

3.1. Model description

For the purposes of CFD simulation, surface water waves will be considered in the context of two-phase (air and water) flow. For this purpose the turbulence model defined

by (2.1) and (2.2) will be used to close a CFD model solving incompressible Reynolds-averaged Navier-Stokes (RANS) equations

$$\frac{\partial \rho u_i}{\partial t} + u_j \frac{\partial \rho u_i}{\partial x_j} = -\frac{\partial p^*}{\partial x_i} - g_j x_j \frac{\partial \rho}{\partial x_i} + \frac{\partial}{\partial x_j} (2\mu S_{ji} + \tau_{ij}), \quad (3.1)$$

and the local continuity equation

$$\frac{\partial u_i}{\partial x_i} = 0. \quad (3.2)$$

In the above p^* is the pressure in excess of hydrostatic. A scalar field γ is used to track the two fluids, where $\gamma = 0$ represents pure air and $\gamma = 1$ pure water, with any intermediate value representing a mixture. The distribution of γ is governed by an advection equation

$$\frac{\partial \gamma}{\partial t} + u_j \frac{\partial u_i \gamma}{\partial x_j} + u_j^r \frac{\partial u_i^r \gamma (1 - \gamma)}{\partial u_j^r} = 0 \quad (3.3)$$

where u_j^r is a relative velocity used to compress the interface, as documented in Berberovic *et al.* (2009). Any fluid property Φ in the flow is assumed to be given by

$$\Phi = \gamma \Phi_{water} + (1 - \gamma) \Phi_{air}. \quad (3.4)$$

The governing equations are solved within the open-source CFD environment OpenFOAM (version `foam-extend 3.1`), making use of the `waves2FOAM` toolbox developed by Jacobsen *et al.* (2012) for wave generation/absorption or specification of initial conditions. This toolbox is built upon the widely used `interFoam` solver, which utilizes the volume of fluid method (VOF). For further details on this solver the interested reader is referred to Deshpande *et al.* (2012). In all forthcoming cases the time step has been adjusted such that a maximum Courant number $Co = |u_i| \Delta t / \Delta x_i = 0.05$ is maintained at all times. This ensures accurate velocity kinematics and enables nearly constant-form propagation of wave trains for long durations. Boundary conditions will be clarified on a case-by-case basis in what follows.

3.2. Simulation of a simple progressive wave train

In this section computed results will be presented for the long term propagation of a periodic surface wave train. This is perhaps the simplest of computational wave problems, and is a test that should ideally be passed by CFD models prior to their application on more complicated problems. As an initial condition, a numerically exact stream function wave (potential flow) solution of Fenton (1988) is specified, with zero Stokes drift, and with period $T = 2$ s, wave height $H = 0.125$ m, and water depth $h = 0.4$ m (hence $k_w h = 0.664$ and $k_w H = 0.207$). It should be noted that this wave is the same as that generated for the forthcoming simulation of the Ting & Kirby (1994) spilling breaker experiments. Being intermediately deep and moderately nonlinear, these wave conditions are indeed well suited for generic study.

The computational domain is discretized into regular cells having horizontal and vertical size $\Delta x = \Delta z = 0.01$ m (corresponding to $H/\Delta z = 12.5$ cells per wave height). This resolution has been experienced to be sufficient for the accurate propagation of this specific wave in a laminar set-up. This mesh also maintains an aspect ratio $\Delta x/\Delta z = 1$, which can be important for accuracy, as noted by Jacobsen *et al.* (2012), Jacobsen *et al.* (2014) and Roenby *et al.* (2017). The computational domain spans a single wavelength, making use of periodic lateral boundaries. At the bottom boundary a slip condition is applied. This is primarily for canonical demonstration purposes, making the computational situation as close to potential flow as possible, such that a turbulence closure model should ideally not influence the physics of the wave propagation.

To demonstrate the performance of the proposed new turbulence closure relative to standard approaches, we will compare computed results from the standard Wilcox (1988) k - ω model (with the buoyancy production term also included in (2.1), henceforth taken as granted) with those from our new closure with $\lambda_1 = 0$ and $\lambda_2 = 0.05$. All other model settings are kept identical. We initially set $\omega = \omega_\infty = 2.71\sqrt{p_0}$, where $p_0=0.66$ s^{-2} is the depth- and period-averaged value computed from the initial conditions, and with $k = k_0 = \omega_\infty\nu$ to initially yield $\nu_T/\nu = 1$. This is intended as a direct test of the preceding simplified analysis in an actual surface wave computation, where the standard closure should exhibit unstable behaviour from the outset, whereas the proposed new closure should remain stable indefinitely. We consider the initial condition for ω above to be most sensible in the present context, since as shown previously, it will always tend to approximately this value in the potential flow region beneath waves.

Figure 3 shows the computed temporal development of the (depth- and period-averaged) non-dimensional eddy viscosity $\langle\nu_T\rangle/\nu$ with both closure models considered. Included in the figure (dashed line) is also the predicted development of $\langle\nu_T\rangle/\nu = \exp(\Gamma_\infty t)$ with the growth rate from (2.22). Figure 3 clearly shows that the Wilcox (1988) k - ω model is indeed initially unstable, resulting in an exponentially growing eddy viscosity (hence also k) that ultimately becomes several orders of magnitude larger than the kinematic viscosity, before eventually levelling off. The computed exponential growth rate is near that expected based on the simplified analysis, which has neglected several terms. It is emphasized that the growth of turbulence does not come from the bottom boundary layer, which is non-existent as a slip condition has again been used. Nor does it stem from the free-surface, where the buoyancy production term in equation (2.7) dissipates turbulent kinetic energy in this region. Rather, it is due to the instability of the potential flow region, as confirmed via the close match with the theoretical growth rate. In contrast, also consistent with the preceding analysis, our new modified closure remains stable, with the eddy viscosity quickly decaying to physically insignificant levels.

The eventual levelling off of the eddy viscosity with the standard k - ω of Wilcox (1988) can be explained as due to declining wave heights, which are a direct consequence of the un-physical growth of the turbulent kinetic energy and eddy viscosity. These eventually reach levels that are sufficiently high to cause un-physical turbulent diffusion of the wave, with energy thus being extracted from the mean flow. As a result of the decreased wave height the turbulence production quantity p_0 is likewise reduced. This can be seen from the surface elevation time series depicted in figure 4(a), where the waves begin to decline after only $t \approx 20T$. The decay in wave height is similar to what was shown by Mayer & Madsen (2000) and Devolder *et al.* (2017). In contrast, the wave evolution computed with the new stabilized closure maintains a nearly constant wave height, as seen from figure 4(b). The slight decay seen is clearly due to minor numerical diffusion associated with the numerical scheme, and not in any way related to the new turbulence closure, as it has effectively switched itself off. This is clear from the previously-mentioned extremely small eddy viscosity in figure 3, as well as through comparison with an additional (otherwise identical) simulation with the turbulence model switched off entirely, which results in visually identical behaviour (not directly shown here for the sake of brevity). Note that we have also made other, similar, simulations as above, with $0.02 \leq \lambda_2 \leq 0.1$, which result in similar surface elevations as in figure 4(b).

This example demonstrates how the instability identified by Mayer & Madsen (2000), and which is inherent in standard two-equation turbulence closure models as shown herein, can manifest in their rather spectacular failure in even the simplest of surface wave computations. The comparison above likewise demonstrates that such failure can be avoided entirely by employing the simple new (stabilized) closure proposed herein.

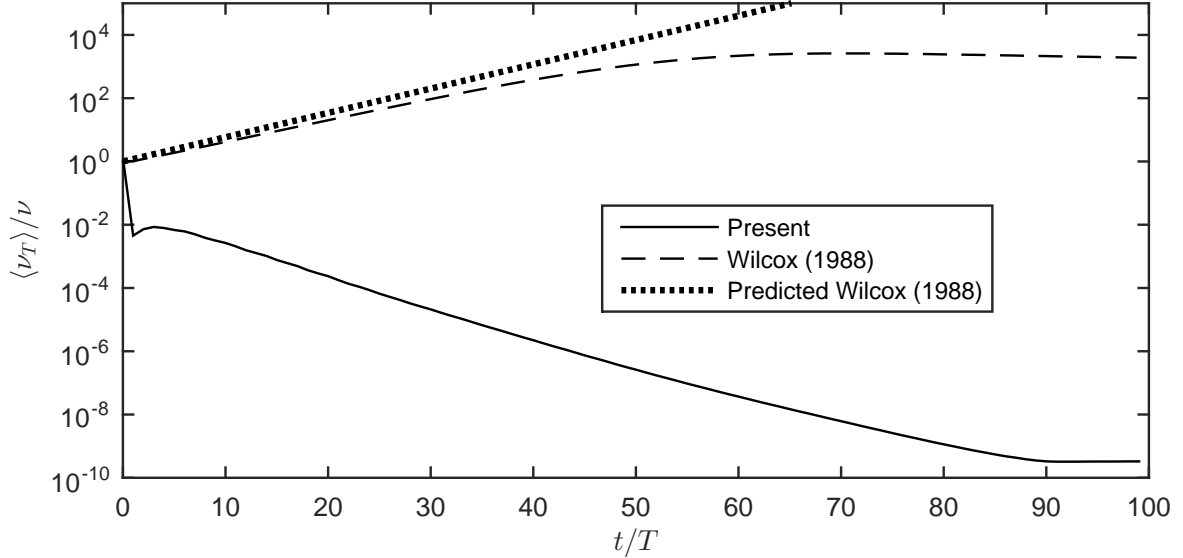


FIGURE 3. Computed temporal development of the depth- and period-averaged eddy viscosity beneath a periodic wave train using the present k - ω closure model with $\lambda_1 = 0$ and $\lambda_2 = 0.05$ (full line), the Wilcox (1988) k - ω model (dashed line), as well as the predicted development from (2.22) (dotted line).

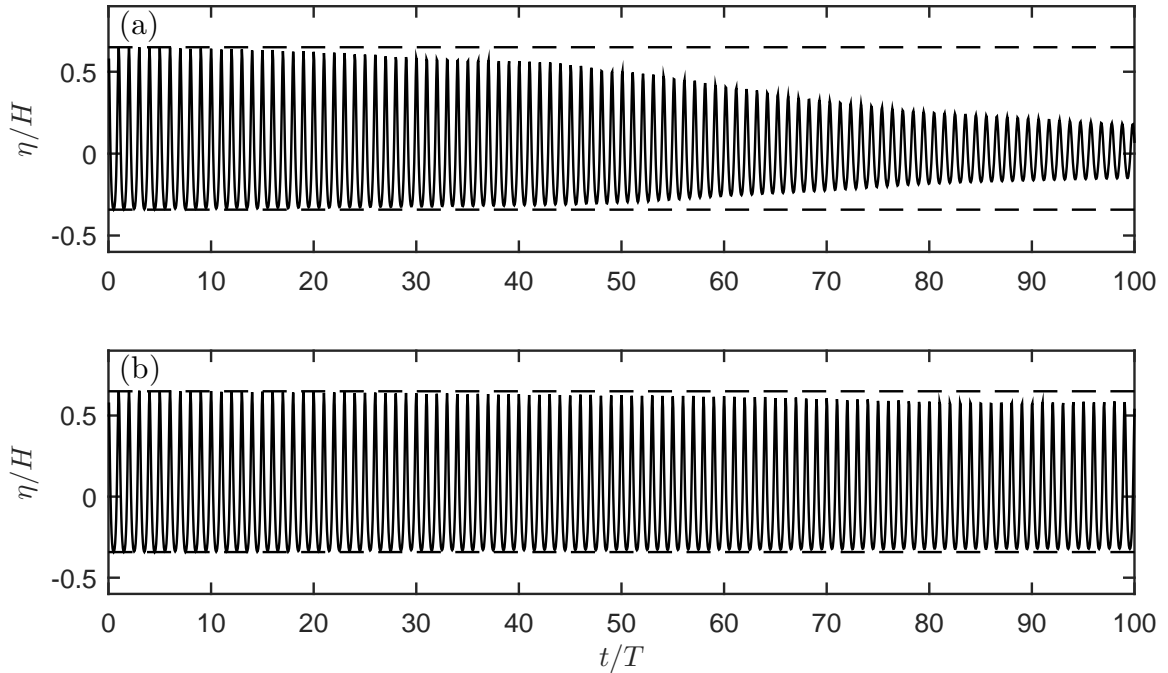


FIGURE 4. Computed time series of surface elevations in the simulation of a periodic wave train using (a) the standard Wilcox (1988) k - ω model and (b) the proposed new closure model with $\lambda_1 = 0$ and $\lambda_2 = 0.05$. The horizontal dashed lines represent the crest and trough levels of the initial wave, for comparison.

3.3. Simulation of spilling breaking waves

As a follow-up to the preceding example, let us now consider simulations of the spilling breaking wave experiment of Ting & Kirby (1994), to demonstrate the performance of the new model in a more physically complex situation. We focus here on their spilling, rather than plunging, case as it is these incoming wave conditions where the over-production of turbulence has consistently been observed in prior studies. Quantitatively the reason for this can be explained by equation (2.13) which yields $\langle p_0 \rangle = 0.55 \text{ s}^{-2}$ and $\langle p_0 \rangle = 0.08 \text{ s}^{-2}$ for their spilling and plunging cases respectively, i.e. a much lower turbulence production

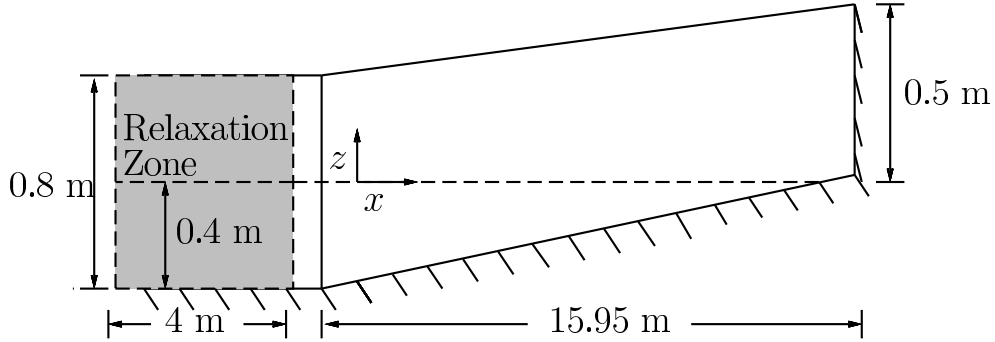


FIGURE 5. Layout of the computational domain for the simulation of the spilling breaking wave experiments of Ting & Kirby (1994).

and hence unstable growth rate for the plunging case. It is emphasized that the strength of the instability does not strictly depend on the breaker type (which also depends on the slope encountered), but rather only on the characteristics of the incoming waves.

The model domain for these simulations consists of a flat region having water depth $h = 0.4$ m, connected to a region having constant 1:35 slope. For these simulations, the same waves as considered previously ($T = 2$ s and $H = 0.125$ m with zero Stokes drift; $k_w h = 0.664$ and $k_w H = 0.207$) are generated on the horizontal bed. At the left inlet boundary a relaxation zone of 4 m is used, which serves to absorb any waves reflected by the slope, thus the incoming waves do not change over time. In figure 5 a layout of the computational domain is seen. For the purposes of consistent comparison, the origin is positioned at the same depth ($h = 0.38$ m) as in the experiments. No roughness was indicated in the experiment, but it was stated that the bed was made of plywood, and therefore the model bed is assigned a Nikuradse equivalent sand roughness $k_s = 10^{-4}$ m.

The initial condition for ω is again taken as $\omega = \omega_\infty = 2.71\sqrt{p_0}$, with p_0 calculated from (2.13) and with $k = k_0 = 0.1\omega_\infty\nu$ such that $\nu_T/\nu = 0.1$ (this is one order of magnitude below that used in the previous progressive wave train test case in §3.2). In contrast to the previous idealized simulation in §3.2, a no-slip boundary condition is imposed at the bottom, meaning that a wave boundary layer will now develop near the bed, as in reality. Turbulence quantities in the first cell near the bottom are prescribed using the generalized wall functions presented in Fuhrman *et al.* (2014), which build upon the generalized van Driest profile of Cebeci & Chang (1978). These wall functions have been used successfully in the simulation of various scour processes, see e.g. Baykal *et al.* (2015), Bayraktar *et al.* (2016), Larsen *et al.* (2016), Larsen *et al.* (2017) and Larsen *et al.* (2018), and allow for near-bed cells to lie in either the logarithmic or viscous sub-layer. On the flat region the domain is discretized into cells with $\Delta x = \Delta z = 0.01$ m, and on the slope the mesh is gradually refined towards the shore while keeping a constant aspect ratio of unity. At the right end of the domain the cells have a size $\Delta x = \Delta z = 0.0063$ m. Near the bed layers of cells are refined in the vertical direction with near bed cells having height $\Delta z = 7.5 \cdot 10^{-4}$ m. This ensures that $\Delta z^+ = \Delta z U_f / \nu < 30$ during the simulation, with U_f being the friction velocity.

For the sake of systematic comparison, simulations of these experiments will be considered using five different turbulence closure variants. These correspond to: (1) the standard Wilcox (1988) $k-\omega$ model, (2) the Wilcox (2006) $k-\omega$ model, as well as three variants of the new modified $k-\omega$ closure with fixed $\lambda_2 = 0.05$ and: (3) $\lambda_1 = 0$, (4) $\lambda_1 = 0.875$, and (5) $\lambda_1 = 0.2$. These λ_1 values correspond to those associated with the models of Wilcox (1988) and Wilcox (2006) (thus allowing direct comparison), as well as an intermediate value, more in line with Eq. (9) of Durbin (2009) (corresponding

Case	Model	λ_1	λ_2	$\tilde{\omega}$	$\tilde{\omega}$	Line type (Figs. 10 & 11)
1	Wilcox (1988)	0	0	$= \omega$	$= \omega$	Dashed light (blue) line
2	Wilcox (2006)	0.875	0	$= \tilde{\omega}$	Eq. (2.29)	Dotted light (blue) line
3	Present	0	0.05	$= \omega$	Eq. (2.35)	Dashed dark (black) line
4	Present	0.875	0.05	Eq. (2.34)	Eq. (2.35)	Dotted dark (black) line
5	Present	0.2	0.05	Eq. (2.34)	Eq. (2.35)	Solid dark (black) line

TABLE 2. Summary of parameters used in the five different simulations of the Ting & Kirby (1994) spilling breaking wave experiment.

to $\lambda_1 = 0.26$). For ultimate clarity, the parameter settings used in these five cases are listed in table 2. We shall henceforth refer to these simulations by their case number, as indicated in table 2 and in the text immediately above.

Figure 6 shows computed snapshots depicting the surface and non-dimensional eddy viscosity ν_T/ν from each of the five model variants mentioned above, following a long simulation time of 100 periods, such that steady (repeatable) conditions have effectively been reached. (As an indication of simulation time, each run requires approximately three weeks when simulated in parallel on eight modern processors.) Each plot is frozen at an instant where the wave is very close to breaking, such that the location of the surf zone is evident (beginning approximately at $x = x_b = 6.4$ m). As can be seen, both the standard Wilcox (1988) (Case 1, figure 6(a)) and the Wilcox (2006) $k-\omega$ models (Case 2, figure 6(b)) result in uniformly high eddy viscosity (orders of magnitude larger than ν), even in the pre-breaking region. These high values are in no way physical, as in real waves significant turbulence should not be expected prior to breaking, see e.g. the measured turbulence levels from Ting & Kirby (1994) and van der A *et al.* (2017), the PIV experiments of Chang & Liu (1998), Kimmoun & Branger (2007), Belden & Techet (2011), and Grue & Jensen (2006) or the dye experiment of Duncan *et al.* (1999). Rather, these high values are again an artefact related to the inherent instability of these models in the nearly-potential flow regions which are prevalent leading up to the surf zone. Conversely, regardless of the value of λ_1 , the three results using the proposed new stabilized closure (figures 6(c)–(e) corresponding to Cases 3–5) predict negligible eddy viscosity in the bulk region beneath the waves prior to breaking; Significant eddy viscosity with these stabilized models is rightly confined to the near bed boundary layer and surf zone, demonstrating a clear and qualitative correction over existing models. Figure 6 is hence a clear demonstration of how, due to their inherent instability, existing standard turbulence closure models in wide use can result in severely polluted results prior to wave breaking, often the very phenomenon of interest in CFD studies where such models are employed. This figure likewise definitively demonstrates that the new stabilized closure model proposed herein eliminates this problem altogether.

We will now further demonstrate the differences between results computed with standard (unstable) and new closure models via further quantitative comparison against the spilling breaker data set of Ting & Kirby (1994). To make proper comparisons, as in the experiments, a relatively long warm up period is needed to establish stable conditions in the computational flume. Before extracting data, models have therefore been run for 60 periods. Such a long warm up period has not been common in most previous numerical studies of the Ting & Kirby (1994) experiments. Jacobsen *et al.* (2012) demonstrated,

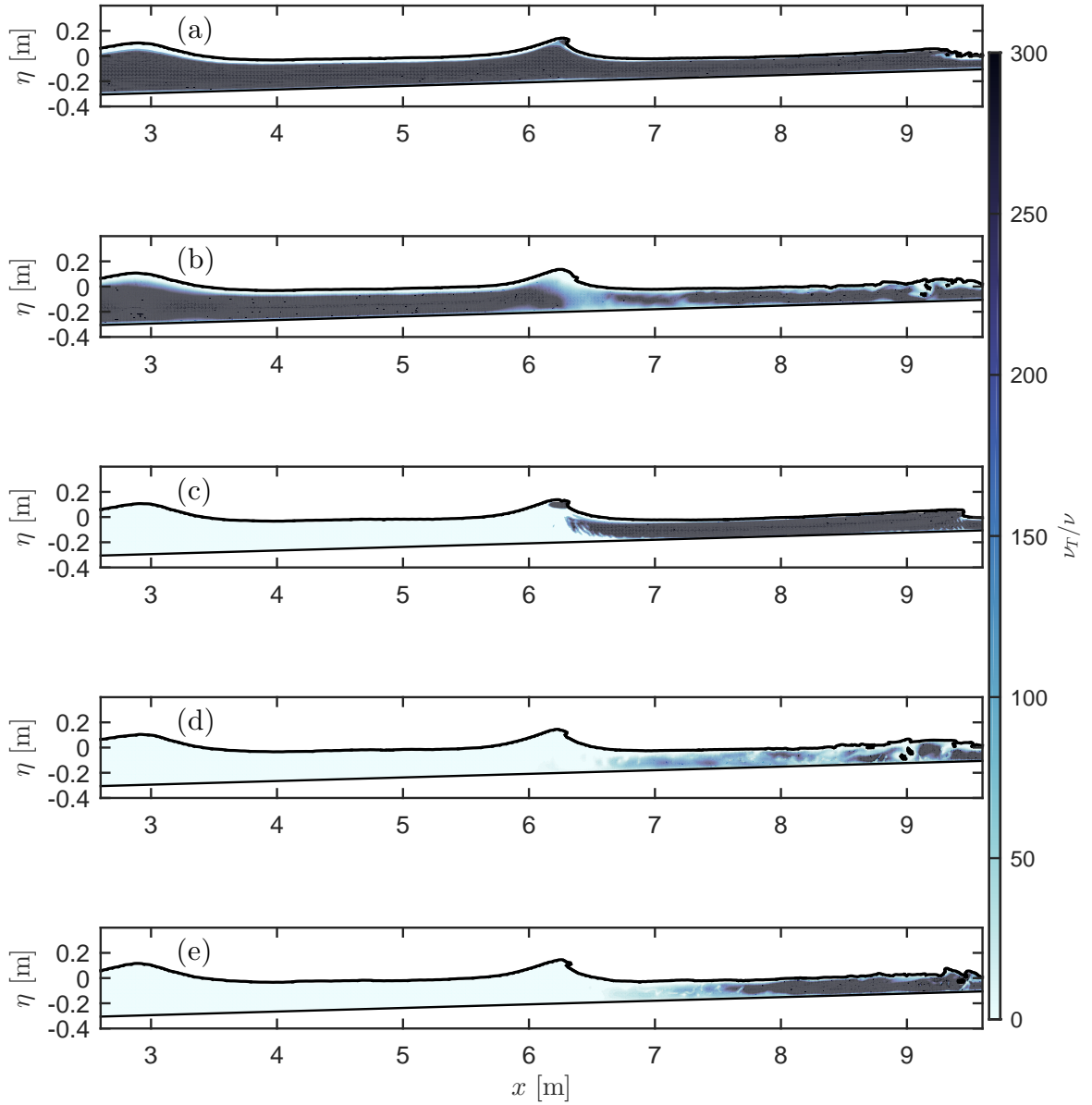


FIGURE 6. Snapshots of ν_T/ν at $t/T = 100$ with the wave right at breaking computed with the (a) standard Wilcox (1988) $k-\omega$ model (Case 1), (b) Wilcox (2006) $k-\omega$ model (Case 2), and (c)–(e) present stabilized $k-\omega$ closure model (respectively, Cases 3–5), where parameters for each case are indicated in table 2. The free surface and bottom are marked by a solid line.

however, that at least 40 periods were necessary in order to reach a constant volume of water in their domain. We have similarly found that an additional 20 periods were necessary to achieve a convincing quasi-steady situation. For comparison, it can be noted that the warm up length in the experiments was 600 periods. Furthermore, in order to achieve stable mean values, the results presented in the following have been obtained by averaging over an additional 60 periods following the warm up (i.e. simulations have been run for a total of 120 periods). For comparison, in the original experiments the results were averaged over a comparable duration corresponding to 102 periods.

Figure 7 shows comparison of the computed and experimental surface elevation envelopes as well as the mean water levels for the five models mentioned above. The solid lines represent the mean (ensemble averaged) values, whereas the shaded area represents plus or minus one standard deviation, to give an indication of wave-to-wave variability. It can be seen that all five models, in general, capture the evolution of the mean surface elevations well. The horizontal position of the breaking point and surface elevation at breaking is well captured, as is the subsequent decay in wave heights in the surf zone. These results compare well with surface elevations presented in other numerical studies of these experiments, see e.g. Jacobsen *et al.* (2012), Hieu *et al.* (2004), Xie (2013) and Brown *et al.* (2016). The most notable difference between the models is the standard deviation in the surface elevations in the surf-zone. As seen, those results sharing $\lambda_1 = 0$ (i.e. the Wilcox (1988) model, Case 1 shown in figure 7(a) and our stabilized version of this model, Case 3 shown in figure 7(c)) demonstrate little wave-to-wave variability. Conversely, the three results with the Wilcox (2006) limiter active ($\lambda_1 > 0$, Cases 2, 4 and 5, respectively depicted in figure 7(b),(d),(e)) result in significant wave-to-wave variability during the breaking process, much more in line with the experiments (see e.g. figure 3 of Ting & Kirby 1994).

Further inspection has revealed that this lack in wave-to-wave variability computed with $\lambda_1 = 0$ is due to the waves not breaking properly. This is due to large eddy viscosity computed in the crest (see figure 6(a),(c)), leading to turbulent dissipation of the wave rather than a convincing sequence of spilling breaking. This is illustrated in figure 8, where snapshots of typical waves computed during the breaking process are compared for Cases 3 ($\lambda_1 = 0$) and 4 ($\lambda_1 = 0.875$) i.e. two variants of the present stabilized model having different λ_1 , but being otherwise identical. As a result of this failure of the waves to properly spill with $\lambda_1 = 0$, there is little deviation in the surface elevations experienced in successive waves in the surf-zone. In contrast, the cases computed with $\lambda_1 > 0$, figure 7(b),(d),(e), spilling breaking occurs, leading to a much more dynamic surf zone. These results indicate that using a Wilcox (2006)-type limiter in the turbulent production is necessary to qualitatively capture the spilling breaking process. In the authors' opinion, while at first glance the five results in figure 7 may appear similar, the inability of the k - ω models with $\lambda_1 = 0$ (figure 7 (a),(c)) to predict proper spilling breakers (and corresponding wave-to-wave variability) can be regarded as an important qualitative shortcoming.

Considering the previous example from §3.2, it may be somewhat surprising that the Wilcox (1988) and Wilcox (2006) models perform reasonably in terms of the mean surface elevations (figure 7(a),(b)). One might have expected that the large eddy viscosity would cause the waves to decay even prior to breaking, as was seen in the previous demonstration involving a propagating wave train (figure 4(a)). This is, in fact, a real possibility, and the reason why this did not occur in the previous examples is merely due to the short propagation distance (in this case only a few wavelengths) allotted prior to the onset of breaking, which limits the extent of the turbulence over-production problem. Such pre-breaking wave decay would most certainly occur if the pre-slope distance was extended sufficiently further. To show this we have performed one additional simulation, but with the flat region now being 40 m instead of 4.7 m. The resulting surface elevations using the Wilcox (1988) model are shown in figure 9. Here it can be seen that the unstable growth in the eddy viscosity has caused the incoming wave to decline significantly, and as a consequence the horizontal position of the breaking point has shifted to be further onshore. Importantly, this recognition implies that previously computed results of breaking waves with non-stabilized closure models (prevalent in the literature) are not unique, instead being heavily dependent on both the initial conditions and the allotted

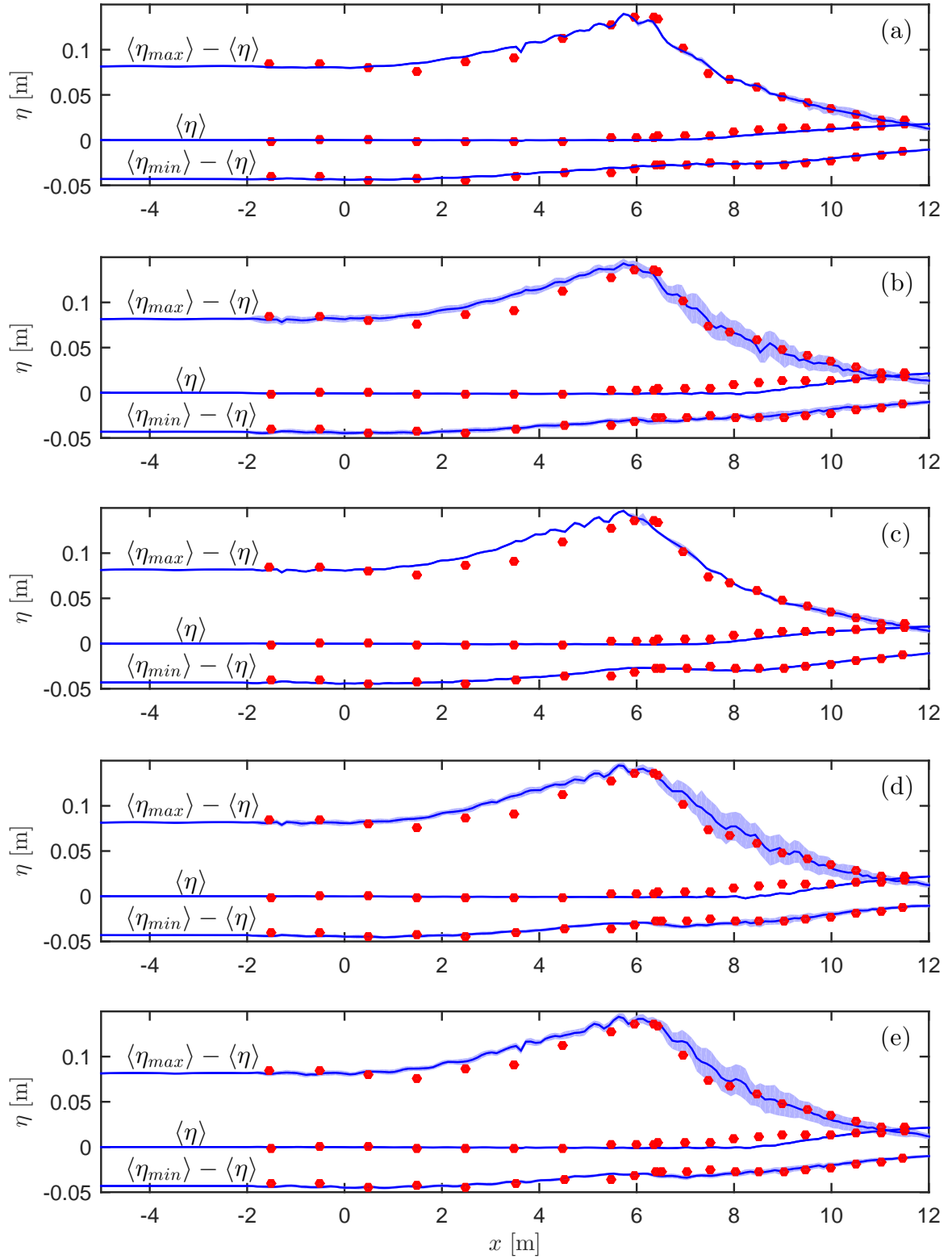


FIGURE 7. Comparison of modelled (lines) and measured (circles, from Ting & Kirby 1994) surface elevation envelopes (top and bottom lines) and mean water levels (middle lines). Results in (a)–(e) correspond to Cases 1–5, respectively. Solid lines represents the mean surface elevation and the shaded area represents plus and minus one standard deviation.

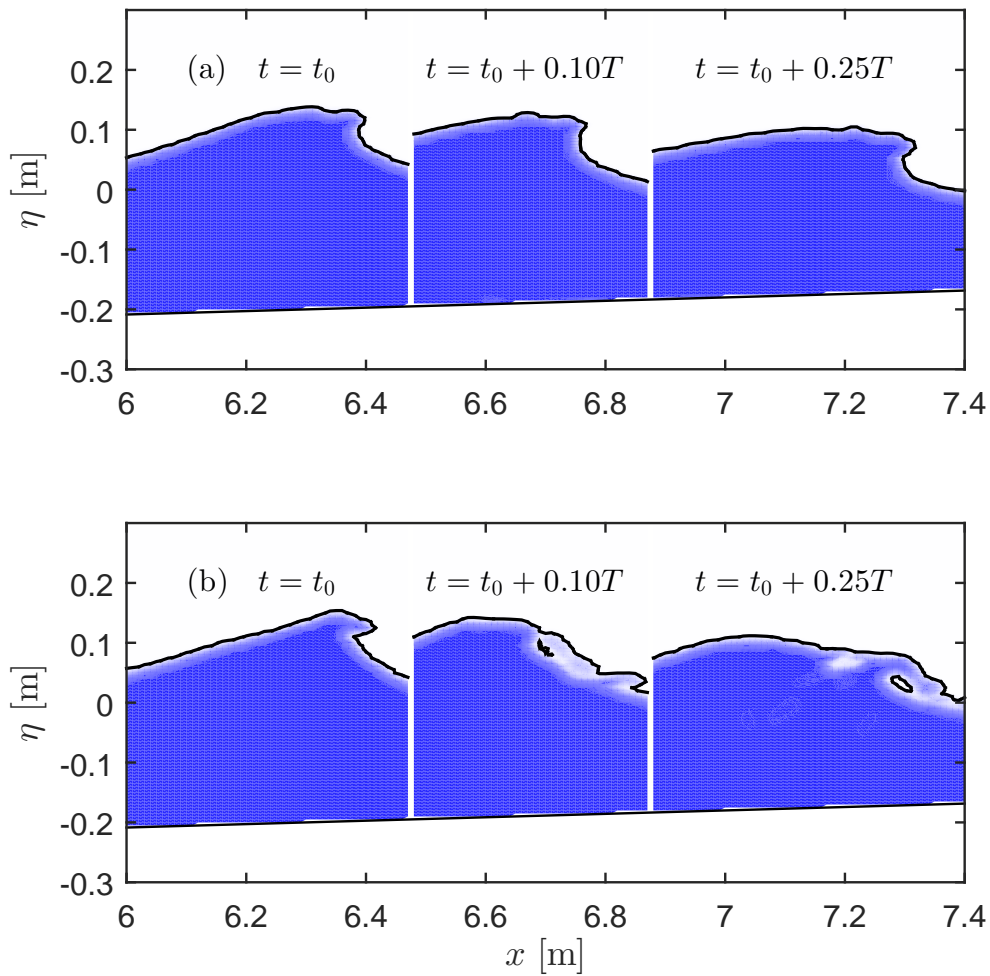


FIGURE 8. Snapshots of the breaking process computed in (a) Case 3 ($\lambda_1 = 0$, $\lambda_2 = 0.05$) and (b) Case 4 ($\lambda_1 = 0.875$, $\lambda_2 = 0.05$), beginning at $t = t_0 = 110T$. Here dark represents water, white represents air, and light shades represent air-water mixtures. The wave shown in (a) never actually spills.

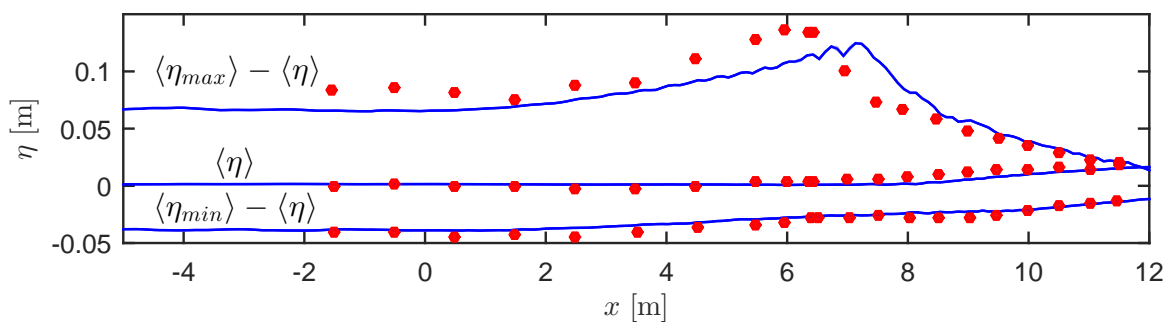


FIGURE 9. Comparison of computed (lines) and measured (Ting & Kirby 1994, circles) surface elevation envelopes and mean water levels using the Wilcox (1988) model with a long (40 m) flat region. This plot can be compared directly with figure 7(a), which depicts results computed with the same model, but where the flat region is only 4.7 m.

propagation distance prior to shoaling and breaking. Results computed with the new stabilized closure, on the other hand, will be fundamentally insensitive to these issues.

As further comparison, figure 10 presents computed and measured (Ting & Kirby 1994) averaged turbulent kinetic energy k profiles at a total of eight positions, corresponding to two pre-breaking positions (figure 10(a),(b)), as well as six in the surf zone (figure 10(c)–(h)). In the experiments only two components of the velocity were measured, so k was approximated by $k \approx 1.33/2(\overline{u'^2} + \overline{w'^2})$. This approximation was also used by Stive & Wind (1982) and Svendsen (1987), and comes from the results of a plane wake from Townsend (1976). However more recent results from Scott *et al.* (2005) indicate that

$$k \approx 0.75(\overline{u'^2} + \overline{w'^2}) \quad (3.5)$$

in the surf-zone, and this approximation has been used in what follows. Ting & Kirby (1994) did not provide approximate k -profiles in the two pre-breaking positions and the first post-breaking position (figure 10(a)–(c)) as well as the top three measurement positions, but did provide profiles of the single component $\overline{u'^2}$. At these positions we have alternatively utilized the approximation

$$k \approx 1.25\overline{u'^2}, \quad (3.6)$$

again based on the measurements of Scott *et al.* (2005). It is thus emphasized that the experimental k -profiles must all be regarded as approximate, but are still likely reasonably indicative. For further discussions or indications on the uncertainties of such approximations see e.g. Scott *et al.* (2005) and Ting & Kirby (1996).

To ease comparison the computed results in figure 10 are organized such that results with light shaded (blue) lines correspond to non-stabilized closures ($\lambda_2 = 0$, Cases 1 and 2), whereas dark (black) lines correspond to formally stabilized models ($\lambda_2 = 0.05$, Cases 3–5). Moreover, results having the same line type share common λ_1 values, see again table 2. As might by now be expected, the standard Wilcox (1988) (Case 1) and Wilcox (2006) (Case 2) k - ω models severely over-predict the turbulence pre-breaking (light shaded/blue lines in figure 10(a),(b)), which may again be regarded as a direct consequence of the instability of these models. The depicted over-production of turbulence using the Wilcox (1988) and Wilcox (2006) models is typical of previous studies. In contrast, the new stabilized closure models (Cases 3–5) predict low turbulent kinetic energy pre-breaking (dark black lines in figure 10(a),(b), see also again figure 6), much more in line with the experiments. The improvement seen with the new stabilized closures in figure 10(a),(b), and related effects further shoreward, can be regarded as the principal achievement of the present work: Only waves computed with the new stabilized closure arrive at the surf zone un-polluted.

The over-production of turbulence prior to breaking using the non-stabilized models also has an effect on the post-breaking turbulence. As can be seen, both the Wilcox (1988) and Wilcox (2006) models (Cases 1 and 2) predict higher turbulence levels than their stabilized counterparts (respectively, Cases 3 and 4) during the initial breaking process (figure 10(c)–(e)). This demonstrates that the unphysically high levels of pre-breaking turbulence predicted by the non-stabilized models can indeed pollute results extending well into the outer surf zone. Once the inner surf zone is reached (figure 10(f)–(h)) the differences between the stabilized (dark black lines) and standard (light shaded/blue lines) turbulence models become smaller. Rather, the results in the inner surf zone are more governed by the value of the Wilcox (2006) stress limiter coefficient λ_1 . This can be clearly seen in figure 10, where the results having the same line type i.e. Cases 1 and 3 (dashed lines), and Cases 2 and 4 (dotted lines), which were initially quite different in figure 10(a)–(c), have become quite similar in figure 10(f)–(h). Thus, the stabilization of

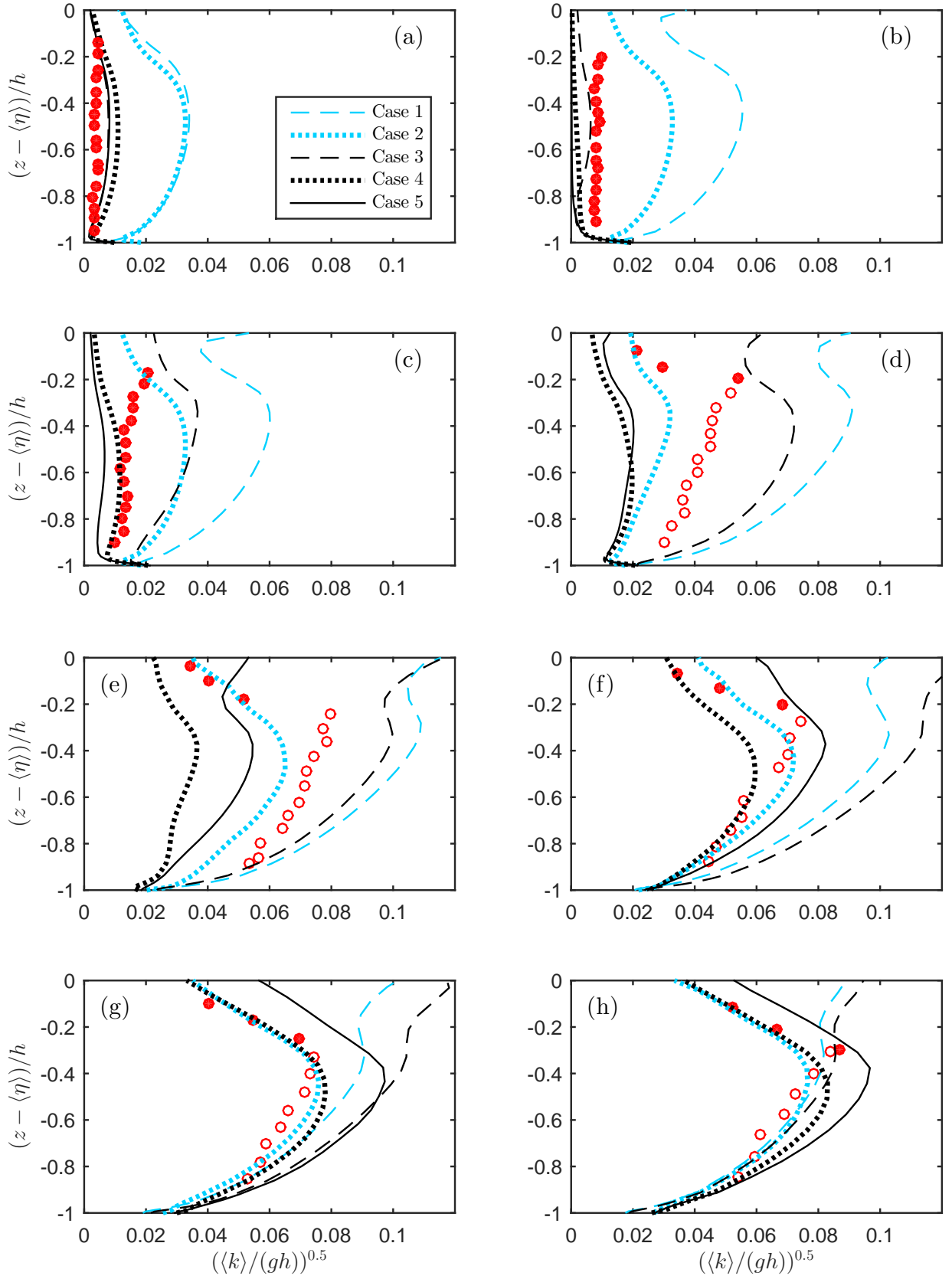


FIGURE 10. Comparison of modelled (lines) and measured (empty circles: from (3.5), filled circles: from (3.6)) turbulent kinetic energy k profiles at (a) $x = -1.265$ m ($\tilde{x} = (x - x_b)/h_b = -38.518$), (b) $x = 5.945$ m ($\tilde{x} = -2.286$), (c) $x = 6.665$ m ($\tilde{x} = 1.332$), (d) $x = 7.275$ m ($\tilde{x} = 4.397$), (e) $x = 7.885$ m ($\tilde{x} = 7.462$), (f) $x = 8.495$ m ($\tilde{x} = 10.528$), (g) $x = 9.11$ m ($\tilde{x} = 13.618$) and (h) $x = 9.725$ m ($\tilde{x} = 16.709$).

the closure models achieved by utilizing $\lambda_2 > 0$, as introduced herein, plays an important role both prior to breaking and in the outer surf zone, while expectedly becoming less important in the inner surf zone. This behaviour is as intended, as it has again been the aim of the present work to produce a formally stabilized closure model in potential flow regions, which default to existing closures in sheared regions (i.e. the surf zone in the present context). The results in figure 10, as a whole, demonstrate that this has indeed been achieved.

To demonstrate the consequences directly on the flow properties, the computed and measured averaged undertow velocity profiles $\langle u(z) \rangle$ are finally compared in figure 11, at the same eight positions as in figure 10. Figure 11(a),(b) clearly illustrates the adverse effects associated with the pre-breaking over-production of turbulence inherent within the standard Wilcox (1988) and Wilcox (2006) models (Cases 1 and 2, respectively). The negative peaks in the computed undertow with these models are consistently near the sea bed, whereas the measurements show these to be much higher up. This qualitative difference is important and can be explained by the artificially high ν_T in the upper part of the wave increasing the flow resistance, thus resulting in the strongest undertow near the bottom (similar to those profiles measured deeper into the surf zone). In contrast, in the experiments, as well as with the proposed new stabilized closure models (dark lines, Cases 3-5), the flow resistance is largest near the bed at these positions, and hence the undertow is strongest in the upper part of the flow.

The effects of over-produced turbulence in the outer surf-zone are also clearly visible, with the two models having $\lambda_1 = 0$ (Cases 1 and 3, dashed lines) maintaining an erroneous undertow structure (figure 11(c),(d)) while the cases with $\lambda_1 > 0$ (Cases 2, 4 and 5) show a better evolution of the undertow structure at these positions. These results thus, again, highlight the positive influence of the Wilcox (2006) stress limiter, which was previously found essential to obtain properly spilling waves (figure 8). The model which best matches the evolution of the measured undertow structure from pre-breaking and throughout the outer surf zone (figure 11(a)–(e), corresponding to $-1.265 \text{ m} \leq x \leq 7.885 \text{ m}$) is Case 5, corresponding to the present closure with the intermediate value $\lambda_1 = 0.2$. Notably, this transition from shoaling to the outer surf zone is a physically important and complex region of great interest, as the physics associated with the pre-to-post breaking transformation are related e.g. to the formation and dynamics of nearshore breaker bars, which play an important role in coastal protection.

Consistent with the trends seen previously in the computed turbulent kinetic energy, the results in the inner surf zone become grouped largely based on the value of λ_1 utilized (figure 11(f)–(h)) i.e. the results using (otherwise identical) formally stabilized or non-stabilized models are essentially similar in this region. The velocity profiles computed with $\lambda_1 > 0$ (Cases 2, 4 and 5) remain qualitatively correct in structure, but become exaggerated by a factor of approximately two relative to those measured. It can be noted that very similar results for the undertow in the inner surf-zone have been shown with various RANS closure models in Brown *et al.* (2016), as well as with a LES model in Christensen (2006). In contrast, the models using $\lambda_1 = 0$ (Cases 1 and 3, dashed lines) produce more accurate undertow profiles in the inner surf zone. These results are certainly interesting, though in the authors' opinion they may well be fortuitous, given that these models did not result in properly spilling waves or correct turbulence/undertow structure at many positions leading up to the inner surf. Upon inspection of the present results, the quantitative differences in the undertow in the inner surf zone achieved with $\lambda_1 = 0$ (Cases 1 and 3, dashed lines) and the other models are believed to be related to the increased eddy viscosity (hence flow resistance), especially in the upper part of the flow, predicted with $\lambda_1 = 0$ in this region. This is demonstrated in figure 12, where the average

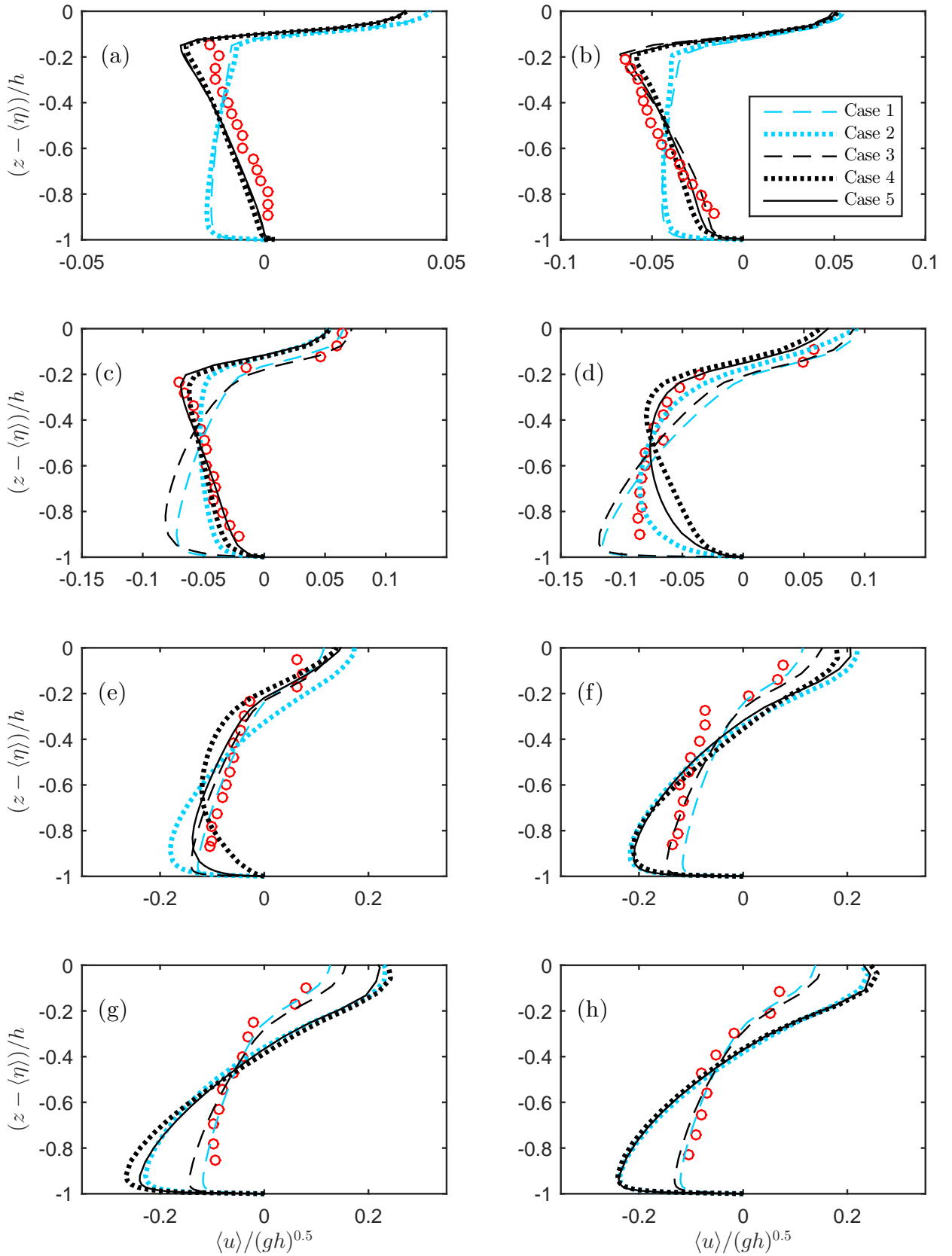


FIGURE 11. Comparison of modelled (lines) and measured (circles) undertow velocity profiles at (a) $x = -1.265$ m ($\tilde{x} = (x - x_b)/h_b = -38.518$), (b) $x = 5.945$ m ($\tilde{x} = -2.286$), (c) $x = 6.665$ m ($\tilde{x} = 1.332$), (d) $x = 7.275$ m ($\tilde{x} = 4.397$), (e) $x = 7.885$ m ($\tilde{x} = 7.462$), (f) $x = 8.495$ m ($\tilde{x} = 10.528$), (g) $x = 9.11$ m ($\tilde{x} = 13.618$) and (h) $x = 9.725$ m ($\tilde{x} = 16.709$).

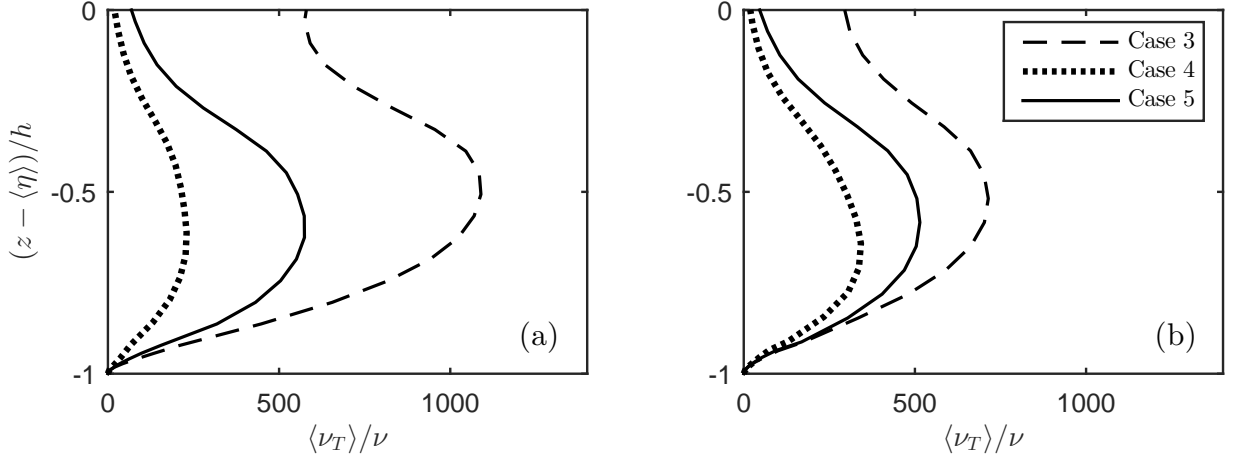


FIGURE 12. Comparison of modelled eddy viscosity profiles at (a) $x = 9.11$ m ($\tilde{x} = (x - x_b)/h_b = 13.618$) and (b) $x = 9.725$ m ($\tilde{x} = 16.709$).

eddy viscosity profiles for Cases 3-5 at the two inner-most positions of the surf-zone are shown.

In summary, the present case definitively demonstrates that the new stabilized closure proposed herein avoids entirely the important problem of non-physical over-production of turbulence prior to breaking, a long-standing problem in the CFD simulation of surface waves and the primary aim of the present paper. This, in turn, significantly improves both the prediction of turbulent kinetic energy and the evolution of the undertow as waves progress from the shoaling region to the outer surf zone. Conversely, due to their inherent instability, surface waves propagated with existing standard closure models can arrive at the surf zone already polluted, adversely affecting their results, and making the validity of any subsequently simulated breaking process, as a whole, rather questionable. As intended, results with otherwise identical non-stabilized and stabilized closures become similar once the inner surf-zone is reached. In the authors' opinion, in light of the present work, avoiding un-physical over-production of turbulence during wave propagation prior to breaking should henceforth be a pre-requisite for the further simulation of the breaking process. Indeed, we regard this to be necessary for the true performance of existing closures in the surf zone to be properly assessed. Given that the instability addressed in the present work is inherent within the nearly-potential flow region beneath waves, it is thus recommended that formally stabilized closure models, such as those presented herein, be utilized in any future studies involving the RANS-based CFD study of surface waves.

4. Conclusions

In this work the instability of two-equation turbulence closure models in a nearly-potential flow region beneath surface waves has been re-visited, a long-standing problem originally diagnosed by Mayer & Madsen (2000). It has been shown analytically that this problem is widespread and seemingly plagues most (all that the authors have analyzed) commonly used two-equation closure models. These have been demonstrated to be unconditionally (rather than conditionally, as shown by Mayer & Madsen 2000) unstable, and the asymptotic exponential growth rates for the turbulent kinetic energy and eddy viscosity for several closures have been derived in closed form. Working within the confines of an established stress limiting feature in the k - ω model, a new and formally stable closure model is proposed. The new closure model, by design, defaults to a desired

un-modified k - ω model in uniform boundary layer flows and other sheared regions, remains true to theoretically-based terms in the k -equation, is fully consistent with the Boussinesq approximation, and does not require modification of any standard closure coefficients.

The new stabilized turbulence model has been implemented as closure to a computational fluid dynamics model solving Reynolds-averaged Navier-Stokes (RANS) equations, and directly tested for problems involving both non-breaking and breaking surface waves. As a first idealized test a simple periodic progressive wave train has been considered, which has been kept as close to potential flow as possible. Consistent with analytic expectations, it is demonstrated that the standard k - ω model results in exponential growth of the turbulent kinetic energy and eddy viscosity, ultimately destroying the simulation by leading to non-physical decay of the wave. Conversely, the new stabilized closure yields an eddy viscosity that decays to insignificant levels, enabling a nearly-constant form wave propagation over long durations. This test has demonstrated how standard turbulence closure models in wide use can, due to their inherent instability, fail quite spectacularly when applied to even in the simplest of computational surface wave problems. The new stabilized closure, on the other hand, does not adversely affect such simulations.

As a subsequent computational test, the spilling breaking experiment of Ting & Kirby (1994) has been considered, corresponding to the precise incoming wave conditions where the over-production of turbulence beneath surface waves has been most pronounced in the literature. Consistent with several previous studies, it has been shown that standard closure models can lead to severely over-predicted turbulence levels even prior to wave breaking, with pre-breaking turbulent kinetic energy being the same order of magnitude as within the surf zone. This is not physical, but again a direct consequence of their instability, and implies that standard model results in such applications may well be polluted before the phenomenon of physical interest (i.e. the breaking process) has even begun. It is demonstrated that such pollution results in erroneous structure of the undertow velocity profile, both pre-breaking and extending into the outer surf zone. In contrast, the new stabilized closure has been demonstrated to avoid un-physical over-production of pre-breaking turbulence altogether, and results in a model that is able to produce the correct evolution of the undertow structure from outside to within the surf zone. The new closure model has been demonstrated to predict accurate surface elevations throughout the breaking process, as well as reasonable turbulence and undertow profiles, especially prior to breaking and in the outer surf zone. The effect of the formal stabilization in the potential flow regions becomes expectedly less important in the inner surf zone, where results of otherwise identical stabilized or non-stabilized models become similar.

While the main text has focused on variations of the k - ω turbulence closure model, analysis of several other widely used closures (both k - ω and k - ϵ types) are similarly considered in Appendix A. These are likewise demonstrated to be unconditionally unstable, but can fortunately be formally stabilized through similar simple modifications to their stress limiting features. Given the potentially adverse effects of doing otherwise, apparent from several previous studies as well as demonstrated herein, it is recommended that these (or otherwise formally stabilized approaches) be utilized in any future CFD studies involving surface waves based on RANS equations coupled with two-equation closure models. The authors hope that the present study will both raise awareness of this important problem, and that the remedies proposed will enable more accurate simulations of surface waves with such computational models going forward.

5. Acknowledgements

The authors acknowledge financial support from the European Union project ASTARTE–Assessment, Strategy And Risk Reduction for Tsunamis in Europe, Grant no. 603839 (FP7-ENV-2013.6.4-3). The authors also thank Prof. Erik Damgaard Christensen for providing valuable feedback on an earlier version of the manuscript.

REFERENCES

- VAN DER A, D. A., VAN DER ZANDEN, J., O'DONOGHUE, T., HURTHER, D., CACERES, I., MCLELLAND, S. J. & RIBBERINK, J. S. 2017 Large-scale laboratory study of breaking wave hydrodynamics over a fixed bar. *J. Geophys. Res.* **122** (4), 3287–3310.
- BAYKAL, C., SUMER, B. M., FUHRMAN, D. R., JACOBSEN, N. G. & FREDSE, J. 2015 Numerical investigation of flow and scour around a vertical circular cylinder. *Phil. Trans. Roy. Soc. A* **373**, article no. 20140104.
- BAYRAKTAR, D., AHMAD, J., LARSEN, B. E., CARSTENSEN, S. & FUHRMAN, D. R. 2016 Experimental and numerical study of wave-induced backfilling beneath submarine pipelines. *Coast. Eng.* **118**, 63–75.
- BELDEN, J. & TECHET, A. H. 2011 Simultaneous quantitative flow measurement using PIV on both sides of the air-water interface for breaking waves. *Exp. Fluids* **50** (1), 149–161.
- BERBEROVIC, E., VAN HINSBERG, N. P., JAKIRLIC, S., ROISMAN, I. V. & TROPEA, C. 2009 Drop impact onto a liquid layer of finite thickness: Dynamics of the cavity evolution. *Phys. Rev. E* **79** (3), article no. 036306.
- BRADFORD, S. F. 2000 Numerical simulation of surf zone dynamics. *J. Waterw. Port C-ASCE* **126** (1), 1–13.
- BRADFORD, S. F. 2011 Nonhydrostatic model for surf zone simulation. *J. Waterw. Port C-ASCE* **137** (4), 163–174.
- BROWN, S. A., GREAVES, D. M., MAGAR, V. & CONLEY, D. C. 2016 Evaluation of turbulence closure models under spilling and plunging breakers in the surf zone. *Coast. Eng.* **114**, 177–193.
- BURCHARD, H. 2002 *Applied Turbulence Modelling for Marine Waters*. Springer.
- CEBECI, T. & CHANG, K. C. 1978 Calculation of incompressible rough-wall boundary-layer flows. *AIAA J.* **16**, 730–735.
- CHANG, K. A. & LIU, P. L. F. 1998 Velocity, acceleration and vorticity under a breaking wave. *Phys. Fluids* **10** (1), 327–329.
- CHEN, L. F., ZANG, J., HILLIS, A. J., MORGAN, G. C. J. & PLUMMER, A. R. 2014 Numerical investigation of wave-structure interaction using OpenFOAM. *Ocean Eng.* **88**, 91–109.
- CHRISTENSEN, E. D. 2006 Large eddy simulation of spilling and plunging breakers. *Coast. Eng.* **53** (5-6), 463–485.
- DESHPANDE, S. S., ANUMOLU, L. & TRUJILLO, M. F. 2012 Evaluating the performance of the two-phase flow solver interFoam. *Comput. Sci. Discov.* **5** (1), article no. 014016.
- DEVOLDER, B., RAUWOENS, P. & TROCH, P. 2017 Application of a buoyancy-modified $k-\omega$ SST turbulence model to simulate wave run-up around a monopile subjected to regular waves using OpenFOAM (R). *Coast. Eng.* **125**, 81–94.
- DUNCAN, J. H., QIAO, H. B., PHILOMIN, V. & WENZ, A. 1999 Gentle spilling breakers: crest profile evolution. *J. Fluid Mech.* **379**, 191–222.
- DURBIN, P. A. 2009 Limiters and wall treatments in applied turbulence modeling. *Fluid Dyn. Res.* **41** (1), article no. 012203.
- FENTON, J. D. 1988 The numerical solution of steady water wave problems. *Comput. Geosci.* **14**, 357–368.
- FUHRMAN, D. R., BAYKAL, C., SUMER, B. M., JACOBSEN, N. G. & FREDSE, J. 2014 Numerical simulation of wave-induced scour and backfilling processes beneath submarine pipelines. *Coast. Eng.* **94**, 10–22.
- FUHRMAN, D. R., SCHLØER, S. & STERNER, J. 2013 RANS-based simulation of turbulent wave boundary layer and sheet-flow sediment transport processes. *Coast. Eng.* **73**, 151–166.
- GRUE, J. & JENSEN, A. 2006 Experimental velocities and accelerations in very steep wave events in deep water. *Eur. J. Mech. B/Fluids* **25** (5), 554–564.

- HARLOW, F. H. & WELCH, J. E. 1965 Numerical calculation of time-dependent viscous incompressible flow of fluid with free surface. *Phys. Fluids* **8** (12), 2182–2189.
- HIEU, P. D., KATSUTOHI, T. & CA, V. T. 2004 Numerical simulation of breaking waves using a two-phase flow model. *Appl. Math. Mod.* **28** (11), 983–1005.
- HIGUERA, P., LARA, J. L. & LOSADA, I. J. 2013 Simulating coastal engineering processes with OpenFOAM (R). *Coast. Eng.* **71**, 119–134.
- HIRT, C. W. & NICHOLS, B.D. 1981 Volume of fluid VOF method for the dynamics of free boundaries. *J. Comput. Phys.* **39** (1), 201–225.
- HSU, T., HSIEH, C., TSAI, C. & OU, S. 2015 Coupling VOD/PLIC and embedding method for simulating wave breaking on a sloping beach. *J. Marine Sci. Tech.-Taiwan* **23** (4), 498–507.
- HSU, T. J., SAKAKIYAMA, T. & LIU, P. L. F. 2002 A numerical model for wave motions and turbulence flows in front of a composite breakwater. *Coast. Eng.* **46** (1), 25–50.
- HU, Z. Z., GREAVES, D. & RABY, A. 2016 Numerical wave tank study of extreme waves and wave-structure interaction using OpenFoam (R). *Ocean Eng.* **126**, 329–342.
- JACOBSEN, N. G., FREDSSØE, J. & JENSEN, J. H. 2014 Formation and development of a breaker bar under regular waves. Part 1: Model description and hydrodynamics. *Coast. Eng.* **88**, 182–193.
- JACOBSEN, N. G., FUHRMAN, D. R. & FREDSSØE, J. 2012 A wave generation toolbox for the open-source CFD library: OpenFOAM (R). *Int. J. Numer. Meth. Fluids* **70**, 1073–1088.
- JACOBSEN, N. G., VAN GENT, M. R. A. & WOLTERS, G. 2015 Numerical analysis of the interaction of irregular waves with two dimensional permeable coastal structures. *Coast. Eng.* **102**, 13–29.
- KIMMOUN, O. & BRANGER, H. 2007 A particle image velocimetry investigation on laboratory surf-zone breaking waves over a sloping beach. *J. Fluid Mech.* **588**, 353–397.
- LARSEN, B. E., ARBØLL, L. K., FRIGAARD, S., CARSTENSEN, S. & FUHRMAN, D. R. 2018 Experimental study of tsunami-induced scour around a monopile foundation. *Coast. Eng.* **138**, 9–21.
- LARSEN, B. E., FUHRMAN, D. R., BAYKAL, C. & SUMER, B. M. 2017 Tsunami-induced scour around monopile foundations. *Coast. Eng.* **129**, 36–49.
- LARSEN, B. E., FUHRMAN, D. R. & SUMER, B. M. 2016 Simulation of wave-plus-current scour beneath submarine pipelines. *J. Waterw. Port C-ASCE* **142** (5), article no. 08216001.
- LAUNDER, B. E. & SHARMA, B. I. 1974 Application of the energy-dissipation model or turbulence to the calculation of flow near a spinning disc. *Lett. Heat Mass Transfer* **1** (2), 131–7, 131–137.
- LEMOS, C. M. 1992 Wave breaking: A numerical study. In *Lecture Notes in Engineering*, , vol. 71, pp. 1–185. Berlin: Springer.
- LIN, P. Z. & LIU, P. L. F. 1998 A numerical study of breaking waves in the surf zone. *J. Fluid Mech.* **359**, 239–264.
- MAKRIS, C. V., MEMOS, C. D. & KRESTENITIS, Y. N. 2016 Numerical modeling of surf zone dynamics under weakly plunging breakers with sph method. *Ocean Model.* **98**, 12–35.
- MAYER, S. & MADSEN, P. A. 2000 Simulations of breaking waves in the surf zone using a Navier-Stokes solver. In *Proc. 25th Int. Conf. Coast. Eng.*, pp. 928–941. Sydney, Australia.
- MENTER, F. R. 1994 Two-equation eddy-viscosity turbulence models for engineering applications. *AIAA J.* **32** (8), 1598–1605.
- PAULSEN, B. T., BREDMOSE, H., BINGHAM, H. B. & JACOBSEN, N. G. 2014 Forcing of a bottom-mounted circular cylinder by steep regular water waves at finite depth. *J. Fluid Mech.* **755**, 1–34.
- RODI, W. 1987 Examples of calculation methods for flow and mixing in stratified fluids. *J. Geophys. Res.* **92** (C5), 5305–5328.
- ROENBY, J., LARSEN, B. E., BREDMOSE, H. & JASAK, H. 2017 A new volume-of-fluid method in OpenFOAM. In *7th Int. Conf. Comput. Methods Marine Eng.*, pp. 1–12. 7th Int. Conf. Comput. Methods Marine Eng. Nantes, France.
- RUESSINK, B. G., VAN DEN BERG, T. J. J. & VAN RIJN, L. C. 2009 Modeling sediment transport beneath skewed asymmetric waves above a plane bed. *J. Geophys. Res.* **114**, article no. C11021.

- SAKAI, T., MIZUTANI, T. TANAKA, H. & TADA, Y. 1986 Vortex formation in plunging breakers. In *Proc. 20th Conf. Coast. Eng.*, pp. 711–723. Taipei, Taiwan.
- SCHMITT, P. & ELSAESSER, B. 2015 On the use of OpenFOAM to model oscillating wave surge converters. *Ocean Eng.* **108**, 98–104.
- SCHUMANN, U. & GERZ, T. 1995 Turbulent mixing in stably stratified shear flows. *J. Appl. Meteorol.* **34** (1), 33–48.
- SCOTT, C. P., COX, D. T., MADDUX, T. B. & LONG, J. W. 2005 Large-scale laboratory observations of turbulence on a fixed barred beach. *Meas. Sci. Technol.* **16** (10), 1903–1912.
- SHAO, S. 2006 Simulation of breaking wave by SPH method coupled with k - ϵ model. *J. Hydraul. Res.* **44** (3), 338–349.
- STIVE, M. J. F. & WIND, H. G. 1982 A study of radiation stress and set-up in the nearshore region. *Coast. Eng.* **6** (1), 1–25.
- SVENDSEN, I. A. 1987 Analysis of surf zone turbulence. *J. Geophys. Res.* **92** (C5), 5115–5124.
- TING, F. C. K. & KIRBY, J. T. 1994 Observation of undertow and turbulence in a laboratory surf zone. *Coast. Eng.* **24** (1-2), 51–80.
- TING, F. C. K. & KIRBY, J. T. 1996 Dynamics of surf-zone turbulence in a spilling breaker. *Coast. Eng.* **27** (3-4), 131–160.
- TOWNSEND, A.A. 1976 *The Structure of Turbulent Shear Flow*. Cambridge University Press.
- UMLAUF, L., BURCHARD, H. & HUTTER, K. 2003 Extending the k - ω turbulence model towards oceanic applications. *Ocean Model.* **5** (3), 195–218.
- WATANABE, Y. & SAEKI, H. 1999 Three-dimensional large eddy simulation of breaking waves. *Coast. Eng. J.* **41** (3-4), 281–301.
- WILCOX, D. C. 1988 Reassessment of the scale-determining equation for advanced turbulence models. *AIAA J.* **26** (11), 1299–1310.
- WILCOX, D. C. 2006 *Turbulence Modeling for CFD*, 3rd edn. La Canada, California: DCW Industries, Inc.
- WILCOX, D. C. 2008 Formulation of the k - ω turbulence model revisited. *AIAA J.* **46**, 2823–2838.
- XIE, Z. 2013 Two-phase flow modelling of spilling and plunging breaking waves. *Appl. Math. Model.* **37** (6), 3698–3713.
- YAKHOT, V., THANGAM, S., SPEZIALE, C. G., ORSZAG, S. A. & GATSKI, T. B. 1991 Development of turbulence models for shear flows by a double expansion technique. *Inst. Computer Application Sci. Eng.* **NAS1-18605**.

Appendix A. Analysis of additional turbulence closure models

In this appendix three additional popular two-equation turbulence closure models are analyzed for stability in a region of nearly-potential flow with finite strain. It is demonstrated that, in their standard forms, these models are likewise unconditionally unstable. Moreover, it is shown that each may be formally stabilized via the addition of similar stress-limiting modifications, as devised in §2.6. It is recommended that the stabilized versions of these these models be utilized in any future CFD simulations of free surface waves, to avoid non-physical exponential growth of the turbulent kinetic energy and eddy viscosity in the nearly-potential flow region, the significant benefits of which have been demonstrated in the main text.

A.1. k - ω SST model

In addition to the standard k - ω models considered in the main text, another widely used variant is the k - ω SST (shear stress transport) model of Menter (1994). Neglecting convective and diffusive terms as before, in this model the k equation is

$$\frac{\partial k}{\partial t} = \min(\nu_T p_0, c_1 \beta^* \omega k) - \beta^* \omega k, \quad (\text{A } 1)$$

combined with the ω equation from (2.18), from which it is evident that ω will ultimately tend to ω_∞ from (2.20). In this model the eddy viscosity is defined by

$$\nu_T = \frac{a_1 k}{\max(a_1 \omega, F_2 \sqrt{p_0})} \quad (\text{A } 2)$$

where the denominator includes a stress limiting feature somewhat similar to that used in the Wilcox (2006) model. In the above $c_1 = 10$, $a_1 = 0.31$, and α and β are closure coefficients, which are a blend of inner (subscript 1) and outer constants (subscript 2) based on

$$\phi = F_1 \phi_1 + (1 - F_1) \phi_2, \quad (\text{A } 3)$$

where ϕ represents either of these coefficients. The inner coefficients are $\alpha_1 = 0.5532$ and $\beta_1 = 0.075$, whereas the outer coefficients correspond to $\alpha_2 = 0.4403$ $\beta_2 = 0.0828$. This model utilizes the following two blending functions:

$$A_1 = \min \left\{ \max \left(\frac{\sqrt{k}}{\beta^* \omega z_w}, \frac{500\nu}{z_w^2 \omega} \right), 10 \right\}, \quad (\text{A } 4)$$

$$A_2 = \min \left(\max \left[\frac{2\sqrt{k}}{\beta^* \omega z_w}, \frac{500\nu}{z_w^2 \omega} \right], 100 \right), \quad (\text{A } 5)$$

where $F_1 = \tanh(A_1^4)$ and $F_2 = \tanh(A_2^2)$, and z_w represents the distance to the nearest wall.

Due to the blending of inner and outer constants, the min condition in the production term in the k equation (A 1) and the max condition in ν_T (A 2), the analysis of the k - ω SST model is not as simple as in the standard k - ω model variations. It is therefore necessary to split the analysis into three different cases: First, if the first arguments in (A 1) and (A 2) are active, then this model is the same as the standard k - ω model, and hence will result in exponential growth at the rate predicted analytically by (2.22). As this rate is inevitably positive (i.e. regardless if inner or outer coefficients are used) the model will be unstable, and it is hence clear that the model will eventually tend to the inner coefficients, yielding $F_1 = 1$ and $\Gamma_\infty \approx 0.124\sqrt{p_0}$. Second, suppose that the second term in the max condition of (A 2) is active. Inserting the threshold $\omega = \omega_\infty$ into the k equation (A 1) yields

$$\frac{1}{k} \frac{\partial k}{\partial t} = \Gamma_\infty, \quad \Gamma_\infty = \sqrt{p_0} \left(\frac{a_1}{F_2} - \frac{\sqrt{\alpha\beta^*}}{\sqrt{\beta}} \right). \quad (\text{A } 6)$$

Here Γ_∞ is again inevitably positive, and thus inserting $F_2 = 1$ and the inner coefficient values yields $\Gamma_\infty \approx 0.0656\sqrt{p_0}$. Third, suppose that the second term in the min condition (A 1) is active. Inserting $\omega = \omega_\infty$ into (A 1) then similarly yields the growth rate

$$\Gamma_\infty = (c_1 - 1)\beta^* \sqrt{\frac{\alpha}{\beta}} \sqrt{p_0}. \quad (\text{A } 7)$$

This is also inevitably positive, and inserting inner coefficients yields $\Gamma_\infty \approx 2.20\sqrt{p_0}$.

To conclude, the k - ω SST model is also unconditionally unstable, with an asymptotic growth rate that is at least $\Gamma_\infty \approx 0.0656\sqrt{p_0}$, though it may exhibit preliminary exponential growth that is considerably larger. To independently demonstrate the validity of the analysis above, the two differential equations (A 1) and (2.18) (complete with the blending functions above, utilizing $z_w = 10\sqrt{k_0 p_0}$) are again solved numerically, with the same initial conditions as in §2.3 (these are maintained throughout the Appendix). The

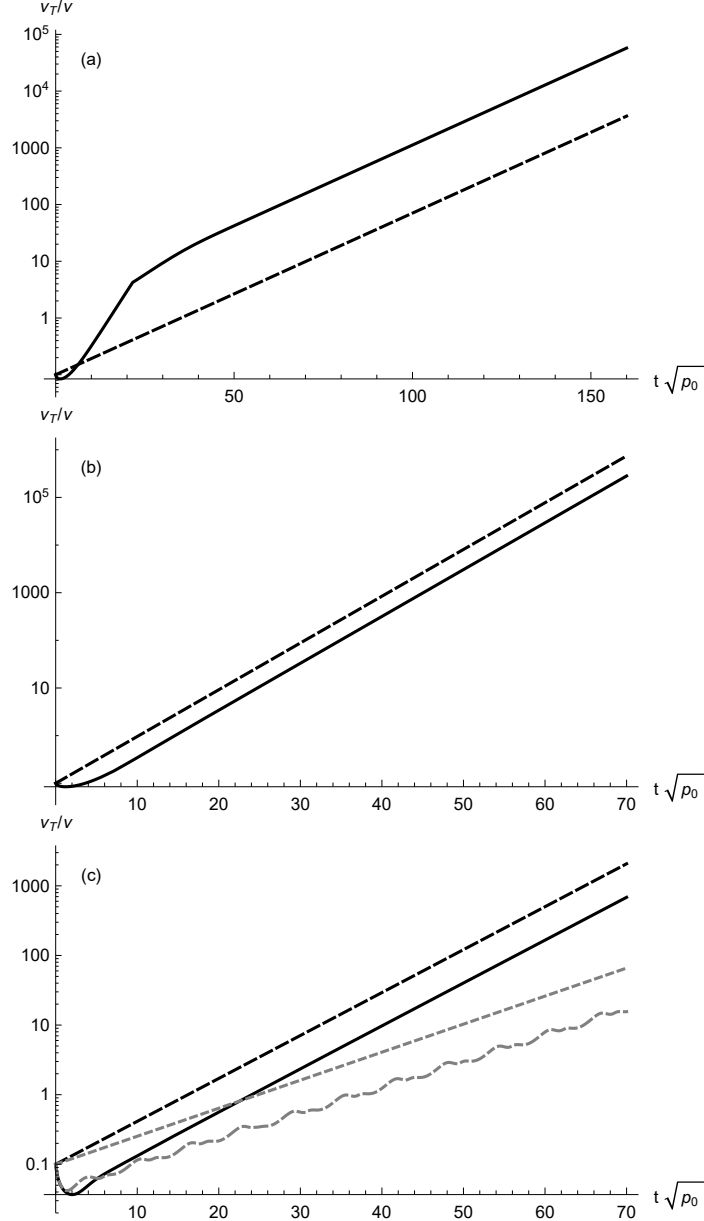


FIGURE 13. Simulated development of ν_T/ν (full lines) compared to the asymptotic exponential growth $\exp(\Gamma_\infty t)$ (dashed lines) for the (a) k - ω SST, (b) k - ϵ , and (c) RNG k - ϵ models. In (c) the grey dashed-dotted line presents numerical results when an oscillation in the production is added as $p_0 + \tilde{p}_0 \sin(\sqrt{p_0}t)$ and the grey dotted line depicts the predicted exponential growth with Γ_∞ calculated analytically from (A 21) with $\omega = \omega_\infty$ from (A 22). After some initial development all numerical results are seen to follow precisely the analytically predicted asymptotic exponential growth rates.

result for ν_T/ν of the numerical solution is shown in figure 13(a), where it is seen that after the initial evolution, the model (full line) is unstable at an accelerated rate, before ultimately arriving at the asymptotic $\Gamma_\infty \approx 0.0656\sqrt{p_0}$ (dashed line) predicted above.

Similar to the standard variants, the k - ω SST model can be stabilized via a slight modification to the stress limiting feature. In this case the necessary modification corresponds e.g. to re-defining the eddy viscosity from (A 2) according to

$$\nu_T = \frac{a_1 k}{\max\left(a_1 \omega, F_2 \sqrt{p_0}, a_1 \lambda_2 \frac{\beta}{\beta^* \alpha} \frac{p_0}{p_\Omega} \omega\right)} \quad (\text{A } 8)$$

where a new (third) argument has been added within the max function, designed to only

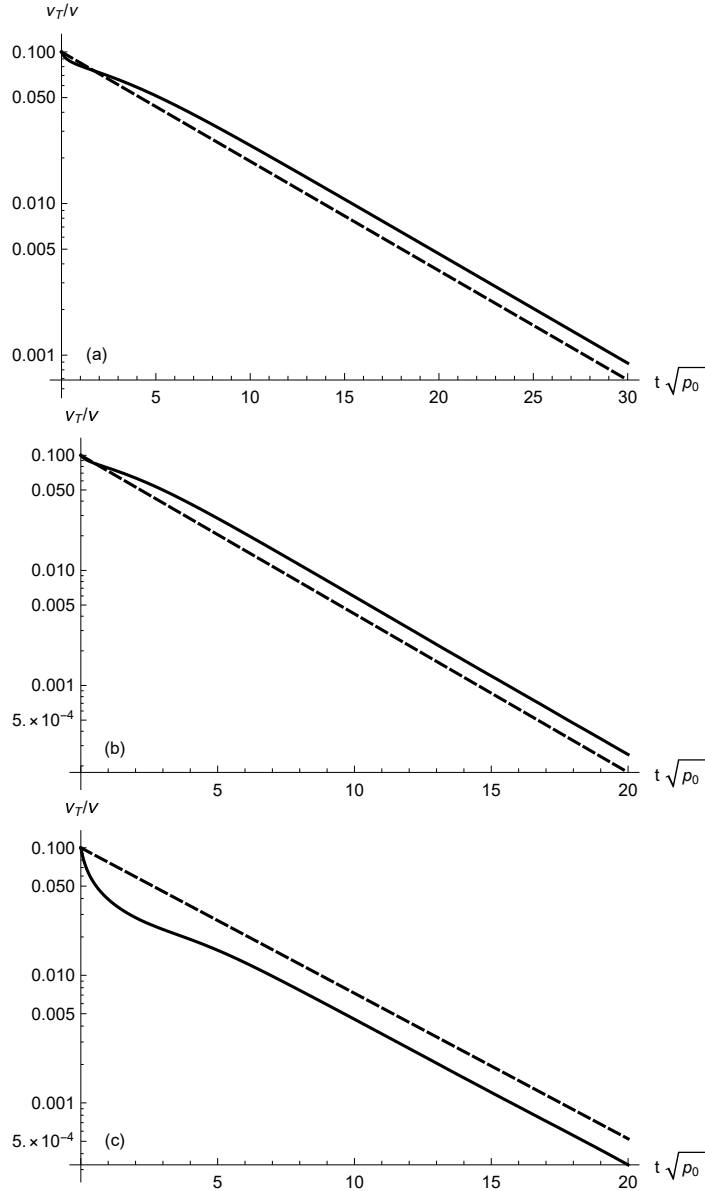


FIGURE 14. Simulated development of ν_T/ν (full lines) compared to the predicted exponential decay $\exp(\Gamma_\infty t)$ (dashed lines) for stabilized versions of the (a) $k-\omega$ SST, (b) $k-\epsilon$, and (c) RNG $k-\epsilon$ models. After some initial development all numerical results are seen to follow precisely the analytically predicted asymptotic exponential decay rates.

be active in a region of nearly-potential flow i.e. where $p_\Omega \ll p_0$. Adopting this value within ν_T , and repeating the analysis above leads to the asymptotic growth rate

$$\Gamma_\infty = \frac{(p_\Omega - \lambda_2 p_0)\beta^*}{\lambda_2} \sqrt{\frac{\alpha}{p_0\beta}}. \quad (\text{A } 9)$$

This is formally stable provided that $p_\Omega/p_0 \leq \lambda_2$, in accordance with (2.38), such that λ_2 defines the effective potential flow threshold, as before. Note that at the pure potential flow limit (where $p_\Omega = 0$) the growth (or in this case, decay) rate is $\Gamma_\infty \approx -0.244\sqrt{p_0}$. Exponential decay in line with that predicted by (A 9) is independently confirmed by numerical solution of the reduced modified model equations in figure 14(a).

A.2. $k-\epsilon$ model

Another widely used class of turbulence closure models are those in the $k-\epsilon$ family. Neglecting convective and diffusive terms, the standard high Reynolds number $k-\epsilon$ model

of Launder & Sharma (1974) reduces to the following two equations

$$\frac{\partial k}{\partial t} = \nu_T p_0 - \varepsilon, \quad (\text{A } 10)$$

$$\frac{\partial \varepsilon}{\partial t} = C_1 C_\mu k p_0 - \frac{C_2 \varepsilon^2}{k}, \quad (\text{A } 11)$$

where the eddy viscosity is defined as

$$\nu_T = \frac{C_\mu k^2}{\varepsilon}. \quad (\text{A } 12)$$

It is emphasized that, similar to the k - ω models considered previously, the eddy viscosity is here retained as a variable only within the k equation; It has been explicitly eliminated within the ε equation by invoking the definition (A 12). This makes no difference to the model in its standard form, but is an important detail in its formal stabilization, to be presented in what follows. The closure coefficients are $C_\mu = 0.09$, $C_1 = 1.44$ and $C_2 = 1.92$.

To analyze the stability of this model, it turns out to be convenient to utilize an equivalent equation for the specific dissipation rate $\omega = \varepsilon/(C_\mu k)$:

$$\frac{\partial \omega}{\partial t} = \frac{1}{C_\mu k} \frac{\partial \varepsilon}{\partial t} - \frac{\varepsilon}{C_\mu k^2} \frac{\partial k}{\partial t} = (C_1 - 1)p_0 - C_\mu(C_2 - 1)\omega^2. \quad (\text{A } 13)$$

Although it is not directly modelled, this variable will still (regardless of the initial conditions) evolve asymptotically to the constant

$$\omega_\infty = \sqrt{\frac{(C_1 - 1)p_0}{C_\mu(C_2 - 1)}} \approx 2.31\sqrt{p_0} \quad (\text{A } 14)$$

such that $\partial\omega/\partial t = 0$. Substituting $\varepsilon = C_\mu\omega k$ with $\omega = \omega_\infty$ back into (A 10) and (A 11) leads to linearized equations of the form (2.21) where the unstable growth rate is

$$\Gamma_\infty = \frac{C_\mu(C_2 - C_1)\sqrt{p_0}}{\sqrt{(C_1 - 1)(C_\mu(C_2 - 1))}} \approx 0.226\sqrt{p_0}. \quad (\text{A } 15)$$

Hence, similar to the pre-existing k - ω models considered previously, the standard k - ε model is likewise unconditionally unstable for the conditions considered. The analysis above is confirmed through independent numerical simulation of (A 10) and (A 11), the results of which are shown in figure 13(b).

It can be noted that Mayer & Madsen (2000) stated, but did not directly show, that the standard k - ε model would also have conditional uncontrollable growth of ν_T when used to simulate surface waves. The analysis above demonstrates this formally, and extends their conditional finding to be unconditional. The instability of the k - ε model is also widely evidenced in simulation of surface waves, with the model resulting in severely over-predicted turbulent kinetic energy, especially pre-breaking as shown by several authors e.g. Bradford (2000) and Xie (2013)

The standard k - ε model presented above can be formally stabilized via the following simple modification to the eddy viscosity:

$$\nu_T = \frac{C_\mu k^2}{\tilde{\varepsilon}}, \quad \tilde{\varepsilon} = \max\left(\varepsilon, \lambda_2 \frac{C_2}{C_1} \frac{p_0}{p_\Omega} \varepsilon\right) \quad (\text{A } 16)$$

In most circumstances (sheared flow regions) the first argument in the max function will be active, and the model is then identical to the standard k - ε model. In a region

of nearly-potential flow, however, the second argument is designed to become active. Letting $\tilde{\varepsilon}$ take this value, and repeating the analysis above leads to the growth rate

$$\Gamma_\infty = \frac{(p_\Omega - \lambda_2 p_0) C_\mu}{\sqrt{\lambda_2 C_2 p_0 - p_\Omega}} \sqrt{\frac{C_1 C_2}{\lambda_2 (C_\mu (C_2 - 1))}}. \quad (\text{A } 17)$$

This is formally stable provided that $p_\Omega/p_0 \leq \lambda_2$, where λ_2 again defines the effective potential flow threshold. Note that the singularity in (A 17) at $p_\Omega/p_0 = C_2 \lambda_2$ is outside the range $p_\Omega/p_0 < C_2 \lambda_2 / C_1$, when the new limiter introduced in (A 16) is active. Note also that at the limit where $p_\Omega = 0$ the growth rate is $\Gamma_\infty \approx -0.375 \sqrt{p_0}$. Exponential decay of the eddy viscosity in accordance with (A 17) is demonstrated via independent numerical solution of (A 10) and (A 11), while invoking (A 16), in figure 14(b) using the same initial conditions as before.

A.3. RNG k - ε model

Neglecting convective and diffusive terms as before, the RNG k - ε model of Yakhot *et al.* (1991) is again comprised of (A 10) and (A 11), but with C_1 now defined as

$$C_1 = C_{1\varepsilon} - \frac{\eta(1 - \eta/\eta_0)}{1 + \beta_{rng} \eta^3} \quad (\text{A } 18)$$

where $\eta_0 = 4.38$, $\beta_{rng} = 0.012$, and $\eta = \sqrt{p_0} k / \varepsilon$, with closure coefficients $C_\mu = 0.0845$, $C_{1\varepsilon} = 1.42$ and $C_2 = 1.68$. The eddy viscosity is again defined according to (A 12). Due to the added complexity of this model our analysis will be performed with all coefficient values invoked. Similar to before, we invoke the above into the equivalent ω equation (A 13), which in this case leads to a complicated polynomial in ω . To find the asymptotic value $\omega = \omega_\infty$ we set $\partial\omega/\partial t = 0$ and look for solutions of the form

$$\omega_\infty = A \sqrt{p_0}. \quad (\text{A } 19)$$

After some simplification, this ultimately leads to the following fifth-order polynomial:

$$A^5 - c_3 A^3 + 225.846 A^2 - 556.477 A - c_0 = 0 \quad (\text{A } 20)$$

where $c_3 = 7.30943$ and $c_0 = 145.377$. This has the lone physical (real and positive) root $A = 2.702$. Invoking this back into (A 10) and (A 11) then leads to linearized equations of the form (2.21), with unstable growth rate

$$\Gamma_\infty = \frac{p_0}{\omega_\infty} - C_\mu \omega_\infty \quad (\text{A } 21)$$

yielding $\Gamma_\infty \approx 0.142 \sqrt{p_0}$. Hence, this model is also unconditionally unstable. The unstable growth rate found analytically above is confirmed via independent numerical simulation of (A 10) and (A 11), after invoking (A 18), in figure 13(c).

Interestingly, in the study of breaking waves by Brown *et al.* (2016), the RNG k - ε model was the only closure model of those tested not to result in excessive turbulence prior to breaking. To investigate the potential reasons for this observation, we have extended the analysis above to also consider the addition of an oscillatory production component i.e. $p_0 + \tilde{p}_0 \sin(\sigma t)$. Repeating the analysis above, it can be shown that, to leading-order in \tilde{p}_0 , the addition of the oscillating components modifies the (now period-averaged) asymptotic value for ω to

$$\langle \omega_\infty \rangle \approx 2.702 \sqrt{p_0 + 0.1795 \frac{\tilde{p}_0^2}{p_0}}, \quad (\text{A } 22)$$

which is obviously an extension of the steady-state result (A 19). We have likewise simulated such a case numerically, taking $\sigma = \sqrt{p_0} = \sqrt{\bar{p}_0}$ for simplicity, and the resulting time evolution of the eddy viscosity is depicted as the dashed-dotted line in figure 13(c). From (A 22) this case yields $\langle \omega_\infty \rangle \approx 2.93\sqrt{p_0}$, which when inserted back into (A 21) results in the predicted period-averaged growth rate $\langle \Gamma_\infty \rangle \approx 0.0927\sqrt{p_0}$. While still positive, this is considerably less than would be expected from the strictly steady-state analysis from either the standard or RNG k - ε models. This predicted exponential growth is likewise depicted on figure 13(c) as the dotted line, which matches nearly perfectly the long-term (period-averaged) growth rate exhibited by the independent numerical simulation. Hence, this extension of the steady-state analysis (as well as the simple numerical simulation) likely demonstrates why reduced growth rates in the CFD simulation of surface waves have seemingly been observed in practice with the RNG k - ε model. Note that similarly adding oscillatory components to p_0 e.g. in the numerical simulation of the reduced standard k - ε or k - ω models does not lead to significant deviations from the growth rates Γ_∞ predicted by the steady-state linear stability theory. Hence, this behaviour is seemingly a rather unique feature of the RNG k - ε model, and can clearly be attributed to the modified term in the ε equation. Nevertheless, despite the potentially reduced growth, this closure is still formally unconditionally unstable at the steady-state limit, and its performance as a whole for simulating surface waves leaves much to be desired. For example, it was ranked as the least accurate of all of the closure models tested by Brown *et al.* (2016), severely overestimating turbulence levels in the inner surf zone.

In any event, similar to the standard k - ε model, the RNG k - ε model can be formally stabilized via the following simple modification to the eddy viscosity:

$$\nu_T = \frac{C_\mu k^2}{\tilde{\varepsilon}}, \quad \tilde{\varepsilon} = \max \left(\varepsilon, 1.2603\lambda_2 \frac{C_2}{C_{1\varepsilon}} \frac{p_0}{p_\Omega} \varepsilon \right). \quad (\text{A } 23)$$

As before, in most circumstances (sheared flow regions) the first term in the max argument will be active, and the model is then identical to the standard RNG k - ε model, whereas in a region of nearly-potential flow the second term will be active. Letting $\tilde{\varepsilon}$ take this value, we will seek a solution for the (steady-state) asymptotic value value for ω of the form

$$\omega_\infty \approx A \sqrt{p_0 + B \frac{p_\Omega}{\lambda_2}}. \quad (\text{A } 24)$$

To accomplish this we set $\partial\omega/\partial t = 0$, and Taylor expand the resulting ω equation about $p_\Omega = 0$. Collecting $O(1)$ terms leads, after some simplification, to a polynomial of the form (A 20), now with $c_0 = 491.512$ and $c_3 = 24.7128$. This has the lone physical (real and positive) root $A = 3.716$. Inserting this value for A and then requiring that $O(p_\Omega)$ terms vanish subsequently yields $B = -0.425254$, thus defining the leading-order contributions for ω_∞ . Inserting $\omega = \omega_\infty$ from (A 24) back into (A 10) and (A 11) leads to linearized equations of the form (2.21), where the asymptotic growth rate is

$$\Gamma_\infty = \frac{0.3140(p_\Omega - \lambda_2 p_0)}{\lambda_2 \sqrt{p_0 - \frac{0.4253 p_\Omega}{\lambda_2}}}. \quad (\text{A } 25)$$

This is again formally stable provided that $p_\Omega/p_0 \leq \lambda_2$, where λ_2 again defines the effective potential flow threshold. Note that the singularity in (A 25) at $p_\Omega/p_0 \approx 2.351\lambda_2$ is outside the range $p_\Omega/p_0 < 1.2603C_2/C_{1\varepsilon}\lambda_2 \approx 1.49\lambda_2$ where the new limiter introduced in (A 23) is active. Note also that at the limit where $p_\Omega = 0$ the growth rate is $\Gamma_\infty \approx -0.314\sqrt{p_0}$. Exponential decay in accordance with (A 25) is demonstrated via

independent numerical solution of the modified RNG k - ε equations, i.e. after invoking (A 23), in figure 14(c).

Appendix B. Derivation of the buoyancy production closure coefficient α_b^*

To derive a value for the buoyancy production closure coefficient α_b^* , consider a sheared flow region such that $\tilde{\omega} = \tilde{\tilde{\omega}}$. Neglecting convective and diffusive terms, but retaining shear and buoyancy production terms, we may reduce (2.1) and (2.2) to

$$\frac{\partial k}{\partial t} = p_0 \nu_T - \alpha_b^* N^2 \nu_T - \beta^* k \omega \quad (\text{B } 1)$$

$$\frac{\partial \omega}{\partial t} = \alpha \frac{\omega}{k} p_0 \nu_T - \beta \omega^2 \quad (\text{B } 2)$$

where the eddy viscosity is intentionally kept general. To find steady state conditions, we set both equations above equal to zero, and solve for p_0 and N^2 . This leads to the steady-state Richardson number

$$Ri_\infty = \frac{N^2}{p_0} = \frac{\beta - \alpha \beta^*}{\alpha_b^* \beta} \approx \frac{0.339}{\alpha_b^*}. \quad (\text{B } 3)$$

According to Schumann & Gerz (1995) (see also Burchard 2002) the constraint $Ri_\infty \leq 0.25$ should be satisfied, implying that, at minimum, we must require $\alpha_b^* \approx 1.36$, which is the value adopted throughout the present work. Note that this is quite similar to the value $1/0.7 \approx 1.4$ used by several other authors (e.g. Rodi 1987; Ruessink *et al.* 2009; Fuhrman *et al.* 2013), and conveniently enables the constraint above to be satisfied without requiring an additional buoyancy production closure term in the ω equation.

Chapter 6

Full-scale CFD simulation of tsunamis. Part 1: Model validation and run-up

This Chapter is under preparation as:

Larsen, B. E., Fuhrman, D. R. (2018). *Full-scale CFD simulation of tsunamis. Part 1: Model validation and run-up.*

Full-scale CFD simulation of tsunamis. Part 1: Model validation and run-up

Bjarke Eltard Larsen^{a,*}, David R. Fuhrman^a

^aTechnical University of Denmark, Department of Mechanical Engineering, Section of Fluid Mechanics, Coastal and Maritime Engineering, DK-2800 Kgs. Lyngby, Denmark

Abstract

This paper presents numerical simulations of the propagation, shoaling and run-up of full-scale tsunami waves. The simulations are performed with a model solving Reynolds-averaged Navier-Stokes equations with $k-\omega$ turbulence closure, and is one of very few studies involving CFD simulations at full tsunami scale, involving full resolution of short scale dispersive effects as well as wave breaking. It is demonstrated that previous analytical expressions for run-up heights match those simulated well. This indicates that these are reasonable even in cases where the underlying assumption of linearity of the incoming tsunami is violated as well as in cases where breaking occurs, though they slightly underestimate the run-up height in these cases. It is shown that the run-up of tsunamis can manifest in different ways depending on the initial wave shape and slope of the coast, and three qualitative run-up types previously identified in the literature are described in detail. It is further shown that the smaller waves of an undular bore, which appear during lengthy propagation in shallow water, can either maintain their shape the entire distance to shore, or break far offshore creating a breaking bore. It is demonstrated the previously identified "wall of water" will not appear in the case of leading depression N-waves, because these need to re-wet the drawn-down region before reaching the original shoreline. Finally, the importance of the smaller waves riding at the front of the tsunami is discussed, and it is shown that they have little impact on the run-up height and inundation distance, but are important in terms of local flow velocities. The results presented here are Part 1 of a larger study, where Part 2 involves details of the tsunami-induced boundary layer dynamics, bed shear stress and implication for sediment transport.

Keywords: Tsunamis, Computational Fluid Dynamics, Run-up, inundation, RANS, Turbulence modelling

1. Introduction

When tsunamis hit a coast they are potentially catastrophic as seen with the two recent major tsunami incidents, the Boxing day tsunami in 2004 in the Indian Ocean, and the Tohoku tsunami in Japan in 2011 where 230,000 and 20,000 people were killed, respectively (Suppasri et al., 2012). These tsunamis also caused severe damage to buildings and structures, and in many places houses and bridges were washed away. With the destructive force of the tsunamis, run-up and inundation have naturally received considerable attention in the past.

Experimentally, however, the run-up of tsunami waves is difficult to study due to the scales involved, even at model scale with a large scaling factor. Jiang et al. (2015) boldly stated that: "both the length and time scales of an actual tsunami wave cannot be down-scaled in wave flume experiments according to the Froude similarity law." A similar point was made by Chen et al. (2012). As a result many have used solitary or other short wave forms, which might be interesting in itself, but their resemblance to geophysical tsunamis is at best questionable (Madsen et al., 2008).

Despite the challenges mentioned above a limited number of studies have been made where reasonable scaling was achieved,

using large scale facilities. Matsuyama et al. (2007) did a properly scaled tsunami experiment in their 200 m long wave flume. Their waves were sinusoidal and ran up different bathymetries. While propagating, the waves developed into undular bores which shoaled, and the individual waves ultimately broke. In this study they did not focus on run-up height, but rather wave transformation, wave breaking and velocities during breaking. To our knowledge this is the first experiment of its sort where undular bores show up in an experimental study involving the run-up of tsunamis. Recently Schimmels et al. (2016) and Sri-ram et al. (2016) generated properly scaled tsunami waves with a piston. The waves propagated on a flat bed, before running up a 1/6 slope. Here the run-up heights were not measured, but they demonstrated the splitting of the wave front into an undular bore, similar to Matsuyama et al. (2007), and they also showed the reflected wave. Others have achieved reasonable scaling using other generation methods, see e.g. the pump generated tsunami experiments by Goseberg et al. (2013), Goseberg (2013), Drahe et al. (2016) and Larsen et al. (2018a).

The run-up of tsunamis has also been studied numerically, often using either non-linear shallow water (NLSW) or Boussinesq models. For good reviews of NLSW models, the reader is referred to Synolakis and Bernard (2006) and Levin and Nosov (2016). Despite not being able to handle dispersion NLSW models have, as stated by Madsen et al. (2016), had reasonable success in simulating geophysical tsunamis. Over long

*Corresponding author

Email address: bje1t@mek.dtu.dk (Bjarke Eltard Larsen)

propagation distances however, a dispersive tail might evolve and when the undular bores form in shallow water dispersion likewise becomes important. (For a more in depth discussion on the role of dispersion for tsunami waves please see Grue et al. (2008), Kim and Lynett (2011), Glimsdal et al. (2013), Løvholt et al. (2012), Grilli et al. (2013).) Dispersion can obviously be handled by Boussinesq type models (see e.g Lynett and Liu (2002), Lynett and Liu (2005) and Fuhrman and Madsen (2009)), but such models are limited to a single-valued free surface and still require a largely empirical breaking model to capture the breaking.

Computational Fluid Dynamics (CFD) models, on the contrary, can in principal handle both non-linearity and dispersion, and in contrast to NLSW and Boussinesq models, actually resolve the breaking process directly. CFD studies of tsunamis are few, however. Horrillo et al. (2006) simulated the propagation of the Indian Ocean tsunami using both a NLSW model, a Boussinesq model and a Reynolds-averaged Navier Stokes (RANS) model and concluded that over long propagation distances dispersion became important, which only the Boussinesq and CFD model could handle. Horrillo et al. (2006) did not go into details regarding the simulated run-up with the CFD model, however. Biscarini (2010) first validated their CFD model against an experimental landslide generated tsunami, and was subsequently able to accurately predict the run-up height of the 1958 Lituya Bay (Alaska) landslide generated tsunami. Montagna et al. (2011) validated their CFD model (Flow 3D) with an experimental landslide generated tsunami and concluded that the model was able to accurately reproduce surface elevations near the generation as well as in inundated areas, but did not proceed to simulate full-scale tsunami events. Tomita and Takahashi (2014) used the STOC-IC model, developed by Tomita et al. (2006), and were able to accurately reproduce an experiment where undular bores showed up at the tsunami wavefront. The STOC-IC model used, however, is not a standard CFD model, as the surface elevation is solved for using a depth-averaged continuity equation. Finally, Qu et al. (2017) compared run-up heights of properly scaled tsunamis with those obtained using a solitary wave. They concluded, similar to Madsen et al. (2008), that there were great differences between solitary waves and properly scaled tsunami waves.

Despite the large number of studies on tsunami run-up, the process is still not fully understood in detail. In this work we will use CFD to study and clarify how tsunamis run-up in different scenarios, both in terms of run-up height, inundation speed as well as a more qualitative description of the run-up sequence. With the latter we intend to focus on the various ways tsunamis can appear at the coast. Often in experiments a breaking bore is assumed, but a tsunami can run-up in other ways as well. We wish to characterise these scenarios and describe when they appear. Finally, as the CFD model naturally handles dispersion and resolves the breaking process without empiricism, this study also aims to investigate the quantitative importance of shorter dispersive waves, sometimes appearing at the tsunami wave front, on both the run-up, inundation speed and local flow velocities. The generated knowledge can potentially be important for hazard assessment by describing run-up heights and in-

undation speeds for different scenarios, as well as design of experimental campaigns (as it can help identify more appropriate run-up scenarios).

The simulations presented here are also used in Larsen and Fuhrman (2018a) (hereafter referred to as Part 2). Here details of the tsunami-induced boundary layer dynamics, bed shear stress and implication for sediment transport are discussed.

The remainder of the study is organized as follows: Model description and boundary conditions are given in Section 2. In Section 3 the model is validated first for propagation of long non-linear waves over large distances by comparing to result by Sriram et al. (2016), and then for its performance on surface elevations and bed shear stresses in the surf and swash zone by comparing to measurements of Sumer et al. (2011). In Section 4 the case selection and model setup is described. Section 5 shows the model results for run-up heights of two archetype tsunami signals using different slopes. Section 6 entails a detailed description of different run-up types, and in Section 7 a discussion of when the different run-up types appear are performed. Finally, in section 8 overall conclusions are drawn.

2. Model description

The simulations are performed in the two-phase volume of fluid method (VOF) flow model `waves2FOAM` developed by Jacobsen et al. (2012). Here the Reynolds-averaged Naviers Stokes (RANS) (1) and continuity (2) equations are solved

$$\frac{\partial \rho u_i}{\partial t} + u_j \frac{\partial \rho u_i}{\partial x_j} = -\frac{\partial p^*}{\partial x_i} - g_j x_j \frac{\partial \rho}{\partial x_i} + \frac{\partial}{\partial x_j} (2\mu S_{ji} + \tau_{ij}), \quad (1)$$

$$\frac{\partial u_i}{\partial x_i} = 0. \quad (2)$$

Here u_i are the ensemble averaged components of the velocities, x_i are the Cartesian coordinates, $\mu = \rho\nu$ is the dynamic molecular viscosity, ν is the kinematic viscosity, ρ is the density, p^* is the pressure in excess of hydrostatic, t is time, S_{ij} is the mean strain rate tensor given by

$$S_{ij} = \frac{1}{2} \left(\frac{\partial u_i}{\partial x_j} + \frac{\partial u_j}{\partial x_i} \right), \quad (3)$$

and τ_{ij} is the Reynolds stress tensor, which is expressed according to the Boussinesq approximation

$$\frac{\tau_{ij}}{\rho} = -\overline{u'_i u'_j} = 2\nu_T S_{ij} - \frac{2}{3} k \delta_{ij}. \quad (4)$$

Here the overbar signifies time (ensemble) averaging, ν_T is the eddy viscosity, δ_{ij} is the Kronecker delta, and

$$k = \frac{1}{2} \overline{u'_i u'_i} \quad (5)$$

is the turbulent kinetic energy density. In the above a prime superscript denotes turbulent (fluctuating) velocity components.

To close the system the $k-\omega$ model of Larsen and Fuhrman (2018b) is used, which is an extension of the Wilcox (2006) model. This model solves transport equations for k

$$\frac{\partial \rho k}{\partial t} + u_j \frac{\partial \rho k}{\partial x_j} = \rho P_k - \rho P_b - \rho \beta^* k \omega + \frac{\partial}{\partial x_j} \left[\left(\mu + \rho \sigma^* \frac{k}{\omega} \right) \frac{\partial k}{\partial x_j} \right] \quad (6)$$

and the specific dissipation rate ω :

$$\frac{\partial \rho \omega}{\partial t} + u_j \frac{\partial \rho \omega}{\partial x_j} = \rho P_\omega - \rho \beta \omega^2 + \rho \frac{\sigma_d}{\omega} \frac{\partial k}{\partial x_j} \frac{\partial \omega}{\partial x_j} + \frac{\partial}{\partial x_j} \left[\left(\mu + \rho \sigma \frac{k}{\omega} \right) \frac{\partial \omega}{\partial x_j} \right]. \quad (7)$$

The shear production term for k is

$$P_k = \tau_{ij} \frac{\partial u_i}{\partial x_j} = p_0 \nu_T, \quad p_0 = 2S_{ij}S_{ij}. \quad (8)$$

Similarly, the buoyancy production for k is formulated as

$$P_b = -\frac{g_i}{\rho} \overline{\rho' u_i'} = p_b \nu_T, \quad p_b = \alpha_b^* N^2, \quad N^2 = \frac{g_i}{\rho} \frac{\partial \rho}{\partial x_i}, \quad (9)$$

where $(g_1, g_2, g_3) = (0, 0, -g)$ is gravitational acceleration and N^2 is the square of the Brunt-Vaisala frequency. The production of ω is likewise taken as

$$P_\omega = \alpha \frac{\omega}{k} \frac{\tilde{\omega}}{\tilde{\omega}} P_k = \alpha \frac{\omega}{\tilde{\omega}} p_0. \quad (10)$$

In this model the eddy viscosity is defined as

$$\nu_T = \frac{k}{\tilde{\omega}} \quad (11)$$

with

$$\tilde{\omega} = \max \left[\omega, \lambda_1 \sqrt{\frac{p_0 - p_b}{\beta^*}} \right], \quad (12)$$

$$\tilde{\omega} = \max \left[\tilde{\omega}, \lambda_2 \frac{\beta}{\beta^* \alpha} \frac{p_0}{\rho \Omega} \omega \right]. \quad (13)$$

The formulation of the Larsen and Fuhrman (2018b) k - ω model above was designed to maintain stability in potential flow regions, while defaulting to a standard closure in sheared regions. Mayer and Madsen (2000) showed that two-equation closure models could be unstable in the potential flow region beneath surface waves, resulting in exponential growth of the turbulent kinetic energy and eddy viscosity, leading to wide-spread over production of turbulence in the literature (see e.g. the recent state-of-the art applications of Brown et al. (2016)). As shown by Larsen and Fuhrman (2018b), the inclusion of the two stress limited versions of ω (i.e. $\tilde{\omega}$ and $\tilde{\tilde{\omega}}$) arranged as above formally solves this wide-spread and long-standing problem.

The standard closure coefficients utilized are those of Wilcox (2006): $\alpha = 0.52$, $\beta = 0.0708$, $\beta^* = 0.09$, $\sigma = 0.5$, $\sigma^* = 0.6$, $\sigma_{do} = 0.125$, with

$$\sigma_d = H \left(\frac{\partial k}{\partial x_j} \frac{\partial \omega}{\partial x_j} \right) \sigma_{do}, \quad (14)$$

where $H(\cdot)$ is the Heaviside step function, which takes a value of unity if the argument is positive and zero otherwise. Additionally, we adopt the value $\alpha_b^* = 1.36$, which was derived by

Larsen and Fuhrman (2018b) as well as the stress limiting terms $\lambda_1 = 0.2$ and $\lambda_2 = 0.05$.

A scalar field γ is used to track the two fluids, where $\gamma = 0$ represents pure air and $\gamma = 1$ pure water, with any intermediate value representing a mixture. The distribution of γ is governed by the advection equation

$$\frac{\partial \gamma}{\partial t} + u_j \frac{\partial u_i \gamma}{\partial x_j} + u_j^r \frac{\partial u_i^r \gamma (1 - \gamma)}{\partial u_i^r} = 0 \quad (15)$$

where u_j^r is a relative velocity used to compress the interface. The method is developed by OpenCFD, and it is documented in Berberovic et al. (2009). Any fluid property Φ in the flow is assumed to be given by

$$\Phi = \gamma \Phi_{water} + (1 - \gamma) \Phi_{air} \quad (16)$$

The boundary conditions are as follows: The bottom will have a no-slip condition imposed such that velocities are zero. For the turbulence quantities at the bottom a generalized wall function approach is used. The friction velocity is determined from the tangential velocity at the nearest cell center, based on the profile of Cebeci and Chang (1978):

$$\frac{u}{U_f} = 2 \int_0^{y_c^+} \frac{dy^+}{1 + [1 + 4\kappa^2(y^+ + \Delta y_{cc}^+)^2 C]^{1/2}}, \quad (17)$$

$$C = [1 - \exp(-(y^+ + \Delta y_{cc}^+)/25)]^2, \quad (18)$$

$$\Delta y_{cc}^+ = 0.9 \left[\sqrt{k_s^+} - k_s^+ \exp\left(-\frac{k_s^+}{6}\right) \right], \quad (19)$$

who generalized the van Driest van Driest (1956) profile to incorporate potential roughness effects, with $y_c = \Delta y/2$ being the normal distance from the wall to the cell center, where Δy is the thickness of the near wall cell, $k_s = 2.5d$ is Nikuradse's equivalent sand roughness and $y_c^+ = y_c U_f / \nu$. The boundary conditions for k and ω are then as described by Fuhrman et al. (2014)

$$\frac{k}{U_f^2} = \min \left\{ A y_c^{+2}, \frac{1}{\sqrt{\beta^*}} \right\}, \quad (20)$$

$$\frac{\omega \nu}{U_f^2} = \max \left\{ \frac{B}{y_c^{+2}}, \frac{1}{\sqrt{\beta^* \kappa} y_c^+} \right\}. \quad (21)$$

The first arguments in these functions ensure that these variables follow their proper scaling $k \sim y^2$ and $\omega \sim 1/y^2$ for near wall cells within the viscous sub-layer (see e.g. Wilcox (2006)). The values $A = 1/(\delta^{+2} \sqrt{\beta^*}) = 0.02466$ and $B = \delta^+ / (\sqrt{\beta^*} \kappa) = 96.885$ are utilized, which ensure a continuous transition to the (fully-turbulent) second arguments at $y_c^+ = \delta^+$, where $\delta^+ = 11.626$ is taken as the viscous sub-layer thickness (in dimensionless wall coordinates). In the first cells nearest the bed, the eddy viscosity is not calculated from (11), but is instead calculated from

$$U_f^2 = \frac{\tau_b}{\rho} = (\nu + \nu_T) \frac{dU}{dz}. \quad (22)$$

The wall functions described above have also been used to a great extent, see e.g. Baykal et al. (2015), Larsen et al. (2016) and Bayraktar et al. (2016).

The tsunami waves in this study, will be specified either as initial conditions or generated at the inlet. Specifically these will be represented by a general N-wave form (the summation of a positive and negative single wave) inspired by Madsen and Schäffer (2010), but with x variation now included. The free-surface is given by

$$\eta(x, t) = A_1 \operatorname{sech} \left[\Omega_1 \left((t - t_1) - \frac{x - x_0}{\sqrt{gh}} \right) \right]^2 - A_2 \operatorname{sech} \left[\Omega_2 \left((t - t_2) - \frac{x - x_0}{\sqrt{gh}} \right) \right]^2 \quad (23)$$

where A_1 and A_2 are the amplitudes of the two single waves, the effective frequencies Ω_1 and Ω_2 defines the time span of the two single waves according to $\Omega_i = 2\pi/T_i$ where T_i can be interpreted as the effective period of the corresponding single wave, defined as the time separating where the surface elevations drops below 0.7% of the amplitude. x_0 defines the center of the wave and t_1 and t_2 can be used to phase shift the two single waves. This signal can be reduced to a single wave by setting $A_2=0$. The horizontal velocity is then given by linear shallow water theory

$$u(x, t) = \sqrt{\frac{g}{h}} \eta(x, t) \quad (24)$$

The vertical velocity is derived from the local continuity equation, and the pressure is calculated as hydrostatic.

3. Model validation

Before simulating the actual tsunami-scale events it is important to validate that the model can, in fact handle the necessary and relevant physics. It is therefore important to show that the model is capable of handling the propagation and wave deformation of long waves over long distances. It is also important to show that the model can handle potential breaking of short waves as well as run-up in situations where breaking occurs.

3.1. Long wave propagation over long distances

In this section the model results are compared to one of the experiments of Sriram et al. (2016). Sriram et al. (2016) investigated how long waves with different shapes and amplitudes propagated on a flat bed and subsequently ran up a steep slope of $S=1/6$. The model will be compared to test "2/3" of Sriram et al. (2016). The incoming wave was a single wave (hence $A_2 = 0$), with a period $T = 30$ s, and an amplitude $A_1 = 0.12$ m at a water depth $h = 1$ m. This wave signal was used as an inlet condition with the inlet of the flume positioned at $x = 0$ m and the toe of the slope at $x = 251.5$ m. Figure 1 shows a sketch of the domain used in the simulations. The mesh in the majority of the domain has a height of $\Delta y = 0.01$ m and $\Delta x = 0.02$ m. This means that 12 cells are used to discretize

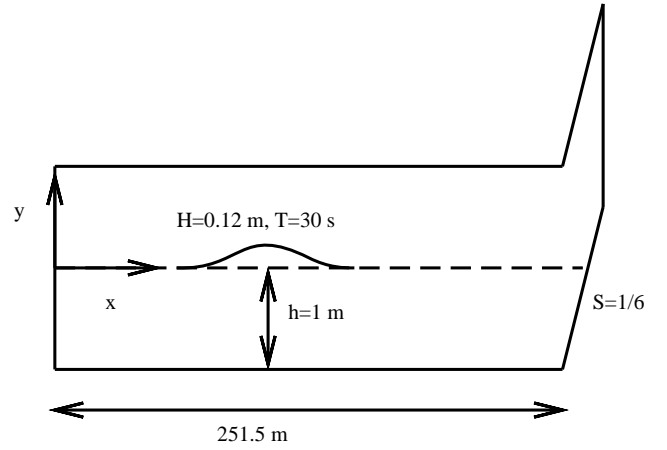


Figure 1: Layout of the computational domain for the Sriram et al. (2016) experiment

the amplitude. This was shown by Larsen et al. (2018b) to be a reasonable resolution for propagating waves. All forthcoming simulations will have at least this number of cells per wave amplitude and keep the same aspect ratio, $\Delta x/\Delta y$. Near the bed the cells were gradually refined in the vertical, with near bed cells having $\Delta y = 6 \cdot 10^{-4}$ m. In this and all future simulations the time step was adjusted such that a maximum Courant number $Co = |u_i|\Delta t/\Delta x_i = 0.15$ is maintained at all times. This is lower than used in most CFD studies, but a low Courant number was shown by Larsen et al. (2018b) to be necessary to accurately simulate free surface waves with the `interFOAM` solver.

Figure 2 shows the modelled and experimental surface elevations at two different locations in the flume. Included for comparison as a dashed line is also the initial analytical single wave expression, with the peak shifted to match the experiments. It can be seen that at $x = 60$ m (Figure 2a) the wave has deformed slightly, now having a steeper wave front, compared to the single wave expression. At $x = 225$ m (Figure 2b) the wave is starting to split and two clear peaks are visible. The third peak in Figure 2b (at approximately $t=117$ s) is the reflected wave. In general the comparison between the CFD model and the experiment is good. The model captures both the initial deformation of the wave (Figure 2a) and the subsequent split and reflection (Figure 2b). This shows that the model, with the present mesh resolution, is capable of handling both dispersion and nonlinearity. That the model is able to capture the reflection accurately also suggests that it is capable of handling the run-up and run-down of a non-breaking long single wave accurately.

3.2. Surface elevations and bed shear stresses in the surf and swash zone

Having shown that the model can handle propagation, deformation and reflection of long waves, we will now validate that the model can handle the more complex surf and swash zone. The model will therefore be compared with experimental results involving a plunging solitary wave by Sumer et al. (2011). Here a solitary wave with amplitude $A_1 = 0.071$ m

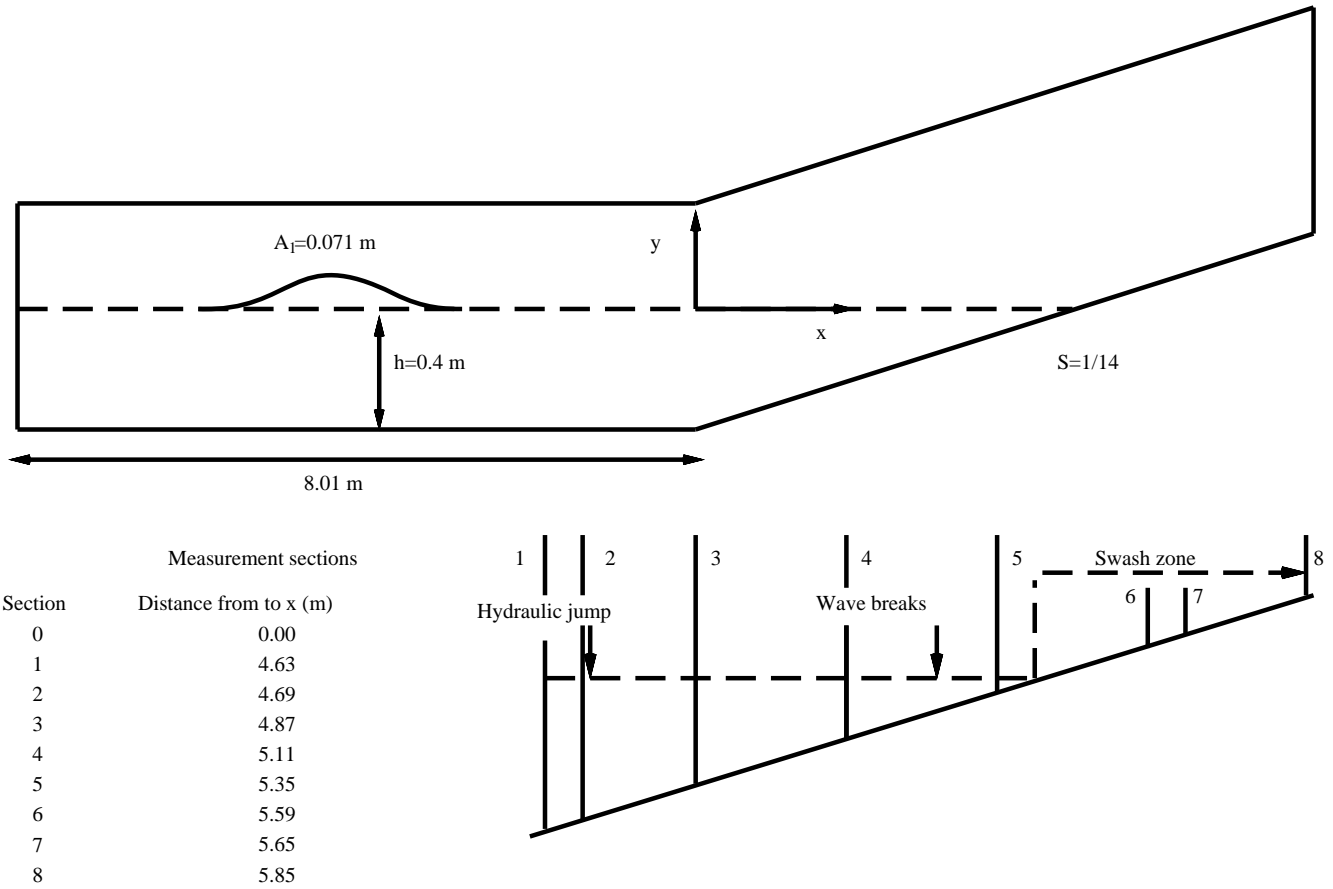


Figure 3: Layout of the computational domain and positions of the measurement sections for the Sumer et al. (2011) experiment

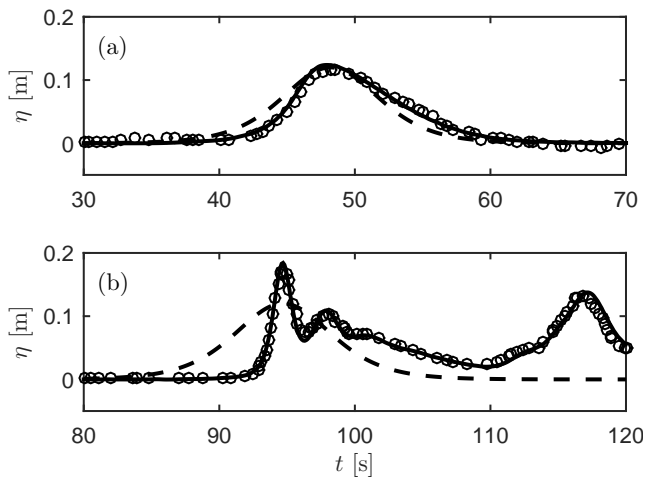


Figure 2: Comparison between modelled (-), experimental (o) from Sriram et al. (2016) and initial single wave (-) surface elevations at (a) $x=60$ m and (b) $x=225$ m.

was generated on a water depth $h = 0.4$ m. The solitary wave can be viewed as a special case of the single wave with $\Omega_1 = \sqrt{3gA_1/(4h)}$. In the experiments, the wave propagated on a flat bed which was 8.01 m long, before continuing up a slope of $S \approx 1/14$. Surface elevations were measured with wave gauges at nine different cross shore positions, and bed shear stresses were measured with hot film at eight different cross shore positions. The toe of the slope is positioned at $x = 0$ m. The layout of the computational domain, as well as the measurement positions (with the exception of section 0, which is positioned at the toe of the slope) are shown in Figure 3. The majority of the domain is discretized into cells having a size of $\Delta y = 0.005$ m and $\Delta x = 0.01$ m, which corresponds to approximately 14 cells per wave amplitude, and an aspect ratio of 2. This is a very similar resolution as in the previous validation case. Near the bed the grid is refined in the vertical with near bed cells having $\Delta y = 6 \cdot 10^{-4}$ m. A solitary wave is initialized in the domain with the crest of the wave positioned 4.5 m from the toe of the slope.

Figure 4 shows a sequence of the computed breaking and run-up of the solitary wave. In Figure 4a,b, a clear plunger is seen, with a small amount of air trapped beneath the plunging wave (Figure 4b). In Figure 4c it is at the maximum run-up height. In Figure 4d a hydraulic jump is forming as the wave is

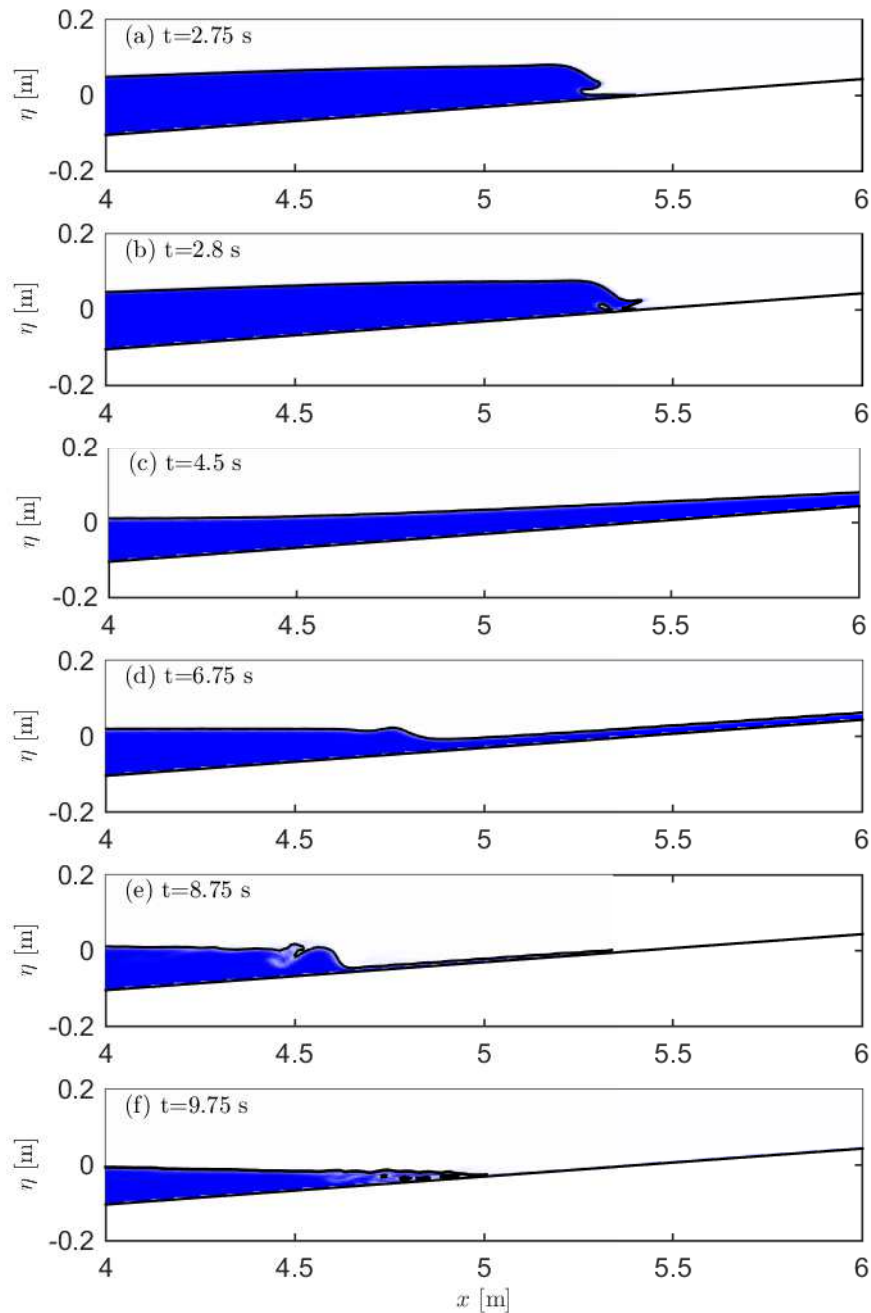


Figure 4: Sequence of the run-up of the solitary wave. The wave can be seen plunging in (a),(b), at full run-up height in (c), the initialization of the hydraulic jump in (d), the hydraulic jump moving seawards in (e) and the trailing wave in (f)

drawing down. This hydraulic jump travels seaward as shown in Figure 4e, and a complicated air-water mixture is seen just seaward of the hydraulic jump. Finally, in Figure 4f a trailing wave, involving a mixture of air and water can be seen. The sequence presented here, is very similar to that shown in Figure 2 of Sumer et al. (2011).

Figure 5 shows the comparison between the experimental and modelled surface elevations at five different cross shore positions. It can be seen that the model is capable of capturing the surface elevation at the toe (Figure 5a), in the shoaling region

(Figure 5b-c), in the surf zone (Figure 5d) and in the swash zone (Figure 5e). The largest discrepancy is found at section 1 during the run-down (Figure 5b at $t=8-10$ s). The reason for this discrepancy is probably that the hydraulic jump forms just onshore of the measurement position at this time, as seen in Figure 4d,e. The hydraulic jump in the experiments occurred at this position (see Figure 2 in Sumer et al. (2011)), but it seems that there are discrepancies in the measured and computed surface elevations (these may, at least in part, be related to the difficulties in clearly defining the surface elevation in this complex region) compared

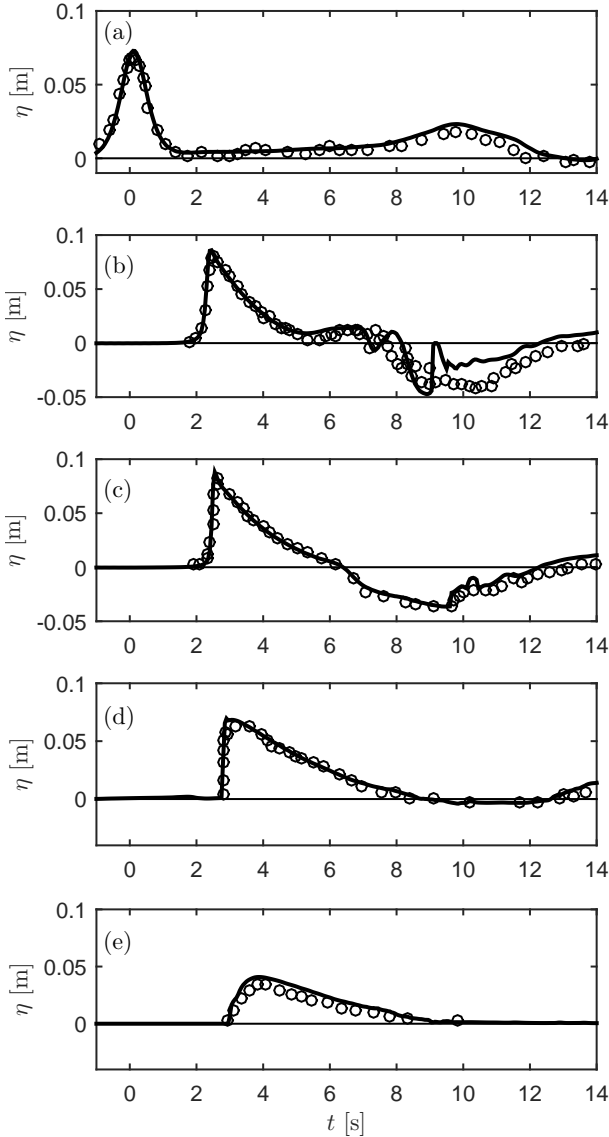


Figure 5: Comparison between modelled (-) and experimental (o) from Sumer et al. (2011) surface elevations at a) section 0, b) section 1, c) section 3, d) section 5) and e) section 8.

to the model.

The run-up height in the experiments was estimated as 18 cm whereas in the simulation it was 21 cm, and is thus slightly overestimated. This is perhaps a bit surprising taking into account the good surface elevation comparison in the swash-zone (Figure 5e). The explanation for this is probably due to the near bed cells having somewhat large aspect ratios. In a VOF model, if γ is larger than zero, there will be a flux over the cell faces, irrespective of the actual location of the water within the cell. Large aspect ratios may therefore cause the tip of the wave to "smear out." Additionally, spurious velocities in the air phase may have added to the overestimation. (The presence of the spurious velocities can be explained by the large density ratio between air and water, meaning that just a small erroneous transfer of momentum across the interface from the heavy to the light fluid will cause a large acceleration of the

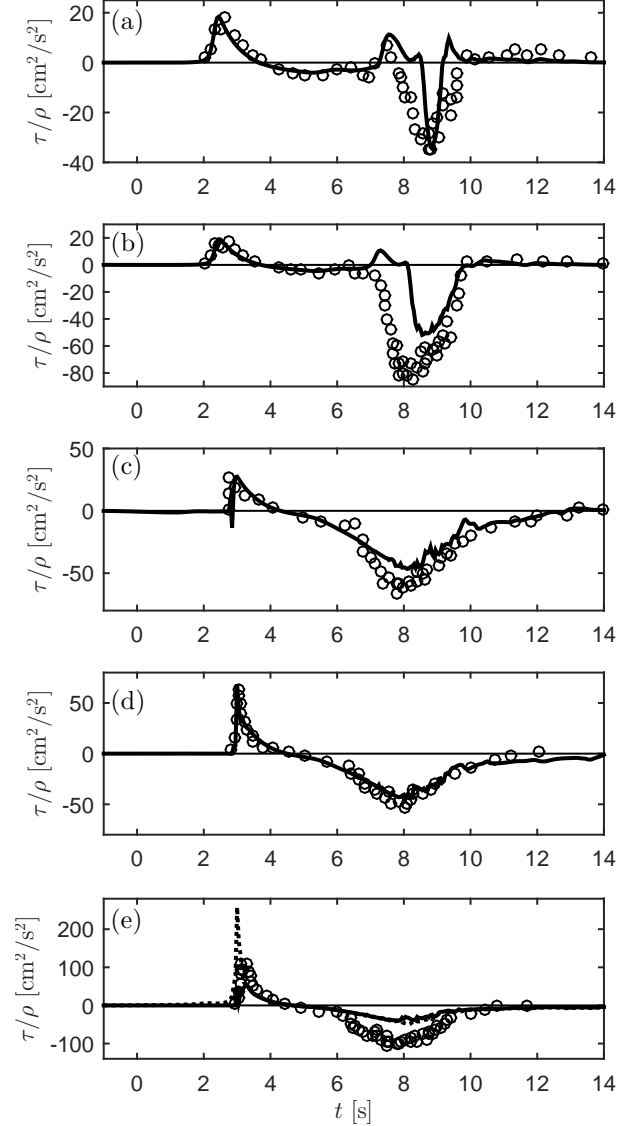


Figure 6: Comparison between modelled using $\rho = 1000 \text{ kg/m}^3$ (-), using ρ_{cell} (·) and experimental (o) from Sumer et al. (2011) bed shear stresses at (a) section 1, (b) section 2, (c) section 5, (d) section 6) and (e) section 8.

light fluid). Such spurious velocities have been documented in many places see e.g. Deshpande et al. (2012) and Wemmenhove et al. (2015). In Larsen et al. (2018b), it was shown that these only affect the wave very near the interface, but at the tip of the swash tongue, there are only one or two cells containing water, suggesting that it might have an effect here. In relation to tsunamis, this effect can be considered small, however, as the tsunamis are much longer, and the tip of swash tongue (with only a few cells of water) will only represent a very small fraction of the full tsunami wave.

The comparison between the bed shear stresses at five different cross shore positions is additionally shown in Figure 6. It can be seen that at all five measurement positions the bed shear stress during run-up is well captured (the first peak). It is slightly underestimated in section 8 (Figure 6a). Here, however, it is expected that the flow consist of a mixture of air and water,

and it is therefore questionable exactly what shear stress was measured by the hot film in the experiments, which was calibrated for pure water. Furthermore, the model in this position also contained a mixture of air and water. For the comparison in Figure 6 (full line) a constant density of $\rho = 1000 \text{ kg/m}^3$, was used, but using the actual density of the near bed cell (shown as the dotted line), the non-dimensional shear stress would have been slightly higher than was measured.

During the draw-down larger differences are seen. In sections 1 and 2 (Figure 6a,b) the negative bed shear stress occurs slightly later in the model than in the experiments. These sections are however placed right around the position where the hydraulic jump forms (see Figure 3). Here slight differences between modelled and experimental surface elevations were seen (Figure 5b). The poorer comparison at this position is therefore apparently more due to the inability of the model to capture details within the hydraulic jump. At sections 5 and 6 the bed shear stress of the draw-down is also well captured by the model (Figure 6c,d). Finally in section 8 the bed shear stress during the draw-down is underestimated. We ascribe this underestimation to the presence of spurious velocities in the air, which are in the opposite direction of the flow. In general the comparison of the bed shear stress is acceptable. There is some uncertainty regarding the performance right around the air/water/bed interface, but in relation to tsunamis this uncertainty can be considered small, as a given cross shore position will either be fully in air or in water for the vast majority of a tsunami event.

4. Case selection and model setup

In this study we will now consider the simple canonical case of 2D tsunami waves propagating over an initial constant depth region, before running up a constant slope. As an inspiration for the present study we use the well-known Mercator yacht signal, which similarly has inspired other tsunami studies see e.g. Williams and Fuhrman (2016) and Larsen et al. (2017). The leading wave was estimated by Madsen and Fuhrman (2008) to be approximately sinusoidal and to have a wave height of 5 m, a period of $T=13$ min at a water depth of $h = 14$ m. This shape, wave height and period is obviously just one realization of a tsunami signal. As an example of the variability of tsunami signals please see Kawai et al. (2013). For the present simulations we will use various generalized N-waves, but all with a crest-to-trough wave height of $H = 5$ m and a period of $T=13$ min at a water depth of $h = 14$ m, similar to the measurements from the Mercator yacht.

Unless stated otherwise the waves will be initialized on a flat bed, which is one wave length long, such that the flat part of the domain houses the entire wave. The waves will then propagate and deform before reaching a constant slope region, where the slope will be systematically varied. A general setup of the computational domain can be seen in Figure 7. Note that $x = 0$ defines the initial shoreline.

It is important to stress that the wave reaching the slope will no longer be precisely given by equation (23), as the wave, similar to the validation case in Figure 2, deforms while propagating. Furthermore, as will be shown later, the presence of the

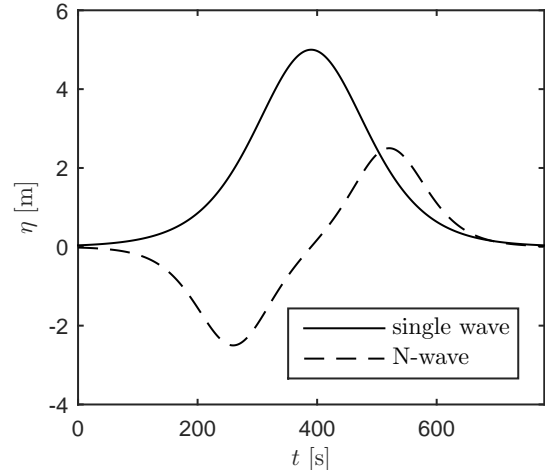


Figure 8: Time signal of the initial waves

toe also effects the incoming wave, such that the surface elevations at the toe of the slope will be slightly different for differing slopes, even with the same initial wave form.

Table 1 gives a summary of the considered cases. In the first half of the table $A_2=0$ and therefore these waves are single waves, with only a positive displacement. The second half of the table contains the N-waves with a leading depression. The periods and phase shifts of the N-waves are chosen to yield the same wave length and crest-to-trough wave height as the single wave cases. Only a leading depression wave was chosen, and not a leading elevation N-wave, as this would run-up similar to the single wave. A_0 is the maximum wave amplitude at the toe of the slope and ξ is the surf similarity parameter given by

$$\xi = \sqrt{\pi} \left(\frac{A_0}{h_0} \right)^{-1/2} \left(\frac{\Omega^2 h_0}{g S^2} \right)^{-1/2}, \quad (25)$$

where $h_0=14$ m is the depth at the toe and $\Omega = 2\pi/T$ is the effective frequency.

Figure 8 shows a time signal of the initial single wave and N-wave used in the simulations. Here it can clearly be seen that the two initial signals represent quite different tsunami realizations despite having the same crest-to-trough height and period. For all cases the domain is discretized into cells $\Delta y = 0.25$ m and $\Delta x = 0.5$ m and from 5 m above the bed and lower the grid is gradually refined in the vertical with near bed cells having $\Delta y = 0.0014$ m. The roughness for the present cases is given by $k_s = 0.001$ m. The simulations to be presented in what follows each took between two weeks and two months to complete when simulated in parallel on 12 modern processors.

5. Model results and run-up heights

This section will describe and discuss the modelled run-up heights. Before continuing, the effect of the slope on the incoming wave will be discussed, as this affects the analysis of the run-up.

As previously stated, the slope itself actually has an impact on the surface elevation at the toe of the slope, such that

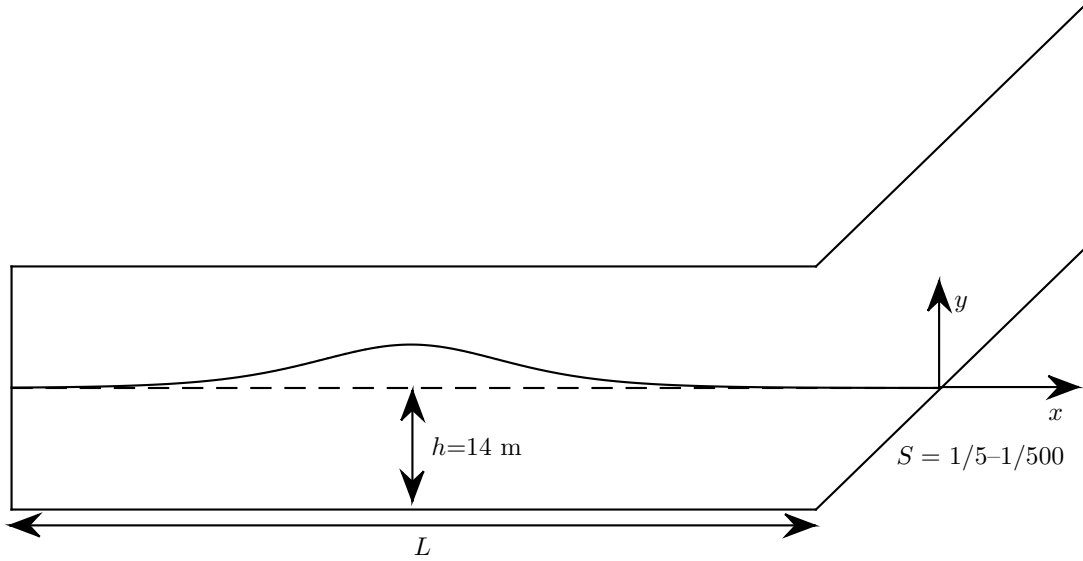


Figure 7: Layout of the computational domain, with origo positioned at the original shoreline.

Table 1: Names, slopes and initial wave parameters of the simulated cases.

Name	S	A_1 [m]	A_2 [m]	T_1 [s]	T_2 [s]	t_1 [s]	t_2 [s]	x_0 [m]	A_0 [m]	ξ
S005	1/5	5	0	780	0	0	0	-4640.5	10.8	41.9
S015	1/15	5	0	780	0	0	0	-4780.5	10.1	14.4
S030	1/30	5	0	780	0	0	0	-4990.5	8.03	8.11
S075	1/75	5	0	780	0	0	0	-5620.5	5.49	3.92
S100	1/100	5	0	780	0	0	0	-5970.5	5.34	2.98
S200	1/200	5	0	780	0	0	0	-7370.5	5.13	1.52
S500	1/500	5	0	780	0	0	0	-11571	5.02	0.62
S030L	1/30	5	0	780	0	0	0	-9561	8.56	7.86
N005	1/5	2.52	2.52	520	520	130	-130	-4640.5	5.45	59.1
N015	1/15	2.52	2.52	520	520	130	-130	-4780.5	4.87	20.8
N030	1/30	2.52	2.52	520	520	130	-130	-4990.5	4.38	11.0
N075	1/75	2.52	2.52	520	520	130	-130	-5620.5	3.21	5.13
N100	1/100	2.52	2.52	520	520	130	-130	-5970.5	2.93	4.03
N200	1/200	2.52	2.52	520	520	130	-130	-7370.5	2.67	2.11

tsunamis with identical initial wave fields, running up different slopes, will have different surface elevation signals at the toe of the slope. To illustrate this Figure 9 shows the surface elevations as a function of time for both single waves and N-waves for three different slopes. Most noticeably both cases with $S=1/5$ result in much larger wave heights than the initial wave signal (see Figure 8) and are substantially higher than the other cases. This can be explained by the tsunami being reflected even before the crest of the tsunami arrives at the slope. The reflected part of the tsunami is then super positioned on top of the incoming wave, resulting in higher surface elevations. This is essentially a transient standing wave, similar to the periodic form shown in Madsen and Fuhrman (2008). For the cases with $S=1/30$ the peak of the surface elevations comes at a later time. This is again due to reflection and the reflected wave interacting with the incoming wave. For the single wave with $S=1/100$, the surface elevation signal shows two distinct peaks,

one for the incoming and one for the reflected wave. However, following the crest of the incoming wave, the surface elevations never return to the still water level before the arrival of the reflected wave. For the single wave, this only occurs for the very mild slope of $S=1/500$ (not included in the figure). For the N-waves, the slope of $S=1/100$ is mild enough that the reflected and the incoming wave can be clearly distinguished.

The surface elevations presented here demonstrate the difficulty in identifying incoming and reflected tsunami waves from a surface elevation signal alone. This can pose a challenge when trying to reproduce a tsunami event, using a measured surface elevation signal as an inlet condition in model simulations.

In Madsen and Schäffer (2010) expressions for the run-up height were given as a function of the surf-similarity parameter ξ for both single waves and N-waves propagating on a constant depth before running up a constant slope, very similar to this study. Their analysis assumes a linear wave at the

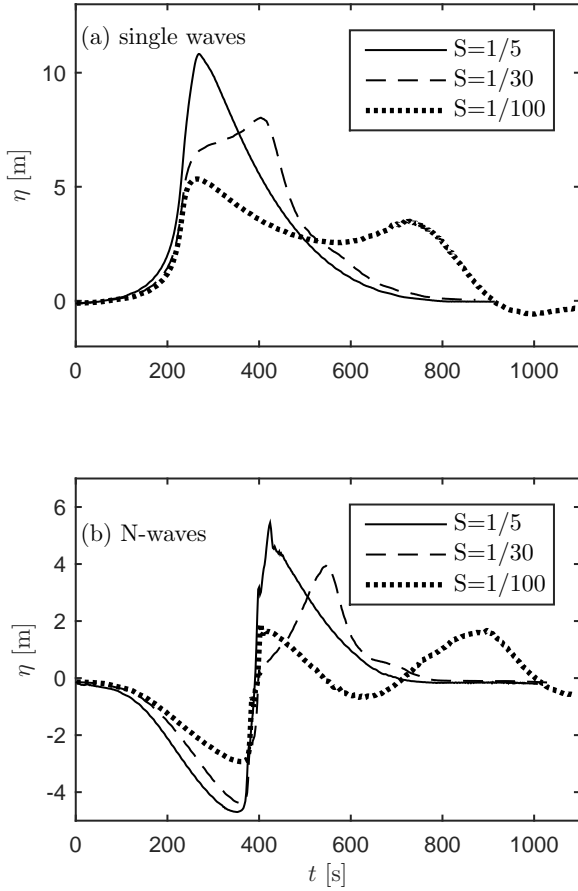


Figure 9: Development of the surface elevation at the toe of the slope for (a) single waves and (b) N-waves.

toe of the slope and although this is not entirely the case in the present study, we will now compare the run-up heights from the simulations to the analytical results from Madsen and Schäffer (2010). Their analysis builds on the hodograph transform by Carrier and Greenspan (1958). They then expressed their solution in terms of both inverse Fourier transformations and convolution integrals to arrive at a solution for the time varying run-up. They provided a breaking criterion which corresponds to the theory breaking down, which happens when the Jacobian vanishes. This corresponds to the time and position where the wave front becomes vertical.

By this analysis the maximum run-up is then given by

$$R_{up}^* = \min(R_{up}, R_{up}^{limit}) \quad (26)$$

where

$$\frac{R_{up}}{A_0} = \chi_{elev} \pi^{1/4} \left(\frac{A_0}{h_0} \right)^{-1/4} \xi^{-1/2}, \quad (27)$$

and

$$\frac{R_{up}^{limit}}{A_0} = \frac{\chi_{elev} \chi_{break}}{\pi} \xi^2. \quad (28)$$

Here χ_{elev} and χ_{break} comes from the analytical analysis of Madsen and Schäffer (2010). They are different for sinusoidal,

Table 2: Values for χ_{elev} and χ_{break} for single waves and N-waves, taken from Madsen and Schäffer (2010).

Wave type	χ_{elev}	χ_{break}
single wave	3.043	0.1561
N-wave	4.243	0.084
Sinusoidal wave	$2\sqrt{\pi}$	$2(\sqrt{\pi})^{-1}$

single- and N-waves and the values used are presented in Table 2

Figure 10 compares the simulated run-up heights with those obtained with equations (25)–(28), for the single waves (included in the figure are also selected labels for those cases described in detail in the next section). As previously shown the amplitudes of the incoming waves are not identical with the different slopes. Therefore the analytical curve has been created using the initial wave amplitude $A_0 = 5$ m, whereas the simulated results are based on the actual A_0 at the toe (indicated in Table 1). This is the most legitimate comparison possible since the Madsen and Schäffer (2010) incident wave contained both the incoming and reflected wave. The analytical solutions of Madsen and Schäffer (2010) are actually a family of curves, and for the cases with A_0 higher than 5 m, the analytical curve would be positioned slightly, but not significantly, lower than that shown in Figure 10.

The analytical curve has two distinct regions. Starting from $\xi = 0$ and increasing the expected run-up heights increase rapidly. This part of the curve (full line) represents the line given by (28), which is the breakdown limit of the theory. To the right of the peak, the curve follows a line given by (27) which corresponds to full reflection at the shore. Included in the figure is also a linear function given by

$$\frac{R_{up}^{Hunt}}{A_0} = \xi, \quad (29)$$

which was suggested by Hunt (1959) to be a better estimate for breaking waves, see also Madsen and Fuhrman (2006). An alternative formulation for the run-up is therefore

$$R_{up}^* = \min(R_{up}, R_{up}^{Hunt}) \quad (30)$$

which is depicted as a dashed line.

It can be seen that, even though the assumption of linearity at the toe is violated the analytical solution and the simulated results agree reasonably well. Similar to observations by Park et al. (2015), the run-up heights are slightly underestimated with the analytical expressions in the region where (28) is dominating. Here the expression by Hunt (1959) seems to give more accurate predictions. This can be explained by the breakdown of NLSW theory not directly corresponding to breaking. Furthermore, even after NLSW theory predicts a vertical surface elevation (approximately interpreted as the tsunamis breaking), the tsunami waves continue to run-up.

Figure 11 compares the simulated run-up heights with those obtained utilizing equations (25)–(28), for the N-waves. Similar to before the analytical curve is made using the initial wave amplitude $A_0 = 2.5$ m and the modelled results have used actual

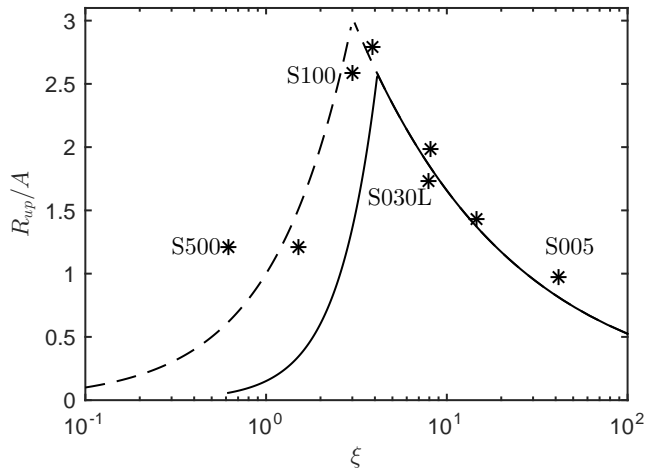


Figure 10: Comparison between modelled (*), analytical (26)(-) and (30) (- -) run-up of the single wave as a function of surf-similarity parameter.

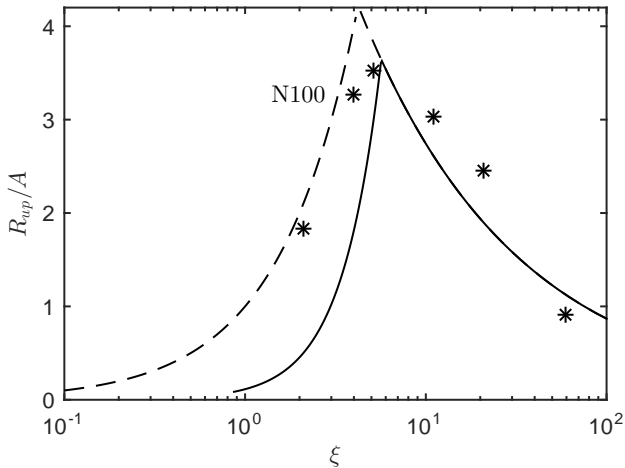


Figure 11: Comparison between modelled (*), analytical (26) (-) and (30) (- -) run-up of the N-wave as a function of surf-similarity parameter.

A_0 at the toe. Here, in general, a good agreement between the modelled run-up heights and the analytical run-up heights is again achieved. Similar to before, the modelled run-up heights are slightly above those obtained with the analytical approach in the region dominated by (28) and the expression by Hunt (1959) (30), seems more appropriate.

Overall, based on the decent match with the more advanced CFD simulations, we would argue that the combined expressions from Madsen and Schäffer (2010) and Hunt (1959), expressed in (30), do a reasonably good job of predicting the run-up heights across a wide range of cases and can be used as a quite reasonable first assessment of the run-up height. As they are based on NLSW equations, however, the detailed information of the actual process is limited. This information can, in contrast, be gathered by the advanced CFD model, as will be done in the next sections.

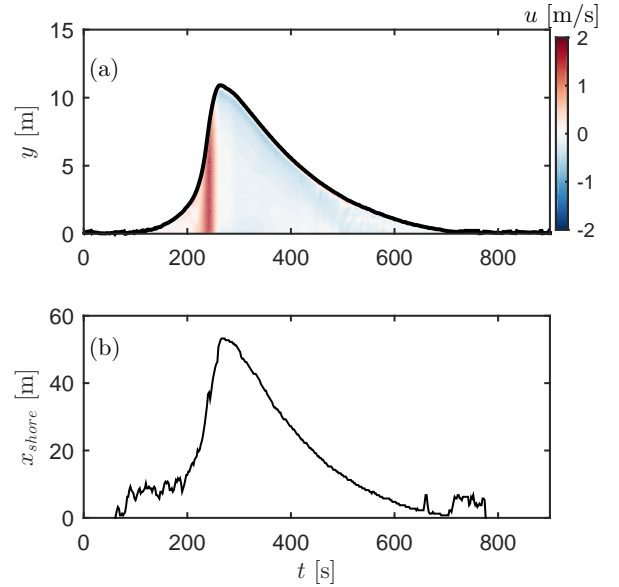


Figure 13: Results for case S005 showing (a) Velocities and surface elevations at $x = 0$, (b) the horizontal position of the shoreline.

6. Qualitative run-up description

The various tsunami signal and slope combinations can yield a wide array of different run-up types. According to Sriram et al. (2016), Shuto (1985) states that the observed tsunamis hitting the coast can broadly be placed into three categories:

- 1) Rapidly rising "tide" (we prefer the phrase "tide-like")
- 2) Breaking bore or "wall of water"
- 3) Undular bore

These three run-up types have all been experienced in the present simulations though we would like to add an additional category, namely:

- 4) An undular bore turning into a breaking bore

In what follows, based on the highly resolved CFD results, we will now describe and study in detail the characteristics of the run-up process for each of these categories. Additionally, we will discuss different run-up features between single- and N-waves. The cases chosen to illustrate these different run-up categories are listed in Table 3.

6.1. "Tide-like" run-up

Now, we will consider the "tide-like" run-up type. As a representation of this type we choose case S005 which is a single wave running up a steep $1/5$ slope. Figure 12 shows results of surface elevations and velocities from case S005 at several different instants. In Figure 12a the initial wave can be seen. In Figure 12b the wave has steepened slightly and has started to inundate the coast, and in Figure 12c the wave is at its maximum run-up. Finally, in Figure 12d the reflected wave can be seen with a steep wave front which ultimately evolves into an undular bore as shown in Figure 12e. From this representation it is very clear that the steep slope of $1/5$ is seen almost as vertical wall by the tsunami, which is fully reflected.

It is noteworthy that there is a phase shift between the maximum velocity and the maximum surface elevation as can be

Table 3: Sections, run-up types, case names and maximum inundation speed of the cases used for the detailed discussion.

Section	Run-up type	Case	Max inundation speed [m/s]
6.1	Tide-like	S005	0.7
6.2	Breaking-bore/wall of water	S100	13
6.3	Undular bore turning into a breaking bore	S500	14
6.4	Undular bore	S030L	6.5
6.5	Breaking bore	N100	12

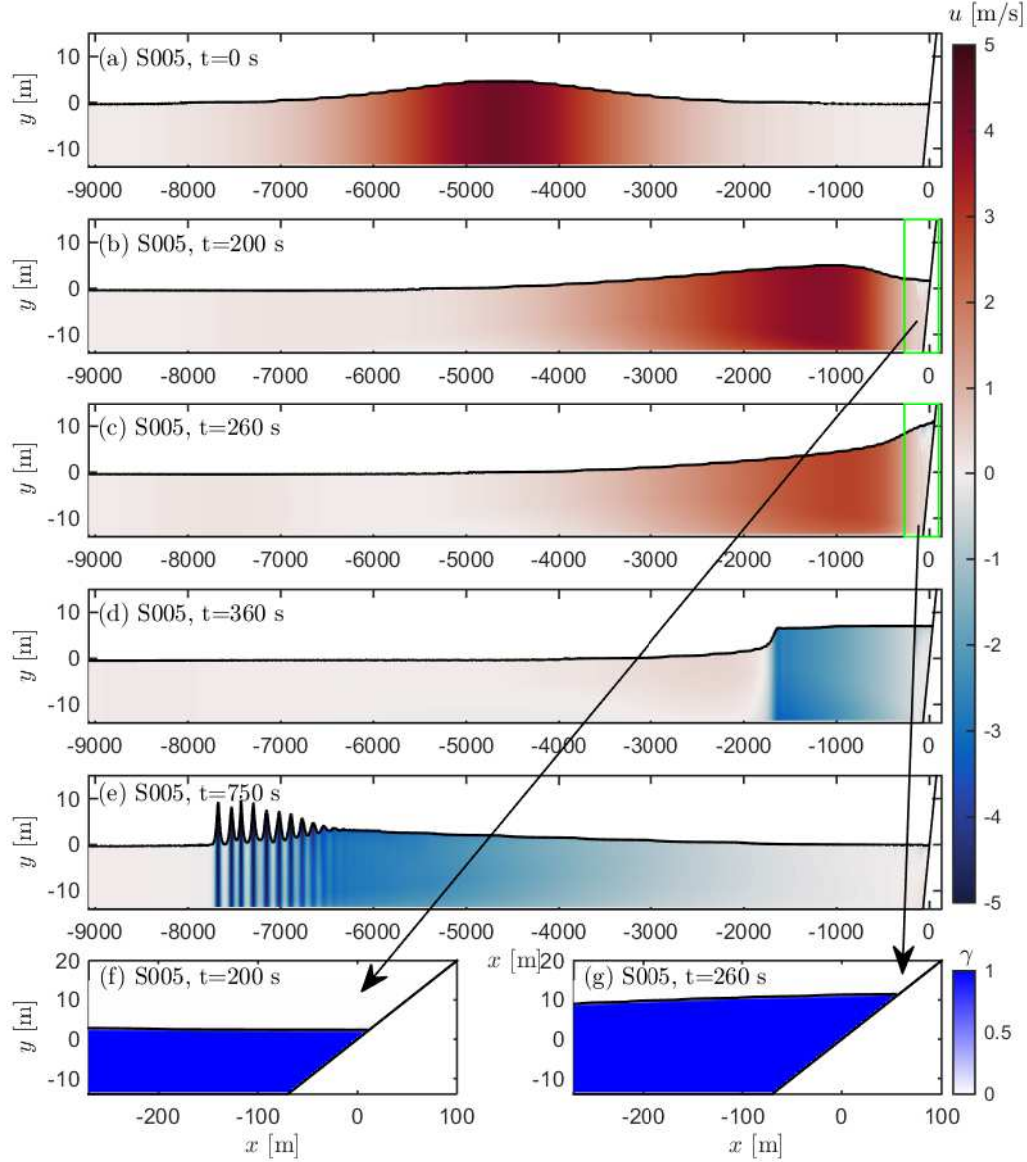


Figure 12: Surface elevation and velocities of S005 at different times.

seen in Figure 12c. This shift can more clearly be seen from a time perspective and therefore Figure 13a shows a time series of the surface elevations and velocities at $x = 0$, corresponding to the original shoreline. In Figure 13b the temporal evolution of the horizontal position of the shoreline, x_{shore} , is shown. From Figure 13a the phase-shift between the maximum free stream velocity and the maximum surface elevation is completely clear.

This phase shift is very similar to what has been observed beneath a real geophysical tsunami by Lacy et al. (2012), and is a result the steep slope acting as a vertical wall, essentially creating a standing wave. This explanation, we believe, provides an alternative and more likely explanation for the phase shift, than that given by Lacy et al. (2012). They explained the phase shift through a near-bed momentum balance, where the bed friction,

they argued, resulted in the 90° phase lag between η and u . The analogy to a standing wave explains this observation in a much simpler manner.

While inundating the tsunami wave front is almost horizontal as can also be seen in Figure 12f-g, which shows zoomed in positions of the wave fronts. At the same time, the increase in water depth at the original shoreline is not very rapid, as illustrated in Figure 13a. Over the initial approximately 3 min the depth at the shore goes from 10 cm to 1 m. From here the increase in water depth is faster and after additionally 1.5 min the depth increases from approximately 1 m to 10 m. Although the increase in surface elevation is large, the duration is still the order of minutes rather than seconds. Finally, Figure 13b illustrates that the inundation speed defined as

$$V_{in} = \frac{\partial x_{shore}}{\partial t}, \quad (31)$$

is very low. The fastest inundation speed (averaging over a minute) is reached during $t = 200\text{--}260$ s, where it reaches approximately 0.7 m/s (2.52 km/h). This present tsunami, could thus easily be outrun. The above observations means, that the tsunami will not be seen as a steep wave, but rather "tide-like." A real life example of this run-up type can be found in the video in TD Interesting Topics Tube (2017) at the time 3:50 to 5:05 and also at 10:25–12:40. These two sequences show the tsunami running into the harbour of Miyako with a seemingly constant, but gradual, increase in water depth. The tsunami enters the harbour next to a seawall, which is finally over-topped in the second video sequence.

As previously mentioned, an undular bore forms at the front of the reflected wave (Figure 12e). This actually also happened in cases S015, S030, N005, N015 and N030. That the undular bore develops in front of the reflected wave is also interesting, and can perhaps help explain why undular bores have been observed at many places in real tsunami events, as reflected tsunami waves will have travelled a long distance in shallow water. The run-up behaviour of undular bores will be discussed later in this section.

6.2. Breaking bore or "wall of water"

To represent the scenario of tsunamis running up as a breaking bore or "wall of water", we will now show results of case S100, which is a single wave running up a 1/100 slope. Figure 14 shows surface elevations and velocities of case S100 at different instants. In Figure 14a the initial wave is shown. Figure 14b shows the shoaled wave with a steep wave front, and significantly higher velocities, as would be expected. The wave front has actually split at this time, and an undular bore is starting to form, as can be seen in the zoom-in of the wave front in Figure 14e. The short wave riding on top of the main tsunami wave cannot maintain its shape for very long, however, as this wave shoals and steepens. After only four seconds, the smaller wave riding on the front of the tsunami breaks, as seen in Figure 14c, and in more detail in the zoom in of the front in Figure 14f. From here the tsunami runs-up the beach like a breaking bore or "wall of water", before it reaches its maximum run-up shown in Figure 14d.

According to the breaking criterion by Madsen and Schäffer (2010) this bulk tsunami would be predicted to break (Figure 10), though it is right near the theoretical threshold. It is important to note, however, that in this case, it was not the main tsunami wave that broke, but rather a short wave riding on the wave front. In all the simulated cases appearing as breaking bores or "walls of water", the wave front initially split into one or more short waves which broke, and turned the entire wave into a breaking bore. Behind the breaking wave front (Figure 14c,f), the surface elevations actually continue to increase, indicating that only a very small fraction of the entire wave is affected by breaking.

In contrast to the previous case (S005) this case did not result in a standing wave, and as a result the free surface elevations and the velocities are in phase. This can be seen more clearly in Figure 15a where the velocities and free-surface elevations at $x = 0$ m are shown. In Figure 15b the temporal development of the shoreline position is shown. From the representation in Figure 15a it is evident that this tsunami runs up as a "wall of water" or breaking bore (the front of the wave is breaking). Similar to before, the depth goes from 10 cm to 1.3 m in the initial approximately 3 min, but hereafter the depth increases rapidly to 4 m in a matter of 4 s. Additionally the inundation speed is also much faster, as can be seen from Figure 15b. The fastest inundation speed (averaging over a minute) at $t = 344\text{--}414$ s corresponds to approximately 13 m/s (47 km/h). This is in sharp contrast to the low inundation speed seen in case S005, and this tsunami could not be outrun.

This rapid increase in water depth, the much larger inundation speed, together with the steep wave front (as seen in Figure 14f), can surely be deemed a wall of water. Breaking bores or "walls of water" have been observed in many instances, and have also often been used as tsunami representations in experiments. Real examples of breaking bores can e.g. be found in videos of the Tohoku tsunami in TD Interesting Topics Tube (2015) at times 3:00–3:15, 4:40–4:48 and 7:50–8:50. This case demonstrates the potential devastation that can arise when tsunamis are near the peak correspondence of the two curves in Figure 10, i.e. where

$$\xi = \chi_{lev}^{-2/3} \pi^{-1/6} \left(\frac{A_0}{h} \right)^{1/6}. \quad (32)$$

6.3. Undular bore turning into a breaking bore

As could be seen from the previous case, the tsunami started evolving towards an undular bore, but the resulting short waves quickly broke before turning into a full undular bore. There were cases where several smaller waves were riding on the wave front, thus forming a more proper undular bore. Similar to before, the individual waves broke before reaching the shore, and as a result turned into a breaking bore. This gave rise to our fourth category namely "an undular bore turning into a breaking bore". This category we will now illustrate using case S500, which is a single wave running up a 1/500 slope (see Figure 10 for its position on the run-up curve).

Figure 16 shows results of surface elevations and velocities at different instants from case S500. Figure 16a shows the initial

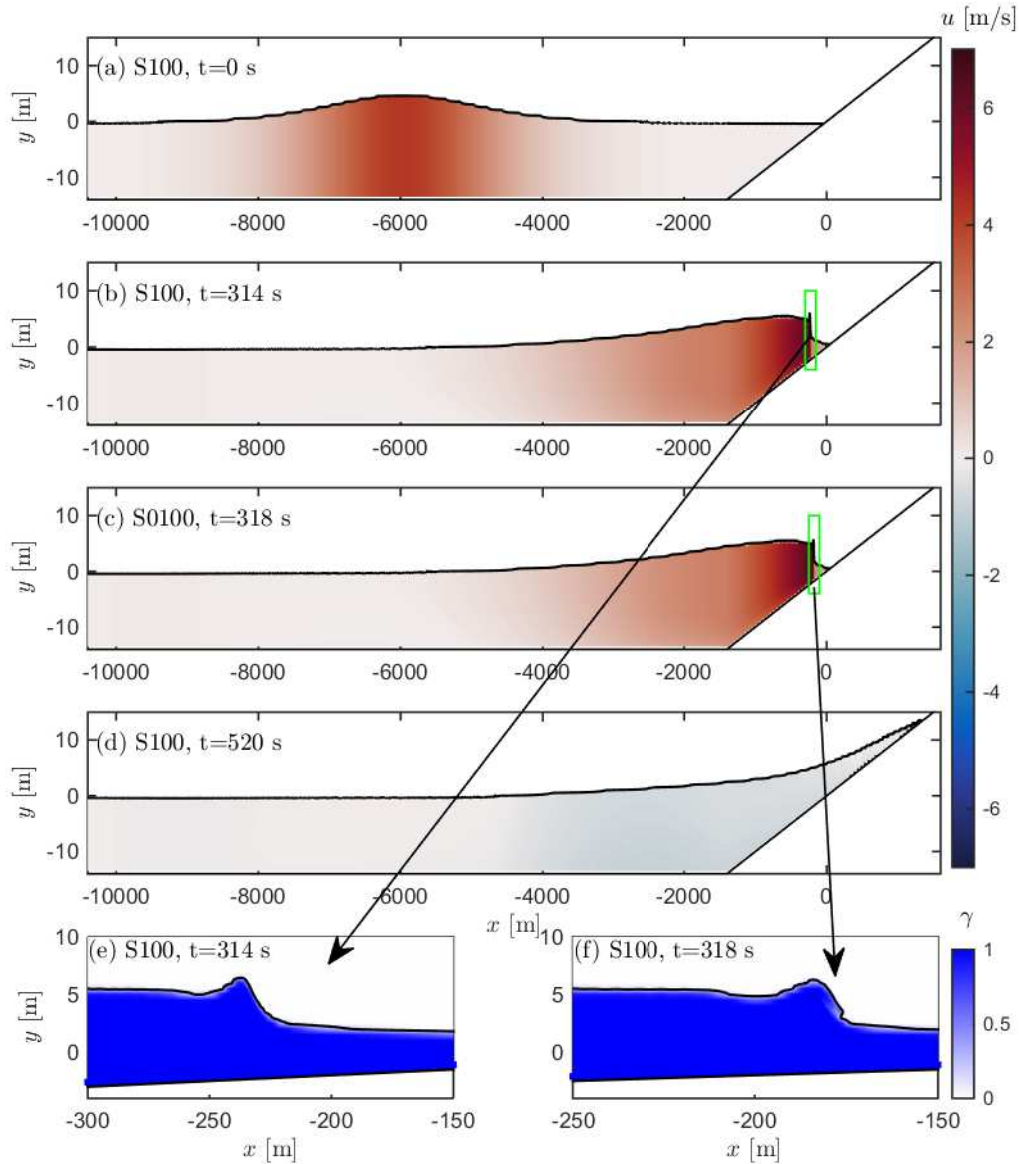


Figure 14: Surface elevation and velocities of S100 at different times.

wave. During shoaling an undular bore forms on the tsunami wave front as seen in Figure 16b. Figure 16e shows a zoomed in portion of the wave front, and here the shorter waves riding on the front are clearly visible. These waves, even though we refer to them as "shorter" are still rather large, with wave lengths of approximately 100 m and wave heights of approximately 10 m, very similar to what have been observed in many places, see e.g. Madsen and Fuhrman (2008) or the videos of the Tohoku tsunami in TD Interesting Topics Tube (2015) from at time 2:10–2:25.

As the tsunami propagates, the waves riding on the wave front shoal and steepen until they at some point break. This is illustrated in Figure 16c as well as the zoom-in Figure 16f where the tsunami is seen after propagating approximately 2 km further than in Figure 16b. Figure 16f clearly shows that the front waves are breaking. Traces of the undular bore can

still be seen, but when this tsunami finally hits the coast (Figure 16d) there are no undulations at the wave front which is purely a breaking bore or "wall of water". This is also illustrated in Figure 17a where the time series of the surface elevations and velocities are shown at the original shoreline ($x = 0$ m). Here it can be seen that for the first 12 min, only small increases in water depth are seen, but then in 6 s the depth suddenly increases to approximately 2 m, before gradually increasing to a maximum of 4 m. From the figure it can also be seen that the milder slope, compared to case S100 (Figure 15), causes the duration that the shore is inundated to be substantially longer. The total inundation is approximately 3 km in this case, which is around twice the inundation distance of case S100. From the temporal development of the shoreline, shown in Figure 17b, it can be gathered that the fastest inundation speed (averaged over a minute) occurs from $t = 794$ – 854 s, and results in an inundation

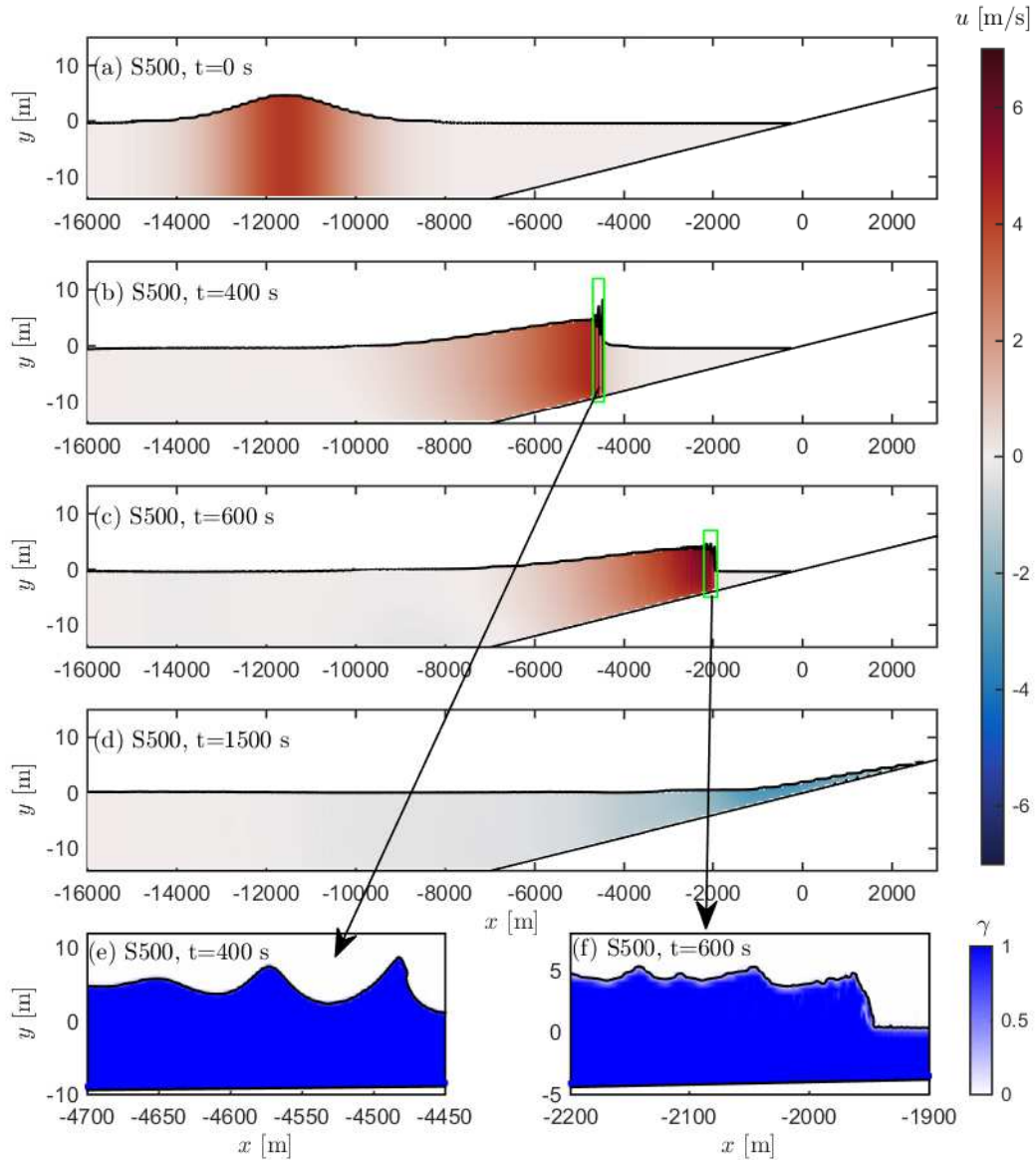


Figure 16: Surface elevation and velocities of S500 at different times.

speed of approximately 13.5 m/s (48.6 km/h), very similar to the previous case (S100), running up as a breaking bore. Obviously, this tsunami could also not be outrun.

6.4. Undular bore

As none of the cases with the initial set-up, with the flat part of the domain being one wave length long, resulted in an undular bore reaching all the way to the coast, an additional simulation has also been made (S030L). This simulation entailed the single wave running onto a slope of $S=1/30$, but with the flat part of the domain being two wave lengths long instead of one, and with the initial tsunami positioned an entire wave length away from the shore. This was done as the formation of undular bores is dependent on the propagation distance in shallow water, as highlighted by Madsen et al. (2008), among others.

Figure 18 shows surface elevations and velocities from case S030L at different times. In Figure 18a the initial wave can be seen, positioned now further away from the coast. While propagating an undular bore evolves at the front of the tsunami as seen in Figure 18b. The undular bore keeps growing with more and more individual waves forming as shown in Figure 18c and in the zoom in in Figure 18e. While shoaling these waves, similar to the previous case S500, steepen and break, as shown in Figure 18d,f. However, due to the steeper slope ($1/30$ relative to $1/500$) the individual waves do not lose all their energy while breaking and survive all the way to the shore as seen in Figure 18f.

The smaller waves riding in front of the tsunami have been given much importance in the past, and the appearance of these is probably one of the reasons why solitary waves have often been used to study tsunamis in the past, despite the previous

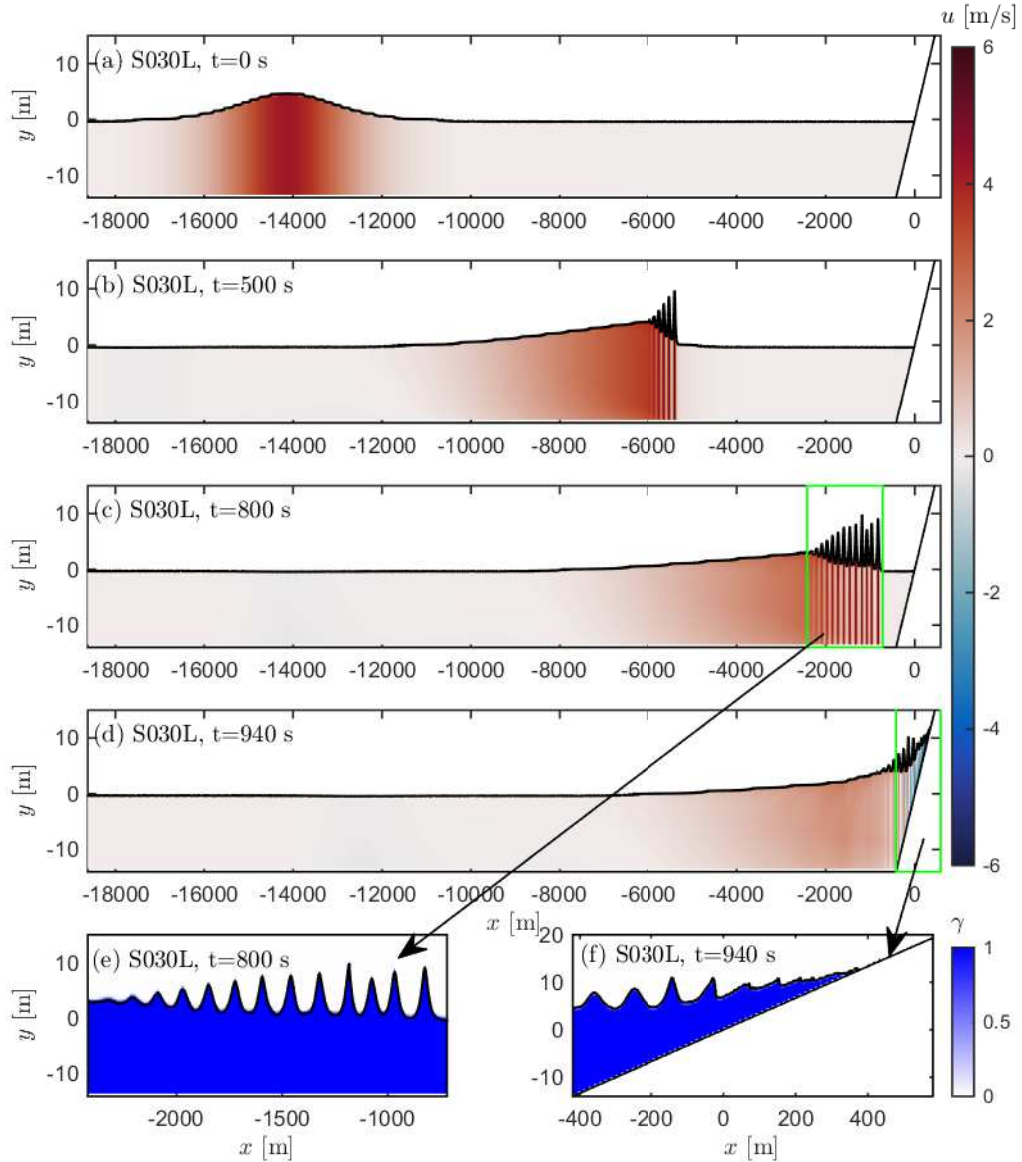


Figure 18: Surface elevation and velocities of S30L at different times.

mentioned scaling issues. To discuss the importance of these smaller waves relative to the bulk tsunami, we will now compare directly case S030 with S030L. These cases have the same initial wave form and are running up the same slope, but have propagated different distances before reaching the slope. Figure 19 shows surface elevations at two different times for S030 and S030L. At the first instant, the wave is approaching the shore. In Figure 19a the wave has steepened slightly compared to the initial single wave, whereas the undular bore is clearly visible in Figure 19b. At the second instant the tsunamis are at their respective maximum run-up. Despite the difference in the approaching wave, it can be seen that the final run-up heights of the two cases are very similar. The run-up height of case S030L is slightly lower, and this can be interpreted as the breaking of the smaller waves extracting small amounts of energy from the main wave. This has not significantly altered the run-up process

as a whole, however.

Another interesting comparison is the inundation speed of the two cases. Figure 20 shows the temporal evolution of the shoreline for cases S030 and S030L. To ease the comparison they are plotted against $t^* = t - t_p$, where t_p is the time where the maximum inundation distance is reached. From this figure it can clearly be seen that the initial inundation speed of case S030L is slightly larger (steeper initial slope), but overall the inundation speed of both cases are very similar. For case S030 the largest inundation speed over a minute is 6.3 m/s (22.7 km/h) and for case S030L it is only slightly larger, namely 6.5 m/s (23.4 km/h). It is worth noting, that despite not breaking, the inundation speed of case S030 is substantially larger than that of case S005, but still also significantly lower than case running up as breaking bores.

The similar run-up height and inundation speed of these two

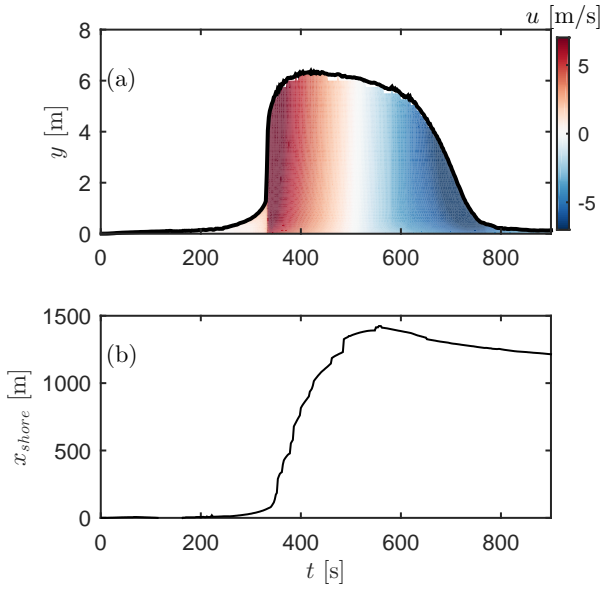


Figure 15: Results for case S100 showing (a) Velocities and surface elevations at $x = 0$, (b) the horizontal position of the shoreline.

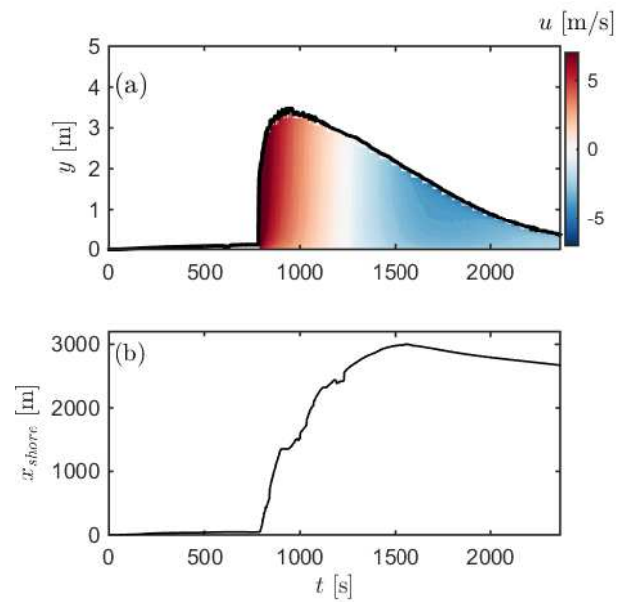


Figure 17: Results for case S500 showing (a) Velocities and surface elevations at $x = 0$, (b) the horizontal position of the shoreline.

cases indicates that the bulk tsunami is much more important than the relatively smaller waves riding on top of it. This point was also previously hypothesized by Madsen et al. (2008) and Madsen and Schäffer (2010), but is more clearly and directly demonstrated in the present fully resolved CFD simulations. Photographs of the tsunami events show undular bores on the tsunami front without showing the main and much longer tsunami wave. This is natural due to the long wave length, but can result in too much importance given to the "shorter" waves. To illustrate this, Figure 21 shows the undular bore seen from the side (Figure 21a) and from a perspective view (Figure 21b). This illustration is very similar to that shown in Madsen et al. (2008), but it raises an important point which needs to be emphasized. When seen from the side, it can clearly be seen that front waves are riding on a much longer main wave. However, when looking from above, only the smaller waves are visible, which is similar to photographs and videos of real tsunami events.

While it has been shown that the undular bore forming in front of a tsunami does not matter much for the run-up distance and inundation speed, it does however matter in terms of local flow velocities. These will be important when assessing forces on structures or estimating sediment transport. To illustrate this Figure 22 shows the velocities and surface elevation of the front of the tsunami for cases S030 and S030L with the front of the tsunami having just inundated past the original shoreline ($x = 0$). It can be seen, that the maximum flow velocity of case S030 is right at the tip of the inundating tsunami with velocities reaching approximately 10 m/s. The maximum flow velocities of case S030L, on the other hand, are reached in the tip of the breaking short waves, with velocities here reaching up to 19 m/s. These differences in velocities may be important for the impact forces on structures. This indicates, that if attempting to model tsunami forces on structures, choosing a model which

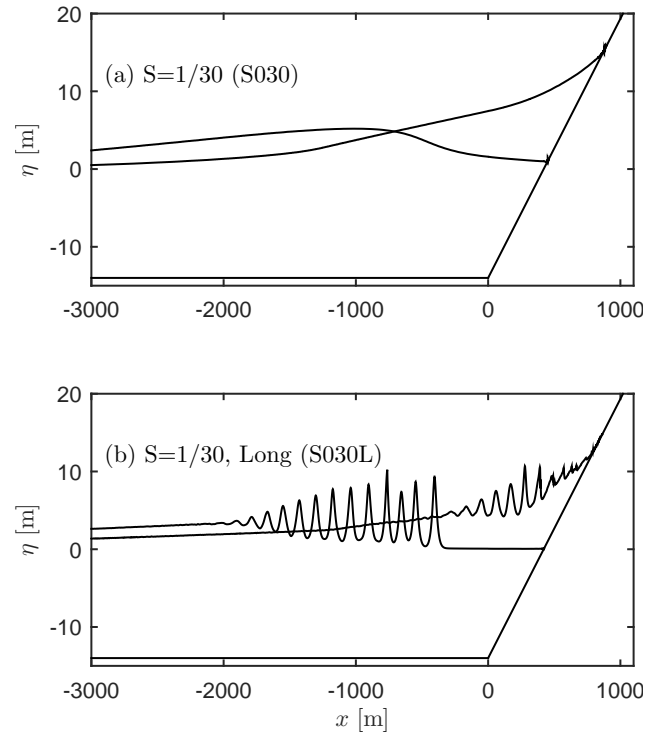


Figure 19: Comparison of run-up of singles wave on a $S=1/30$ slope.

can handle dispersion and wave breaking is important.

6.5. N-waves

Thus far all examples of run-up types have been illustrated using single waves. The same run-up types as just described (except the undular bore, which required a longer domain to fully evolve) have also been experienced with the leading depression N-waves. There are, however, also some distinct dif-

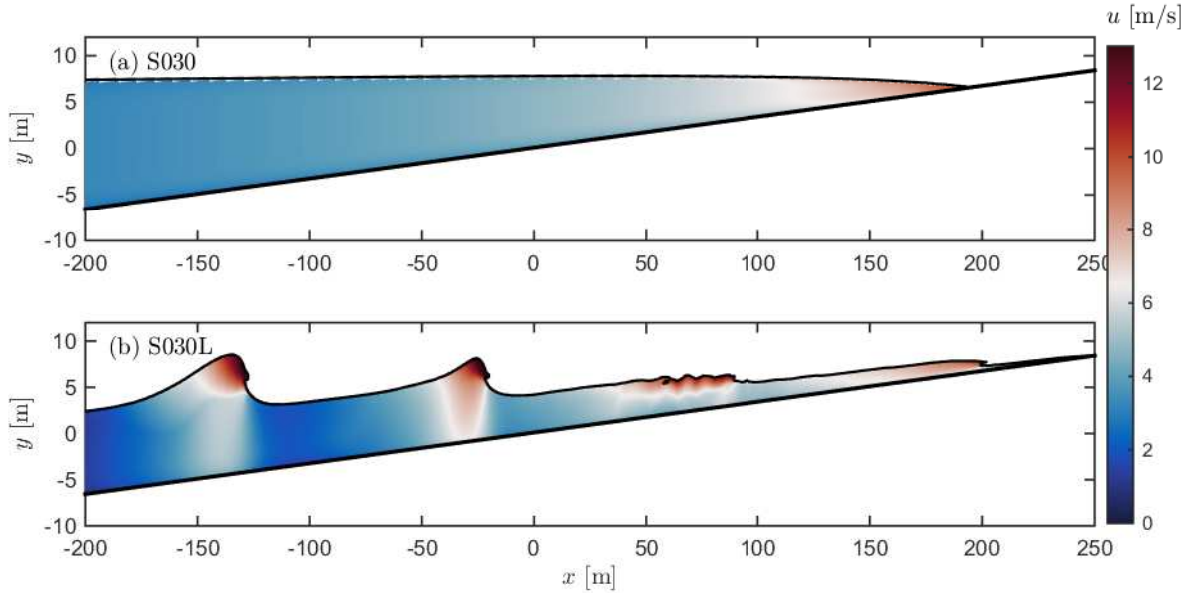


Figure 22: Surface elevations and velocities of (a) case S030 and (b) case S030L.

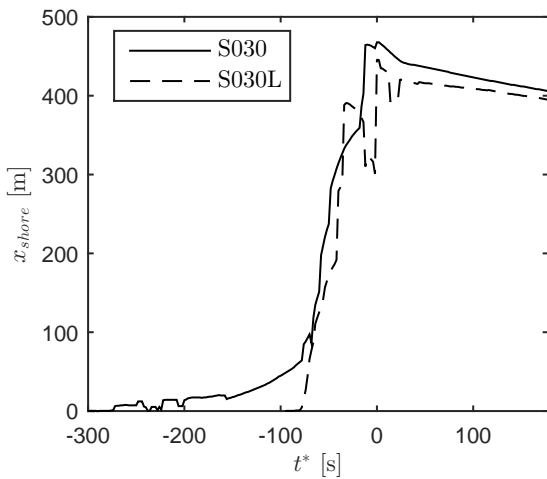


Figure 20: Development in shoreline position for cases S030 and S030L.

ferences between the run-up of single waves and leading depression N-waves. These will be discussed in what follows, by considering specifically case N100 (See Figure 11 for this case's position on the run-up curve).

Figure 23 shows surface elevations and velocities at different instants for case N100. In contrast to the previous cases, the initial wave shown in Figure 23a now has a leading depression. The leading depression results in an initially retreating shoreline, as seen in Figure 23b. Leading depression tsunamis with retreating shorelines have been observed many places; One of the most memorable and unfortunate situations is probably the tourist standing on a dry beach in Thailand with the front of the Indian Ocean tsunami approaching, see Figure 1 of Foster (2014).

Figure 23b also reveals an additional feature which is dis-

tinctly different than the previously simulated single waves, namely that the split of the front wave is not happening at the crest of the tsunami, but rather in between the trough and the crest. This can more clearly be seen in Figure 23e. A similar observation was also made in the experimental study Matsuyama et al. (2007), where it was shown that the individual waves in some cases evolved in front of the crest of the wave. Here the waves were leading elevation sinusoidal-like waves, and thus the split occurring in front of the crest in the simulation is not due to the leading depression. The split rather occurs where the local surface elevation steepness is largest. In these simulations this was the case between the trough and crest, whereas in the experiments, due to the imperfect initial sinusoidal shape, it happened in front of the wave crest.

Similar to case S100 the individual wave seen in Figure 23b,e cannot sustain its shape during shoaling, and breaks before reaching the slope. This wave therefore runs up as a breaking bore as shown in Figure 23c,f. We will however not classify the run-up of the present case as a "wall of water". As can be seen in Figure 23f, the front of the bore is only approximately 1 m high. At the same time the increase in water depth is not nearly as rapid as in cases S100 and S500 (Figures 15 and 17). This can be seen in Figure 24a where the time series of the surface elevations and velocities at $x = 0$ m are shown for case N100. Here it can clearly be seen that the depth increases much more gradually than case S100 and S500 going from 0–3 m in slightly over a minute. The reason for this could be the leading depression, which causes the shoreline to retreat as seen in Figure 24b. The breaking tsunami front will therefore re-wet the drawn-down region prior to reaching the original shoreline at $x = 0$. The appearance of this tsunami wave front is more similar to the appearance of cases S100 and S500 further inland.

The inundation velocity of the present case is ultimately very similar to the single wave cases running up as a breaking bore.

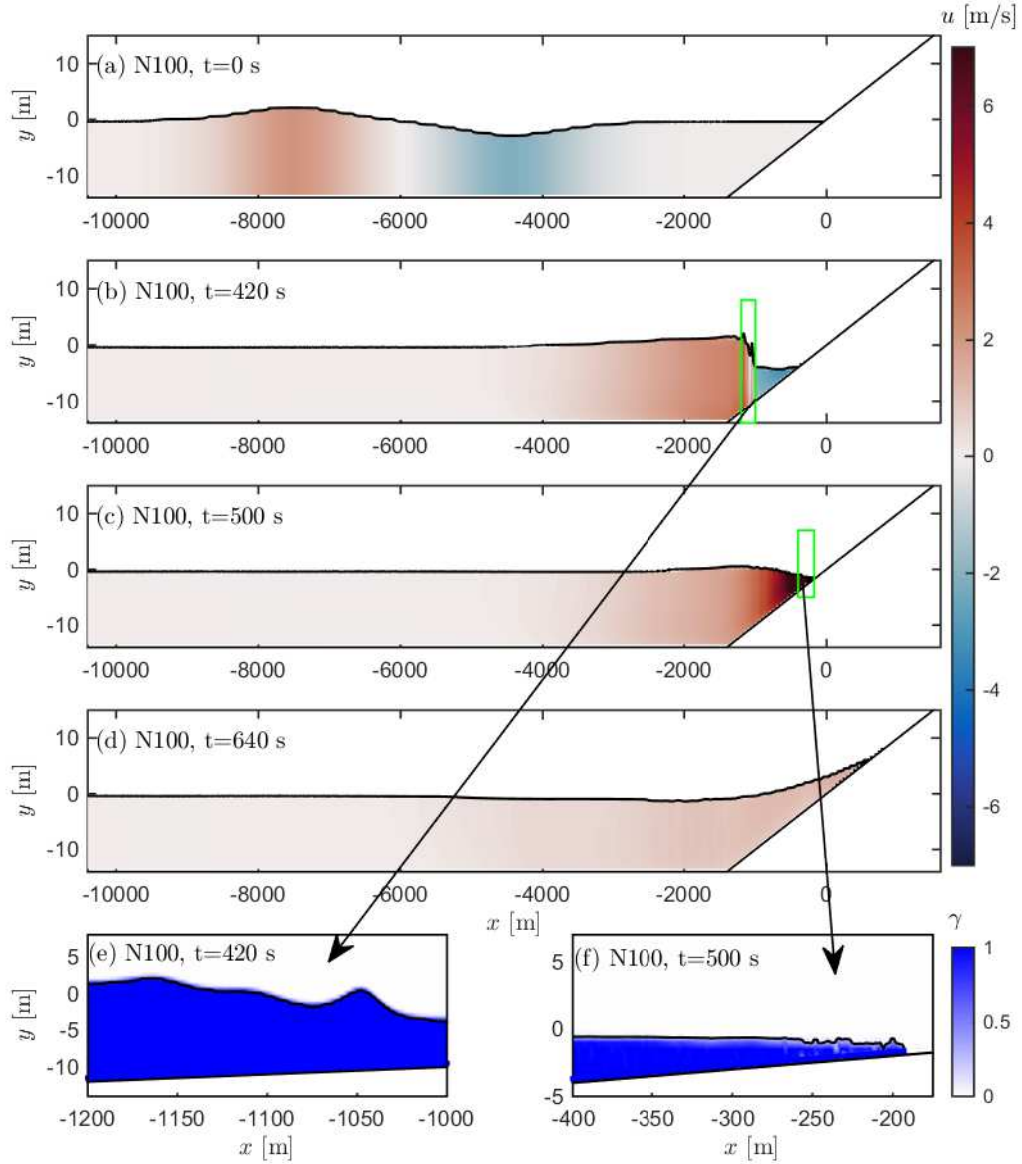


Figure 23: Surface elevation and velocities of N100 at different times.

The maximum inundation speed (averaging over a minute) occurs at $t = 542\text{--}602$ s with a value of 12 m/s (43 km/h), indicating again that it would be impossible to outrun this tsunami run-up type.

7. Expected occurrence of the run-up types

In the previous subsections the run-up types have been described in detail and a new run-up type has likewise been framed. We will now discuss in which situations these run-up types can be expected to show up.

The first identified category, was the "tide like" tsunami. This run-up type was only experienced in cases where the slope was very steep. In fact, it was only experienced in cases where the run-up from (27), from the analysis of Madsen and Schäffer (2010) was less than (29), corresponding to the right solid line

in Figures 10 and 11. In that sense the surf-similarity parameter can be used to access whether a "tide like" scenario is possible. However, as shown in case S030L, if the tsunami has propagated sufficiently far before reaching the toe of slope, an undular bore can develop. In this case the wave at the toe of slope was no longer at all described by (23). Furthermore, near the intersection of the two curves, it is not certain that a clear distinction between breaking and non-breaking cases can be made. We therefore believe it is fair to assume, that if the tsunami reaching the slope is linear (as was a pre-requisite for the Madsen and Schäffer (2010) analysis), then cases far to the right of the intersection between (27) and (29), will appear "tide-like". This can be expressed in terms of the surf-similarity parameter by

$$\xi \gg \chi_{elev}^{-2/3} \pi^{-1/6} \left(\frac{A_0}{h}\right)^{1/6} \quad (33)$$

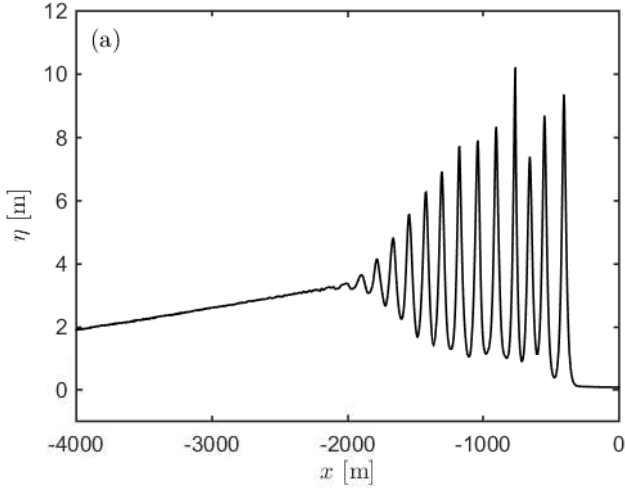


Figure 21: A side looking (a) and a perspective view (b) of the undular bore

or alternatively

$$\Upsilon = \frac{h_0^{1/6} \sqrt{gS}}{\Omega A_0^{2/3}} \gg (\chi_{elev} \pi)^{2/3} \quad (34)$$

The second category, the breaking bores or "wall of water", all appeared in situations near the intersection of (27) and (29) or where $\xi < \chi_{elev}^{-2/3} \pi^{-1/6} \left(\frac{A_0}{h}\right)^{1/6}$, alternatively expressed as $\Upsilon < (\chi_{elev} \pi)^{2/3}$. The latter corresponds to cases where wave breaking is predicted to be present, corresponding to the left dashed line in Figures 10 and 11. However, this will not alone make the tsunami run-up as a breaking bore or wall of water. In situations where the slope is very mild, an undular bore can form on the front of the tsunami. Furthermore, for leading depression waves, the tsunami will be re-wetting the drawn-down region prior to reaching the original shoreline, and therefore the wall of water has not been observed in these cases, but the wave instead runs-up as a breaking bore.

The third category, an undular bore turning into a breaking bore, was only experienced in situations where $\xi \ll \chi_{elev}^{-2/3} \pi^{-1/6} \left(\frac{A_0}{h}\right)^{1/6}$ or $\Upsilon \ll (\chi_{elev} \pi)^{2/3}$. For the undular bore

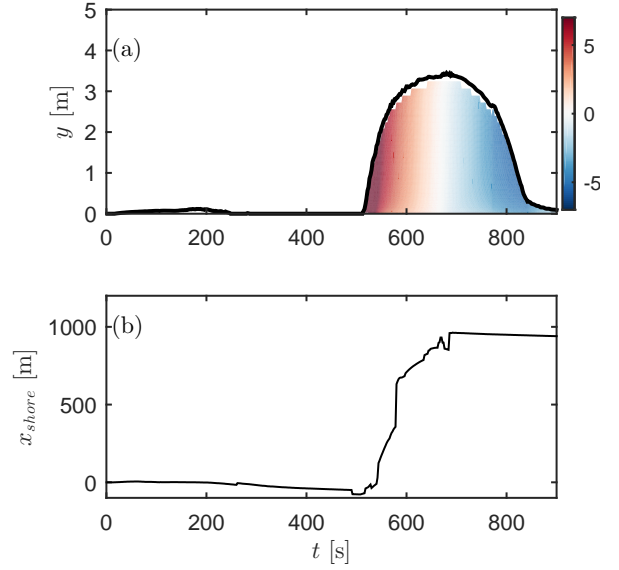


Figure 24: Results for case N100 showing (a) Velocities and surface elevations at $x = 0$, (b) the horizontal position of the shoreline.

to properly form, the slope had to be very mild, otherwise resulting in immediate breaking of the small wave riding on the front of the tsunami, due to shoaling effects.

The fourth category, an undular bore, has only been experienced in one case, and required the tsunami to propagate a long distance in shallow water, and subsequent run-up a steep slope. In reality tsunamis will not propagate on a flat bed, before going up a constant slope region. Often it might propagate very mild slope before going up a steeper slope. As this is similar to the scenario of S030L, this could explain why undular bores have been observed in so many places with real geophysical tsunamis. With this kind of bed profile the undular bore developed on the very mild slope will be able to reach all the way to the shore due to the subsequent steeper slope.

The different tsunami categories exemplify the variety of ways a tsunami can appear. In research tsunamis have often been treated as breaking bores, but the classification and descriptions shown here, can be used as an inspiration for alternative scenarios in experiments. An attempt to capture the undular bore followed by the much longer main tsunami wave was presented very recently in the study by Aniel-Quiroga et al. (2018), where breakwater stability due to a tsunami attack was investigated experimentally. Here the tsunami was represented first by a series of solitary waves followed by a continuous inflow of water, to represent the main wave. As mentioned, bores have been used as tsunami representations, and the results shown in Figure 14 could be used as a full-scale inspiration. Here the breaking bore lasted approximately 500 seconds, and the maximum bore velocity was close to 10 m/s. Assuming a scaling factor of 100, this would (by Froude scaling) result in a model scale bore duration of approximately 50 seconds, and a model scale bore velocity of 1 m/s. The "tide-like" scenario has, to our knowledge, not been used in tsunami experiments previously. This is perhaps because they are less dangerous than the other run-up types. As illustrated here, however, if considering

a very steep beach, this is the most likely run-up type and representing the tsunami as a bore (though conservative) would not represent a likely tsunami scenario.

8. Conclusion

In this paper the results of 14 full scale tsunami simulations have been presented. The simulations have been performed with a RANS models, using the new stabilized $k-\omega$ model of Larsen and Fuhrman (2018b). The model is first validated by comparing with surface elevation from a properly scaled tsunami experiment by Sriram et al. (2016). The model was shown to be capable of predicting the initial deformation and steepening of the wave as well as the subsequent splitting of the wave front, run-up and reflection. The model was further validated for surface elevations and bed shear stresses in the surf and swash zone by comparing to the plunging solitary wave experiments by Sumer et al. (2011). In general the model predicted both the surface elevations and the bed shear stresses well, although some differences were seen around the hydraulic jump during run-down as well as, for the bed shear stresses at the air/water/bed interface.

Using single waves and N-waves as generic tsunami wave forms, simulations were performed of full-scale tsunamis propagating on a flat bed before running up a constant slope. The modelled run-up heights for both the single waves and the N-waves were shown to compare reasonably well with the analytical expression by Madsen and Schäffer (2010). In cases where breaking could be expected to be present, the analytical solution slightly underestimated the run-up height, and the expression from Hunt (1959) gave better estimations. The overall good comparison between analytical expression and the modelled run-up heights indicates that the combined non-breaking expression of Madsen and Schäffer (2010) and the empirical breaking expression from Hunt (1959) is suitable as a first estimate of the run-up height even in situations where the wave is non-linear at the slope, and in situations where waves break.

It has been demonstrated, that despite identical initial waves, the time series of the surface elevations at the toe of the slope can be quite different for different slopes due to the long tsunami waves being reflected. It has been emphasized that this can pose a challenge in identifying incoming and reflected wave signals, even for what appears to be the leading wave.

Three previously defined run-up types were identified in the simulations, and their characteristics were described. Additionally a fourth run-up type was identified and described. It was shown that the tsunami can appear both (1) "tide like", (2) as a "wall of water" or breaking bore (3) as an "undular bore turning into a breaking bore" and finally (4) as an undular bore. In the "tide like" scenarios the surface elevations are essentially horizontal and the inundation speeds are generally lower. Furthermore, these cases are characterized by full reflection from the beach, resulting in a standing wave, causing a phase shift between the maximum surface elevation and flow velocity. The "tide-like" tsunami would primarily occur in situations where the slope was sufficiently steep to be felt more or less as a vertical wall. If the tsunami is linear at the toe of the slope, the

simulated results indicated that cases clearly predicted to be non-breaking by the analytical method of Madsen and Schäffer (2010) would appear "tide-like".

On milder slopes, the tsunami steepened significantly, and the wave front split into shorter waves. In most situations these waves broke almost immediately, turning the whole tsunami into a breaking bore. In some situations more and more short waves developed, turning the front of the tsunami into an undular bore which some times broke before reaching the shore and one time survived all the way to the shore.

It was shown that the shorter waves of the undular bores, could appear at the crest of the tsunami, but also in front of the crest depending on the local surface elevation steepness. It was further shown that these smaller waves had little impact on the run-up height and inundation speed. They were however shown to be important in relation to local flow velocities, which were demonstrated to be significantly higher in when shorter waves were present.

It is hoped that the present paper will shed light on, in general, how tsunamis run-up and from this understanding contribute to improved hazard assessment.

9. Acknowledgements

The authors acknowledge support from the European Union project ASTARTE-Assessment, Strategy And Risk Reduction for Tsunamis in Europe, Grant no. 603839 (FP7-ENV-2013.6.4-3).

References

- Aniel-Quiroga, I., Vidal, C., Lara, J. L., Gonzales, M., Sainz, A., 2018. Stability of rubble-mound breakwaters under tsunami first impact and overflow based on laboratory experiments. *Coast. Eng.* 135, 39–54.
- Baykal, C., Sumer, B. M., Fuhrman, D. R., Jacobsen, N. G., Fredsøe, J., 2015. Numerical investigation of flow and scour around a vertical circular cylinder. *Phil. Trans. Roy. Soc. A* 373, article no. 20140104.
- Bayraktar, D., Ahmad, J., Larsen, B. E., Carstensen, S., Fuhrman, D. R., 2016. Experimental and numerical study of wave-induced backfilling beneath submarine pipelines. *Coast. Eng.* 118, 63–75.
- Berberovic, E., van Hinsberg, N. P., Jakirlic, S., Roisman, I. V., Tropea, C., 2009. Drop impact onto a liquid layer of finite thickness: Dynamics of the cavity evolution. *Phys. Rev. E* 79 (3), article no. 036306.
- Biscarini, C., 2010. Computational fluid dynamics modelling of landslide generated water waves. *Landslides* 7 (2), 117–124.
- Brown, S. A., Greaves, D. M., Magar, V., Conley, D. C., 2016. Evaluation of turbulence closure models under spilling and plunging breakers in the surf zone. *Coast. Eng.* 114, 177–193.
- Carrier, G. F., Greenspan, H. P., 1958. Water waves of finite amplitude on a sloping beach. *J. Fluid Mech.* 4, 97–109.
- Cebeci, T., Chang, K. C., 1978. Calculation of incompressible rough-wall boundary-layer flows. *AIAA J.* 16, 730–735.
- Chen, J., Huang, Z., Jiang, C., Deng, B., Long, Y., 2012. An experimental study of changes of beach profile and mean grain size caused by tsunami-like waves. *J. Coast. Res.* 28 (5), 1303–1312.
- Deshpande, S. S., Anumolu, L., Trujillo, M. F., 2012. Evaluating the performance of the two-phase flow solver interFoam. *Comput. Sci. Discov.* 5 (1), article no. 014016.
- Drahne, U., Goseberg, N., Vater, S., Beisiegel, N., Behrens, J., 2016. An experimental and numerical study of long wave run-up on a plane beach. *J. Marine Sci. Eng.* 4 (1), 1 (23 pp.).
- Foster, P., 2014. Boxing day tsunami, 10 years on: 'the water came my family is gone. *The telegraph*.

- Fuhrman, D. R., Baykal, C., Sumer, B. M., Jacobsen, N. G., Fredsøe, J., 2014. Numerical simulation of wave-induced scour and backfilling processes beneath submarine pipelines. *Coast. Eng.* 94, 10–22.
- Fuhrman, D. R., Madsen, P. A., 2009. Tsunami generation, propagation, and run-up with a high-order boussinesq model. *Coast. Eng.* 56 (7), 747–758.
- Glimsdal, S., Pedersen, G. K., Harbitz, C. B., Lovholt, F., 2013. Dispersion of tsunamis: does it really matter? *Nat. Haz. and Earth Sys. Sci.* 13 (6), 1507–1526.
- Goseberg, N., 2013. Reduction of maximum tsunami run-up due to the interaction with beachfront development - application of single sinusoidal waves. *Nat. Haz. and Earth Sys. Sci.* 13 (11), 2991–3010.
- Goseberg, N., Wurpts, A., Schlurmann, T., 2013. Laboratory-scale generation of tsunami and long waves. *Coast. Eng.* 79, 57–74.
- Grilli, S. T., Harris, J. C., Bakhsh, T. S. T., Masterlark, T. L., Kyriakopoulos, C., Kirby, J. T., Shi, F., 2013. Numerical simulation of the 2011 Tohoku tsunami based on a new transient FEM co-seismic source: Comparison to far- and near-field observations. *Pure and App. Geophys.* 170 (6-8), 1333–1359.
- Grue, J., Pelinovsky, E. N., Fructus, D., Talipova, T., Kharif, C., 2008. Formation of undular bores and solitary waves in the strait of Malacca caused by the 26 December 2004 Indian Ocean tsunami. *J. Geophys. Res.* 113 (C5), C05008.
- Horrillo, J., Kowalik, Z., Shigihara, Y., 2006. Wave dispersion study in the Indian Ocean tsunami of December 26, 2004. *Sci. of Tsunami Ha.*
- Hunt, I. A., 1959. Design of seawalls and breakwaters. *J. Waterw. Harbors Division ASCE* 85, 123–152.
- Jacobsen, N. G., Fuhrman, D. R., Fredsøe, J., 2012. A wave generation toolbox for the open-source CFD library: OpenFOAM (R). *Int. J. Numer. Meth. Fluids* 70, 1073–1088.
- Jiang, C., Chen, J., Yao, Y., Liu, J., Deng, Y., 2015. Study on threshold motion of sediment and bedload transport by tsunami waves. *Ocean Eng.* 100, 97–106.
- Kawai, H., Satoh, M., Kawaguchi, K., Seki, K., 2013. Characteristics of the 2011 Tohoku tsunami waveform acquired around Japan by NOWPHAS equipment. *Coast. Eng. J.* 55 (3), 1350008.
- Kim, D.-H., Lynett, P. J., 2011. Dispersive and nonhydrostatic pressure effects at the front of surge. *J. Hydraul. Eng. ASCE* 137 (7), 754–765.
- Lacy, J. R., Rubin, D. M., Buscombe, D., 2012. Currents, drag, and sediment transport induced by a tsunami. *J. Geophys. Res.- Oceans* 117 (9), –.
- Larsen, B. E., Arboell, L. K., Frigaard, S., Carstensen, S., Fuhrman, D. R., 2018a. Experimental study of tsunami-induced scour around a monopile foundation. *Coast. Eng.* 138, 9–21.
- Larsen, B. E., Fuhrman, D. R., 2018a. Full-scale CFD simulation of tsunamis. part 2: Boundary layers and bed shear stresses. Under preparation.
- Larsen, B. E., Fuhrman, D. R., 2018b. On the over-production of turbulence beneath surface waves in RANS models. In review.
- Larsen, B. E., Fuhrman, D. R., Baykal, C., Sumer, B. M., 2017. Tsunami-induced scour around monopile foundations. *Coast. Eng.* 129, 36–49.
- Larsen, B. E., Fuhrman, D. R., Roenby, J., 2018b. Performance of interFoam on the simulation of progressive waves. available at axiv.org. ID: 1804.01158.
- Larsen, B. E., Fuhrman, D. R., Sumer, B. M., 2016. Simulation of wave-plus-current scour beneath submarine pipelines. *J. Waterw. Port C-ASCE* 142 (5), article no. 08216001.
- Levin, B., Nosov, M., 2016. *Physics of Tsunamis*. Springer Netherlands.
- Løvholt, F., Kaiser, G., Glimsdal, S., Scheele, L., Harbitz, C. B., Pedersen, G., 2012. Modeling propagation and inundation of the 11 March 2011 Tohoku tsunami. *Nat. Haz. and Earth Sys. Sci.* 12 (4), 1017–1028.
- Lynett, P., Liu, P. L.-F., 2002. A numerical study of submarine-landslide-generated waves and run-up. *Proc. R. Soc. Lond. A* 458, 2885–2910.
- Lynett, P., Liu, P. L.-F., 2005. A numerical study of the run-up generated by three-dimensional landslides. *J. Geophys. Res.* 110, C03006/1–16.
- Madsen, P. A., Fuhrman, D. R., 2006. Third-order theory for bichromatic bidirectional water waves. *J. Fluid Mech.* 557, 369–397.
- Madsen, P. A., Fuhrman, D. R., 2008. Run-up of tsunamis and long waves in terms of surf-similarity. *Coast. Eng.* 55, 209–223.
- Madsen, P. A., Fuhrman, D. R., Schäffer, H. A., 2008. On the solitary wave paradigm for tsunamis. *J. Geophys. Res.* 113, article no. C12012.
- Madsen, P. A., Schäffer, H. A., 2010. Analytical solutions for tsunami runup on a plane beach. *J. Fluid Mech.* 645, 27–57.
- Madsen, P. A., Schffer, H. A., Fuhrman, D. R., Toledo, Y., 2016. Uniform asymptotic approximations for transient waves due to an initial disturbance. *J. Geophys. Res.* 121 (1), 60–84.
- Matsuyama, M., Ikeno, M., Sakakiyama, T., Takeda, T., 2007. A study of tsunami wave fission in an undistorted experiment. *Pure and App. Geophys.* 164 (2-3), 617–631.
- Mayer, S., Madsen, P. A., 2000. Simulations of breaking waves in the surf zone using a Navier-Stokes solver. In: *Proc. 25th Int. Conf. Coast. Eng. Sydney, Australia*, pp. 928–941.
- Montagna, F., Bellotti, G., Di Risio, M., 2011. 3D numerical modeling of landslide-generated tsunamis around a conical island. *Nat. Haz.* 58 (1), 591–608.
- Park, H., Cox, D. T., Petroff, C. M., 2015. An empirical solution for tsunami run-up on compound slopes. *Nat. Haz.* 76 (3), 1727–1743.
- Qu, K., Ren, X. Y., Kraatz, S., 2017. Numerical investigation of tsunami-like wave hydrodynamic characteristics and its comparison with solitary wave. *App. Ocean Res.* 63, 36–48.
- Schimmels, S., Sriram, V., Didenkulova, I., 2016. Tsunami generation in a large scale experimental facility. *Coast. Eng.* 110, 32–41.
- Shuto, N., 1985. Nihonkai-Chubu earthquake tsunami on the north Akita coast. *Coast. Eng. Japan* 28, 255–264.
- Sriram, V., Didenkulova, I., Sergeeva, A., Schimmels, S., 2016. Tsunami evolution and run-up in a large scale experimental facility. *Coast. Eng.* 111, 1–12.
- Sumer, B. M., Sen, M. B., Karagali, I., Ceren, B., Fredsøe, J., Sottile, M., Zilioli, L., Fuhrman, D. R., 2011. Flow and sediment transport induced by a plunging solitary wave. *J. Geophys. Res.* 116 (1), C01008.
- Suppasri, A., Muhari, A., Ranasinghe, P., Mas, E., Shuto, N., Imamura, F., Koshimura, S., 2012. Damage and reconstruction after the 2004 Indian Ocean tsunami and the 2011 Great East Japan tsunami. *J. Nat. Disaster Sc.* 34 (1), 19–39.
- Synolakis, C. E., Bernard, E. N., 2006. Tsunami science before and beyond Boxing Day 2004. *Phil. Trans. Roy. Soc. Lond. A* 364, 2231–2265.
- TD Interesting Topics Tube, 2015. Largest and best tsunami compilation of japan tohoku earthquake 2011. URL <https://www.youtube.com/watch?v=S2Z0mMH4WHA> , retrieved February 14, 2018
- TD Interesting Topics Tube, 2017. Giant tsunami in Miyako - final documentary - japan 2011. URL <https://www.youtube.com/watch?v=xtd6xUuu1s> , retrieved February 14, 2018
- Tomita, T., Honda, K., Kakinuma, T., 2006. Application of Storm surge and Tsunami simulator in Oceans and Coastal areas (STOC) to tsunami analysis. In: *Joint Panel Conference of the U.S.-Japan Cooperative Program in Natural Resources*, Volume 38, pp. 109–115.
- Tomita, T., Takahashi, K., 2014. Simulation of tsunami accompanied by breaking short-period waves. *Coast. Eng. Proc.* 1 (34), 2.
- van Driest, E. R., 1956. On turbulent flow near a wall. *J. Aeronautical Sciences* 23, 1007–1011, 1036.
- Wemmenhove, R., Luppens, R., Veldman, A. E. P., Bunnik, T., 2015. Numerical simulation of hydrodynamic wave loading by a compressible two-phase flow method. *Computers and Fluids* 114, 218–231.
- Wilcox, D. C., 2006. *Turbulence Modeling for CFD*, 3rd Edition. DCW Industries, Inc., La Canada, California.
- Williams, I. A., Fuhrman, D. R., 2016. Numerical simulation of tsunami-scale wave boundary layers. *Coast. Eng.* 110, 17–31.

Chapter 7

Full-scale CFD simulation of tsunamis. Part 2: Boundary layers and bed shear stresses

This Chapter is under preparation as:

Larsen, B. E., Fuhrman, D. R. (2018). *Full-scale CFD simulation of tsunamis. Part 2: Boundary layers and bed shear stresses.*

Full-scale CFD simulation of tsunamis. Part 2: Boundary layers and bed shear stresses

Bjarke Eltard Larsen^{a,*}, David R. Fuhrman^a

^aTechnical University of Denmark, Department of Mechanical Engineering, Section of Fluid Mechanics, Coastal and Maritime Engineering, DK-2800 Kgs. Lyngby, Denmark

Abstract

This paper presents results from numerical simulations of the propagation and run-up of full scale tsunamis, using a Reynolds-Averaged Navier Stokes model, with emphasis on the resulting boundary layers and bed shear stresses. Spatial distributions of the Shields parameter and Rouse number during run-up and draw-down show that for tsunamis of the sizes considered, with a grain size corresponding to medium sand, considerable sediment transport can be expected during run-up and that the sediment transport can be expected to be dominated by suspended sediment. The results likewise show that the expected sediment transport during draw-down will similarly be considerable and dominated by suspension. The tsunami-induced boundary layers are shown (as expected) to grow in time and at flow reversal a new boundary layer forms. The observed boundary layers thickness ranges from spanning only a small fraction of the water depth to spanning the entire depth. The velocity profiles beneath the tsunamis are shown to have good correspondence with a logarithmic profile within the boundary layer. Similarly, the bed shear stresses beneath the tsunamis are investigated and a new and simple engineering model is developed for predicting the temporal variation of the bed shear stress based only on a free-stream velocity signal. The new engineering model is shown give better predictions for the bed shear stress than the standard Mannings approach. It is likewise shown how the temporal evolution of the boundary layer thickness can be predicted based only on a free-stream velocity signal. The results presented here are Part 2 of a larger study, where Part 1 involved the model validation and detailed descriptions of the run-up process.

Keywords: Tsunamis, Computational Fluid Dynamics, Boundary layers, Shear stress, Turbulence modelling

1. Introduction

The potentially fatal impact of large tsunamis is well known. The two recent major tsunami incidents, the Boxing day tsunami in 2004 in the Indian Ocean, and the Tohoku tsunami in Japan in 2011 were responsible for 230,000 and 20,000 fatalities respectively (Suppasri et al., 2012). Therefore, it is natural that most tsunami research in the past has rightly focused on predicting run-up height and inundation distance, as increased knowledge in these areas can potentially save humans lives.

In addition to fatalities, tsunamis can also potentially have a long term effect on entire coastal regions. Beaches can get eroded, scour can occur around coastal structures, large sediment deposits can enter harbors, and sediment deposited inland can hinder recovery work. Following the Tohoku tsunami, it was reported reported that 90% of the beach disappeared in the Takata Matsubara area (Japan) and it was estimated that the total volume of morphological change in this area was 1.9×10^6 m³ (Yamashita et al., 2016). Before -and-after satellite images of the beaches of Banda Aceh, Indonesia from the 2004 Indian Ocean tsunami likewise show large scale erosion, with the coast locally retreating up to 200 m (Paris et al., 2009; Borrero et al., 2006). For other field studies of the morphological impacts of tsunamis see e.g. Udo et al. (2016) and Kuriyama et al. (2014).

The above-mentioned field studies all provide some useful insight on tsunami induced sediment transport and morphology. They do not, however, give insight into the detailed transport patterns that emerge, which is needed if prediction of tsunami-induced sediment transport should be improved.

Despite the potentially large effect on beaches and coastal profiles, the tsunami induced sediment transport and morphology has, apart from the previous mentioned surveys, received relatively little attention compared to e.g. run-up height and inundation distance. The few studies that have treated this have primarily been numerical using the non-linear shallow water (NLSW) models. These have either been two-dimensional horizontal (2DH) where the flow is assumed uniform across the depth (e.g. Li et al. (2012b), Kuriyama et al. (2014), Ontowirjo et al. (2013), Sugawara et al. (2014b)) or three-dimensional where the vertical direction is resolved by using a number of σ -layers. Often these have been reduced to two-dimensional vertical models (2DV), however (e.g. Apotsos et al. (2011a), Apotsos et al. (2011b), Apotsos et al. (2011c)). For a more detailed review on numerical modelling of tsunami induced sediment transport using NLSW models see Sugawara et al. (2014a). Such models are reasonably good at handling tsunami propagation and inundation. They do not describe dispersion, however, and will therefore not be able to capture the splitting of steep tsunami wave fronts into an undular bore, nor do they solve wave breaking accurately. Furthermore, in 2DH models the flow is uniform across the depth, and hence bed shear stress

*Corresponding author

Email address: bje1t@mek.dtu.dk (Bjarke Eltard Larsen)

and resulting sediment transport is typically based on either a Manning coefficient, a Colebrook-White type friction formula or an assumed logarithmic velocity profile. Due to the very limited number of studies on tsunami-induced boundary layers, it is however not known how well these approximations work in such instances.

Studies relating to tsunami induced boundary layers are seemingly limited to the field measurement by Lacy et al. (2012), as well as the numerical studies by Williams and Fuhrman (2016) and Tanaka et al. (2016). Lacy et al. (2012) showed that the tsunami induced boundary layer spanned more than typical wind wave boundary layers, though only spanning a small portion of the entire depth. In a one dimensional vertical (1DV) Reynolds Averaged Navier-Stokes (RANS) model Williams and Fuhrman (2016) simulated a series of tsunami-scale boundary layers, emphasizing that they are both current-like due to their long duration, but also wave-like, in the sense that they are unsteady and that the boundary layer may not span the entire water depth, similar to that observed by Lacy et al. (2012). Williams and Fuhrman (2016) likewise proposed formulas for predicting tsunami boundary layer thickness and friction factors for various tsunami signals and various roughnesses. Their study was limited to offshore regions to prevent the boundary layer being depth-limited, and the driving tsunami signal was treated as a time varying current. Treating the tsunami induced boundary layer as a time varying current has also been utilized in studies of tsunami induced scour around monopiles by Larsen et al. (2017) and Larsen et al. (2018). In an attempt to combat the uncertainties of the NLSW models regarding the bed-shear stress Tanaka et al. (2016) simulated tsunami run-up with a NLSW model coupled with a RANS model, using a $k-\omega$ turbulence model for describing the boundary layer. They showed this gave different shear stress approximations compared to those that would be predicted using a Manning coefficient. It is unclear, however, exactly how they coupled the two models. Despite this, it is an interesting attempt to remedy some of the uncertainties regarding the bed shear stresses predicted by NLSW models.

Finally, tsunami-induced sediment transport has also been considered in a branch of the paleo-tsunami research community trying to predict flow characteristics of historic tsunamis based on sediment deposits, using what is normally referred to as inverse models. Many different inverse models exists see e.g. Moore et al. (2007), Soulsby et al. (2007) and Jaffe and Gelfenbaum (2007). These models all rely on numerous assumptions, and amongst the most common are that sediments travel in suspension, and are not re-suspended during draw down. For a more complete overview of the inverse models see Sugawara et al. (2014a).

With the use of Computational Fluid Dynamics (CFD) the present work aims at both qualitatively and quantitatively describing tsunami-induced boundary layers and shear stresses as well as the implication for sediment transport. The knowledge on boundary layers and shear stresses can be useful for implementation in "simpler" potential flow models (i.e. NLSW type or Boussinesq type), potentially improving their sediment transport predictive capabilities. The results can likewise be useful

for the previously described inverse models, as it will shed light on some of the used assumptions in these models.

The results presented in this work builds on the same simulations presented in Larsen and Fuhrman (2018a) (hereafter referred to as Part 1). Here, the numerical model was described, validated (for free surface elevations, run-up, wave breaking and bed shear stresses) and used to describe in detail the run-up process of full-scale tsunamis.

The remainder of the paper is organized as follows: In Section 2 the model is briefly described and the set-up of the model is provided. In Section 3 the model result are presented. Finally, in Section 4 overall conclusions are drawn.

2. Model description and setup

For a complete description of the model used the reader is referred to Part 1. For the sake of efficiency, only an abbreviated description is provided here. The CFD simulations are performed in the two-phase volume of fluid method (VOF) flow model `waves2FOAM` developed by Jacobsen et al. (2012). Here the Reynolds-averaged Naviers Stokes (RANS) equations are solved. To close the system the $k-\omega$ model of Larsen and Fuhrman (2018b) is used, which is an extension of the Wilcox (2006) model. For the turbulence quantities at the bottom the generalized wall function approach, presented in Fuhrman et al. (2014) is used. These wall functions have also been used by e.g. Baykal et al. (2015), Larsen et al. (2016) and Bayraktar et al. (2016).

The tsunami waves in this study, will be specified as initial conditions and are the same as considered in Part 1. Specifically these will be represented by a general N-wave form (the summation of a positive and negative single wave) inspired by Madsen and Schäffer (2010), but with x -variation now included. The free-surface is given by

$$\eta(x, t) = A_1 \operatorname{sech} \left[\Omega_1 \left((t - t_1) - \frac{x - x_0}{\sqrt{gh}} \right) \right]^2 - A_2 \operatorname{sech} \left[\Omega_2 \left((t - t_2) - \frac{x - x_0}{\sqrt{gh}} \right) \right]^2 \quad (1)$$

where A_1 and A_2 are the amplitudes of the two single waves, h is the water depth and g is the gravitational acceleration. The effective frequencies Ω_1 and Ω_2 defines the time span of the two single waves according to $\Omega_i = 2\pi/T_i$ where T_i can be interpreted as the effective period of the corresponding single wave, defined as the time where the surface elevations drops below 0.7% of the amplitude. In the above x_0 defines the center of the wave and t_1 and t_2 can be used to phase shift the two single waves. This signal can be reduced to a single wave by setting $A_2=0$. The horizontal velocity is then given by linear shallow water theory

$$u(x, t) = \sqrt{\frac{g}{h}} \eta(x, t). \quad (2)$$

The vertical velocity is derived from the local continuity equation, and the pressure is calculated as hydrostatic.

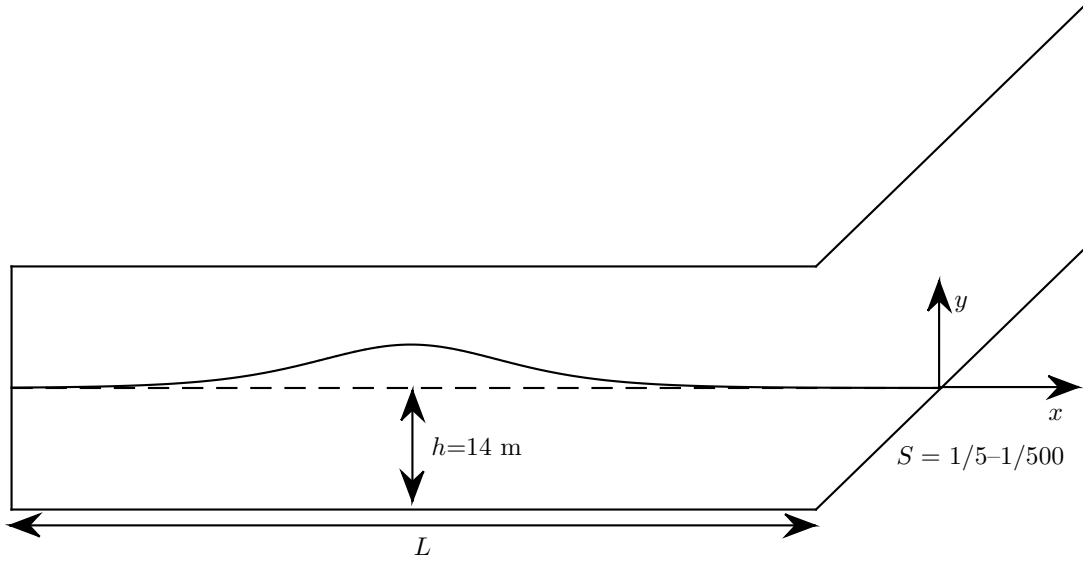


Figure 1: Layout of the computational domain, with origo positioned at the original shoreline. This sketch is a repeat from Part 1.

In the simulations we consider the simple canonical case of 2D tsunami waves propagating over an initial constant depth, before running up a constant slope. The waves will be initialized on a flat bed, which is one wave length long, such that the flat part of the domain houses the entire wave. The waves will then propagate and deform before reaching a constant slope region, where the slope will be systematically varied. A general setup of the computational domain can be seen in Figure 1.

Table 1 gives a summary of the cases considered to be in detail in this study, corresponding to a sub-set of those in Part 1. In the first two rows of the table $A_2=0$ and therefore these waves are single waves, with only a positive displacement. The third row contains an N-wave with a leading depression. The periods and phase shifts of the N-wave are chosen to yield the same wave length and crest-to-trough wave height as the single wave cases. In Part 1 a total of 14 cases were presented, but here we only go into great detail with three of these. These three are specifically chosen to represent different run-up scenarios as detailed in Part 1. For all cases the domain is discretized into cells $\Delta y = 0.25$ m and $\Delta x = 0.5$ m and from 5 m above the bed and down the grid is gradually refined in the vertical with near bed cells having $\Delta y = 0.0014$ m. The grain size of the bed is taken as $d = 0.4$ mm (medium sand) such that the roughness for the present cases is given by $k_s = 2.5d = 0.001$ m.

3. Model results

In this section the modelled results will be presented. The first part of this section will focus on the spatial distribution of the Shields parameters and Rouse numbers during run-up and draw-down of the three characteristic tsunami events. The next part will focus on the tsunami induced boundary layers, describing both the development in boundary layer thickness and the shape of the velocity profiles. Finally, based on the results

from the detailed boundary layer analysis a new engineering approach for estimating the friction velocity will be developed.

In this section some mentioning of the run-up characteristics of the tsunami will be made, but for a full discussion on this, please see Part 1.

3.1. Shields parameters and Rouse numbers

In the present study, sediment transport was not directly solved for. However, some conclusions regarding sediment transport can be made by looking at the Shields parameter and the Rouse number. The Shields parameter is a non-dimensional number proportional to the ratio between driving and stabilizing forces on a sediment grain and is defined as

$$\theta = \frac{U_f |U_f|}{g(s-1)d} \quad (3)$$

where $s = 2.65$ is the relative sediment density. The Rouse number can be interpreted as the ratio between settling velocity and near-bed turbulent fluctuations, and is defined as

$$Z = \frac{w_s}{\kappa U_f} \quad (4)$$

where $w_s = 0.0527$ m/s is the Stokes fall velocity (Fredsoe and Deigaard, 1992). According to Fredsoe and Deigaard (1992) $Z < 2$ is typically necessary for sediment to go into suspension, and sediment will be distributed more uniformly across the boundary layer as Z is lowered

It is important to stress that the result for θ and Z , presented here, are based on the single used grain size. Other grain sizes would naturally result in different values for θ and Z and as a result conclusions regarding sediment transport must be interpreted in this context.

As a first case we will consider case S200 (a single wave running up a slope of $S=1/200$). This wave runs up as a breaking bore, and for more details regarding the characteristics of

Name	S	A_1 [m]	A_2 [m]	T_1 [s]	T_2 [s]	t_1 [s]	t_2 [s]	x_0 [m]
S030	1/30	5	0	780	0	0	0	-4990.5
S200	1/200	5	0	780	0	0	0	-7370.5
N100	1/100	2.52	2.52	520	520	130	-130	-5970.5

Table 1: Names, slopes and initial wave parameters of the simulated cases

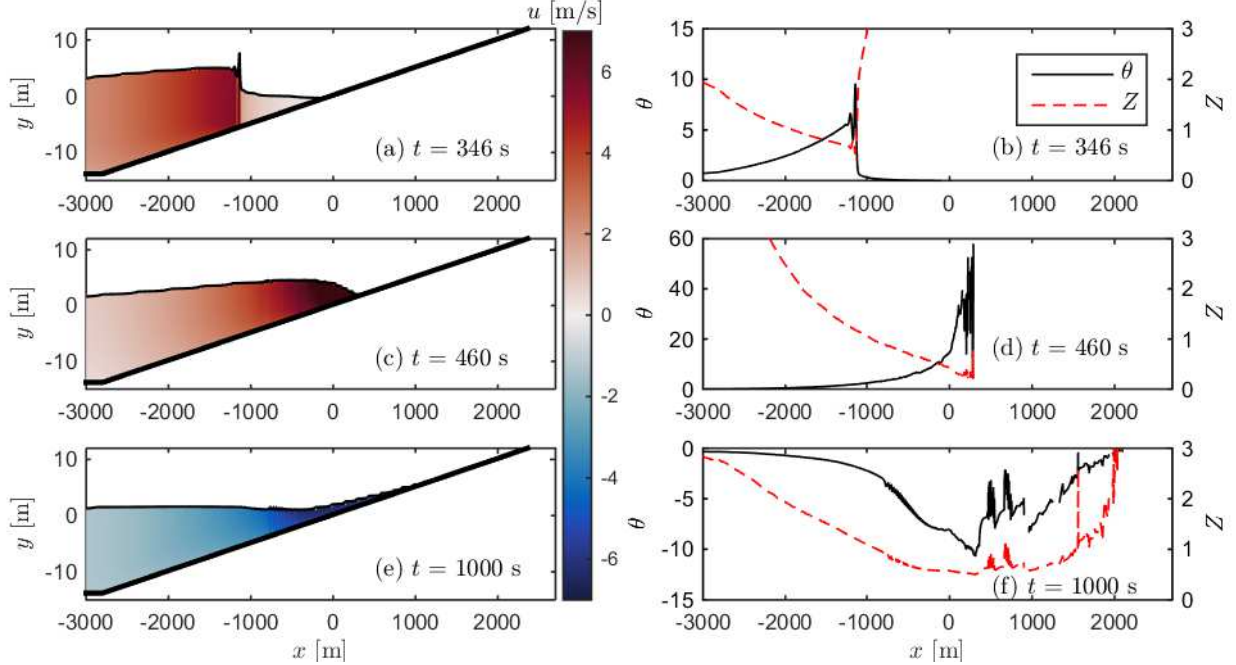


Figure 2: Surface elevations, velocities, Shields parameters (θ) and Rouse numbers (Z) of case S200 at different times.

tsunamis running up as breaking bores please see Part 1. Figure 2 shows surface elevations, velocities, Shields parameters and Rouse numbers from case S200 at three different instants. The times correspond to the tsunami shoaling (Figure 2a,b), inundating (Figure 2c,d) and drawing down (Figure 2e,f). During shoaling it can be seen that the steep tsunami wave front has split, and that a short wave is riding on the front (Figure 2a). The short wave was not able to maintain its shape, however, and it broke before reaching the shore (this was shown in Part 1 to be typical of tsunamis running up as breaking bores). The very steep tsunami wave front in Figure 2a can be seen to give a very sudden increase in the velocity. This increase in velocity, of course, causes θ to increase and Z to decrease, as shown in Figure 2b. Behind the wave front θ decreases. This is due to the decreasing velocity, but also, as will be shown in the coming subsections, due to the boundary layer increasing behind the tsunami front. This reduces the velocity gradients and in turn the bed shear stresses. During shoaling θ is already high and $Z < 2$ for most of the wave front meaning that sediment can be expected to be transported largely in suspension. It is important to stress that the boundary layer may or may not span the entire water depth, as will be discussed in the following section. Thus even in cases with very low Z , the suspended sediment may not necessarily span across the entire depth. It should be noted that the tsunami is much longer (approximately 9 km) than shown in

Figure 2a, and further behind the tsunami front $Z > 2$ meaning that bed load transport would likely start to dominate.

While inundating the velocities increase further as seen in Figure 2c. This results in significantly higher θ with a maximum value close to 60 as seen in Figure 2d. Here it is also evident that the tsunami front is breaking, as large fluctuations in θ can be seen. Z on the other hand drops down to approximately 0.25, which indicates that the suspended sediment will be present to a large degree throughout the boundary layer. Behind the breaking tsunami front Z is increasing meaning that suspended sediment will likely be more and more confined to the lower part of the tsunami-induced boundary layer.

During draw-down (Figure 2e,f) it can be seen that the velocities and resulting θ values are somewhat lower than those near the breaking tsunami front. It can however be seen that high-magnitude θ values are present over a much longer span (> 2 km). This can be explained by the water depth being much lower compared to the height of the tsunami front, and as a result velocity gradients and shear stresses become larger. This likewise results in a much broader region with low Z , meaning that the sediment transport during the draw-down would likewise also seemingly be characterized to a high degree by suspended sediment load.

The θ values and Z values will also naturally depend on how the tsunami runs-up. To demonstrate other characteristic

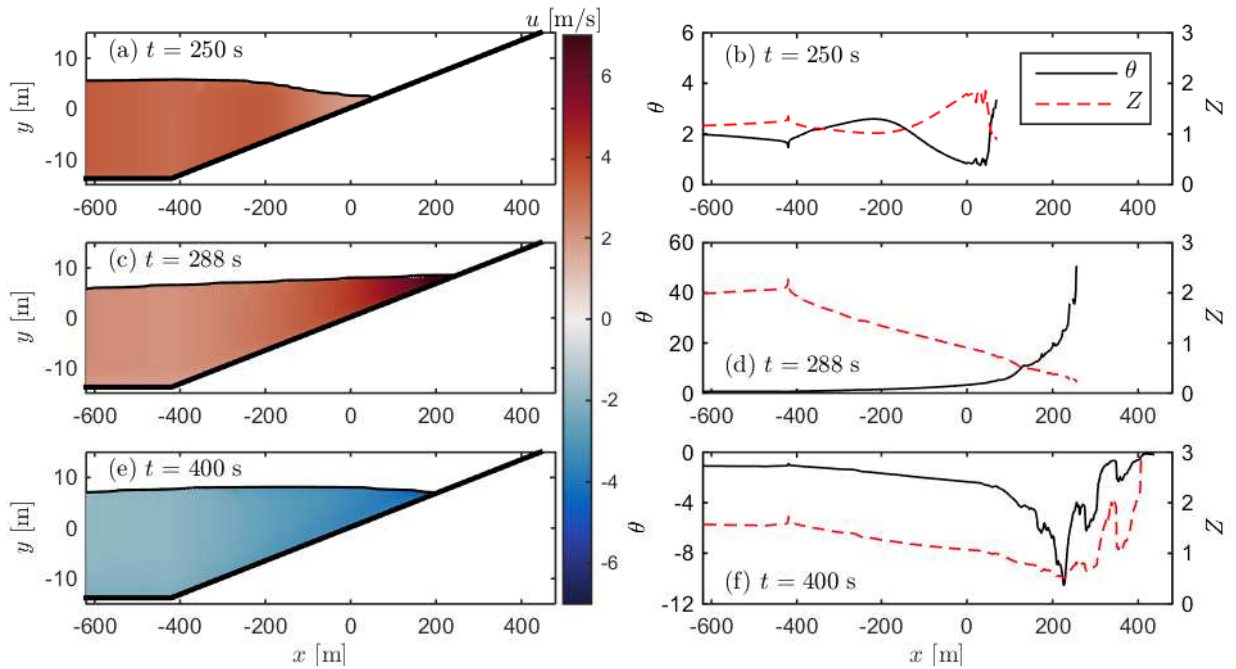


Figure 3: Surface elevations, velocities, Shields parameters (θ) and Rouse numbers (Z) of case S030 at different times.

scenarios, we will now show results for two additional cases, namely case S030 and case N100 (Table 1). These were chosen to also demonstrate the results in cases where the tsunami is not breaking (case S030, categorised as being "tide-like", see Part 1) or have a leading depression (case N100) which runs up as a breaking bore similar to case S200.

Figure 3 shows surface elevations, velocities, Shields parameters and Rouse numbers at three different instants for case S030, which is a single wave running up a slope of $S = 1/30$. The times were again selected to show the tsunami shoaling (Figure 3a,b), inundating (Figure 3c,d) and drawing down (Figure 3e,f). While shoaling the tsunami wave front is not very steep, as seen in Figure 3a. This results in lower velocities and as result also lower θ values, compared to case S200 (Figure 2a,b). As a result $Z > 1$ is generally the case while shoaling. As $Z < 2$, this still means that sediment will likely travel in suspension, but due to the larger values relative to those from case S200 (Figure 2b) the sediment would not be expected to be as uniformly distributed across the boundary layer, and would likely be more confined to the bottom part of the boundary layer. During inundation (Figure 3c,d) it can be seen that the tsunami wave front has accelerated significantly and the velocities and resulting θ values are of the same size as in case S200 during inundation (Figure 2c,d), as are the Z values, which remain below two all the way to the toe of the slope. Similar to case S200, it can be seen that during draw-down (Figure 3e,f), θ does not reach such large extreme values as near the front of the tsunami. Values exceeding unity are still observed all the way to the toe of the slope, again indicating significant sediment transport also during draw-down.

Finally, in Figure 4 the surface elevations, velocities, Shields parameters and Rouse numbers are shown for case N100. This

case is running up a slope of $S = 1/100$ and has a leading depression, as can be seen in the shoaling position in Figure 4a. Here a region with lower surface elevations and negative velocities are clearly visible in front of the tsunami wave front. Similar to case S200, the front of the tsunami has split, and a few shorter waves can be seen riding on the main tsunami wave. Also similar to case S200, these shorter waves cannot sustain their shape during shoaling, and break some distance from the shore. The resulting Shields parameter near the crest of the tsunami is high, but not as high as case S200, where a significantly larger wave front was present. It can also be seen that the leading depression, causing the shoreline to retreat, has the potential to move significant amounts of sediment as the value of θ is generally larger than one. In this scenario it seems likely that the tsunami would form some sort of bar offshore, around the location where θ changes sign (Figure 4a, $x \approx -1000$ m), as this would seemingly correspond to a region of rapid deposition. This was also observed in the numerical study by Li et al. (2012a) in the case of a leading depression tsunami. During inundation (Figure 4c,d) and draw-down (Figure 4e,f) the image is very similar to the two previous cases. Here, the front of the inundating tsunami has very high Shields parameters and low Rouse numbers, indicating significant sediment transport as well as significant amount of sediment transported in suspension. During draw-down the Shields parameters are again generally high, the Rouse numbers generally low, again indicating, likely, significant suspended sediment transport during draw-down.

To summarize: Tsunamis of the size considered in the present work, have the potential to move a considerable amount of sediment. The largest magnitude Shields parameters are seen at the tsunami front while inundating, indicating highest sedi-

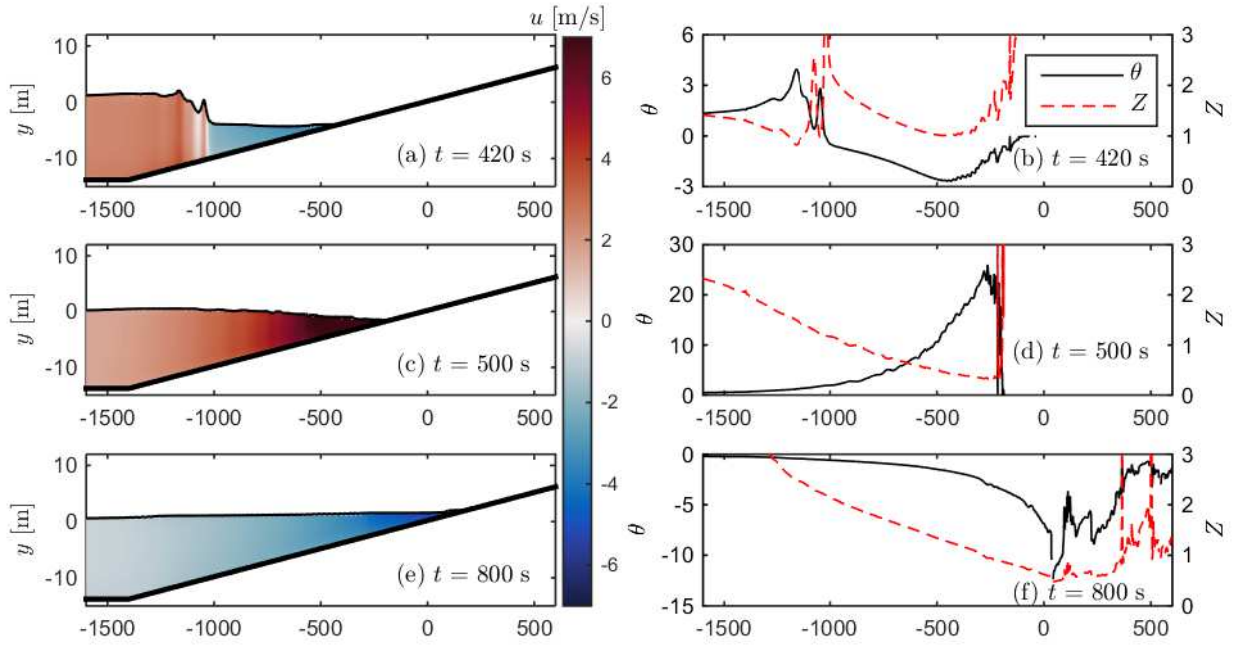


Figure 4: Surface elevations, velocities, Shields parameters (θ) and Rouse numbers (Z) of case N100 at different times.

ment transport rates here. Generally the Rouse numbers in the considered cases were so low that the sediment transport would be expected to be dominated by suspension. At the front of the inundating tsunami the Rouse numbers were even lower, such that suspended sediment could be expected to be present throughout the boundary layer and potentially mixed further via any breaking waves.

The results presented here can help assess the assumption used by inverse paleo tsunami models. In the models by Moore et al. (2007), Soulsby et al. (2007) and Jaffe and Gelfenbaum (2007) it was assumed that sediment was transported only during run-up, and not re-suspended during draw down. As just shown, during the draw-down phase, suspended sediment transport can be expected to be present to a large degree. It should however be said that the present tsunami cases can all be considered to be rather large tsunamis, and smaller tsunamis would naturally have less sediment transport potential. The Shields parameters during draw-down are generally slightly lower than those present near the tsunami wave front. If the sediment was comprised of widely varying grain sizes, this would mean that the largest grains, which could be carried by the tsunami wave front will not necessarily move during draw-down, and the assumption that sediment will not be re-suspended during draw-down would probably be more reasonable for the largest grains in a sample. This scenario, however, would mean the grains will not fine inland (sediment deposits having smaller grain sizes inland), as assumed by many inverse models, as the finer sediments will be re-suspended and be drawn seaward, while the coarser sediments would remain. This is similar, in fact, to the experimental finding by Yoshii et al. (2017).

3.2. Boundary layers

In this section we will focus on the the tsunami induced-boundary layers from the CFD simulations. For brevity, we will not go detail in all three cases. Rather, we will discuss in detail the tsunami-induced boundary layer of case S200 which is sufficiently typical. Figure 5 shows the free-stream velocity signal (Figure 5e) as well as the velocity profiles (Figure 5a-d) at different times for case S200 at the toe of the slope ($x = -2800$ m). Included in the figure as asterisks are also the modelled boundary layer thickness δ , which has been estimated as the lowest vertical position where

$$\frac{y - y_0}{|u|} \frac{\partial |u|}{\partial y} < 0.03. \quad (5)$$

Here y_0 is the bed elevation. If the above is not fulfilled at any position the boundary layer thickness is taken as the water depth. This is somewhat different from the standard way of estimating boundary layer thickness, which is sometimes taken as the vertical position where $u < 0.99u_0$, u_0 being free stream velocity. From the modelled results, however, it was difficult to estimate u_0 , as the crest of the steep waves sometimes had higher velocities than the near bed flow. Overcoming this difficulty therefore led to the above formulation, and as can be seen from Figure 5 the modelled boundary layer thicknesses corresponds well with visual expectations. For the remainder of this study u_0 is defined as the velocity at $y = y_0 + \delta$.

Williams and Fuhrman (2016) proposed that the boundary layer thickness beneath the peak flow in a tsunami could be predicted by

$$\frac{\delta}{a} = 0.05 \left(\frac{a}{k_s} \right)^{-0.11} \quad \text{or} \quad \delta = 0.05 a^{0.89} k_s^{0.11} \quad (6)$$

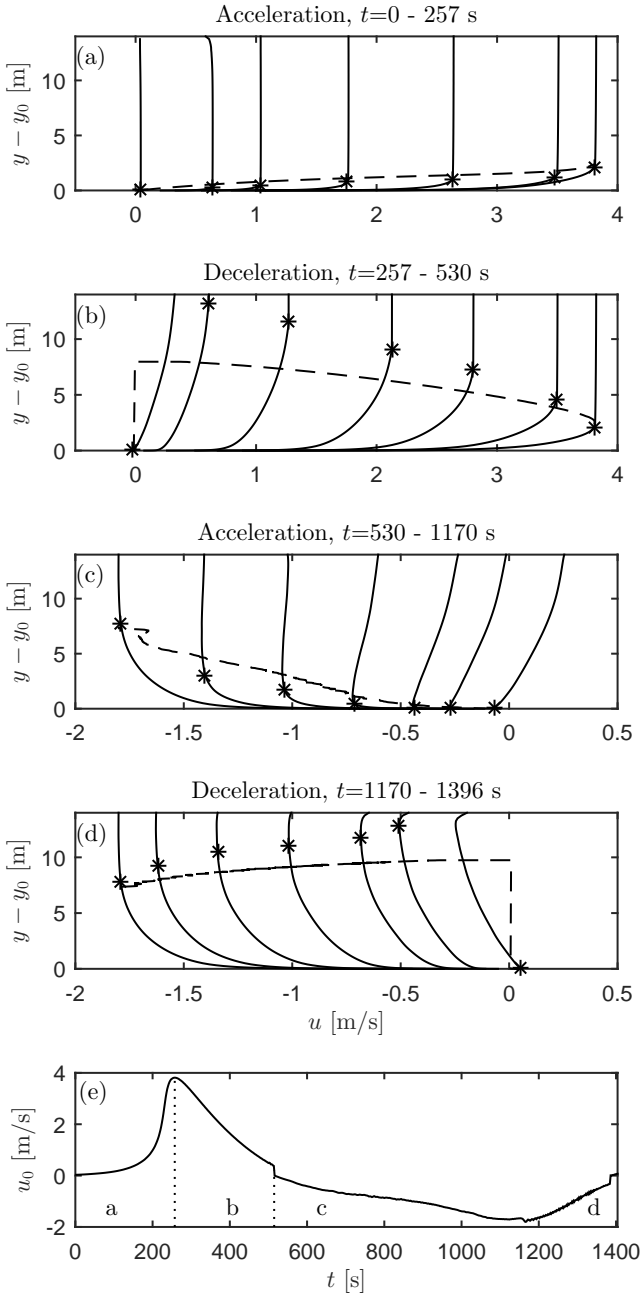


Figure 5: (a)-(d) Modelled velocity profiles (-), modelled boundary layer thickness (*), predicted from (7) boundary layer thickness (- -) and (e) free-stream velocity signal for case S200 at the toe of the slope ($x = -2800$ m). (:) marks the separation between the phases shown in (a)-(d)

where $a = U_m/\Omega$ is the amplitude of the orbital motion and U_m is the maximum free-stream velocity. As we would like to predict the time varying boundary layer thickness, we propose to extend this formula such that

$$\delta(t) = \min(0.05a(t)^{0.89}k_s^{0.11}, h) \quad (7)$$

The first argument is similar to (6) except that the second argument ensures that the predicted boundary layer thickness will

not exceed the water depth. $a = U_m/\Omega$ has been replaced with

$$a(t) = \int_{t_0}^t |u_0(t)| dt \quad (8)$$

which is a measure of the distance travelled by a near bed particle following flow reversal. This definition of $a(t)$ will for the standard sinusoidal wave case give the same boundary layer thickness at the peak velocity as the formulation by Williams and Fuhrman (2016). t_0 is the time of the previous zero crossing of the free stream velocity. The predicted value for the boundary layer thickness using (7) is included in the figure as a dashed line.

The first acceleration phase is shown in Figure 5a, the subsequent deceleration phase in Figure 5b, the second acceleration phase, which is the tsunami drawing down in Figure 5c, and finally the second deceleration phase in Figure 5d.

During the first acceleration phase (Figure 5a) and the first deceleration phase (Figure 5b) it can be seen that the boundary layer continually grows. It starts as only a small fraction of the water depth, but grows nearly to the free surface by the end of the first deceleration phase. This supports the results by Williams and Fuhrman (2016) which highlighted that the tsunami-induced boundary layers may be both wave-like and current-like. During the draw-down (Figure 5c-d) it can be seen that the boundary layer grows both during the acceleration and deceleration phases. It can also be seen that the predicted boundary layer thickness from (7) agrees well during the acceleration phase, but slightly under-predicts the boundary layer thickness during the deceleration phase.

When the tsunami shoals, the wave front steepens and velocities increase, as seen in Figure 2a. Figure 6 shows the velocity profiles (Figure 6a-d) and free-stream velocity (Figure 6e) of the now shoaled wave at $x = -1200$ m corresponding to a water depth of $h = 6$ m. Included in the figure is also the modelled and predicted boundary layer thickness, similar to before. During the first acceleration phase (Figure 6a) it can be seen that the initial acceleration is not that large but from $t = 336$ s to $t = 348$ s the wave accelerates from approximately 2 m/s to approximately 6 m/s. This corresponds to the arrival of the very steep wave front. Due to the very large acceleration, the boundary layer barely has time to grow, and at the peak velocity the boundary layer thickness is only around 1 m high. This development is well predicted by equation (7), shown as the dashed line. During the subsequent deceleration (Figure 6b) the boundary layer grows all the way to the free surface, which is also captured by (7). During the draw-down (Figure 6c) a new boundary layer forms. Here the water depth is almost constant, and the boundary layer eventually stretches all the way to the free-surface. In the deceleration phase of the draw-down (Figure 6d), the boundary layer remains depth limited. Again an excellent agreement between the modelled and predicted boundary layer thickness is achieved.

When the tsunami hits the coast it becomes even steeper than at the shoaling position, and the front of the tsunami is breaking as seen in Figure 2b. Figure 7 shows the velocity profiles (Figure 7a-d) and free-stream velocity (Figure 7e) at the original

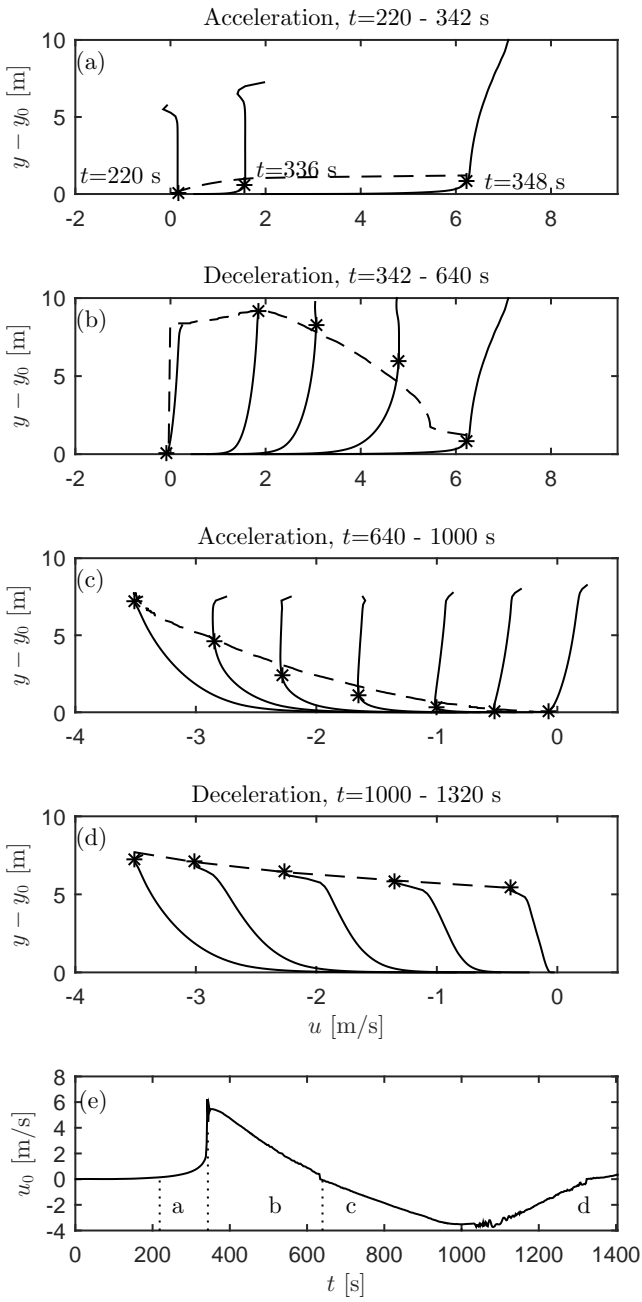


Figure 6: (a)-(d) Modelled velocity profiles(-), modelled boundary layer thickness (*), predicted from (7) boundary layer thickness (- -) and (e) free-stream velocity signal for case S200 in a shoaling position at $x = -1200$ m. (:.) marks the separation between the phases shown in (a)-(d)

shoreline ($x = 0$ m). Included in the figure is also the modelled and predicted boundary layer thickness, similar to before. As a result of the increase steepness the initial acceleration phase is only approximately 1% of the period where it accelerates from zero to 12 m/s in just 8 s, as seen in Figure 7a. In this case the wave is running up like a breaking bore, and the boundary layers are at all times limited by the water depth. This behaviour is not perfectly captured by (7), but as can be seen during the sub-

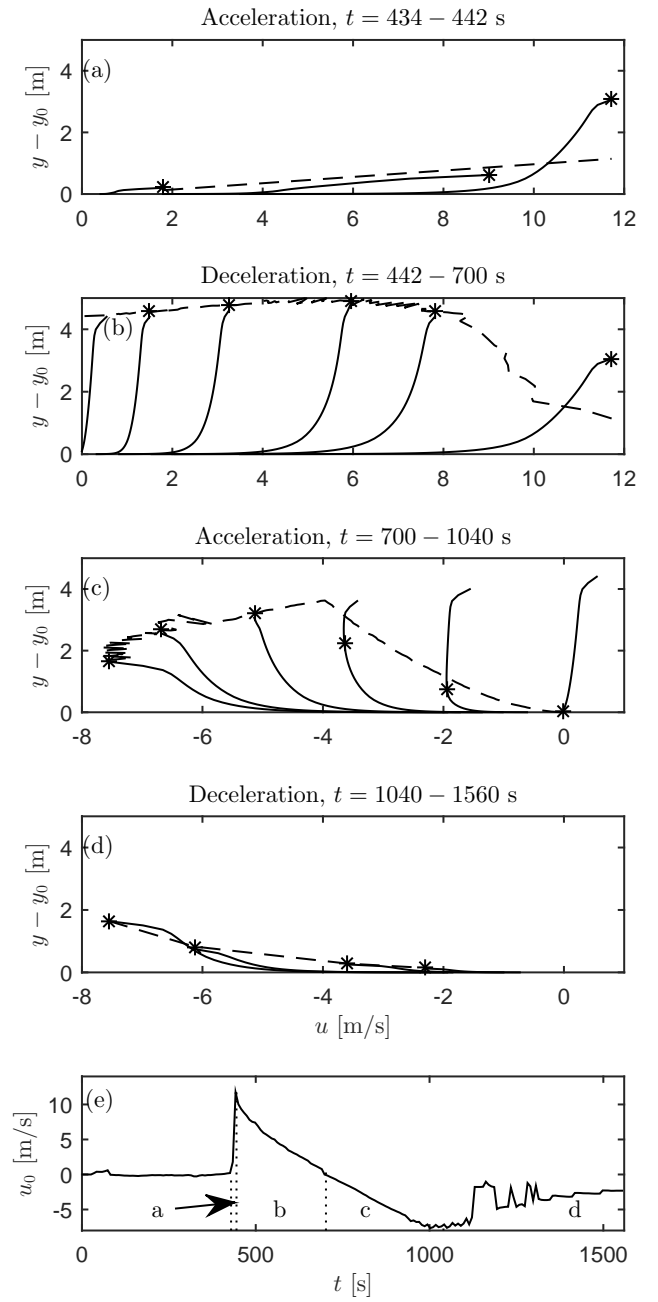


Figure 7: (a)-(d) Modelled velocity profiles (-), modelled boundary layer thickness (*), predicted from (7) boundary layer thickness (- -) and (e) free-stream velocity signal for case S200 at the shore ($x = 0$ m). (:.) marks the separation between the phases shown in (a)-(d)

sequent longer deceleration phase (Figure 7b) (7), due to the high velocities, quickly predicts that the boundary layer will extend all the way to the free-surface, similar to the modelled results. Similar to the shoaling position, Figure 7c shows that a new boundary layer is forming during the acceleration phase of the draw-down, and this boundary layer eventually reaches the free-surface. During the final deceleration stage (Figure 7d), the boundary layer remains limited by the water depth, which

slowly declines towards zero.

In some studies logarithmic velocity profiles have been assumed, see e.g. Kuriyama et al. (2014) and Sugawara et al. (2014b). This assumption was partially backed up by Lacy et al. (2012), who showed a clear logarithmic profile beneath the 2010 Chilean tsunami, though this logarithmic profile did not span the entire water depth. To demonstrate the appearance of the tsunami induced boundary layers, Figure 8 shows the velocity profiles of the first acceleration and deceleration phase from case S200 at both the toe of the slope at $x = -2800$ m (Figure 8a,b) and in the shoaling position at $x = -1200$ m (Figure 8c,d) now using a logarithmic vertical scale. Figure 8 clearly illustrates that the tsunami-induced boundary layers are indeed logarithmic, as nearly perfect straight lines near the bed are shown. The results, however, also indicate that the velocity profiles do not follow a logarithmic profile all the way to the free-surface, but rather a limited part of the water depth. It can likewise be seen that (7) depicted as a dashed line, gives a reasonable approximation for the region where the velocity profiles are logarithmic. This is typical for all the cases simulated. This indicates that assumed logarithmic velocity profiles could work reasonable for sediment transport purposes provided that the limited thickness of the boundary layer is taken into account.

3.3. Predicting the friction velocity

With the good agreement between the modelled and predicted time varying boundary layer thickness, it seem obvious to extend this approach to likewise predict the bed shear stress (or friction velocity), which is often regarded as the primary factor governing sediment transport. Williams and Fuhrman (2016) showed that standard wave friction factor expressions also applied reasonably to the tsunami-scale waves at peak flow. We therefore suggest the following simple engineering model to predict the friction velocity beneath tsunami waves:

$$U_f = \sqrt{\frac{f(t)}{2}} u_0(t) \quad (9)$$

where $f(t)$ is a time varying friction factor. For rough flows, the constant friction factor is traditionally given as a function of a/k_s . There exists many formula for the friction factor as a function of a/k_s , see e.g. Fredsøe and Deigaard (1992), Nielsen (1992) or Fuhrman et al. (2013). In what follows, we will utilize the expression from Fuhrman et al. (2013), but again substituting a with $a(t)$ from (8), leading to the following time-varying wave friction factor:

$$f_w(t) = \exp\left(5.5\left(\frac{a(t)}{k_s}\right)^{-0.16} - 6.7\right) \quad (10)$$

From this equation it can be seen that large orbital free stream motion will lead to smaller friction factors. The reason for this is that the boundary layer will have longer time to grow, and thus the velocity gradients become smaller. In addition to this, it is important to recognize (as just shown) that the tsunami boundary layer may extend all the way to the free surface, and

at this stage it would be more current-like. Therefore, to also account for this possibility we define $f(t)$ generally as

$$f(t) = \max(f_w(t), f_c) \quad (11)$$

where f_c is the current friction factor given by the Colebrook-White formula

$$f_c = \frac{2}{(C - 2.5 \log(k_N/h))^2} \quad (12)$$

with $C = 8.5$. The change from the traditional coefficient $C = 6.5$ from Colebrook and White to $C = 8.5$ is because the present formulation is based on the free-stream velocity ($u_0 = u(y = \delta)$) rather than the depth averaged velocity. The above formulation ensures a continuous transition to a current based friction factor in positions where the boundary layer extends all the way to the free-surface. The model described above may also be utilized in conjunction with depth-averaged velocities e.g from NLSW models, by setting $C = 6.5$. Additionally, for comparison, we will also estimate the friction velocity by what we will deem a standard approach for NLSW models. In the literature different approaches have been used. Kuriyama et al. (2014) and Cheng and Weiss (2013) e.g. used an assumed logarithmic profile and Yamashita et al. (2016) as well as Li et al. (2012b) used a Manning approach. Here we will compare with the Manning approach, where the friction velocity for the present cases can be alternatively calculated as

$$U_f = \langle U \rangle n h^{-1/6} \sqrt{g} \quad (13)$$

where

$$\langle U \rangle = \frac{1}{h} \int_{y_b}^{\eta} u dy \quad (14)$$

is the depth averaged velocity and n is the Manning coefficient, which can be calculated by

$$n = \frac{k_s^{1/6}}{8.1 \sqrt{g}} = 0.0085 \frac{\text{s}}{\text{m}^{1/3}} \quad (15)$$

In what follows we will now compare the predicted values using both the new engineering approach and the Manning approach for cases N100 and S030. We will likewise compare the modelled and predicted boundary layer thickness for these two cases, to illustrate the performance of (7) for two additional cases.

Figure 9 shows free-stream velocities (Figure 9a-c), surface elevations, modelled- and predicted boundary layer thickness (Figure 9d-f) and modelled friction velocities as well as predicted friction velocities using both the present engineering approach and the Manning approach (Figure 9g-i) for case N100 at the toe of the slope ($x = -1400$ m), in a shoaling position ($x = -900$ m), and at the shore ($x = 0$ m). For the Manning approach we have used the calculated free-stream velocity rather than the depth averaged velocity. The difference between the depth-averaged and free-stream velocity is small, although using the depth-averaged velocity resulted in slightly lower friction velocity predictions than are presented here.

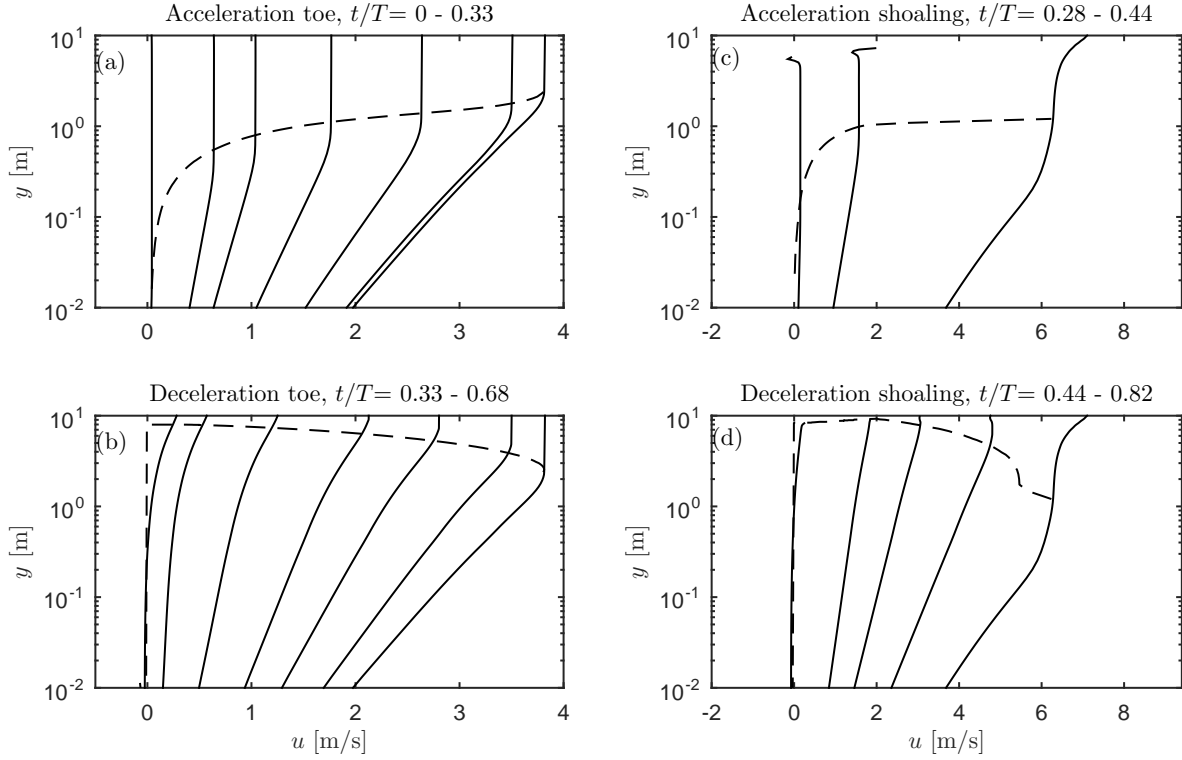


Figure 8: Modelled velocity profiles (-) and predicted boundary layer thickness (- -) for case S200 at (a),(b) $x = -2800$ m and (c),(d) $x = -1200$ m.

Figure 9g-i shows the friction velocity being lowest at the toe of slope and highest at the shore. This is both due to an increased velocity as the wave shoals (see the increasing free stream velocity in 9a-c), but also an increased asymmetry resulting in smaller boundary layer thickness and higher velocity gradients. The predicted friction velocity using both the Manning approach (13) as well as the engineering model (9) follow the shape of the modelled friction velocity. There is, however, a tendency to under-predict the magnitude of the friction velocity using the Manning approach at the toe of the slope and in the shoaling position. This can be explained by the Manning approach not capturing the effect of the time varying boundary layer thickness, which at these position only spans a small fraction of the water depth, when the front of the tsunami arrives (Figure 9g-h). This physical feature, by design, seems to be well captured by the present approach. It can also be seen that (7), in general, does a consistently good job at predicting the time varying boundary layer thickness of case N100. The largest discrepancies are found at the shoaling position during the second and third deceleration phases (Figure 9e, $t = 430 - 670$ s and $t = 900 - 950$ s).

Figure 10 shows free-stream velocities (Figure 10a-c), surface elevations as well as modelled- and predicted boundary layer thickness (Figure 10d-f) and modelled friction velocities as well as predicted friction velocities using both the present engineering approach and the Manning approach (Figure 10g-i) for case S030 at the toe of the slope ($x = -420$ m), in a shoaling position ($x = -180$ m,) and at the shore ($x = 0$ m). Similar to before both the present engineering model and the

Manning approach follows the shape of the modelled friction velocity (Figure 10g-i), but again there is a tendency to under-predict the magnitude of the friction velocity using the Manning approach at the toe of the slope and in the shoaling position (Figure 10g,h). The proposed engineering model again captures this effect. It is also worth noting, that in this case, where the wave is not breaking, the boundary layer only stretches the entire depth in the deceleration phase of the draw-down in the shoaling position (Figure 10e, $t = 550 - 800$ s) as well as the deceleration phase of the draw-down at the shore (Figure 10f, $t = 430 - 600$ s). This indicates that the tsunami induced boundary layer is very dependent on the run-up type. Finally, it can be seen that the match between the modelled boundary layer thickness and that predicted by (7) is again reasonable.

To demonstrate further the performance of the proposed engineering model and the difference between this and the standard Manning approach, Figure 11 shows the computed and predicted friction velocity at both the toe of the slope, at a shoaling position and at the shore, for 13 of the 14 cases simulated in Part 1, taken at a 2 seconds interval (The only case not included is case S030L, which ran up as a undular bore. In this case the estimations for u_0 , based on the approach described in the previous section, were not very accurate). Here it can clearly be seen that the proposed model improves the prediction of the friction velocity significantly at the toe of the slope (Figure 11a,b) and in the shoaling position (Figure 11c,d), but remains very similar to the prediction using the Manning approach at the shore (Figure 11e,f). The greatest improvement is seen at the higher friction velocities, which corresponds to the arrival of the steep

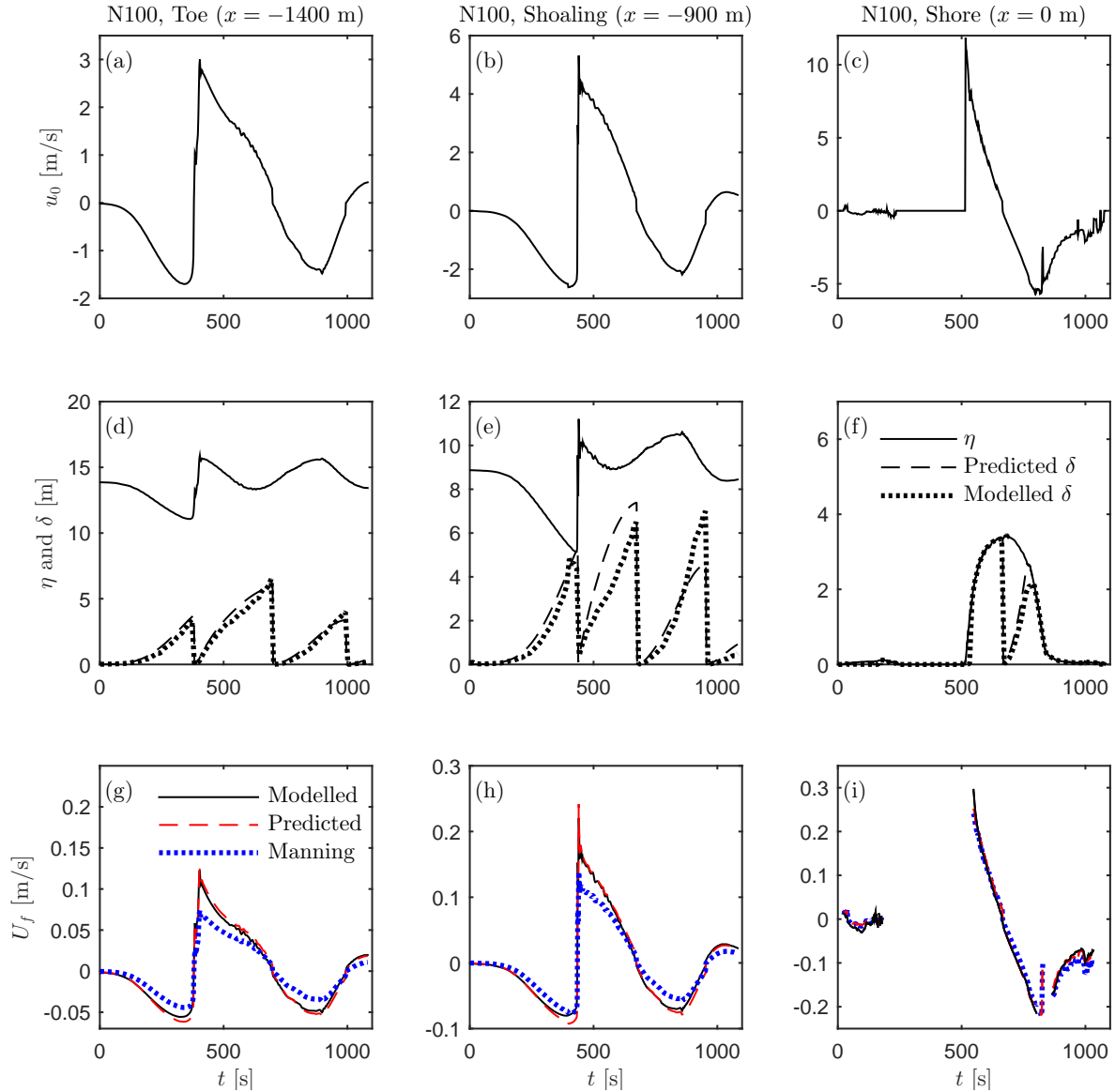


Figure 9: Time series of free-stream velocities (a)-(c), surface elevation and boundary layer thickness (d)-(f) and friction velocities (g)-(i) for case N100 at the toe of the slope ($x = -1400$ m), at one shoaling position ($x = -900$ m) and at the shore ($x = 0$ m).

wave front where the tsunami-induced boundary layer has not had time to grow much. At the shore, where wave breaking occurs in many of the cases, the scatter is naturally larger for both methods.

4. Conclusions

In this work results from numerical simulations of full scale tsunamis running up different constantly sloped regions are presented, with a special focus on tsunami-induced boundary layers, bed shear stress and implications for sediment transport. The results presented here is connected to Part 1, where the run-up process of the same full scale simulations were discussed.

Spatial distributions of Shields parameters and Rouse numbers have revealed that, for the cases considered, significant sediment transport could be expected to occur, and that this sed-

iment transport would in general be dominated by suspended sediment transport, provided that the sediment corresponds to medium sand. Large Rouse numbers beneath the inundating tsunami front have indicated that the sediment in suspension would probably span the entirety of the boundary layer. Furthermore, behind the tsunami front the lower Rouse numbers indicate that suspended sediment transport would still be dominant, but that it would likely be confined to the lower part of the boundary layer. During the draw-down both Shields parameters and Rouse numbers likewise indicate that substantial suspended sediment transport could be expected. This thus questions one of the main assumptions of many inverse paleo tsunami research models, namely that sediment will not get re-suspended during draw-down.

Subsequently the detailed physics of the tsunami-induced boundary layers have been discussed. The boundary layers be-

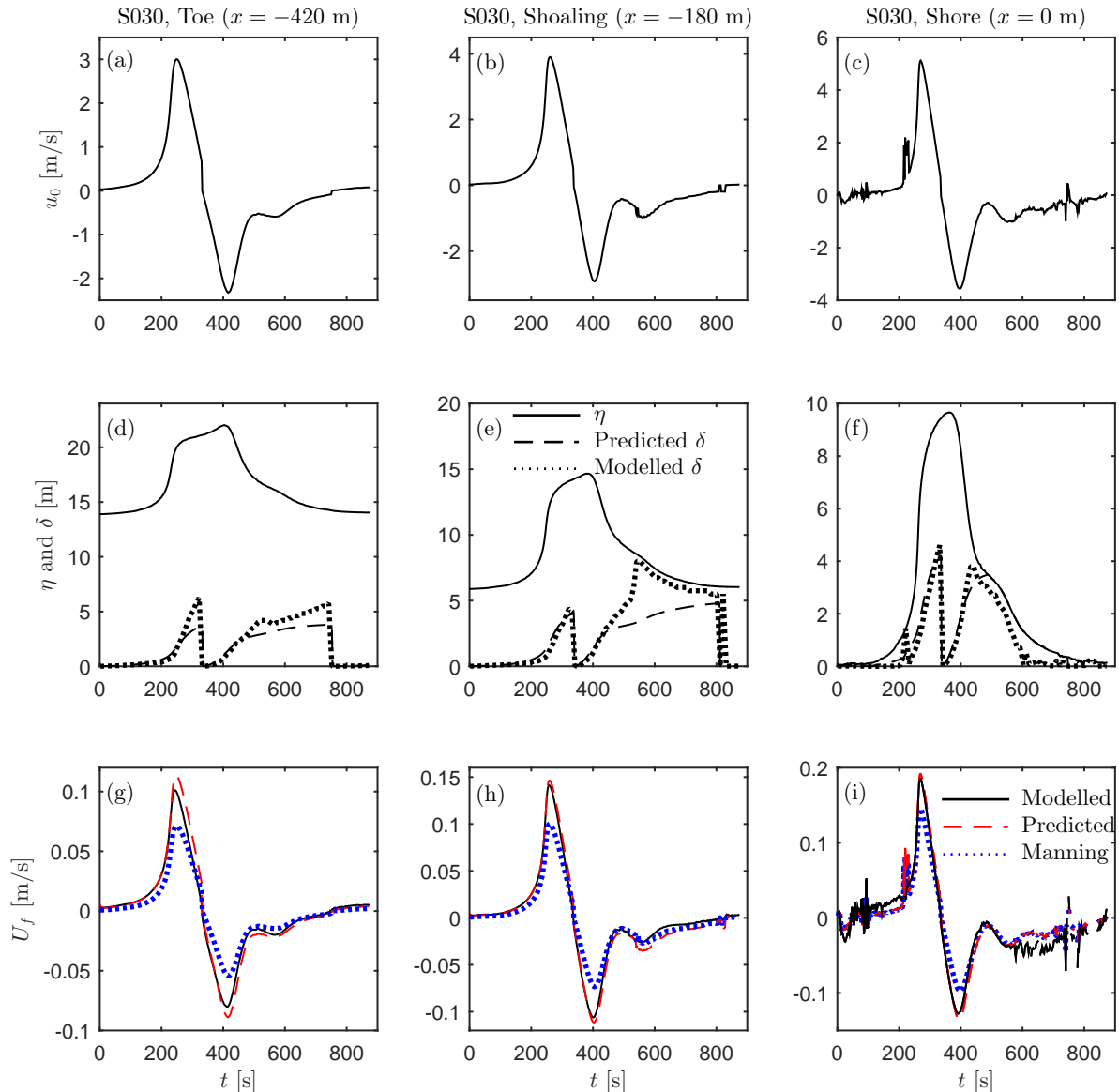


Figure 10: Time series of free-stream velocities (a)-(c), surface elevation and boundary layer thickness (d)-(f) and friction velocities (g)-(i) for case S030 at the toe of the slope ($x = -420$ m), at one shoaling position ($x = -180$ m) and at the shore ($x = 0$ m).

neath the tsunamis have been shown to grow in time beneath the tsunami, reaching a maximum height just before flow reversal. After flow reversal a new boundary layer forms and grows. The observed boundary layer thicknesses have ranged from spanning a small proportion of the water depth to spanning the entire depth. Especially in the non-breaking case considered, the boundary layer rarely stretched the entire depth. In the cases running up as breaking bores, the boundary layers stretched the entire water depth during run up, but during draw-down a new boundary layer formed which was not depth limited.

It was shown that the temporal variation of the boundary layer thickness can be reasonably predicted using standard empirical engineering formulas, but replacing the orbital amplitude with the total distance travelled by a free-stream particle following each flow reversal. The velocity profiles beneath the tsunami were shown to yield a good match with a logarithmic

profile up to the predicted boundary layer thickness.

Finally, it has been shown that the time varying friction velocity could be similarly well predicted by an engineering model building on a time varying friction factor, while also taking into account the time varying boundary layer thickness described above. This approach was shown to give better estimates for the friction velocity beneath the steep tsunami wave front than a standard Manning approach. Both the engineering model for the time varying boundary layer thickness and the friction velocity can easily be implemented in any NLSW or Boussinesq model, improving, potentially, their ability to predict sediment transport beneath tsunamis. This can prove valuable in accessing the impact of a tsunami of different coasts.

The general way in which these formula are derived and implemented, suggests that they may well be also applicable for shorter waves, though this is left as a topic for future research.

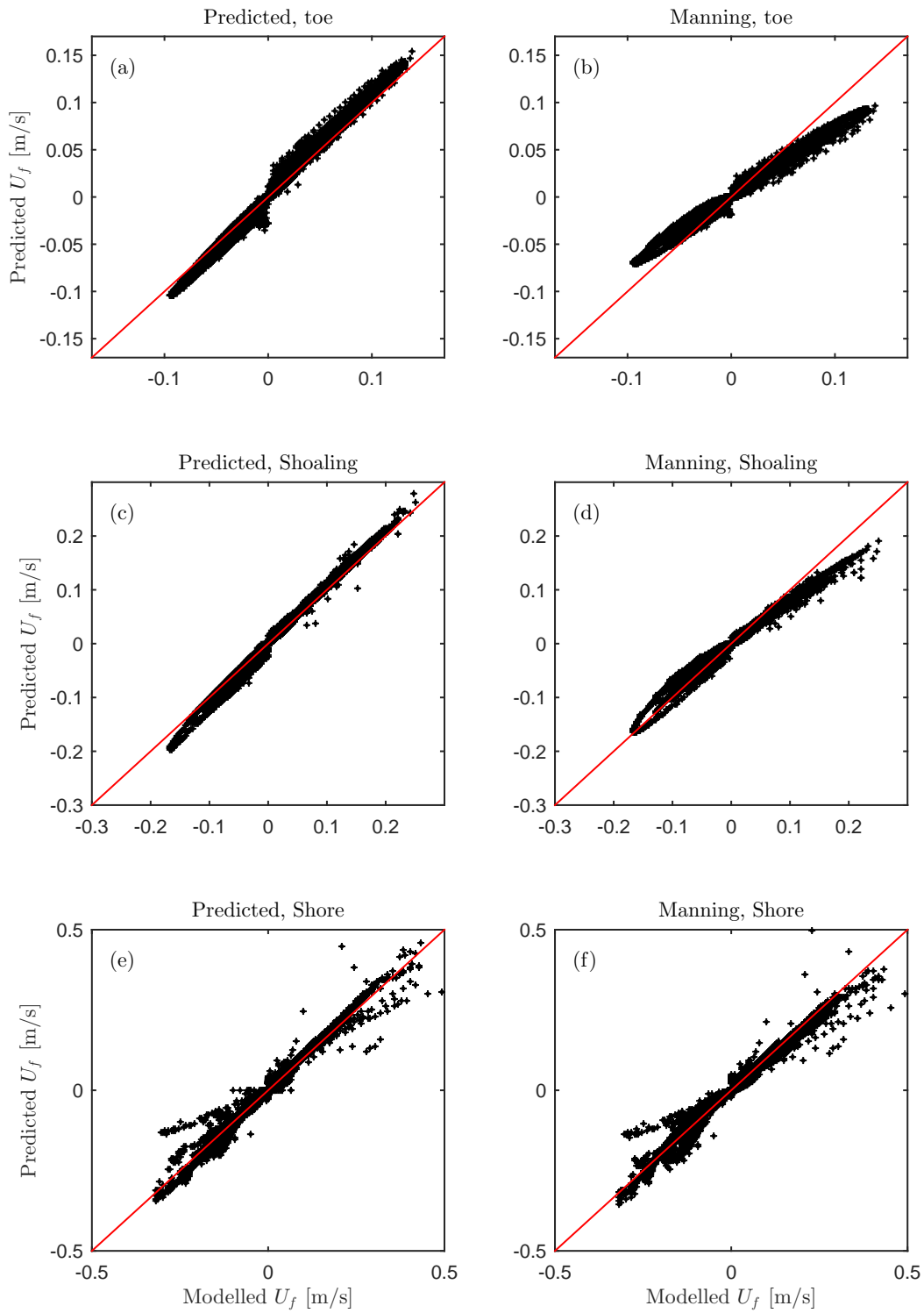


Figure 11: Comparison of modelled and predicted friction velocities using both the new engineering model (9) and the Manning approach (13). (-) marks the line of perfect agreement.

5. Acknowledgements

The authors acknowledge support from the European Union project ASTARTE–Assessment, Strategy And Risk Reduction for Tsunamis in Europe, Grant no. 603839 (FP7-ENV-

2013.6.4-3).

References

- Apotsos, A., Buckley, M., Gelfenbaum, G., Jaffe, B., Vatvani, D., 2011a. Nearshore tsunami inundation model validation: Toward sediment transport applications. *Pure and App. Geophys.* 168 (11), 2097–2119.
- Apotsos, A., Gelfenbaum, G., Jaffe, B., 2011b. Process-based modeling of tsunami inundation and sediment transport. *J. Geophys. Res.* 116 (1), –.
- Apotsos, A., Gelfenbaum, G., Jaffe, B., Watt, S., Peck, B., Buckley, M., Stevens, A., 2011c. Tsunami inundation and sediment transport in a sediment-limited embayment on American Samoa. *Earth-Sci Rev.* 107 (1–2), 1–11.
- Baykal, C., Sumer, B. M., Fuhrman, D. R., Jacobsen, N. G., Fredsøe, J., 2015. Numerical investigation of flow and scour around a vertical circular cylinder. *Phil. Trans. Roy. Soc. A* 373, article no. 20140104.
- Bayraktar, D., Ahmad, J., Larsen, B. E., Carstensen, S., Fuhrman, D. R., 2016. Experimental and numerical study of wave-induced backfilling beneath submarine pipelines. *Coast. Eng.* 118, 63–75.
- Borrero, J. C., Synolakis, C. E., Fritz, H., 2006. Northern Sumatra field survey after the December 2004 Great Sumatra earthquake and Indian Ocean tsunami. *Earthquake Spectra* 22 (3), S93–S104.
- Cheng, W., Weiss, R., 2013. On sediment extent and runup of tsunami waves. *Earth and Planetary Science Letters* 362, 305–309.
- Fredsøe, J., Deigaard, R., 1992. *Mechanics of Coastal Sediment Transport*. World Scientific, Singapore.
- Fuhrman, D. R., Baykal, C., Sumer, B. M., Jacobsen, N. G., Fredsøe, J., 2014. Numerical simulation of wave-induced scour and backfilling processes beneath submarine pipelines. *Coast. Eng.* 94, 10–22.
- Fuhrman, D. R., Schløer, S., Sterner, J., 2013. RANS-based simulation of turbulent wave boundary layer and sheet-flow sediment transport processes. *Coast. Eng.* 73, 151–166.
- Jacobsen, N. G., Fuhrman, D. R., Fredsøe, J., 2012. A wave generation toolbox for the open-source CFD library: OpenFOAM (R). *Int. J. Numer. Meth. Fluids* 70, 1073–1088.
- Jaffe, B. E., Gelfenbaum, G., 2007. A simple model for calculating tsunami flow speed from tsunami deposits. *Sedimentary Geol.* 200 (3–4), 347–361.
- Kuriyama, Y., Takahashi, K., Yanagishima, S., Tomita, T., 2014. Beach profile change at Hasaki, Japan caused by 5-m-high tsunami due to the 2011 off the Pacific coast of Tohoku earthquake. *Mar. Geol.* 355, 234–243.
- Lacy, J. R., Rubin, D. M., Buscombe, D., 2012. Currents, drag, and sediment transport induced by a tsunami. *J. Geophys. Res.- Oceans* 117 (9), –.
- Larsen, B. E., Arbøll, L. K., Frigaard, S., Carstensen, S., Fuhrman, D. R., 2018. Experimental study of tsunami-induced scour around a monopile foundation. *Coast. Eng.* 138, 9–21.
- Larsen, B. E., Fuhrman, D. R., 2018a. Full-scale CFD simulation of tsunamis. part 1: Model validation and run-up. Under preparation.
- Larsen, B. E., Fuhrman, D. R., 2018b. On the over-production of turbulence beneath surface waves in RANS models. In review.
- Larsen, B. E., Fuhrman, D. R., Baykal, C., Sumer, B. M., 2017. Tsunami-induced scour around monopile foundations. *Coast. Eng.* 129, 36–49.
- Larsen, B. E., Fuhrman, D. R., Sumer, B. M., 2016. Simulation of wave-plus-current scour beneath submarine pipelines. *J. Waterw. Port C-ASCE* 142 (5), article no. 08216001.
- Li, L., Huang, Z., Qiu, Q., Natawidjaja, D. H., Sieh, K., 2012a. Tsunami-induced coastal change: scenario studies for Painan, West Sumatra, Indonesia. *Earth Planets and Space* 64 (10), 799–816.
- Li, L., Qiu, Q., Huang, Z., 2012b. Numerical modeling of the morphological change in Lhok Nga, West Banda Aceh, during the 2004 Indian Ocean tsunami: understanding tsunami deposits using a forward modeling method. *Nat. Haz.* 64 (2), 1549–1574.
- Madsen, P. A., Schäffer, H. A., 2010. Analytical solutions for tsunami runup on a plane beach. *J. Fluid Mech.* 645, 27–57.
- Moore, A. L., McAdoo, B. G., Ruffman, A., 2007. Landward fining from multiple sources in a sand sheet deposited by the 1929 Grand Banks tsunami, Newfoundland. *Sedimentary Geol.* 200 (3–4), 336–346.
- Nielsen, P., 1992. *Coastal Bottom Boundary Layers and Sediment Transport*. World Scientific, Singapore.
- Ontowirjo, B., Paris, R., Mano, A., 2013. Modeling of coastal erosion and sediment deposition during the 2004 Indian Ocean tsunami in Lhok Nga, Sumatra, Indonesia. *Nat. Haz.* 65 (3), 1967–1979.
- Paris, R., Wassmer, P., Sartohadi, J., Lavigne, F., Barthomeuf, B., Desgages, E., Grancher, D., Baumert, P., Vautier, F., Brunstein, D., Gomez, C., 2009. Tsunamis as geomorphic crises: Lessons from the December 26, 2004 tsunami in Lhok Nga, West Banda Aceh (Sumatra, Indonesia). *Geomorphology* 104 (1–2), 59–72.
- Soulsby, R. L., Smith, D. E., Ruffman, A., 2007. Reconstructing tsunami run-up from sedimentary characteristics - a simple mathematical model. *Coastal Sediments '07 - Proceedings of 6th International Symposium on Coastal Engineering and Science of Coastal Sediment Processes*.
- Sugawara, D., Goto, K., Jaffe, B. E., 2014a. Numerical models of tsunami sediment transport - current understanding and future directions. *Mar. Geol.* 352, 295–320.
- Sugawara, D., Takahashi, T., Imamura, F., 2014b. Sediment transport due to the 2011 Tohoku-Oki tsunami at Sendai: Results from numerical modeling. *Mar. Geol.* 358, 18–37.
- Suppasri, A., Muhari, A., Ranasinghe, P., Mas, E., Shuto, N., Imamura, F., Koshimura, S., 2012. Damage and reconstruction after the 2004 Indian Ocean tsunami and the 2011 Great East Japan tsunami. *J. Nat. Disaster Sc.* 34 (1), 19–39.
- Tanaka, H., Adityawan, M. B., Mitobe, Y., Widiyanto, W., 2016. A new computation method of bottom shear stress under tsunami waves. *J. of Coast. Res.* 1 (75), 1247–1251.
- Udo, K., Takeda, Y., Tanaka, H., 2016. Coastal morphology change before and after 2011 off the Pacific coast of Tohoku earthquake tsunami at Rikuzen-Takata coast. *Coast. Eng. Journal* 58 (4), 1640016.
- Wilcox, D. C., 2006. *Turbulence Modeling for CFD*, 3rd Edition. DCW Industries, Inc., La Canada, California.
- Williams, I. A., Fuhrman, D. R., 2016. Numerical simulation of tsunami-scale wave boundary layers. *Coast. Eng.* 110, 17–31.
- Yamashita, K., Sugawara, D., Takahashi, T., Imamura, F., Saito, Y., Imato, Y., Kai, T., Uehara, H., Kato, T., Nakata, K., Saka, R., Nishikawa, A., 2016. Numerical simulations of large-scale sediment transport caused by the 2011 Tohoku earthquake tsunami in Hirota Bay, Southern Sanriku Coast. *Coast. Eng. J.* 58 (4), 1640015.
- Yoshii, T., Tanaka, S., Matsuyama, M., 2017. Tsunami deposits in a super-large wave flume. *Mar. Geol.* 391, 98–107.

Chapter 8

Conclusions

Through numerical modelling and an experimental campaign detailed knowledge on tsunami-seabed interactions has been obtained. One of the main goals of this thesis was to use CFD to generate insight, that was otherwise difficult to achieve, either due to experimental constraints or model limitations. This has been achieved in the present thesis, though as also described in Chapters 2 and 6 the simulations still take substantial amount of time. In the simulations of tsunami-induced scour (Chapter 2), it was even necessary to perform these at a model scale rather than full-scale. Despite this the simulations still took approximately four months to complete. From this, it is clear, that using CFD to study tsunami processes require a lot of patience. The aim of using CFD to study tsunamis, should therefore not be to get fast and accurate solutions. This is, with the current available computational power, not possible. The advantage of using CFD, as already mentioned, is that it can be used to generate knowledge, that otherwise would be very difficult to gain.

In what follows I will now conclude on each of the four specific research questions:

RQ 1) How can tsunami-induced scour around offshore monopile foundations be studied, characterized and predicted?

This research question was answered through Chapters 2 and 3. In these chapters the scour process was studied by representing the tsunami by a time varying current. This enabled the use of a rigid lid in the numerical simulations in Chapter 2, and a pump to drive the flow in Chapter 3. This is a novel approach for studying tsunami-induced scour, and could potentially be used for other offshore problems, provided that the depth based Froude number is low enough, such that the effects associated with the free-surface become negligible.

The simulations and experiments in Chapter 2 and 3 were done at a model scale. The difficulties of conducting properly scaled experiments have been mentioned many times in the present thesis. This is an important discussion, and I believe one of the reasons that solitary waves have been used to such a large degree in the past is that scaling considerations were not done. One cannot, however, obtain full similarity. Therefore, similarity should be achieved differently depending on the physical processes being studied. In Chapter 2, a methodology was developed for establishing similarity between model and full-tsunami scales in relation to the tsunami-induced scour process. This methodology is based on a diameter-based Froude number, coupled with the dimensionless ratio of the expected boundary layer thickness to monopile diameter. This ensures similarity between the adverse pressure gradient, induced by the presence of the structure, as well as similarity in the relative size of the horseshoe vortex, which largely governs the scour process.

The tsunami-induced scouring, both for tsunamis represented by sinusoidal (Chapter 2) and single (Chapter 3) waves, were shown to occur in a stepwise cumulative fashion with increasing number of tsunami waves. Some backfilling was experienced in the experiments when the Shields parameter was just above the critical and here sand was transported back into the scour hole. Some backfilling also occurred upon flow reversal in one of the sinusoidal cases in Chapter 2, where the period to time scale ratio was large. In general, however, due to the relatively long times involved, the process occurring during two half cycles of the sinusoidal tsunami seemed to be largely independent of one another.

The bed profiles presented in Chapter 2, were reasonable symmetric beyond the first period and the asymmetry observed at any particular time was primarily due to the directionality of the flow. In the case where the period-to-time scale ratio was large, the simulated bed profiles resembled that of steady currents. The bed profiles in Chapter 3 likewise resembled scour profiles of a steady currents, as could be expected, since the flow was uni-directional.

Tsunamis may both current-like and wave-like. The tsunami-induced scour process resembles that under steady currents, and the scouring can mainly be attributed to the horseshoe vortex similar to steady current scour. This was demonstrated in Chapter 2, where a clear horseshoe vortex was shown in front of the monopile. The scour process will, however, be limited by the finite wave boundary layer thickness rather than the water depth.

Based on the simulations in Chapter 2, it was argued that the scour depths tended

towards an equilibrium value with increasing number tsunami waves. It was suggested that this equilibrium value could reasonably be predicted using empirical expressions for steady current monopile scour, but invoking the predicted tsunami-induced boundary layer thickness. This finding was further supported by the experimental results in Chapter 3, where it was possible to continue the experiments until equilibrium scour depths were reached. This recognition was an important first step towards being able to predict the time varying tsunami-induced scour depth. Furthermore, the high number of periods needed to reach equilibrium, indicates that equilibrium may or may not be reached during a tsunami event.

With the insights just presented, a simple methodology for predicting tsunami-induced scour around monopiles in practice, was developed in Chapter 2. This methodology takes into account the time variation of the scour process as well as finite boundary layer thickness effects. The practical method makes modified use of existing experimentally-based expressions for predicting steady current scour and time scales, and is hence fully-consistent with these at this (infinite period) limit. This practical model was shown to give accurate predictions of the considered tsunami-induced scour cases in Chapter 2.

In Chapter 3, the practical model was slightly modified. Here the parameter ψ , was now calculated analytically, rather than using the fixed value, suggested in Chapter 2. The modified model was shown to be able to predict the tsunami-induced scour depths now also in cases where the tsunami was represented by a single wave.

RQ 2) How can current VOF and RANS models be used and modified to enable accurate simulations of the run-up of a tsunami event?

This research question was answered through Chapters 4 and 5. The chapters themselves, are not directly related to tsunamis, but rather, in general, to the accurate simulation of waves using VOF and RANS models. A good performances of the VOF and RANS models used are, however, necessary for accurately simulating the run-up of tsunamis.

In Chapter 4, the performance of `interFoam`, on the simulation of progressive regular gravity waves, was systematically documented. It was shown that taking `interFoam` "out of the box" (i.e. using basic settings) yielded quite poor results. The wave heights were shown to increase, wiggles appeared at the interface, spurious velocities were present in the air and velocities near the crest were severely overestimated, following a propagation of only a few wave lengths. These undesirable effects would also be present in simulations of tsunami waves, and hence the research into limiting

these.

It was shown that the four problems could be reduced substantially by lowering the time step and increasing the spatial resolution. This can be considered comforting result (for the solver), as it demonstrates that `interFoam` converges towards the stream function solution. A very small Courant number was needed, however, to get a good solution when propagating a wave even a short distance. Such a low Courant number is not normally used when simulating free-surface waves using `interFoam`, and this indicates that previous studies might have not converged.

The effect of the discretization schemes and iterative solution procedures was documented, by changing them one at a time. It was shown that, especially the convective schemes, had a huge impact on the solution, and the choice convection scheme alone could determine whether the wave height decayed or increased while propagating. This effect was largely determined by the numerical diffusivity of the applied scheme. By combining more or less diffusive schemes (not only convective, but also e.g. temporal) it was shown that a diffusive balance could be reached, where it was possible to propagate the wave a full 100 wave lengths while reasonably maintaining its shape. One of these balanced settings also showed a significant improvement in the velocity profile beneath the crest. Furthermore, it was demonstrated that the spurious air velocities only affected the interface cells, as cases with very high air velocities did show significant different results for the velocity profiles.

Using the basic settings, the new open source solver `interFlow`, was (similar to `interFoam`) shown to be able to propagate the wave for 100 wave lengths. In contrast to `interFoam` the wave heights, with the basic settings, slightly decreased rather than increase. Both the spurious velocities and the severely overestimated crest velocities were present using the `interFlow` solver. The interface wiggles were however not present, as `interFlow` advects the surface in a geometric manner, rather than solving the advection-diffusion equation of the volume fractions, as also discussed in Roenby et al. (2017). `interFlow` was able to obtain a similar diffusive balance, and succeeded in accurately propagating the wave for 100 wave lengths, while maintaining a reasonably good match with the stream function solution, both in terms of the surface elevations and velocities.

Despite being able to reach a diffusive balance, the most safe way of obtaining a good solution, both using `interFoam` and `interFlow`, is using small Courant number. With `interFoam`, this can be coupled with a slightly more diffusive convection scheme (e.g. SFCD) to limit the presence of the interface wiggles, as was also done

in subsequent free-surface wave simulations in this thesis.

Although large improvements, relative to using the basic settings, were achieved, the solvers `interFoam` and `interFlow` are not without problems. They are reasonably good at reproducing accurate surface elevations over short propagation distances, but the crest velocities are still severely overestimated, unless very small time steps are used. This is an important recognition as it implies, that solely validating your CFD model against surface elevations does not assure proper wave kinematics.

Solving the problems of `interFoam` and `interFlow` in a more fundamentally satisfying way, rather than reducing the time step or obtaining a diffusive balance, can be considered an important task for future research.

The findings above can improve the basic VOF solver's ability to accurately propagate laminar waves, and was a necessary first step before the run-up process of tsunamis could be accurately simulated. To study run-up of tsunami the effect of turbulence also needed to be accurately represented, and this led to the work presented Chapter 5.

In Chapter 5, a long-standing instability problem for RANS models, when applied to free-surface waves, is treated. The problem was originally diagnosed by Mayer and Madsen (2000), but this study has received very little attention the last 18 years. The problem arises because potential flow waves will have a non-zero production of turbulent kinetic energy, provided that the eddy viscosity is finite. This results in an exponential growth of the turbulence and eddy viscosity. This can cause waves to artificially decay or arrive at the surf-zone polluted, as demonstrated in Chapter 5 and also experienced in many previous studies involving the simulation of breaking waves using RANS models. The instability problem would also be present for tsunami waves, and Chapter 5 can therefore be viewed as a necessary model development, before accurate simulations of actual tsunamis could be made.

It is shown analytically, that standard two-equation turbulence closures are unconditional rather than conditional unstable, and the unstable growth rates are predicted. These models can be formally stabilized through the slight modification of an already established stress-limiting feature. The new stabilized closure models are, by design, as un-intrusive as possible. They default to standard models in uniform boundary layer flows (where these models are calibrated) as well other sheared flow regions. They also remain true to theoretically-based terms in the k -equation, are fully consistent with the Boussinesq approximation, and do not require modification of any standard closure coefficients.

It is demonstrated, that only the stabilized closure can propagate a stream function wave without an artificial decay in the wave heights. This was otherwise experienced with the standard closures, due to the high amounts of eddy viscosity extracting energy from the wave. The exponential growth of the eddy viscosity matched the predicted growth rate well, underlining the validity of the analysis. The propagation of a stream function wave can be considered a simple test case which all turbulence closures should be able to pass before simulating more complex problems.

The stabilized closures were also applied to a more complex case, by simulating the spilling breakers experiment of Ting and Kirby (1994). The results of otherwise identical stabilized and non-stabilized closures were compared and only stabilized models were able to predict low levels of turbulence pre-breaking, similar to the experiments. The standard models, on the other hand, predicted turbulence levels in the pre-breaking region of the same order of magnitude as in the surf zone. This is not physical, but again a direct consequence of their instability, and implies that standard model results, in such applications, may well be polluted before the phenomenon of physical interest (i.e. the breaking process) has even begun. It is demonstrated that such pollution results in an erroneous structure of the undertow velocity profile, both pre-breaking and extending into the outer surf zone. Only the stabilized closure is able to produce the correct evolution of the undertow structure from outside to within the surf zone.

It is hoped that Chapters 4 and 5 will raise awareness and enable users to more properly simulate a wide variety of free-surface wave problems using the open-source CFD package OpenFOAM together with RANS turbulence closure models. These problems involve wave-structure interactions, propagation to breaking and resulting surf zone dynamics, as well as boundary layer and sediment transport processes that occur beneath surface waves. These problems all fundamentally rely on an accurate description of surface waves and their underlying velocity kinematics.

RQ 3) What characterizes the tsunami run-up processes, and what is the importance of the "shorter" waves, sometimes riding on the tsunami front, on run-up height, inundation speed and local flow velocities?

This research question was answered through Chapter 6. Here, full-scale tsunami simulations were performed, with the tsunamis propagating on an initial flat bed, before running a constant slope region. The simulations used the idealized single waves and leading depression N-waves as tsunami representations.

The run-up of tsunami waves is dependent on incoming wave characteristics, such as

period, wave height and shape, but also on the bathymetry the tsunami encounters. This inter-dependence was attempted to be captured analytically by Madsen and Schäffer (2010) who expressed run-up heights and inundation speeds as function of the incoming wave amplitude and surf-similarity parameter. Based on these expressions' decent match with the more advanced CFD simulations, it can be concluded they do a reasonably good job in predicting the run-up heights in cases where breaking is not predicted occur. When breaking is predicted to occur, the expression from Hunt (1959) seem more appropriate. The expression from Hunt (1959) is also based on the surf-similarity parameter, and this indicates that the surf-similarity parameter can be considered one of the main non-dimensional parameters when assessing tsunami run-up. Furthermore, the general good match between the combined expressions of Madsen and Schäffer (2010) and Hunt (1959) indicates that this can be used as a quite reasonable first assessment of the run-up height.

Tsunamis can, however, not be considered as purely breaking or non-breaking. The run-up process is more complex than that. From the highly resolved CFD simulations, three previously defined, tsunami run-up categories were identified and a fourth category was likewise identified.

The tsunami run-up can appear "tide-like". In this situation, no breaking is occurring. The surface elevations of the tsunami are almost horizontal, and if standing on the shore, the tsunami would be experienced as a continuous, but relentless, inflow of water with gradually increasing depth. The inundation speed in one of these cases was shown to be very low, such that the tsunami could in fact be outrun. Such a run-up appearance have been seen with many real geophysical tsunamis as also highlighted in Chapter 6. The "tide-like" scenario only occurs in situations where the slope is steep, such that the slope will essentially be experienced as a vertical wall. In these cases, the very long incoming tsunamis, were reflected even before the crest of the tsunami arrived at the slope, essentially creating a transient standing wave. This caused a phase difference between the maximum velocity and maximum surface elevations. The analogy to a standing wave can be viewed as an alternative, but more likely, explanation for the phase-shift described in the study by Lacy et al. (2012). Furthermore, superposition between the incoming waves and the reflected waves meant that the incoming waves at the toe of slope was different for different slopes. This can pose a challenge if attempting to use measured surface elevations signals in numerical models. The "tide-like" scenario only appeared in situations where the waves were not predicted to break by the Madsen and Schäffer (2010) analysis. It was therefore argued that the surf similarity parameter can be used to

access whether a "tide-like" scenario is possible. This however required that the incoming wave was linear, and that the surf similarity parameter was much larger than the value where breaking would be predicted to occur (from the Madsen and Schäffer (2010) analysis).

Tsunamis can also run-up as a breaking bore or "wall of water". In this situation, the front of the tsunami is breaking, and the wave front is relatively steep. In the cases running up as breaking bores or "walls of water", the depth at the shore was seen to increase with several meters in a manner of a few seconds. At the same time the inundation speed was substantially larger than in the "tide like" scenario, which means that tsunamis running up as breaking bores can generally not be outrun. The breaking bores or "walls of water", can occur in situations where the slope is milder. The milder slopes, result in the tsunami having longer time to steepen compared to the "tide-like" scenarios. In all cases considered, resulting in a breaking bore, the steep tsunami wave front split into one or more shorter waves. These waves could not sustain their shape during shoaling and broke far from the shore, turning the wave front into a breaking bore.

In some cases with very mild slopes the tsunami front developed many shorter waves, forming a more proper undular bore. These shorter waves propagated a significant distance before breaking, but still broke at a distance to the shore, turning the entire wave into a breaking bore. This led the definition of a new category namely the "undular bore turning into a breaking bore". This category is different from the previous category where the shorter waves broke almost immediately. In cases belonging to this new category, the inundation speed was generally also so high that the tsunamis could not be outrun.

By extending the flat part of the domain, such that the tsunami propagated further before reaching the slope, it was shown, that a tsunami can also manifest itself at the coast as an undular bore. This has been observed with many real tsunamis, and is possibly one of the reasons why solitary waves have been used to such a great extend in the past. This run-up type required the tsunami propagating a long distance in shallow water, but at the same time a relatively steep slope, such that the shorter waves riding at the tsunami front, did not break at a large distance to the shore. By comparing two cases with the same slope and initial wave shape, propagating different distances before reaching the slope, it was possible to access the importance of the shorter waves riding at the tsunami wave front. It was shown that these waves have little impact on the run-up height and inundation speed. Here, the much larger main tsunami wave is much more important. It was, however, also shown, that the

local flow velocities of each the shorter waves were significantly higher compared to the case without an undular bore, and thus the shorter waves can be important for impact forces on structures and sediment transport.

Leading depression waves have been seen in relation with many real geophysical tsunamis. The simulated leading depression N-waves resulted in an initially retreating shoreline. As a result, the tsunami front of a leading depression N-wave will necessarily re-wet the drawn down region prior to reaching the original shoreline. This behaviour meant that, the previous observed "wall of water", was not observed for the N-waves at the original shoreline, but rather further offshore. From the simulated N-waves, it was also shown, that the undular bore, does not necessarily appear at the tsunami crest, but rather where the local surface elevation steepness is largest. In these cases, this happened between the trough and the crest.

It is hoped that this chapter will raise general awareness of how tsunamis run-up. This can be important in assessing the potential impact of a tsunami in different places, as it was shown that the combined expression of Madsen and Schäffer (2010) and Hunt (1959) gave reasonable run-up height approximations. Furthermore, the very large differences in inundation speed between the "tide-like" scenario and the other run-up types indicate that steep slopes are less vulnerable and this can be used in hazard assessments. The results can also be important for the design of future research, as it highlights different realistic tsunami scenarios. Tsunamis are definitely not solitary waves as often been used, and they are not necessarily breaking bores (as often taken for granted as the default run-up type), though this is a possible run-up type. In many cases the tsunami will not be breaking and instead just reflected, something which is often overlooked in the literature.

RQ 4) What are the characteristics of tsunami-induced boundary layers, bed shear stresses and resulting sediment transport beneath shoaling, inundating and retreating tsunamis and how can the boundary layer thickness and bed shear stress be predicted as well as included in potential flow models?

This research question is answered through Chapter 7, which builds on the same simulations presented in Chapter 6.

Boundary layers beneath shoaling and inundating tsunamis, may be both current-like and wave-like, similar to the description given by Williams and Fuhrman (2016) for offshore tsunami-induced boundary layers. The boundary layers beneath the tsunamis grow in time, reaching a maximum thickness just before flow reversal. After flow reversal a new boundary layer forms and grows. The modelled boundary

layer thickness ranged from spanning a small proportion of the water depth to spanning the entire depth. Especially in the non-breaking cases, the boundary rarely stretched the entire depth. In the cases running up as breaking bores, the boundary layers stretched the entire water depth during run up, but during draw-down a new boundary layer formed, which did not initially span the entire depth. This demonstrates that the different run-up types have a significant impact on the tsunami-induced boundary layers.

The velocity profiles beneath the tsunamis were shown to have a good match with a logarithmic profile, although only within the boundary layer. This indicates that the log-profiles used in many NLSW models will probably work well, if the effect of the limited boundary layer thickness is taken into account.

Spatial distributions of Shields parameters and Rouse numbers revealed that, for the present cases, significant sediment transport could be expected to occur, and that the sediment transport, in general, would be dominated by suspended sediment transport. Low Rouse numbers beneath the inundating tsunami front indicated that sediment in suspension would probably span the entire boundary layer here. Furthermore, behind the tsunami front the slightly larger Rouse numbers indicate that suspended sediment transport would be confined to the lower part of the boundary layer, though probably still dominating over bed load transport. During the draw-down, both Shields parameters and Rouse numbers likewise indicated that substantial suspended sediment transport could be expected. This thus questioned one of the main assumptions of many inverse paleo tsunami research models, namely that sediment will not get re-suspended during draw down.

It was argued, that the time varying boundary layer thickness can reasonably be predicted, using standard empirical engineering formulas, but replacing the orbital amplitude with the distance travelled by a particle following each flow reversal. It was shown that this approach gave reasonably accurate boundary layer thickness predictions both during shoaling, run-up and draw-down for both breaking and non-breaking tsunami waves. In a similar fashion it was shown that the time varying friction velocity could be well predicted by a new engineering model building on a time varying friction factor, which takes into account the effect of the time varying boundary layer thickness. This approach was shown to give better estimates for the friction velocity beneath the steep tsunami wave front than the standard Manning approach. Both the expression for the time varying boundary layer thickness and the engineering model for the friction velocity can easily be implemented in any NLSW or Boussinesq model, potentially improving their ability to predict sediment

transport beneath tsunamis. The general way in which these formula are implemented also suggest that they might be applicable also for shorter waves, although it was outside the scope of the present work to test this.

Chapter 9

Appendix - Simulation of the Ting and Kirby (1994) plunging breakers experiment

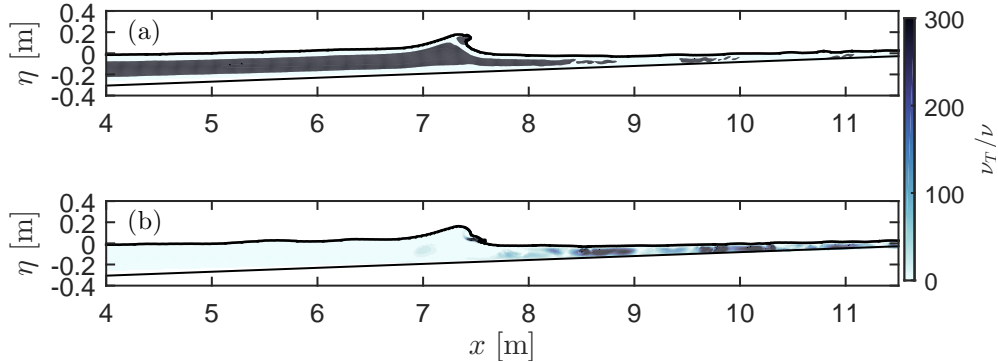


Figure 9.1: Snapshots of ν_T/ν at $t/T = 47.8$ for the plunging wave case of Ting and Kirby (1994), (a) Case 1 (b) Case 5, where the parameters used can be found in Table 2 in Chapter 5.

The notation for this appendix follow that of Chapter 5.

In Chapter 5, the simulated results using the new stabilized turbulence closure was compared to the experiments involving spilling breakers from Ting and Kirby (1994). Ting and Kirby (1994) also presented results for a case involving plunging breaking waves, and in this appendix, the results of the new stabilized turbulence closure will be compared to this experiment. This is done to further validate the model, but also to show that $\lambda_1 = 0.2$ (present in equation (2.34) in Chapter 5) is also the most suitable value for the stress limiter in another breaking wave scenario. In the present appendix only the results of the stabilized version of the turbulence closure will be presented as the plunging wave case will also have the instability problem described in Chapter 5, and there is no reason to proceed with a model that is clearly unstable. To demonstrate that the standard models are in fact unstable also for the plunging case Figure 9.1 shows a snapshot of the non-dimensional eddy viscosity using the standard Wilcox (1988) model (Figure 9.1(a)) and a stabilized model (Figure 9.1(b)). Each plot is again frozen at an instant where the wave is very close to breaking, such that the location of the surf zone is evident. As can be seen (similarly to the spilling case) the Wilcox (1988) model result in uniformly high eddy viscosity (orders of magnitude larger than ν), even in the pre-breaking region.

The stabilized versions considered in what follows are identical to those used for the spilling breakers simulations, and are listed in Table 9.1. The model domain for these simulations consists of a flat region having water depth $h = 0.4$ m, connected to a region having constant 1:35 slope. For these simulations, the waves are again stream function waves, this time with $T = 5$ s and $H = 0.128$ m with a zero Stokes

Case	Model	λ_1	λ_2	Line type (Figs. 9.3 & 9.4)
3	Present	0	0.05	Dashed dark (black) line
4	Present	0.875	0.05	Dotted dark (black) line
5	Present	0.2	0.05	Solid dark (black) line

Table 9.1: Summary of the names and stress parameters used in the plunging breaking wave experiment.

drift. A slightly longer domain and relaxation zone is used compared to the spilling breakers case. The relaxation zone in these simulations is now 8 m rather than 4 m. This is due to the longer wave length relative to the waves used for the spilling breakers. Except for the changed domain length and relaxation zone, the mesh is identical to the spilling breakers case. For a layout of the computational domain see again Figure 5 in Chapter 5.

Similar to the simulations of the spilling breakers a warm up period was needed before a quasi steady state was reached. The simulations were therefore run for 35 periods before data was extracted. Furthermore, in order to achieve stable mean values, the results presented in the following have been obtained by averaging over an additional 30 periods following the warm up (i.e. simulations have been run for a total of 65 periods)

Figure 9.2 shows comparison of the computed and experimental surface elevation envelopes as well as the mean water levels for the three models mentioned above. The solid lines represent the mean (ensemble averaged) values, whereas the shaded area represents plus or minus one standard deviation. It can be seen that all three models predict similar surface elevations, but that Cases 4 and 5 ($\lambda_1 > 0$) predicts a lot more wave to wave variability than Case 3, similar to that experienced in the simulations of the spilling breakers experiments (Figure 7 in Chapter 5). It can also be seen that with all the models the surface elevations during shoaling increase faster than in the experiments, and as a result, the break point is shifted slightly offshore, relative to the experiments. This behaviour is not due to the stabilized turbulence models, as it was also seen in the studies by Brown et al. (2016) and Christensen (2006) using non-stabilized RANS models and a LES model respectively.

As a further comparison, Figure 9.3 presents computed and measured (Ting and Kirby, 1994) averaged turbulent kinetic energy k profiles at a total of seven positions, corresponding to one pre-breaking position (Figure 9.3(a)), as well as six positions in the surf zone (Figure 9.3(b)–(g)). Similar to Chapter 5 the filled circles are calculated from u' alone ((3.6) in Chapter 5) whereas empty circles are calculated from both u' and v' ((3.5) in Chapter 5). In the figure the experimental values for the positions

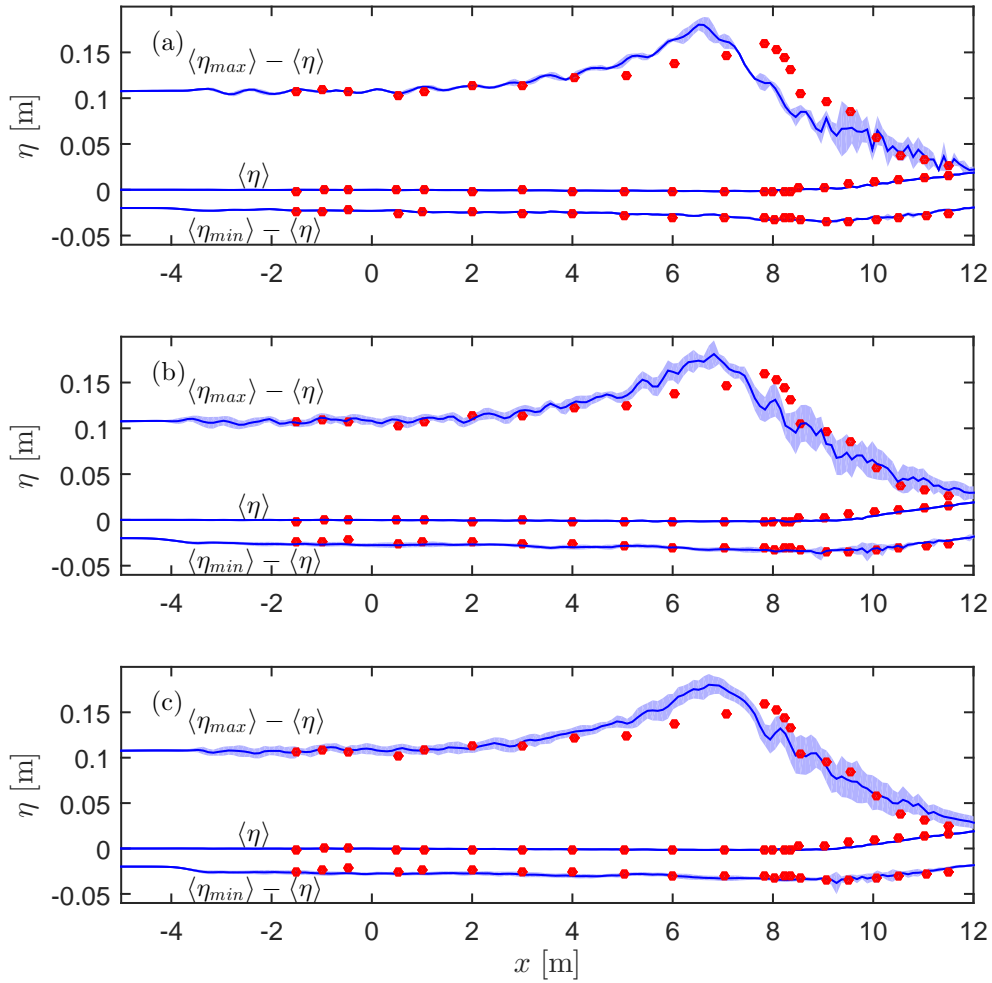


Figure 9.2: Comparison of modelled (lines) and measured (circles, from Ting and Kirby, 1994) surface elevation envelopes (top and bottom lines) and mean water levels (middle lines). Results in (a) Case 3, (b) Case 4 and (c) case 5. Solid lines represents the mean surface elevation and the shaded area represents plus and minus one standard deviation.

of the breakpoint, $x_b = 7.795$ m and depth at breaking $h_b = 0.154$ m are used. It can be seen that all three versions of the stabilized models, as expected, predict low levels of turbulence pre-breaking (Figure 9.3(a)) similar to the experiments. In the two outermost positions in the surf-zone (Figure 9.3(b),(c)) Case 3 (i.e. the stabilized Wilcox (1988) model) predicts much higher levels of turbulence than the experiments, whereas the prediction by the two limited Cases (Case 4 and 5) are more in line with the experiments. Going further into the inner surf-zone, the results from Case 3 and 5 compare reasonably, whereas Case 4 (the stabilized version of the Wilcox (2006) model) severely under-predicts the turbulence levels.

Similar to the spilling breaking case, the huge over-prediction of turbulence of Case

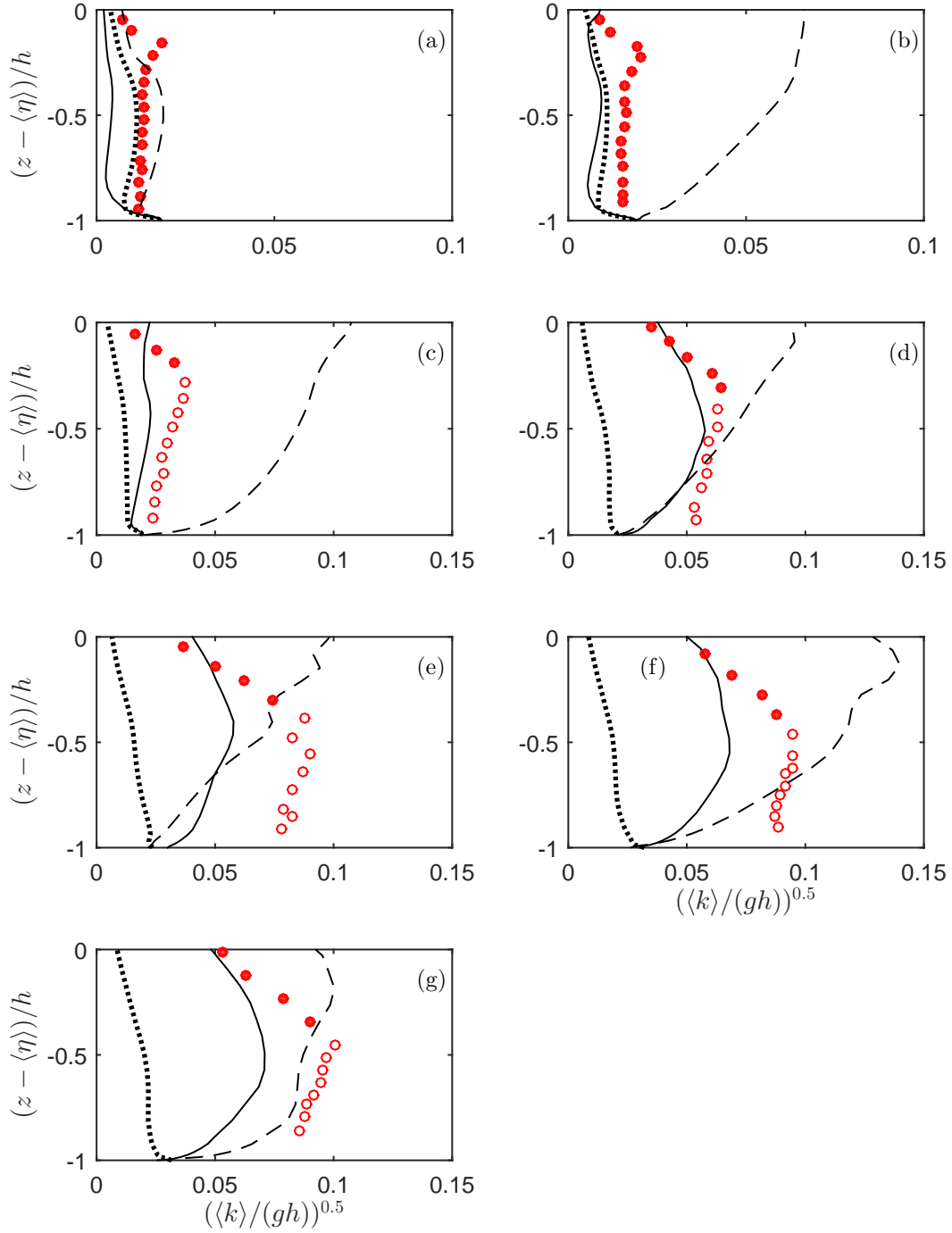


Figure 9.3: Comparison of modelled (lines) and measured (empty circles: from (3.5) in Chapter 5, filled circles: from (3.6) in Chapter 5) turbulent kinetic energy k profiles at (a) $x = 7.295$ m ($\tilde{x} = (x - x_b)/h_b = -3.247$), (b) $x = 7.795$ m ($\tilde{x} = 0$), (c) $x = 8.345$ m ($\tilde{x} = 3.571$), (d) $x = 8.795$ m ($\tilde{x} = 6.494$), (e) $x = 9.295$ m ($\tilde{x} = 9.740$), (f) $x = 9.795$ m ($\tilde{x} = 12.987$), (g) $x = 10.395$ m ($\tilde{x} = 16.883$).

3 in the outer surf zone, indicates that some limiting is necessary when simulating breaking waves. From the results above, however, it is clear that $\lambda_1 = 0.875$ (the stabilized version of the Wilcox (2006) model) limits the production of turbulence too much.

Finally, the undertow profiles are compared in Figure 9.4, at the same seven positions as in Figure 9.3. In the pre-breaking position (Figure 9.4(a)) all three models slightly overpredicts the strength of the undertow. This is probably due to the position of the breakpoint, being positioned slightly more offshore in the simulations than in the experiments. In the outer surf zone ((Figure 9.4(b),(c)) Case 4 and 5 (the two limited versions) maintain the correct structure in the undertow shape, whereas the structures are erroneous for Case 3 (the stabilized version of the Wilcox (1988) model). This can, similarly to the simulations of the spilling breakers, be tied to the over-prediction of turbulence in this region, increasing the flow resistance in the upper part of the flow. In the remaining four positions, the results of all three models are rather similar, and all of them overestimate the strength of the undertow near the bed in the three inner most positions (Figure 9.4(e)-(g)). This is again very similar to the simulated results of the spilling breakers, and is also very similar to what have been observed in previous simulations of these experiments (see e.g. Brown et al. (2016))

Considering the comparison between the modelled results for both the spilling and plunging breakers of Ting and Kirby (1994), as whole, it is clear that some kind of stress limiting is necessary, i.e. $\lambda_1 > 0$. This is both to ensure a proper breaking sequence in the spilling breakers and to limit the level of turbulence in the outer surf zone. It is, however, also clear, that the standard value proposed by Wilcox (2006) ($\lambda_1 = 0.875$) is probably too high, i.e. limiting production of turbulence too much. None of the chosen values give a perfect match in both surface elevations, turbulence levels and undertow profiles. Several other values have been attempted, but $\lambda_1 = 0.2$ was found to give the best results as a whole. This value have therefore been used in Chapters 6 and 7.

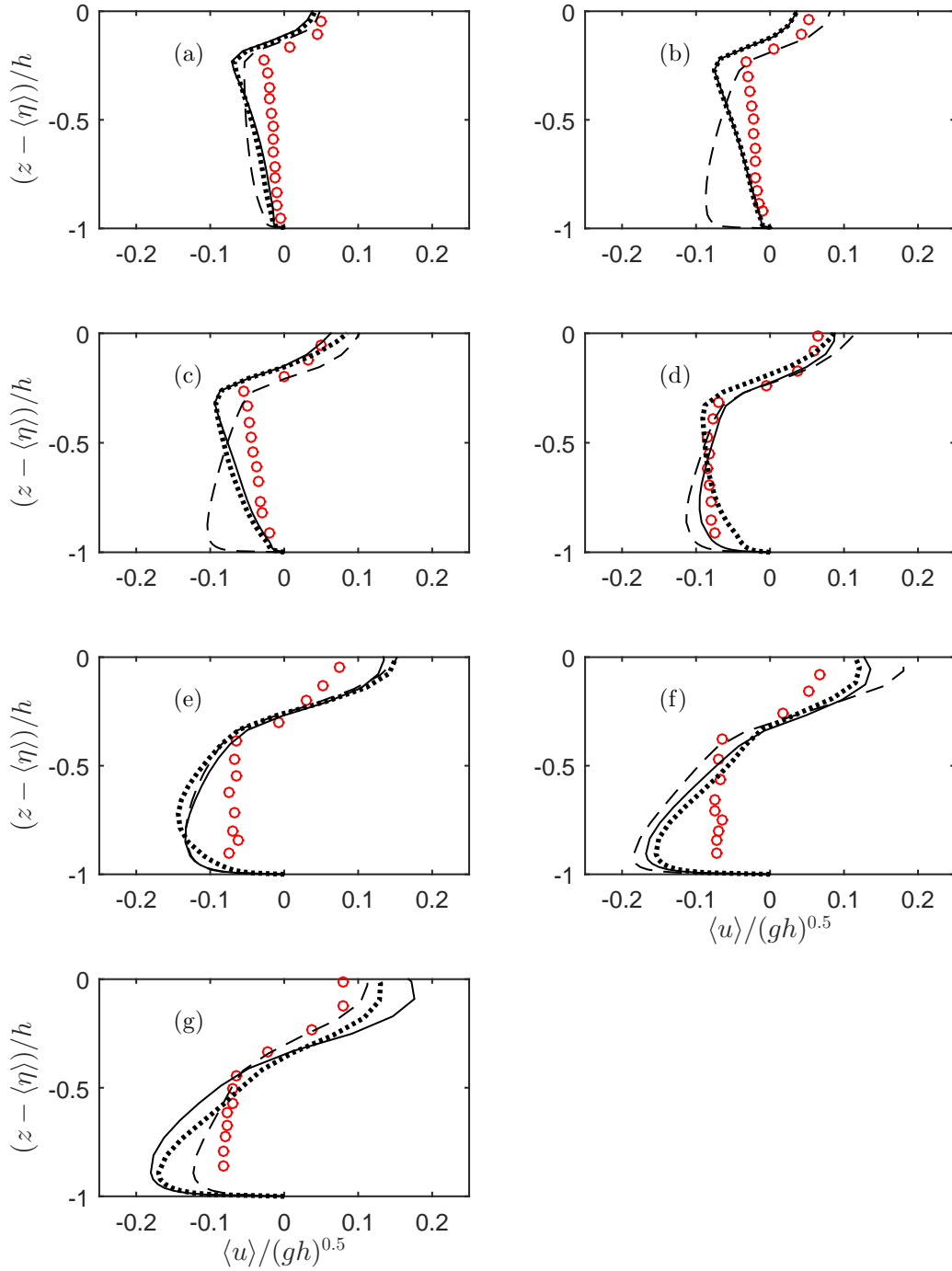


Figure 9.4: Comparison of modelled (lines) and measured (circles) undertow velocity profiles at (a) $x = 7.295$ m ($\tilde{x} = (x - x_b)/h_b = -3.247$), (b) $x = 7.795$ m ($\tilde{x} = 0$), (c) $x = 8.345$ m ($\tilde{x} = 3.571$), (d) $x = 8.795$ m ($\tilde{x} = 6.494$), (e) $x = 9.295$ m ($\tilde{x} = 9.740$), (f) $x = 9.795$ m ($\tilde{x} = 12.987$), (g) $x = 10.395$ m ($\tilde{x} = 16.883$).

References

- Aida, I., 1974. Numerical computation of a tsunami based on a fault origin model of an earthquake. *Zisin* (journal of the Seismological Society of Japan. 2nd Ser.) 27 (2), 141–154.
- Apotsos, A., Buckley, M., Gelfenbaum, G., Jaffe, B., Vatvani, D., 2011a. Nearshore tsunami inundation model validation: Toward sediment transport applications. *Pure and App. Geophys.* 168 (11), 2097–2119.
- Apotsos, A., Gelfenbaum, G., Jaffe, B., 2011b. Process-based modeling of tsunami inundation and sediment transport. *J. Geophys. Res.* 116 (1), 1–20.
- Apotsos, A., Gelfenbaum, G., Jaffe, B., Watt, S., Peck, B., Buckley, M., Stevens, A., 2011c. Tsunami inundation and sediment transport in a sediment-limited embayment on American Samoa. *Earth-Sci Rev.* 107 (1-2), 1–11.
- Arcas, D., Titov, V., 2006. Sumatra tsunami: lessons from modeling. *Surveys in Geophysics* 27 (6), 679–705.
- Baldock, T. E., Cox, D., Maddux, T., Killian, J., Fayler, L., 2009. Kinematics of breaking tsunami wavefronts: A data set from large scale laboratory experiments. *Coast. Eng.* 56 (5-6), 506–516.
- Baptista, A. M., Priest, G. R., Murty, T. S., 1993. Field survey of the 1992 Nicaragua tsunami. *Marine Geodesy* 16 (2), 169–203, 169–203.
- Baykal, C., Sumer, B. M., Fuhrman, D. R., Jacobsen, N. G., Fredsøe, J., 2015. Numerical investigation of flow and scour around a vertical circular cylinder. *Phil. Trans. Roy. Soc. A* 373, article no. 20140104.
- Baykal, C., Sumer, B. M., Fuhrman, D. R., Jacobsen, N. G., Fredsøe, J., 2017. Numerical simulation of scour and backfilling processes around a circular pile in waves. *Coast. Eng.* 122, 87–107.

- Bayraktar, D., Ahmad, J., Larsen, B. E., Carstensen, S., Fuhrman, D. R., 2016. Experimental and numerical study of wave-induced backfilling beneath submarine pipelines. *Coast. Eng.* 118, 63–75.
- Bernard, E. N., Mofjeld, H. O., Titov, V., Synolakis, C. E., Gonzalez, F. I., 2006. Tsunami: scientific frontiers mitigation, forecasting and policy implications. *Phil. Trans. Royal Soc. A.* 364 (1845), 1989–2006.
- Berry, M., 2005. Tsunami asymptotics. *New J. of Phys.* 7 (1), 129.
- Billi, A., Funiciello, R., Minelli, L., Faccenna, C., Neri, G., Orecchio, B., Presti, D., 2008. On the cause of the 1908 Messina tsunami, southern Italy. *Geophys. Res. Letters* 35 (6), L06301.
- Biscarini, C., 2010. Computational fluid dynamics modelling of landslide generated water waves. *Landslides* 7 (2), 117–124.
- Borrero, J. C., Synolakis, C. E., Fritz, H., 2006. Northern Sumatra field survey after the December 2004 Great Sumatra earthquake and Indian Ocean tsunami. *Earthquake Spectra* 22 (3), S93–S104.
- Braddock, R. D., Van Den Driessche, P., Peady, G. W., 1973. Tsunami generation. *J. Fluid Mech.* 59 (4), 817–28, 817–828.
- Bricker, J. D., Francis, M., Nakayama, A., 2012. Scour depths near coastal structures due to the 2011 Tohoku tsunami. *J. Hydraul. Res.* 50 (6), 637–641.
- Briggs, M. J., Synolakis, C. E., Harkins, G. S., Green, D. R., 1995. Laboratory experiments of tsunami runup on a circular island. *Pure Appl. Geophys.* 144, 569–593.
- Brown, S. A., Greaves, D. M., Magar, V., Conley, D. C., 2016. Evaluation of turbulence closure models under spilling and plunging breakers in the surf zone. *Coast. Eng.* 114, 177–193.
- Carrier, G. F., 1971. The physics of tsunamis. In: *Mathematical Problems in Geophysical Sciences. Proceedings of the Sixth Summer Seminar on Applied Mathematics*, Rensselaer Polytechnical Institute, Troy. American Mathematical Society.
- Carrier, G. F., Greenspan, H. P., 1958. Water waves of finite amplitude on a sloping beach. *J. Fluid Mech.* 4, 97–109.

- Chan, I.-C., Liu, P. L. F., 2012. On the runup of long waves on a plane beach. *J. Geophys. Res. - Oceans* 117 (8), 1–17.
- Charvet, I., Eames, I., Rossetto, T., 2013. New tsunami runup relationships based on long wave experiments. *Ocean Modelling* 69, 79–92.
- Chen, J., Huang, Z., Jiang, C., Deng, B., Long, Y., 2012. An experimental study of changes of beach profile and mean grain size caused by tsunami-like waves. *J. Coast. Res.* 28 (5), 1303–1312.
- Chen, J., Huang, Z., Jiang, C., Deng, B., Long, Y., 2013. Tsunami-induced scour at coastal roadways: a laboratory study. *Nat. Haz.* 69 (1), 655–674.
- Chen, J., Jiang, C., Yang, W., Xiao, G., 2016. Laboratory study on protection of tsunami-induced scour by offshore breakwaters. *Nat. Haz.* 81 (2), 1229–1247.
- Christensen, E. D., 2006. Large eddy simulation of spilling and plunging breakers. *Coast. Eng.* 53 (5-6), 463–485.
- Clarisse, J., Newman, J., Ursell, F., 1995. Integrals with a large parameter - water-waves on finite depth due to an impulse. *Proc. Royal Soc.-math. and Phys. Sci.* 450 (1938), 67–87.
- Dawson, A. G., Shi, S., 2000. Tsunami deposits. *Pure and Appl. Geophys.* 157 (6-8), 875–897.
- Drahne, U., Goseberg, N., Vater, S., Beisiegel, N., Behrens, J., 2016. An experimental and numerical study of long wave run-up on a plane beach. *J. Marine Sci. Eng.* 4 (1), 1 (23 pp.).
- Fraser, S., Raby, A., Pomonis, A., Goda, K., Chian, S. C., Macabuag, J., Offord, M., Saito, K., Sammonds, P., 2013. Tsunami damage to coastal defences and buildings in the march 11th 2011 m (w) 9.0 Great East Japan earthquake and tsunami. *Bulletin of Earthquake Engineering* 11 (1), 205–239.
- Fuhrman, D. R., Baykal, C., Sumer, B. M., Jacobsen, N. G., Fredsoe, J., 2014. Numerical simulation of wave-induced scour and backfilling processes beneath submarine pipelines. *Coast. Eng.* 94, 10–22.
- Fuhrman, D. R., Madsen, P. A., 2009. Tsunami generation, propagation, and run-up with a high-order boussinesq model. *Coast. Eng.* 56 (7), 747–758.

- Glinsdal, S., Pedersen, G. K., Harbitz, C. B., Lovholt, F., 2013. Dispersion of tsunamis: does it really matter? *Nat. Haz. and Earth Sys. Sci.* 13 (6), 1507–1526.
- Goring, D. G., 1978. Tsunamis – the propagation of long waves onto a shelf. Ph.D. thesis, California Institute of Technology.
- Goseberg, N., 2013. Reduction of maximum tsunami run-up due to the interaction with beachfront development - application of single sinusoidal waves. *Nat. Haz. and Earth Sys. Sci.* 13 (11), 2991–3010.
- Goseberg, N., Wurpts, A., Schlurmann, T., 2013. Laboratory-scale generation of tsunami and long waves. *Coast. Eng.* 79, 57–74.
- Goto, C., Ogawa, Y., 1997. Numerical method of tsunami simulation with the leap-frog scheme. *IUGG/IOC* 35, 126.
- Green, G., 1838. On the motion of waves in a variable canal of small depth and width. *Trans. Camp. Philos. Soc.* 6, 457–462.
- Grilli, S. T., Harris, J. C., Bakhsh, T. S. T., Masterlark, T. L., Kyriakopoulos, C., Kirby, J. T., Shi, F., 2013. Numerical simulation of the 2011 Tohoku tsunami based on a new transient FEM co-seismic source: Comparison to far- and near-field observations. *Pure and App. Geophys.* 170 (6-8), 1333–1359.
- Grue, J., Pelinovsky, E. N., Fructus, D., Talipova, T., Kharif, C., 2008. Formation of undular bores and solitary waves in the strait of Malacca caused by the 26 December 2004 Indian Ocean tsunami. *J. Geophys. Res.* 113 (C5), C05008.
- Hammack, J. L., 1973. A note on tsunamis: their generation and propagation in an ocean of uniform depth. *J. Fluid Mech.* 60, 769–799.
- Hammack, J. L., Segur, H., 1974. The Korteweg-de Vries equation and water waves. II. Comparison with experiments. *J. Fluid Mech.* 65, 289–314.
- Hammack, J. L., Segur, H., 1978. The korteweg-de vries equation and water waves. iii. oscillatory waves. *J. Fluid Mech.* 84 (2), 337–58, 337–358.
- Horrillo, J., Kowalik, Z., Shigihara, Y., 2006. Wave dispersion study in the Indian Ocean tsunami of December 26, 2004. *Sci. of Tsunami Ha.*
- Hunt, I. A., 1959. Design of seawalls and breakwaters. *J. Waterw. Harbors Division ASCE* 85, 123–152.

- Ioualalen, M., Asavanant, J., Kaewbanjak, N., Grilli, S. T., Kirby, J. T., Watts, P., 2007. Modeling the 26 December 2004 Indian Ocean tsunami: Case study of impact in Thailand. *J. Geophys. Res.* 112 (C7), C07024.
- Jacobsen, N. G., Fredsøe, J., Jensen, J. H., 2014. Formation and development of a breaker bar under regular waves. Part 1: Model description and hydrodynamics. *Coast. Eng.* 88, 182–193.
- Jaffe, B. E., Gelfenbuam, G., 2007. A simple model for calculating tsunami flow speed from tsunami deposits. *Sedimentary Geol.* 200 (3-4), 347–361.
- Jayaratne, M. P. R., Premaratne, B., Adewale, A., Mikami, T., Matsuba, S., Shibayama, T., Esteban, M., Nistor, I., 2016. Failure mechanisms and local scour at coastal structures induced by tsunami. *C. Eng. Journal* 58 (4), 1640017.
- Jiang, C., Chen, J., Yao, Y., Liu, J., Deng, Y., 2015. Study on threshold motion of sediment and bedload transport by tsunami waves. *Ocean Eng.* 100, 97–106.
- Johnson, J. P. L., Delbecq, K., Kim, W., Mohrig, D., 2016. Experimental tsunami deposits: Linking hydrodynamics to sediment entrainment, advection lengths and downstream fining. *Geomorphology* 253, 478–490.
- Kajura, K., 1963. The leading wave of a tsunami. *Bull. Earthquake Res.* 41, 525–571.
- Kato, F., Noguchi, K., Suwa, Y., Sakagami, T., Sato, Y., 2012. Field survey on tsunami-induced topographical change. *Journal of Japan Society of Civil Engineers, Ser. B3* 68 (2), 174–179.
- Kawai, H., Satoh, M., Kawaguchi, K., Seki, K., 2013. Characteristics of the 2011 Tohoku tsunami waveform acquired around Japan by NOWPHAS equipment. *Coast. Eng. J.* 55 (3), 1350008.
- Keller, J. B., Keller, H., 1964. Water wave run-up on a beach. *ONR Res. Rep. Contract NONR-3828(00)*. Dept. of the Navy, Washington, D.C., 40 pp.
- Kim, D.-H., Lynett, P. J., 2011. Dispersive and nonhydrostatic pressure effects at the front of surge. *J. Hydraul. Eng. ASCE* 137 (7), 754–765.
- Kobayashi, N., Lawrence, A. R., 2004. Cross-shore sediment transport under breaking solitary waves. *J. Geophys. Res.* 109, C03047/1–13.
- Kuriyama, Y., Takahashi, K., Yanagishima, S., Tomita, T., 2014. Beach profile change at Hasaki, Japan caused by 5-m-high tsunami due to the 2011 off the Pacific coast of Tohoku earthquake. *Mar. Geol.* 355, 234–243.

- Lacy, J. R., Rubin, D. M., Buscombe, D., 2012. Currents, drag, and sediment transport induced by a tsunami. *J. Geophys. Res.- Oceans* 117 (9), –.
- Lamb, H., 1932. *Hydrodynamics*. Cambridge University Press, Cambridge.
- Larsen, B. E., Arbøll, L. K., Frigaard, S., Carstensen, S., Fuhrman, D. R., 2018a. Experimental study of tsunami-induced scour around a monopile foundation. *Coast. Eng.* 138, 9–21.
- Larsen, B. E., Fuhrman, D. R., 2018a. Full-scale CFD simulation of tsunamis. part 1: Model validation and run-up. Under preparation.
- Larsen, B. E., Fuhrman, D. R., 2018b. Full-scale CFD simulation of tsunamis. part 2: Boundary layers and bed shear stresses. Under preparation.
- Larsen, B. E., Fuhrman, D. R., 2018c. On the over-production of turbulence beneath surface waves in Reynolds-averaged Navier-Stokes models. *J. Fluid Mech.* 853, 419–460.
- Larsen, B. E., Fuhrman, D. R., Baykal, C., Sumer, B. M., 2017. Tsunami-induced scour around monopile foundations. *Coast. Eng.* 129, 36–49.
- Larsen, B. E., Fuhrman, D. R., Roenby, J., 2018b. Performance of interFoam on the simulation of progressive waves. [axiv.org. ID: 1804.01158](https://arxiv.org/abs/1804.01158).
- Larsen, B. E., Fuhrman, D. R., Sumer, B. M., 2016. Simulation of wave-plus-current scour beneath submarine pipelines. *J. Waterw. Port C-ASCE* 142 (5), article no. 08216001.
- Lavictoire, A., 2015. *Bore-Induced Local Scour around a Circular Structure*. University of Ottawa. Canada. 2015.
- Leone, F., Lavigne, F., Paris, R., Denain, J.-C., Vinet, F., 2011. A spatial analysis of the december 26th, 2004 tsunami-induced damages lessons learned for a better risk assessment integrating buildings vulnerability. *App. Geography* 31 (1), 363–375.
- Levin, B., Nosov, M., 2016. *Physics of Tsunamis*. Springer Netherlands.
- Li, L., Huang, Z., Qiu, Q., Natawidjaja, D. H., Sieh, K., 2012a. Tsunami-induced coastal change: scenario studies for Painan, West Sumatra, Indonesia. *Earth Planets and Space* 64 (10), 799–816.

- Li, L., Qiu, Q., Huang, Z., 2012b. Numerical modeling of the morphological change in Lhok Nga, West Banda Aceh, during the 2004 Indian Ocean tsunami: understanding tsunami deposits using a forward modeling method. *Nat. Haz.* 64 (2), 1549–1574.
- Li, Y., 2000. Tsunamis: non-breaking and breaking solitary wave run-up. Ph.D. thesis, California Institute of Technology, Pasadena, California.
- Li, Y., Raichlen, F., 2001. Solitary wave runup on plane slopes. *J. Waterw. Port C-ASCE* 127, 33–44.
- Li, Y., Raichlen, F., 2002. Non-breaking and breaking solitary wave run-up. *J. Fluid Mech.* 456, 295–318.
- Li, Y., Raichlen, F., 2003. Energy balance model for breaking solitary wave runup. *J. Waterw. Port C-ASCE* 129, 47–59.
- Liu, P. L.-F., Cho, Y.-S., Briggs, M. J., Kanoglu, U., Synolakis, C. E., 1995. Runup of solitary waves on a circular island. *J. Fluid Mech.* 302, 259–285.
- Liu, P. L. F., Woo, S. B., Cho, Y. S., 1998. Computer programs for tsunami propagation and inundation. Ph.D. thesis, Natural Science Foundation.
- Løvholt, F., Kaiser, G., Glimsdal, S., Scheele, L., Harbitz, C. B., Pedersen, G., 2012. Modeling propagation and inundation of the 11 March 2011 Tohoku tsunami. *Nat. Haz. and Earth Sys. Sci.* 12 (4), 1017–1028.
- Lynett, P., Liu, P. L.-F., 2002. A numerical study of submarine-landslide-generated waves and run-up. *Proc. R. Soc. Lond. A* 458, 2885–2910.
- Lynett, P., Liu, P. L.-F., 2005. A numerical study of the run-up generated by three-dimensional landslides. *J. Geophys. Res.* 110, C03006/1–16.
- Lynett, P. J., Borrero, J. C., Liu, P. L. F., Synolakis, C. E., 2003. Field survey and numerical simulations: A review of the 1998 Papua New Guinea tsunami. *Pure and Appl. Geophys.* 160 (10-11), 2119–2146.
- Lynett, P. J., Wu, T.-R., Liu, P. L.-F., 2002. Modeling wave runup with depth-integrated equations. *Coast. Eng.* 46, 89–107.
- Madsen, P. A., Fuhrman, D. R., 2008. Run-up of tsunamis and long waves in terms of surf-similarity. *Coast. Eng.* 55, 209–223.

- Madsen, P. A., Fuhrman, D. R., Schäffer, H. A., 2008. On the solitary wave paradigm for tsunamis. *J. Geophys. Res.* 113, article no. C12012.
- Madsen, P. A., Schäffer, H. A., 2010. Analytical solutions for tsunami runup on a plane beach. *J. Fluid Mech.* 645, 27–57.
- Madsen, P. A., Schffer, H. A., Fuhrman, D. R., Toledo, Y., 2016. Uniform asymptotic approximations for transient waves due to an initial disturbance. *J. Geophys. Res.* 121 (1), 60–84.
- Matsuyama, M., Ikeno, M., Sakakiyama, T., Takeda, T., 2007. A study of tsunami wave fission in an undistorted experiment. *Pure and App. Geophys.* 164 (2-3), 617–631.
- Mayer, S., Madsen, P. A., 2000. Simulations of breaking waves in the surf zone using a Navier-Stokes solver. In: *Proc. 25th Int. Conf. Coast. Eng. Sydney, Australia*, pp. 928–941.
- Montagna, F., Bellotti, G., Di Risio, M., 2011. 3D numerical modeling of landslide-generated tsunamis around a conical island. *Nat. Haz.* 58 (1), 591–608.
- Moore, A. L., McAdoo, B. G., Ruffman, A., 2007. Landward fining from multiple sources in a sand sheet deposited by the 1929 Grand Banks tsunami, Newfoundland. *Sedimentary Geol.* 200 (3-4), 336–346.
- Mori, N., Takahashi, T., Yasuda, T., Yanagisawa, H., 2011. Survey of 2011 Tohoku earthquake tsunami inundation and run-up. *Geophys. Res. Letters* 38 (18), L00G14.
- Nakamura, T., Kuramitsu, Y., Mizutani, N., 2008. Tsunami scour around a square structure. *Coast. Eng. J.* 50 (2), 209–246.
- NASA, 2005. Tsunami destroys Lhoknga, Indonesia. NASA Earth Observatory.
 URL <https://earthobservatory.nasa.gov/IOTD/view.php?id=5132>,
 retrieved February 15, 2018
- NOAA, 2011. Tsunami sources 1410 b.c. to a.d. 2011 from earthquakes, volcanoes, landslides and other causes. National Oceanic and Atmospheric Administration.
 URL https://toolkit.climate.gov/sites/default/files/tsunami_prone_map-1.jpg,
 retrieved February 15, 2018

- Ontowirjo, B., Paris, R., Mano, A., 2013. Modeling of coastal erosion and sediment deposition during the 2004 Indian Ocean tsunami in Lhok Nga, Sumatra, Indonesia. *Nat. Haz.* 65 (3), 1967–1979.
- Pan, C., Huang, W., 2012. Numerical modeling of tsunami wave run-up and effects on sediment scour around a cylindrical pier. *J. Eng. Mech. - ASCE* 138 (10), 1224–1235.
- Paris, R., Nandasena, N. A. K., Fournier, J., 2012. Comment on 'reconstructing tsunami run-up from the characteristics of tsunami deposits on the Thai Andaman Coast' by Srisutam and Wagner (2010). *Coast. Eng.* 61 (1), 53–55.
- Paris, R., Wassmer, P., Sartohadi, J., Lavigne, F., Barthomeuf, B., Desgages, E., Grancher, D., Baumert, P., Vautier, F., Brunstein, D., Gomez, C., 2009. Tsunamis as geomorphic crises: Lessons from the December 26, 2004 tsunami in Lhok Nga, West Banda Aceh (Sumatra, Indonesia). *Geomorphology* 104 (1-2), 59–72.
- Park, H., Cox, D. T., Petroff, C. M., 2015. An empirical solution for tsunami run-up on compound slopes. *Nat. Haz.* 76 (3), 1727–1743.
- Qu, K., Ren, X. Y., Kraatz, S., 2017. Numerical investigation of tsunami-like wave hydrodynamic characteristics and its comparison with solitary wave. *App. Ocean Res.* 63, 36–48.
- Roenby, J., Bredmose, H., Jasak, H., 2016. A computational method for sharp interface advection. *Royal Society Open Science* 3 (11), 160405.
- Roenby, J., Larsen, B. E., Bredmose, H., Jasak, H., 2017. A new volume-of-fluid method in OpenFOAM. In: 7th Int. Conf. Comput. Methods Marine Eng. 7th Int. Conf. Comput. Methods Marine Eng. Nantes, France, pp. 1–12.
- Rossetto, T., Allsop, W., Charvet, I., Robinson, D. I., 2011. Physical modelling of tsunami using a new pneumatic wave generator. *Coast. Eng.* 58 (6), 517–527.
- Schimmels, S., Sriram, V., Didenkulova, I., 2016. Tsunami generation in a large scale experimental facility. *Coast. Eng.* 110, 32–41.
- Segur, H., 1973. The Korteweg-de Vries equation and water waves. solutions of the equation. i. *J. Fluid Mech.* 59 (4), 721–36, 721–736.
- Shafiei, S., Melville, B. W., Shamseldin, A. Y., Watts, M. J. H., Hoffman, T. G., 2015. Experimental investigation of tsunami bore induced scour around structures. *Australian Coasts and Ports 2015 Conference*, 807–813.

- Shibayama, T., 2015. 2004 Indian Ocean tsunami. Handbook Coast. Disaster Mitigation for Engineers and Planners, 3–19.
- Song, Y. T., Ji, C., Fu, L. L., Zlotnicki, V., Shum, C. K., Yi, Y. C., Hjorleifsdottir, V., 2005. The 26 december 2004 tsunami source estimated from satellite radar altimetry and seismic waves. *Geophys. Res. Lett.* 32 (20), L20601, 1–5.
- Soulsby, R. L., Smith, D. E., Ruffman, A., 2007. Reconstructing tsunami run-up from sedimentary characteristics - a simple mathematical model. Coastal Sediments '07 - Proceedings of 6th International Symposium on Coastal Engineering and Science of Coastal Sediment Processes.
- Spiske, M., Weiss, R., Bahlburg, H., Roskosch, J., Amijaya, H., 2010. The TsuSed-Mod inversion model applied to the deposits of the 2004 Sumatra and 2006 Java tsunami and implications for estimating flow parameters of palaeo-tsunami. *Sedimentary Geol.* 224 (1-4), 29–37.
- Sriram, V., Didenkulova, I., Sergeeva, A., Schimmels, S., 2016. Tsunami evolution and run-up in a large scale experimental facility. *Coast. Eng.* 111, 1–12.
- Sugawara, D., Goto, K., Jaffe, B. E., 2014a. Numerical models of tsunami sediment transport - current understanding and future directions. *Mar. Geol.* 352, 295–320.
- Sugawara, D., Takahashi, T., Imamura, F., 2014b. Sediment transport due to the 2011 Tohoku-Oki tsunami at Sendai: Results from numerical modeling. *Mar. Geol.* 358, 18–37.
- Suppasri, A., Muhari, A., Ranasinghe, P., Mas, E., Shuto, N., Imamura, F., Koshimura, S., 2012. Damage and reconstruction after the 2004 Indian Ocean tsunami and the 2011 Great East Japan tsunami. *J. Nat. Disaster Sc.* 34 (1), 19–39.
- Synolakis, C. E., 1986. The run-up of long waves. Ph.D. thesis, California Institute of Technology, Pasadena, California.
- Synolakis, C. E., 1987. The run-up of solitary waves. *J. Fluid Mech.* 185, 523–545.
- Synolakis, C. E., Bernard, E. N., 2006. Tsunami science before and beyond Boxing Day 2004. *Phil. Trans. Roy. Soc. Lond. A* 364, 2231–2265.
- Synolakis, C. E., Kong, L., 2006. Runup measurements of the December 2004 Indian Ocean tsunami. *Earthquake Spectra* 22 (3), S67–S91.

- Tanaka, H., Adityawan, M. B., Mitobe, Y., Widiyanto, W., 2016. A new computation method of bottom shear stress under tsunami waves. *J. of Coast. Res.* 1 (75), 1247–1251.
- Tang, H., 2017. Forward and inverse modeling of tsunami sediment transport. Ph.D. thesis, Virginia Polytechnical Institute and State University, Virginia.
- Tang, L., Titov, V. V., Bernard, E. N., Wei, Y., Chamberlin, C. D., Newman, J. C., Mofjeld, H. O., Arcas, D., Eble, M. C., Moore, C., Uslu, B., Pells, C., Spillane, M., Wright, L., Gica, E., 2012. Direct energy estimation of the 2011 Japan tsunami using deep-ocean pressure measurements. *J. Geophys. Res.* 117 (8), C08008.
- Tang, L., Titov, V. V., Chamberlin, C. D., 2009. Development, testing, and applications of site-specific tsunami inundation models for real-time forecasting. *J. Geophys. Res.* 114 (12), C12025.
- Ting, F. C. K., Kirby, J. T., 1994. Observation of undertow and turbulence in a laboratory surf zone. *Coast. Eng.* 24 (1-2), 51–80.
- Titov, V., Kanoglu, U., Synolakis, C., 2016. Development of most for real-time tsunami forecasting. *J. Waterw. Port C-ASCE* 142 (6), 03116004.
- Titov, V. V., Gonzalez, F. I., Bernard, E. N. ., Eble, M. C., Mofjeld, H. O., Newman, J. C., Venturato, A. J., 2005. Real-time tsunami forecasting: Challenges and solutions. *Nat. Haz.* 35 (1), 41–58.
- Titov, V. V., Synolakis, C. E., 1997. Extreme inundation flows during the hokkaido-nansei-oki tsunami. *Geophysical Research Letters* 24 (11), 1315–1318.
- Titov, V. V., Synolakis, C. E., 1998. Numerical modeling of tidal wave runup. *J. Waterw. Port C-ASCE* 124, 157–171.
- Tomita, T., Honda, K., Kakinuma, T., 2006. Application of Storm surge and Tsunami simulator in Oceans and Coastal areas (STOC) to tsunami analysis. In: Joint Panel Conference of the U.S.-Japan Cooperative Program in Natural Resources, , Volume 38. pp. 109–115.
- Tomita, T., Takahashi, K., 2014. Simulation of tsunami accompanied by breaking short-period waves. *Coast. Eng. Proc.* 1 (34), 2.
- Tonkin, S., Yeh, H., Kato, F., Sato, S., 2003. Tsunami scour around a cylinder. *J. Fluid Mech.* 496 (496), 165–192.

- Udo, K., Takeda, Y., Tanaka, H., 2016. Coastal morphology change before and after 2011 off the Pacific coast of Tohoku earthquake tsunami at Rikuzen-Takata coast. *Coast. Eng. Journal* 58 (4), 1640016.
- V. Titov, V., I. Gonzalez, F., 1997. Implementation and testing of the method of splitting tsunami (MOST) model. NOAA Technical Memorandum ERL PMEL-112.
- van Dorn, W., 1965. Tsunamis. *Adv. in Hydrosience* 2, 1–48.
- Wang, D., Li, S., Arikawa, T., Gen, H., 2016. ISPH simulation of scour behind seawall due to continuous tsunami overflow. *Coast. Eng. J.* 58 (3), 16500145.
- Wilcox, D. C., 1988. Reassessment of the scale-determining equation for advanced turbulence models. *AIAA J.* 26 (11), 1299–1310.
- Wilcox, D. C., 2006. *Turbulence Modeling for CFD*, 3rd Edition. DCW Industries, Inc., La Canada, California.
- Williams, I. A., Fuhrman, D. R., 2016. Numerical simulation of tsunami-scale wave boundary layers. *Coast. Eng.* 110, 17–31.
- Wilson, R., Davenport, C., Jaffe, B., 2012. Sediment scour and deposition within harbors in California (USA), caused by the March 11, 2011 Tohoku-oki tsunami. *Sedimentary Geol.* 282, 228–240.
- Yamaguchi, N., Sekiguchi, T., 2015. Effects of tsunami magnitude and terrestrial topography on sedimentary processes and distribution of tsunami deposits in flume experiments. *Sedimentary Geol.* 328, 115–121.
- Yamashita, K., Sugawara, D., Takahashi, T., Imamura, F., Saito, Y., Imato, Y., Kai, T., Uehara, H., Kato, T., Nakata, K., Saka, R., Nishikawa, A., 2016. Numerical simulations of large-scale sediment transport caused by the 2011 Tohoku earthquake tsunami in Hirota Bay, Southern Sanriku Coast. *Coast. Eng. J.* 58 (4), 1640015.
- Yeh, H., Liu, P., Briggs, M., Synolakis, C., 1994. Propagation and amplification of tsunamis at coastal boundaries. *Nature* 372 (6504), 353–355.
- Yoshii, T., Tanaka, S., Matsuyama, M., 2017. Tsunami deposits in a super-large wave flume. *Mar. Geol.* 391, 98–107.

DTU Mechanical Engineering
Section of Fluid Mechanics, Coastal and Maritime Engineering
Technical University of Denmark

Nils Koppels Allé, Bld. 403
DK-2800 Kgs. Lyngby
Denmark
Phone (+45) 4525 1360
Fax (+45) 4588 4325

www.mek.dtu.dk

DCAMM
Danish Center for Applied Mathematics and Mechanics

Nils Koppels Allé, Bld. 404
DK-2800 Kgs. Lyngby
Denmark
Phone (+45) 4525 4250
Fax (+45) 4593 1475
www.dcam.dk
ISSN: 0903-1685